Intercontinental optical clock comparison using the geodetic VLBI technique in K-band

Proceedings of the 26th European VLBI Group for Geodesy and Astrometry Working Meeting

11–15 June 2023
Bad Kötzting, Germany

edited by
R. Haas, E. Schroth, and A. Neidhardt

Proceedings of the 26th European VLBI Group for Geodesy and Astrometry Working Meeting

edited by
Rüdiger Haas, Eva Schroth and Alexander Neidhardt

Cover: Pictures of the Wettzell twin telescopes, WETTZ13S (left) and WETTZ13N (right), taken during EVGA 2023.

December 2023

DOI: 10.14459/2023md1730292
(2023 | eds. Rüdiger Haas, Eva Schroth, Alexander Neidhardt | Proceedings of the 26th European VLBI Group for Geodesy and Astrometry Working Meeting | E-book)

Preface

The 26th Working Meeting of the European VLBI Group for Geodesy and Astrometry (EVGA) was held 11–15 June 2023 at Bad Kötzting, Germany. The meeting started with an ice breaker and registration on Sunday, 11 June, at Hotel-Gasthof zur Post in Bad Kötzting. Since EVGA 2023 was one of the first in-person VLBI meetings after the Covid-19 pandemic, the icebreaker was a great opportunity to meet and talk to dear colleagues that one had not seen and met for long time. This was very much appreciated.

On Monday, 12 June, the scientific program started with oral presentations 09:00–17:45 in the conference hall of Hotel-Gasthof zur Post. The oral presentations on all three days were given in sessions of 3 presentations of 15 minutes each. The presentation sessions were ordered thematically, and each session had a dedicated session chair person. In between the 45 minutes long presentation sessions there were breaks, either shorter "stretch your legs breaks" of 15 minutes, coffee breaks of 30 minutes, or lunch breaks of 90 minutes. The audience thus got a lot of opportunities to move their bodies, and even to interact and talk to colleagues during these breaks. Lunch during EVGA 2023 was served in the Hotel-Gasthof zur Post and could be taken outdoors in the nice and warm summer weather.

The Tuesday morning continues with oral presentations, and the afternoon was dedicated to the poster session 14:30–17:30. The poster session started with voluntary and spontaneous, very short advertisements given by the poster presenters. This was done in order to inform the audience very briefly on the poster contents, and to introduce the poster presenters to the audience very clearly. In the evening, the conference participants attended the EVGA 2023 dinner at the brewery "Lindner Bräu" in Bad Kötzting. This nice outdoor dinner at the brewery included typical Bavarian food and beverages, which was very much appreciated by the conference participants. Since most participants stayed in walking distance, the evening ended for most with a nice stroll in the warm June night back to their accomodations.

The oral presentations on the third conference day, Wednesday, ended at lunch. After that, there were several activities offered, e.g. a guided tour in Bad Kötzting, a visit to a museum, a hiking tour, that all ended in an excursion to the Geodetic Observatory Wettzell, see Fig. 1. At Wettzell, the various scientific instruments could be visited, before going back to Bad Kötzting.

The fourth day, Thursday, 15 June, was dedicated to an IVS Analysis Workshop in the morning, and IVS splinter meetings in the afternoon.

In total there were 90 participants on site, as well as 20 online participants. Counting both groups, we are back on the same level as before the Covid-19 pandemic, see Fig. 2. The EVGA 2023 group photo is shown in Fig. 3. We were very honored that emeritus Prof. James Campbell participated in EVGA 2023. Prof. Campbell is one of the founding fathers of the EVGA and has importantly contributed to research in VLBI for geodesy and astrometry since the late 1970ies. He has been the PhD thesis adviser for a large number of scientists who are active today in VLBI, both within Europe and internationally.

Figure 1: The Geodetic Observatory Wettzell.

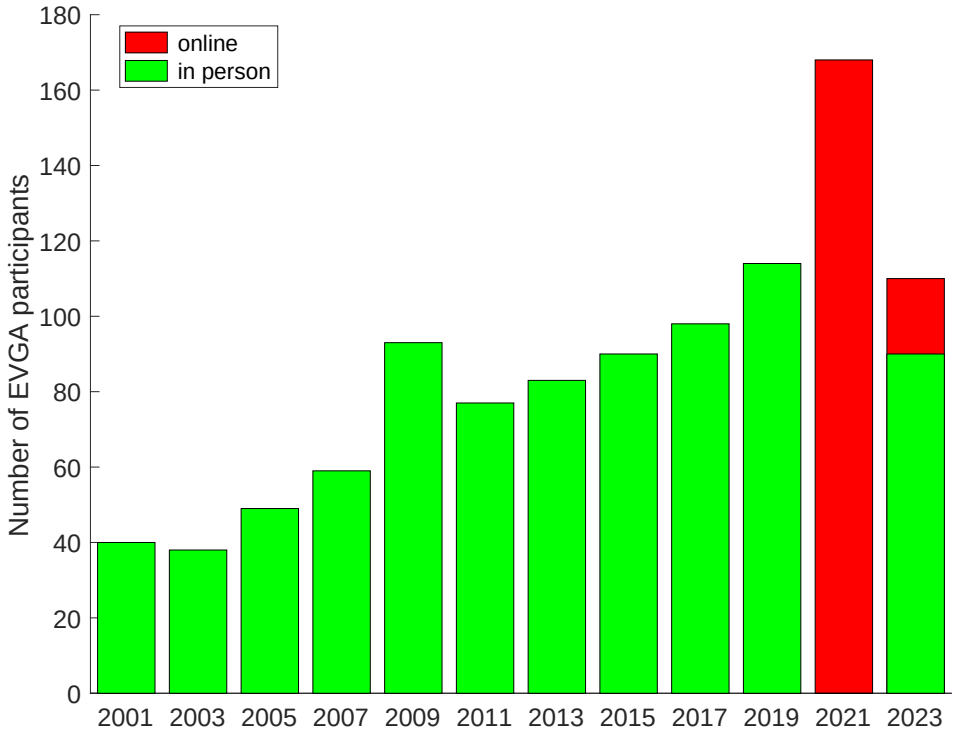

Figure 2: Number of registered participants at EVGA meetings during the last two decades.

In total we had 46 oral presentations and 26 poster presentations. The detailed conference program is provided on the following pages. Most of the presentations are available on `https://zenodo.org/communities/evga2023`.

Figure 3: Group picture of the EVGA 2023 participants.

The large number of participants at the EVGA 2023 Working Meeting, and the high quality of the presented contributions are very strong indicators for an active and prospering European VLBI community. This is very encouraging for the future!

We want to thank all participants for sharing their interesting findings with the audience during interesting oral and poster presentations. We want to thank the scientific organising committee (SOC) for putting together a very interesting meeting program and the local organising committee for organising (LOC) for the excellent arrangement of this conference.

We are grateful to all authors for preparing their interesting proceedings contributions. The proceedings are available in electronic form at the EVGA webpage `evga.org`.

December 2023
Rüdiger Haas (EVGA chair)

EVGA 2023 organising committees

Scientific Organizing Committee (SOC)

- Simone Bernhart (Reichert GmbH/BKG/MPIfR Bonn, DE)
- Sigrid Böhm (Technische Universität Wien, AU)
- Susana Garcia-Espada (Kartverket, NO)
- Rüdiger Haas (Chalmers tekniska högskola, SE)
- Karine Le Bail (Chalmers tekniska högskola, SE)
- Daniela Thaller (BKG Frankfurt, DE)
- Vincenza Tornatore (Politecnico di Milano, IT)
- Nataliya Zubko (Maanmittauslaitos, FI)

Local Organizing Committee (LOC)

- Eva Schroth (LOC chair)
- Torben Schüler (LOC co-chair)
- Alexander Neidhardt
- Christian Plötz
- Thomas Klügel

Series of events during the EVGA 2023

Date	Time	Event
11 June	18:00—21:00	EVGA 2023 Icebreaker and registration
12 June	08:45—17:45	EVGA 2023 Day-1
	18:00—20:00	VTC meeting
13 June	09:00—18:00	EVGA 2023 Day-2
	18:00—23:59	EVGA 2023 conference dinner
14 June	09:00—19:00	EVGA 2023 Day-3 and excursions
15 June	09:00—18:00	IVS Analysis Workshop and splinter meetings

Program of EVGA2023

updated 2023-06-06

2023-06-11

Icebreaker and registration	Register, meet your friends, talk to your colleagues.	18:00–21:00

2023-06-12 EVGA2023 Day-1

Welcome		**Rüdiger Haas, Eva Schroth**	08:45–09:00
Session-1.1 (45 min)		**Chairperson: Sigrid Böhm**	
Garcia Espada	O-09	Status at Ny-Ålesund Geodetic Earth Observatory	09:00–09:15
Azcue	O-01	RAEGE capabilities: a simulation study	09:15–09:30
McCallum	O-27	The AuScope Array - Recent developments	09:30–09:45
Strech your legs break (15 min)			09:45–10:00
Session-1.2 (45 min)		**Chairperson: Susana Gracia Espada**	
Jaradat	O-18	The Australian VGOS Observing Program	10:00–10:15
Kristukat	O-24	VGOS for AGGO	10:15–10:30
Dhar	O-06	Indian space geodesy project “SaptaRishi”: Current status and outlook	10:30–10:45
Coffee break (30 min)			10:45–11:15
Session-1.3 (45 min)		**Chairperson: Simone Bernhart**	
Ruszczyk	O-35	Present state and future outlook for Mark6’s	11:15–11:30
Alef	O-40	Progress on the BRAND extreme-wideband receiver	11:30–11:45
Tuccari	O-41	DBBC4	11:45–12:00
Strech your legs break (15 min)			12:00–12:15
Session-1.4 (45 min)		**Chairperson: Lucia McCallum**	
Neidhardt	O-29	New features in the IVS Seamless Auxiliary Data Archive (IVS SADA)	12:15–12:30
Schüler	O-37	First Experiences with the VLBI Quality Control System at Wettzell	12:30–12:45
Schartner	O-36	Active mitigation of spaceborne radio frequency interference	12:45–13:00
Lunch break (90 min)			13:00–14:30
Session-1.5 (45 min)		**Chairperson: Lisa Kern**	
Choi	O-04	Bonn Correlator Status	14:30–14:45
Plötz	O-32	VLBI correlator Wettzell - One year of experience as IVS correlator	14:45–15:00
Walenta	O-42	The Level 1 Data: availability and benefits	15:00–15:15
Strech your legs break (15 min)			15:15–15:30

Session-1.6 (45 min)		Chairperson: Vincenza Tornatore	
Flohrer	O-08	Enhancing the Bernese GNSS Software for multi-technique analysis at BKG - Focus on the VLBI implementation	15:30–15:45
Hellmers	O-16	Investigating software specific dependencies within the intra-technique VLBI combination	15:45–16:00
Lösler	O-26	On the consideration of frequency-dependent illumination functions in modelling signal path variations	16:00–16:15
Coffee break (30 min)			16:15–16:45

Session-1.7 (60 min)		Chairperson: Hana Krasna	
Glomsda	O-11	Investigating the datum parameters of new solutions by IVS AC DGFI-TUM	16:45–17:00
Le Bail	O-25	Exploring reasons for the ITRF2020 VLBI scale drift	17:00–17:15
Glaser	O-43	Investigating the VLBI Scale w.r.t. different TRFs	17:15–17:30
Nilsson	O-30	Improved modelling for future VLBI contributions to ITRF	17:30–17:45
End of EVGA2023 Day-1, time for splinter meetings, and dinner			17:45–23:59

VTC meeting	18:00–20:00

2023-06-13 EVGA2023 Day-2

Session-2.1 (45 min)		Chairperson: Claudia Flohrer	
Böhm	O-02	Earth orientation parameters estimated from recent Australian mixed-mode and Southern Intensive sessions	09:00–09:15
Gipson	O-10	Operational KOKEE12M–WETTZ13S VGOS Intensives	09:15–09:30
Dieck	O-07	Eliminating the Wiggle in the Wobble	09:30–09:45
Strech your legs break (15 min)			09:45–10:00

Session-2.2 (45 min)		Chairperson: Karine Le Bail	
Charlot	O-03	Imaging ICRF3 sources at 0.2 mas resolution with the European VLBI Network at K band	10:00–10:15
Xu	O-45	Imaging VGOS observations and source structure effect	10:15–10:30
de Witt	O-05	The K-band (24 GHz) Celestial Reference Frame: Current Status and Roadmap	10:30–10:45
Coffee break (30 min)			10:45–11:15

Session-2.3 (45 min)		Chairperson: Aletha de Witt	
Karbon	O-20	Exploring different methods to describe source position variations	11:15–11:30
Kareinen	O-21	Mitigating the effect of source structure in geodetic VLBI using closure delays and baseline-to-jet orientation	11:30–11:45
Krasna	O-23	The benefits of the Australian mixed-mode program (2018 - 2023) for the celestial reference frame at S/X-band	11:45–12:00
Strech your legs break (15 min)			12:00–12:15

Session-2.4 (45 min)		Chairperson: Nataliya Zubko	
Handirk	O-15	Obtaining Local-Tie Vectors from Short-Baseline Interferometry between legacy S/X and VGOS Telescopes	12:15–12:30
Jacobs	O-17	Twin Telescope Tests: Tying Goldstone Antennas at the mm level	12:30–12:45
Kern	O-22	Neglected issues of terrestrial datum definition in VLBI	12:45–13:00
Lunch break (90 min)			13:00–14:30

Poster session	Poster viewing , see list of posters below	14:30–17:30
End of EVGA2023 Day-2, EVGA2023 DINNER @ "Lindner Bräu"		**18:00–23:59**

2023-06-14 EVGA2023 Day-3

Session-3.1 (45 min)		Chairperson: Yoon Kyung Choi	
Jaron	O-19	Cross-polarization bandpasses of VGOS antennas	09:00–09:15
Skeens	O-39	Using a GNSS-radiotelescope interferometer to produce geodetic observables	09:15–09:30
Greiwe	O-12	Close-Range Photogrammetry for Antenna Deformation Measurements	09:30–09:45
Strech your legs break (15 min)			09:45–10:00

Session-3.2 (45 min)		Chairperson: Anastasiia Walenta	
Moreira	O-28	Assessing the consistency of the conventional reference frames (terrestrial and celestial) and their impact on estimated EOP using VLBI-based data	10:00–10:15
Haas	O-13	Atmospheric parameters derived from VGOS sessions observed with the Onsala twin telescopes	10:15–10:30
Habana	O-14	Characterization of the Atmospheric Turbulence using the Outputs of Assimilation Numerical Weather Models	10:30–10:45
Coffee break (30 min)			10:45–11:15

Session-3.3 (45 min)		Chairperson: Maria Karbon	
Zubko	O-46	VGOS dTEC assesment using TEC GIM maps	11:15-11:30
Ricci	O-34	Intercontinental optical clock comparison using the geodetic VLBI technique in K-band	11:30-11:45
Petrov	O-31	On VLBI errors	11:45-12:00
Strech your legs break (15 min)			12:00–12:15

Session-3.4 (45 min)		Chairperson: Daniela Thaller	
Wolf	O-44	Absolute orientation of Galileo orbits from simulated VLBI and GNSS observations	12:15–12:30
Raut	O-33	Simulations of a VLBI transmitter on next-generation GNSS	12:30–12:45
Schunck	O-38	Efforts in Satellite VLBI at the University of Tasmania	12:45–13:00

Closing remarks	Rüdiger Haas	13:00-13:15

Short lunch (60 min)		13:15–14:15
End of EVGA2023 Day-3, Excursion to Wettzell etc.		**14:15–19:00**

POSTERS		On display 2023-06-12/13/14
Bautista-Duran	P-01	The compatibility of DORIS with VGOS
Behrend	P-02	The VGOS High Road: From Inception and Prototyping to Operations to Maturation and Beyond
Coetzer	P-03	Data Identifiers and Metadata for the IVS
de Witt	P-04	Imaging, modelfitting and source structure corrections for the K-band (24 GHz) Celestial Reference Frame
Elgered	P-05	On the use of water vapour radiometry for assessment of wet delay estimates from space geodetic techniques
Elgered	P-06	Radiometry performance of a VGOS receiver
Habana	P-07	Study of Baseline Telemetry at NASA VGOS Sites
Jacobs	P-08	The X/Ka 2023a Celestial Frame
Karatekin	P-09	VLBI signals transmitted from Earth orbiting satellites
Klemm	P-10	Combined Earth Rotation Parameters based on homogenous VLBI and GNSS data: A closer look at today's VLBI Intensives
Kronschnabl	P-11	Performance and technical equipment for the VGOS radio telescope TTW1 (Wn)
Laha	P-12	Comparison between VLBI and other space geodetic techniques for determining Earth orientation parameters
Lemoine	P-13	Update on the VGOS-INT-S Program between MACGO12M and WETTZ13S
Mammadaliyev	P-14	Exploring the Efficacy of Space-Tie Vectors for SLR and VLBI Combination
Matsumoto	P-15	The Australia - Japan VGOS observation
McCallum	P-16	The Australian mixed-mode stations in a nutshell
Modiri	P-17	Closing the Gap: A Redesigned Prediction Package for Enhanced Accuracy of EOP Prediction using Single Space Geodetic Techniques
Neidhardt	P-18	RFI monitoring using mark5access spectra and Python programs
Petrov	P-19	Wide-band phase calibration system
Schwarz	P-20	An overview of Water Vapor Radiometers at the Geodetic Observatory Wettzell and the Argentinean German Geodetic Observatory
Singh	P-21	Analysis of non-tidal loading deformation at VLBI sites
Svehla	P-22	Proposal to IVS: Extension of the ICRF Frame to L-Band for the Observation of GNSS Constellations in the Celestial Frame
Takagi	P-23	Status of Ishioka Geodetic Observing Station
Tornatore	P-24	How to deal with expanding telecommunication networks using spectrum of VLBI?
Walenta	P-25	Current status at BKG IVS-DC
Zubko	P-26	Recent developments at Metsähovi Geodetic Research Station

Contents

Progress on the BRAND extreme-wideband receiver
W. Alef, G. Tuccari, S. Dornbusch, M. Wunderlich, H. Rottmann, A. Felke 4

RAEGE capabilities: Current Status and Analysis RAEGE Group
E. Azcue, M. Karbon, S. Belda, V. Puente, M. Moreira, J. A. López-Péréz 9

The compatibility of DORIS with VGOS
M. Bautista-Duran, J. S. Ferreira, S. García, H. Hase, J. Kallunki, M. Lindqvist, J. A. López-Péréz, W. Madkour, D. McKay, W. Probst, L. M. Tangen, V. Tornatore, B. Winkel 14

The VGOS High Road: From Inception and Prototyping to Operations to Maturation and Beyond
D. Behrend, C. Ruszczyk, P. Elosegui, A. Neidhardt 19

Earth orientation parameters estimated from recent Australian mixed-mode and Southern Intensive sessions
S. Böhm, L. McCallum 24

Imaging ICRF3 sources at 0.2 mas resolution with the European VLBI Network at K band
P. Charlot, M. E. Gómez, R. M. Campbell, A. Collioud, A. Keimpema, M. Kettenis 28

Bonn Correlator Status
Y. K. Choi, S. Bernhart, H. Rottmann, J. Wagner 32

Digital Identifiers and Metadata for the IVS
G. L. Coetzer, Y. Takagi, M. Nickola 36

Imaging, Modelfitting, and Source Structure Corrections for the K-band (24 GHz) Celestial Reference Frame
A. de Witt, C. Jacobs, D. Gordon, M. Bietenholz, H. Krásná, M. Johnson, L. Hunt, N. Mwiya, M. Nickola 40

Radiometry performance of the VGOS receivers of the Onsala twin telescopes
G. Elgered, P. Forkman, R. Haas, E. Varenius 45

On the use of water vapour radiometry for assessment of wet delay estimates from space geodetic techniques
G. Elgered, T. Ning 50

Enhancing the Bernese GNSS Software for multi-technique analysis at BKG - Focus on the VLBI implementation
C. Flohrer, A. Walenta, D. Thaller, C. Gattano, R. Dach, U. Hugentobler 55

Investigating the datum parameters of new solutions by IVS AC DGFI-TUM
M. Glomsda, M. Seitz, M. Bloßfeld, D. Angermann 61

Current Status at BKG IVS Data Center
M. Goltz, A. Walenta, D. Thaller 66

Close-Range photogrammetry for antenna deformation measurements
A. Greiwe, R. Brechtken, M. Lösler, C. Eschelbach, G. Kronschnabl, C. Plötz, A. Neidhardt 70

Atmospheric parameters derived from VGOS sessions observed with the Onsala twin telescopes
R. Haas, G. Elgered 76

Investigating software specific dependencies within the intra-technique VLBI combination
H. Hellmers, S. Modiri, S. Bachmann, D. Thaller, M. Bloßfeld, M. Seitz 81

VLBI signals transmitted from Earth orbiting satellites
Ö. Karatekin, H. Sert, V. Dehant, B. Ritter, H. Vasseur, U. Hugentobler 87

Vienna Combination Software - VieCompy
L. Kern, H. Krásná, J. Böhm, A. Nothnagel, M. Madzak 92

The benefits of the Australian mixed-mode program (2018 - 2023) for the celestial reference frame at S/X-band
H. Krásná, L. McCallum, T. McCarthy 96

A VGOS antenna for the Argentinean-German Geodetic Observatory
C. Kristukat, H. Hase 101

Impact of terrestrial datum on the estimation of Earth Orientation Parameters by geodetic VLBI
A. Laha, J. Böhm, S. Böhm, H. Krásná, N. Balasubramanian, O. Dikshit 104

Exploring reasons for the ITRF2020 VLBI scale drift
K. Le Bail, M. Ishigaki, R. Haas, T. Nilsson, M. Mouyen 109

On the consideration of frequency-dependent illumination functions in modelling signal path variations
M. Lösler, G. Kronschnabl, C. Plötz, A. Neidhardt, C. Eschelbach 114

The Australia-Japan VGOS observation
S. Matsumoto, L. McCallum, J. McCallum, A. Jaradat, M. Ishigaki, H. Yoshifuji, T. Kobayashi 121

RFI monitoring using "mark5access" spectra and Python programs
A. Neidhardt, R. Aktas, L. Rigon, Ch. Plötz 125

New features of the IVS Seamless Auxiliary Data Archive (IVS SADA) and the EVN Monitor
A. Neidhardt, S. Seidl, A. Keimpema 129

Improved modelling for future VLBI contributions to ITRF
T. Nilsson, K. Le Bail, R. Haas 133

VLBI correlator Wettzell - One year of experience as IVS correlator
C. Plötz, W. Probst, R. Wildenauer, B. Fischaleck, A. Neidhardt, M. Seegerer, T. Schüler 138

Intercontinental optical clock comparison using the geodetic VLBI technique in K-band
R. Ricci, M. Negusini, F. Perini, C. Bortolotti, M. Roma, G. Maccaferri, M. Stagni, C. Clivati, D. Calonico, M. Pizzocaro, S. Condio, I. Goti, S. Donadello, M. Risaro, M.-S. Heo, W.-K. Lee, C. Y. Park, D.-H. Yu, H. Kim, S. O. Yi, B. Cho, T. Jung, D.-Y. Byun, D.-H. Je, S. Xu, H. Yoon 141

First Experiences with the VLBI Quality Control System at Wettzell
T. Schüler, W. Probst, C. Plötz, A. Neidhardt, S. Seidl 146

Analysis of Non-Tidal Loading Deformation at VLBI Sites
S. Singh, J. Böhm, H. Krásná, N. Balasubramanian, O. Dikshit 151

Status of Ishioka Geodetic Observing Station
Y. Takagi, M. Ishigaki, T. Nakakuki, H. Yoshifuji, M. Honda, K. Mori, Y. Sato 156

How to deal with expanding spectrum of telecommunication networks threatening VLBI?
V. Tornatore, M. Bautista-Duran, J. S. Ferreira, S. García, H. Hase, J. Kallunki, M. Lindqvist, J.A. López-Pérez, W. Madkour, D. McKay, W. Probst, L. M. Tangen, B. Winkel 160

DBBC4 - A Next Generation VLBI Backend
G. Tuccari, H. Rottmann, W. Alef, S. Buttaccio, S. Dornbusch[2], A. Felke, A. Roy, M. Wunderlich 166

The Level 1 Data: Availability and Benefits
A. Walenta, M. Goltz, D. Thaller, G. Engelhardt, D. Ullrich 171

Absolute orientation of Galileo orbits from simulated VLBI and GNSS observations
H. Wolf, J. Böhm, U. Hugentobler **175**

Recent developments at Metsähovi Geodetic Research Station
N. Zubko, J. Eskelinen, J. Näränen, N. Kareinen, U. Kallio, H. Koivula, M. Poutanen, J. Peltoniemi **180**

Progress on the BRAND extreme-wideband receiver

W. Alef[1,3], G. Tuccari[1,2], S. Dornbusch[1], M. Wunderlich[1], H. Rottmann[1], A. Felke[1]

Abstract The BRAND prototype primary focus receiver with the very wide frequency range from 1.5 GHz to 15.5 GHz has reached another milestone: zero-baseline fringes with the so-called digital frontend. It is a single board which receives up to 2×28 GHz RF signals, samples them and performs a first digital processing in up to four powerful FPGAs. All other components of the receiver are ready. We will report on the present status of the receiver.

Keywords digital receiver, wide-band receiver, VLBI, VLBI backend

1 Introduction

The BRAND receiver is "digital" in the sense that it does not employ analogue down-converters. Instead it digitises simultaneously the frequency band from 1.5 GHz to 15.5 GHz directly utilising a single sampler chip that has been made available to the project. Sampling and initial processing of the extremely high data-rates is done in a so-called digital frontend. After successful testing in the lab, the digital frontend will be installed in the Faraday room at Effelsberg and verified with input from other wideband receivers. The RFI produced by the board will also be measured. The printed circuit board (PCB) with the sampler chip and four powerful FPGAs is going to be housed in a highly shielded box at or close to the analogue parts of the receiver in the focus cabin. The digitised and processed data is sent to the digital backend via optical fibres. Final processing will be done in a DBBC3 VLBI backend (Tuccari et al. , 2018, 2019a,b).

The BRAND development was supported in the years 2017 to 2020 under the RadioNet 'Joint Research Activity' *BRAND EVN* funded by the European Union's Horizon 2020 research and innovation programme. In these first four years of the project a wide-band feed (Flygare & Panteleev , 2020), superconductor filters, a coupler for calibration signals, a wide-band amplifier, analogue signal conditioning and a receiver framework for the Effelsberg telescope's prime focus were successfully developed by our international team (Alef et al. , 2019). It should be noted that as the feed has a good efficiency for the Effelsberg telescope it can serve as a starting design for other telescopes which nearly all have a more favourable geometry.

The digital frontend development has been delayed as its complexity was underestimated. Other factors for the delay are the lack of detailed documentation for the sampler chip which is not a generally available off-the-shelf component. It is programmable in various ways, offers on-chip memory, and some processing options.

2 Digital frontend hardware

The digital frontend consists of a single board with all the electronics including the four inputs from the analogue conditioning box and 64 SFP+ transceivers for output of the digitised data. The board will be

(1) Max Planck Institute for Radio Astronomy, Auf dem Hügel 69, D-53121 Bonn, Germany
(2) INAF Istituto di Radioastronomia, Sezione di Noto, Contrada Renna, 96017 Noto (SR), Italy
(3) Reichert GmbH, Hittorfstr. 26, D-53129 Bonn, Germany

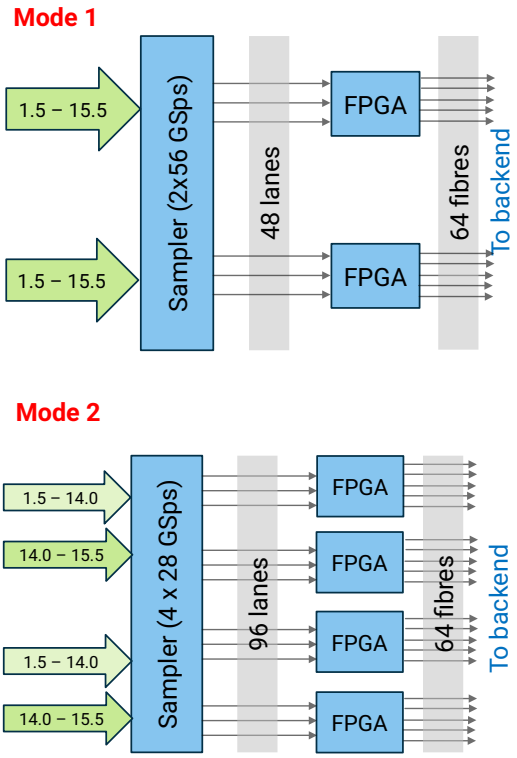

Fig. 1 The analogue data in GHz is input from the left. In "Mode1" two of the four inputs are used which results in the data going out over 48 lanes. In "Mode2" all four inputs are used with half the input bandwidth with half the output data rate on all 96 lanes.

mounted inside a heavily shielded box of which different models are commercially available. In addition there are power supplies and communication ports.

The layout of the board is defined by the characteristics of the sampler/processing chip which offers four input ports and 96 output lanes. The sampler can process roughly 112 gigasamples at 8 bits[1]. This can be realised either via 2×56 GSps or 4×28 GSps (see fig. 1). Early on during the project it was decided to implement "Mode2" as it seemed less risky to input half the data rate from the sampler to the FPGA chips.

Up to four powerful FPGAs on the board receive the data from the sampler. They reconstruct the digitised input bands, form sub-bands and can perform filtering or other operations.

[1] The precise value is: 115.2 GSps, resulting in 57.6 GSps and 28.8 GSps.

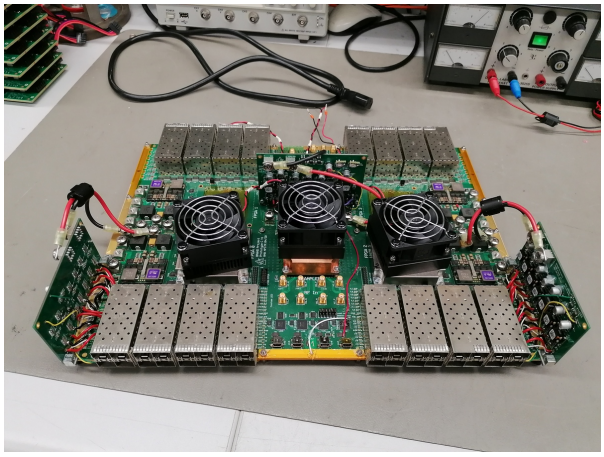

Fig. 2 The digital frontend board. Beneath the three fans are in the centre the sampler chip and two FPGAs on the side. At the four corners of the board there are 2×4 SFP+ cages visible (total of 64). The three upright daughter boards are a later addition as the original power supply circuitry on the board was not sufficiently stable for the sampler chip.

It should be noted that we have now verified that also "Mode1" would work with our board.

Of the so-called C-prototype two boards were manufactured. The first one was used for initial testing and debugging. The documentation of the sampler chip was incomplete and as a result the stability requirements of the power supply to the chip were underestimated. The required stability is less than ± 10 mV at high currents and low voltage.

The second C-prototype includes a lot of modifications, the most visible ones are the three daughter boards which realise the power supply for the three big chips now with sufficient stability at all possible load levels of the chips. (see fig. 2)

Another big problem arose in the data receiving and band reconstruction part of the firmware. Also here the lack of documentation could in the end only be solved by reverse engineering the firmware and software delivered with the evaluation board of the sampler chip.

Version 2 of the C-prototype has been designed (see fig. 3) now taking all lessons learned into account. The power supplies (see fig. 4) are now pluggable via connectors on the backside of C-V2 (see fig. 3). This way the high currents can be provided for sampler and FPGAs with the required high stability. Features added are a 1 PPS output for the FPGAs for monitoring their sync status. The firmware can now be loaded much

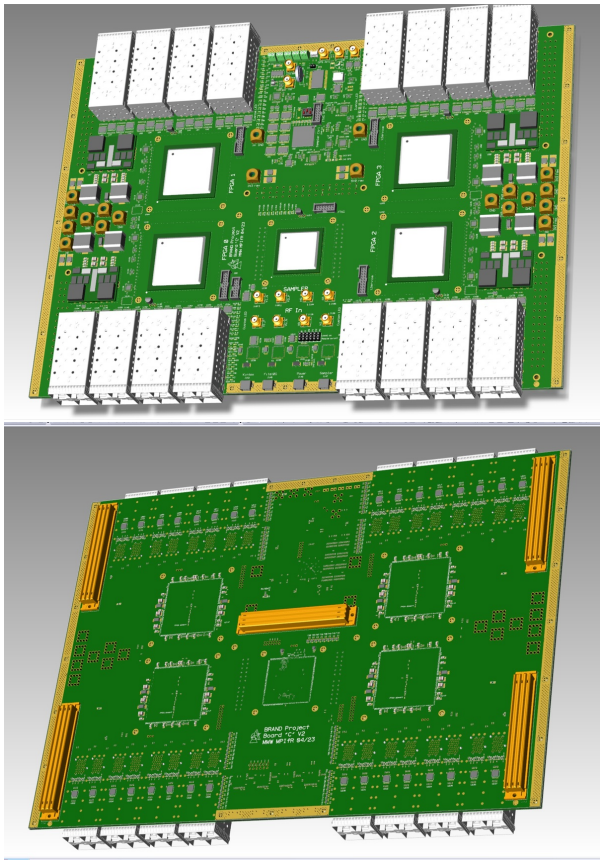

Fig. 3 The design view of the digital frontend board version 2 (top and bottom sides) shows roughly the same layout as version 1. In the centre the sampler chip with four FPGAs on the left and right. At the four corners of the board there are 2×4 SFP+ cages visible (total of 64). New are the five connectors on the backside for power supplies.

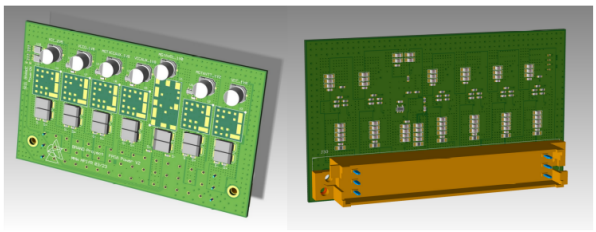

Fig. 4 The design view of the power supply daughter boards (top and bottom view).

faster from an EPROM than via an external connection. The board power can now be switched remotely on or off.

3 Digital frontend firmware and software

The capability for programming the sampler/processing chip is ready and has been tested. Some of the sampling modes have been verified and small amounts of data stored in the chip were retrieved and correlated successfully. Input was from a noise source of limited bandwidth. We found strong fringes in the range of good SNR from the noise source, but very weak fringes could be detected even beyond up to the limit of the chip at 28 GHz.[2]

As mentioned above the significant problems with the data transfer to FPGAs could be solved after a lot of effort. It is now ready and tested. The next stage in the data path is the forming of sub-bands which can be handled more efficiently downstream. OCT filters of 1.8 GHz width are now available. They are compatible to the setup of the Event Horizon Telescope for recording data with Mark 6 recorders. Two such channels with the two polarisations are stored on one disk module easing correlation considerably.

In the future the filter shapes will be improved. Using a common noise source at present zero-baseline fringes between different sampler channels yield already efficiencies of up to 95% for the lower parts of the input band (see fig. 5). At the upper part of the band where our noise source still works we see on average 90% efficiency.

It should be noted that neither the noise source is optimal for this extremely wide band from 0 GHz to 28 GHz nor have we invested more effort yet in optimising the power level of the input signal. Also the calibration of the sampler might be improved to achieve even higher efficiency

4 Conclusions and outlook

A breakthrough has been achieved for the last major unfinished component of the BRAND prototype receiver: the digital frontend. Highly efficient zero-baseline fringes could already be demonstrated and will be improved with a better noise source, properly adjusted input power, better filter shapes, and careful

[2] See slide 17 of presentation at `https://radiowiki.mpifr-bonn.mpg.de/lib/exe/fetch.php?media=na:sustainability:tog:2023_01:brand_evn_status_january_2023.pdf`.

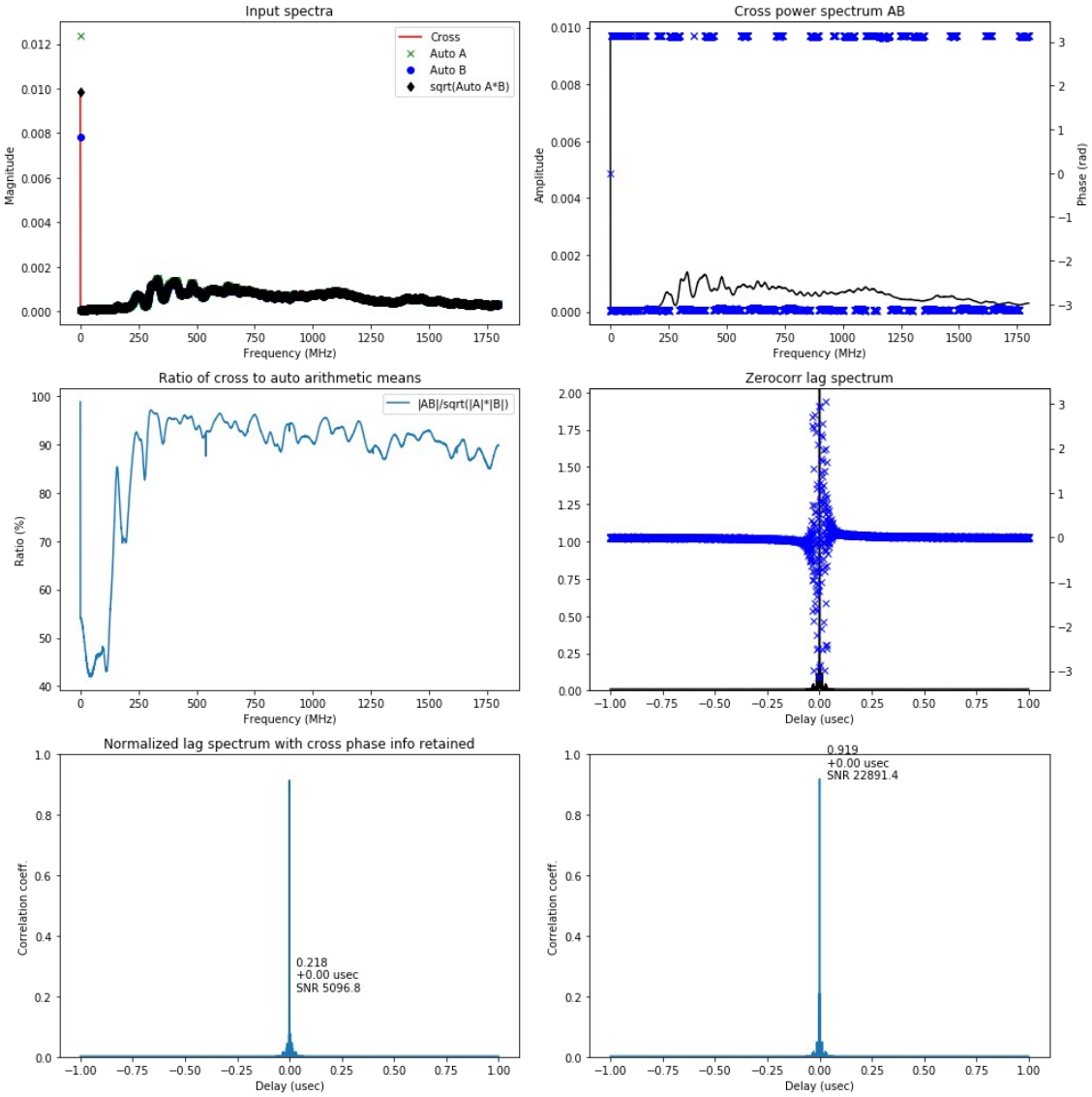

Fig. 5 In the top row the input spectrum of the 1.8 GHz band, and the resulting fringes can be seen. The second row shoes the normalised cross spectral function and the lag spectrum. In the third row the normalised lag spectrum with and without phase information retained are displayed.

calibration of the sampler chip. It is expected that a new wide noise source (0 GHz to 40 GHz) will be ready before the end of 2023.

Work has also started on Digital Down-Converter firmware which will allow channelisation of the input frequency band compatible with the DBBC3. The FPGA boards of the DBBC3 are being modified to be fed with digital data in VDIF format from the digital frontend and other receiver/sampler combinations.

In order to advance the BRAND receiver to become a real EVN receiver MPIfR has purchased 30 sampler chips. About 250 more are available from the manufacturer.

We expect that we can start with the integration of some components followed by laboratory tests before the end of 2023, to be followed hopefully by tests on the telescope in 2024.

References

Tuccari G, Alef W, Dornbusch S, Wunderlich M, Roy A, Rottmann H, Wagner J, Haas R., Johansson K (2018), *"DBBC3 the new wide-band backend for VLBI"* in: *14th European VLBI Network Symposium & Users Meeting (EVN 2018)*, 140, doi: 10.22323/1.344.0140

Tuccari G, Alef W, Dornbusch S, Haas R, Johansson K, Rottmann H, Roy A, Wunderlich M (2019), *"New Observing Modes for the DBBC3"* in : *International VLBI Service for Geodesy and Astrometry 2018 General Meeting Proceedings: "Global Geodesy and the Role of VGOS - Fundamental to Sustainable Development*, 47-49.

Tuccari G, Alef W, Dornbusch S, Haas R, Johansson K, La Porta L, Rottmann H, Roy A, Wagner J, Wunderlich M (2019), *"DBBC3 Towards the BRAND EVN Receiver"* in: *Proceedings of the 24th European VLBI Group for Geodesy and Astrometry Working Meeting*, eds.: Haas, R. and Garcia-Espada, S. and López Fernández, J. A., **24**, 27-30

Flygare J & Pantaleev M (2020), *"Dielectrically Loaded Quad-Ridge Flared Horn for Beamwidth Control Over Decade Bandwidth—Optimization, Manufacture, and Measurement"*, in: *IEEE Transactions on Antennas and Propagation*, **68-1**, 207-216, doi: 10.1109/TAP.2019.2940529

Alef W, Tuccari G, Dornbusch S, Roy A, Wunderlich M, Kasemann C, Nalbach M, Pantaleev M, Flygare J, Gallego J, López Pérez J, Tercero Martínez F., Schoonderbeek G, Hargreaves J de Wild R, Bezrukovs V (2019), *"BRAND - A Wideband Receiver for Astronomy and Geodesy"*, in: *Proceedings of the 24th European VLBI Group for Geodesy and Astrometry Working Meeting*, eds.: Haas, R. and Garcia-Espada, S. and López Fernández, J. A., **24**, 31-36

RAEGE capabilities: Current Status and Analysis RAEGE Group

E. Azcue, M. Karbon, S. Belda, V. Puente, M. Moreira, J.A. López-Pérez

Abstract RAEGE (Red Atlántica de Estaciones Geodinámicas y Espaciales / Rede Atlantica de Estaçoes Geodinamicas e Espaciais) is a project resulting from the cooperation between the National Geographic Institute of Spain (IGE) and the Government of Azores. It is aimed to set up four multi-technique stations: two in Spain (Yebes and Gran Canaria) and two in Azores (Flores and Santa Maria). These stations will stablish a Iberatlantic Very Long Baseline Interferometry VLBI observing network meeting the international requirements needed for VGOS. Currently the VGOS-antennas at Yebes and Santa Maria are operational, the other two are in the planning stage. The RAEGE project focuses not only on the instrumentation and on operating the observations and stations, but also on developing analysis capabilities. With this objective a cooperation between IGN Spain, Azores Government and the University of Alicante was born for exploding the geodetic observations of the RAEGE observatories for geodetic and geodynamic purposes. The key feature of this network is its distribution over three tectonic plates (Eurasian, African and North American), which will augment the estimates of the movements between the plates, both in direction and speed and thus improve the TRF (Terrestrial Reference Frame). Major improvements are expected for constraining the rotational component of the African plate, where we have currently only one VLBI station in South Africa and a very sparse network of about 30 IGS-GNSS antennas over the entire continent. Within this study we want to explore the capabilities of the RAEGE-network in "stand-alone" mode, i.e. which accuracies can be reached with this network in terms of EOP and station position accuracies, and in a second step we evaluate the performance when expanding the network with additional VGOS-antennas of the IVS network.

Keywords RAEGE, VLBI, GGOS, Core Sites, Geodesy

Esther Azcue · Víctor Puente
National Geographic Institute of Spain, Geodesy Department, Madrid, Spain eazcue@mitma.es

María Karbon · Santiago Belda
University of Alicante, Spain

Mariana Moreira
Estação RAEGE de Santa Maria, Associação RAEGE Açores (Santa Maria-Azores), Atlantic International Research Centre (Terceira–Azores), Portugal

José Antonio López Pérez
Yebes Observatory, National Geographic Institute of Spain, Yebes, Spain

1 Introduction: RAEGE

RAEGE commenced in 2011 with a Memorandum of Understanding between the Government of Azores and the Government of Spain to set up a Very Long Baseline Interferometry (VLBI) observing network to meet the international requirements needed for VGOS, the VLBI Global Observing System. Nowadays, the project aims at constructing, installing, and operating four Geodetic Core Sites, two in Spain (in Yebes and Gran Canaria) and two in Azores (in Flores and Santa Maria islands), Fig. 1, as well as two Base Centres for the coordination of activities (in Yebes and São Miguel). Each RAEGE Core Site is equipped with one radio telescope of VGOS specifications (i.e., 13.2 m diameter, high slew rate, capable of operating in

the 2-14 GHz up to 90 GHz), at least one permanent GNSS station, one gravimeter, one maser clock, and a seismograph/accelerograph. Yebes Observatory also counts with an SLR (Satellite Laser Ranging) facility. RAEGE Project does not only focus on instrumentation, but also on developing analysis skills that allow to explote the geodetic observations of the RAEGE observatories. The National Geographic Institute of Spain (IGE) has experience in GNSS data analysis, participating in several national and international projects. The IGNE expanded its analysis activities to VLBI data processing during the last years, starting to send its results to the IVS Combination Centre in february 2020. Since then a VLBI analysis group, in the frame of RAEGE, has been established. The group consists of collaborators from the IGNE, the observatories of Yebes and Santa Maria, and the University of Alicante. The objectives of this group are:

1. Promote the VLBI analysis activities in RAEGE Project.
2. Share knowledge and skills.
3. Expand our research activities.
4. Gain opportunities for participating in other international projects and/or interact with other groups.

The objective of this presentation is to update the current status of RAEGE project as well as to show the first results obtained in the RAEGE analysis group, simulating observations of RAEGE network.

2 Yebes observatory: status

Yebes Observatory is a technological development center of the National Geographic Institute of Spain, classified as a Spanish Unique Scientific and Technical Infrastructure (ICTS). It is located in Yebes (Guadalajara), about 65 km from Madrid. It is equipped with two radio telescopes, 40- and 13.2- meters diameter, GNSS antennas, a future Satellite Laser Ranging station, a local-tie network and gravimetric instrumentation. Being a Technological Development Center, the Yebes Observatory has also various laboratories and workshops for developing the technology that it is used in the observatory or worldwide exported.

Fig. 1 VLBI antennas at Yebes Observatory (up) and Santa María Observatory (down).

2.1 VLBI and correlator

The RAEGE 13.2-m VLBI radio telescope, "Jorge Juan", was integrated into the VGOS network in 2016. It is equipped with a broadband receiver and used in geodetic observations. Its status is full operative, participating in VGOS and EU-VGOS sessions. Highlight the recent updates:

- Maintenance works (cable wrap reparation, January 2022).
- Upgrade VGOS Receiver, June 2022.
- New FO CDMS in progress.
- Construction of receivers for HartRAO, Matera and NARIT in progress.
- Measurement of the radio telescope deformations in collaboration with the Polytechnic University of Valencia. Fig. 2. The measurements were done using drones and Laser Scanner (LS) at 5 angles of elevation. The adjust methods were Least Square Estimation and Orthogonal Distance Regression.

Fig. 2 Campaign for the measurement of the radio telescope deformations by using drones.

Several problems in the campaign were found. The measurements with the LS were affected by wind in the platform used for locating the LS. The point clouds obtained with the drones are still being processing.

A VLBI correlator is being developed. The correlation room is in progress. The software is fully ready. It operates the correlation of VGOS-Intensive-Y sessions, including the weekly 1-hour observations with the stations Gs (GGAO12M), Yj (RAEGYEB) and Sa (RAEGSMAR).

2.2 SLR

A Satellite Laser Ranging station is being built at Yebes Observatory, so-called YLARA (Yebes LAser RAnging). The station is in the phase of site acceptance tests and will start regular operation by early 2024. Upon completion of the construction of YLARA, Yebes Observatory will become a fundamental geodetic station as it will host 3 major space geodetic techniques and a local-tie network to interconnect them. Additionally, YLARA will be capable to track space debris too.

2.3 Gravimetry

The Gravimetry laboratory was specially designed to host gravimeters. Given the delicacy of these instruments and the high sensibility, it is necessary to have control over the thermal behaviour of the building (double chamber with air conditioning system in the external one) and the structural behaviour (isolated concrete pillars). A Superconducting Gravimeter OSG is permanently installed and operating. Other absolute gravimeters (FG5, A10) are occasionally moved to other locations. For example, last September 2023 the FG5 gravimeter was sent to an inter-comparison campaign ICAG23 in Boulder. A GNSS station, meteorological station, seismograph/accelerograph, humidity sensors or underground water level sensors are also located in the laboratory.

2.4 GNSS, SAR Corner Cube Retro-Reflector and Local Tie

Three GNSS antennas are operative: YEBE, that is integrated in the Euref GNSS Permanent Network and IGS network, YEB1 and YEB2. YEBE is used as a reference for a SAR Corner Cube Retro-Reflector. The retro-reflector is installed in collaboration with INTA (National Institute of Aerospace Technology) as reference point for PAZ satellite (SAR images). Local tie in Yebes observatory is observed. Last updates are the new pillars for SLR integration in the network and the use of a new software for the network adjustment, that will be used for the following realizations.

3 Santa María observatory: status

Santa María Observatory is placed in Santa Maria island (Azores, Portugal). It is the second station of RAEGE working and first in Portugal. The station has a VGOS-type radio telescope, a control building which houses three pillars for the installation of gravimeters and seismographs, and GNSS antennas.

3.1 VLBI

The VGOS 13.2m radiotelescope "Colombo" was constructed in 2014 and is part of the International VLBI Service for Geodesy and Astrometry (IVS). It was equipped with a tri-band receiver (S, X and Ka) developed at Yebes laboratories until September 2022, participating routinely in R1, R4 and intensive type sessions. Since then its participation was limited to intensive VGOS sessions and IVS VGOS sessions in tagalone mode. Although the receiver was changed to a VGOS type and the full signal chain was substituted (2 Mark 6, DBCC 3, Base band downconverters and new CDMS). A radar close to the station have impacted in VGOS bands creating full incompatibility between RAEGE radio telescope and the leolabs radar operation from ending 2022 to September 2023. As a first solution a VGOS A band filter was used. On September 2023 a new superconducting filter was successfully developed and installed.

3.2 Gravimetry

An I-Grav superconducting gravimeter was installed on September 2022. It was previously located at Yebes Observatory in parallel to the OSG. A GRAVITON-EG 1183 gravimeter from LaCoste and Romberg, a Centaur-3/Trillium 120PA seismograph from Nanometrics, and a SILEX accelerograph are running also in the gravimetry room. From march 2023 to June 2023 a FG5 absolute gravimeter was also used for measuring the absolute gravity.

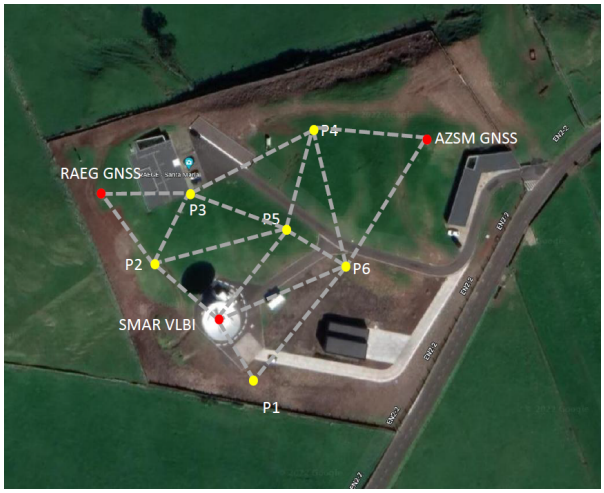

Fig. 3 Local Tie network of pillars in Santa María.

3.3 GNSS and Local Tie

Two permanent GNSS stations are operative. RAEG, integrated in the International (IGS) and European (EUREF) Permanent Networks, and AZSM which is part of the Azorean (REPRAA) regional network.
The local tie network was designed in September 2022 and currently the pillars are being built. Fig. 3.

4 Gran Canaria and Flores observatories: status

Gran Canaria and Flores observatories are still in progress. The observatory of Gran Canaria will be in Temisas, a small village in southeast Gran Canaria. The land has been purchased and the design finished. Currently it is waiting for starting the works.
Flores Observatory is proceeding slowly. The location is decided and there is installed a GNSS station and a weather station, that had technical problems the last years.

5 RAEGE Analysis Group: RAEGE Simulations and Local Tie by VLBI

A data analysis group in the frame of RAEGE has been established. The group consists of collaborators from

the IGNE and Yebes Observatory, Santa Maria observatory and the University of Alicante. The goal of the group is the analysis and exploitation of the observations of RAEGE to obtain useful data and products, but also to transmit them to society.
Last studies were focus on schedule our own observations. The goal is to be able of planning, observing, correlating and analysing in the project. Two main strands of work have been developed. A brief summary is presented here, being the detailed and finished study published in the future. The first area of work is the planning and design of our own experiments for exploiting the possibilities of RAEGE, starting with the simulations of observations of this network and its influence in the EOPs and terrestrial reference frames. Secondly, the observation of local ties by VLBI in the Yebes observatory between the telescopes of 40m and 13.2m.

5.1 RAEGE simulations

The impact of including RAEGE stations in existing sessions was tested in R1/R4 and VGOS sessions. The software used was VieSched++. 64 different schedules were generated for several sessions with different weight factors (number of observations, sky-coverage and duration). The best is selected analyzing Mean Formal Error and Repeatibilities from 1000 simulations of each schedule. EOPs, Coordinates, Troposphere and Sources are solved.
When including RAEGE in existing sessions, the number of observations by baseline of european stations increases but it also happens in the South Africa and South America stations tested. These stations improve the repeatabilities of their coordinates and also the EOP repeteabilities (except for xp, x component of the polar motion). More research is under developed for reaching a valid conclusion.
Additionally, new sessions were proposed. Different tests were done with new network configurations. Very long west-east and north-south baselines including RAEGE stations were simulating. Between the different simulations, it seems to work very well for UT1 estimation the very long west-east baseline K2(Hawai)-RAEGE(Sa+Yj)+ Is(Japan).
Future work: To repeat the test for a SNR based schedule for VGOS sessions and to extend these results to more sessions.

5.2 VLBI Local Tie

The objective is to determine the local tie of the Yebes antennas by using VLBI observations. YEBES40M has some small windows without observations that are used for the joint observation. The first test was done in June 2023 and the second one in July. In both cases a training campaign of 1 hour was observed. The schedule was done by using VieSched++ and the correlation and analysis are still in progress.

6 Conclusions and future works

A general summary of the status of RAEGE project was presented. The goals for the next year are:

- Yebes station: finishing the YLARA station, the VLBI correlator and the ordered VGOS receivers for other stations.
- Santa María station: joining to the VGOS network after some tag-alone observations, building the local-tie pillars, the installation of new weather station, the temporal installation of absolute gravimeter close to superconducting one and the under-ground water level measurements for gravimeter corrections.
- Gran Canaria station: finishing the projects of civil works for the new site, preparation of the tendering process for construction and the installation of a weather station and GNSS receiver.
- Flores station: definition of the contract for antenna design and weather station repairs.
- RAEGE analysis group: finishing and publishing the simulations done and working for observing them with other stations interested.

Acknowledgements

The UA authors were supported partially by Generalitat Valenciana (PROMETEO/2021/030, SEJIGENT/2021/001), the Spanish Ministerio de Ciencia e Innovacion (MCIN/AEI/10.13039/501100011033/, PID2020-119383GB-I00), and the European Union-NextGenerationEU (ZAMBRANO 21-04).

The compatibility of DORIS with VGOS

M. Bautista-Duran, J.S. Ferreira, S. García, H. Hase, J. Kallunki, M. Lindqvist, J.A. López-Pérez, W. Madkour, D. McKay, W. Probst, L.M. Tangen, V. Tornatore, B. Winkel

Marta Bautista-Duran
Instituto Geográfico Nacional, Observatorio Yebes, Cerro de la Palera sn, E-19141 Yebes, Guadalajara, Spain

Joao Salmin Ferreira
Associaçao RAEGE Açores, Estação RAEGE de Santa María, Estrada dos Piquinhos s/n, 9580-324 Vila do Porto, Portugal

Susana García
Kartverket, Geodetic Earth Observatory, P.O. Box 13, N-9173 Ny-Ålesund, Svalbard, Norway

Hayo Hase
Bundesamt für Kartographie und Geodäsie, BKG Wettzell-AGGO, Sackenrieder Str. 25, D-93444 Bad Kötzting, Germany

Juha Kallunki
Aalto University, Metsähovi Radio Observatory, Metsähovintie 114 , FI-02540 Kylmälä, Finland

Michael Lindqvist
Department of Space, Earth and Environment, Chalmers University of Technology, Onsala Space Observatory, S-439 92 Onsala, Sweden

José Antonio López-Pérez
Instituto Geográfico Nacional, Observatorio Yebes, Cerro de la Palera sn, E-19141 Yebes, Guadalajara, Spain

Waleed Madkour
Joint Institute for VLBI ERIC, Oude Hoogeveensedijk 4, NL-7991 PD Dwingeloo, The Netherlands

Derek McKay
Aalto University, Metsähovi Radio Observatory, Metsähovintie 114 , FI-02540 Kylmälä, Finland

Willi Probst
Bundesamt für Kartographie und Geodäsie, BKG Wettzell, Sackenrieder Str. 25, D-93444 Bad Kötzting, Germany

Leif Morten Tangen
Kartverket, Kartverksveien 21, 3511 Hønefoss, Norway

Vincenza Tornatore
Politecnico Milano, Piazza Leonardo da Vinci 32, I-20133 Milano, Italy

Abstract Simulation studies on the compatibility between DORIS and VGOS have been made for European geodetic VLBI stations with the software tool pycraf. We present here only the results for Wettzell and compare them with former real measurements. The results indicate large exclusion zones for the conservation of undisturbed VLBI observations. To avoid harmful radiation of DORIS to a VLBI receiver, a minimum distance of 300 m is suggested. The complete study is available at: `https://www.craf.eu/wp-content/uploads/2023/05/DORIS_VGOS_compatibility_study.pdf`

Keywords VGOS, geodetic VLBI, DORIS, compatbility study, pycraf

1 Introduction

The most precise global geodetic reference frame, the International Terrestrial Reference Frame (ITRF), is based on four geodetic space techniques: Very Long Baseline Interferometry (VLBI), Satellite Laser Ranging (SLR), Global Navigation Satellite Systems (GNSS) and the Doppler Orbitography and Radiopositioning Integrated by Satellite (DORIS). VLBI is the only technique depending on natural, very weak cosmic signals, while the other techniques depend on artificial signals: SLR on optical laser pulses, GNSS on microwave emissions from satellites, and DORIS on microwave emissions from ground beacons. All four techniques comple-

Benjamin Winkel
Max-Planck-Institut für Radioastronomie, Auf dem Hügel 69, D-53121 Bonn, Germany

ment each other with their observations for the terrestrial reference frames, because of the individual advantages: VLBI is unique for the determination of the Earth orientation parameters and the tie of International Terrestrial Reference Frame (ITRF) to the International Celestial Reference Frame (ICRF), SLR is strong in the determination of the center of mass of the planet Earth and of the scale in the ITRF, GNSS is good for densification of global networks and of orientation and DORIS technique is unique in that it has the most homogeneous global network of reference sites. In order to combine these advantages in a synergetic way, a co-location of these techniques in geodetic observatories is an objective for making progress in global geodesy.

The idea of co-location for a better geometry comes along with a hidden disadvantage: DORIS, as a ground-based active transmitting device, counteracts with the efforts of keeping the environment of a radio telescope site for VLBI free of radio frequency interference. The question of how the desired co-location of DORIS at a VLBI site (or vice-versa) can be achieved is under on-going discussion. The VLBI systems are designed to receive extremely faint cosmic signals down to -110 dBm, whereas the DORIS beacon emits signals at a frequency of 2,036 GHz with 40 dBm output power. There is a potential for coupling between DORIS emissions (including harmonics at higher frequencies) and the VLBI receiving chain, thus generating spurious signals. A risk of overloading, or even damaging, the VLBI low noise amplifiers (LNA) is possible. Even if in VLBI the same frequency is not being observed, in the worst case the LNA of the VLBI receiver could be saturated by DORIS transmission leading to useless VLBI observations.

Meanwhile, several geodetic observatories collected measurements, made studies, and even co-located active DORIS beacons. The CRAF-VGOS group presented a compatibility study with simulations of exclusion zones for DORIS with respect to VGOS radio telescopes. It collates site-specific experiences and may be helpful for future decisions on how to co-locate both techniques at new sites.

2 Methodology

The compatibility study between the active DORIS device and the passive radio telescope reflector for several European geodetic VLBI sites is made with the simulation software pycraf (Winkel , 2023). Each compatibility study between a DORIS and VGOS system is based on a single-entry site-specific, whose purpose is to obtain some contour areas to define the minimum distance where the compatibility between the DORIS and VGOS is achieved. We study according to ITU-R Report RA.2507 (ITU-R Report RA.2507 , 2022) three different scenarios:

1. the worst case scenario which provokes the saturation of the LNA at the VLBI receiving chain by interfering emissions. In this case, no useful VLBI results can be expected and it defines an exclusion zone for DORIS beacons;
2. the Very Long Baseline Interferometry observation mode (VLBI) used for detection of Earth rotation or astrometry. This is the most tolerant mode as local interference does not correlate. However, it increases the noise level at the receiver and that lowers the signal-to-noise ratio and results in less accuracy or even outlayer in the analysis;
3. the single-dish (SD) mode used for calibration during a VLBI session. This is the least tolerant mode to local interference because it causes errors in the calibration of the radio source.

The terrain around the radio telescopes has an important impact on signal propagation from the selected DORIS site with respect to the VGOS radio telescope and is taken into account in the study. The propagation model according to ITU-R Recommendation P.452-16 is used (ITU-R Recommendation P.452-16 , 2015, 2021). For this study no clutter has been considered, to provide the worst-case scenario. According to Recommendation ITU-R RA.1513 (ITU-R Recommendation RA.1513 , 2015), RAS has to accept a maximum data loss of 2%. Therefore, for the propagation model, a time-percent value of 2% is used throughout this section. The resolution of the digital terrain model is critical for the results. Lidar data (Lidar data , 2023) have not been freely available for all sites, therefore, SRTM data (SRTM data , 2023) are used as a second choice where Lidar data were not available.

3 Input parameters and simulation results for the example of Wettzell

The pycraf simulation tools require as input several technical parameters listed for the DORIS and VLBI system in tables 1 and 2.

To identify areas in the surroundings of the radio telescope, from which the radio telescope can be illuminated, a so-called attenuation map is computed. For this, a hypothetical transmitter at the position of the radio telescope radiates over the entire azimuth range. Illuminated areas are identified as areas with least attenuation, while other areas are protected mostly by the topographic obstacles receive no radiation (maximum attenuation). The latter are the preferred areas to install a DORIS system (see Figure 1).

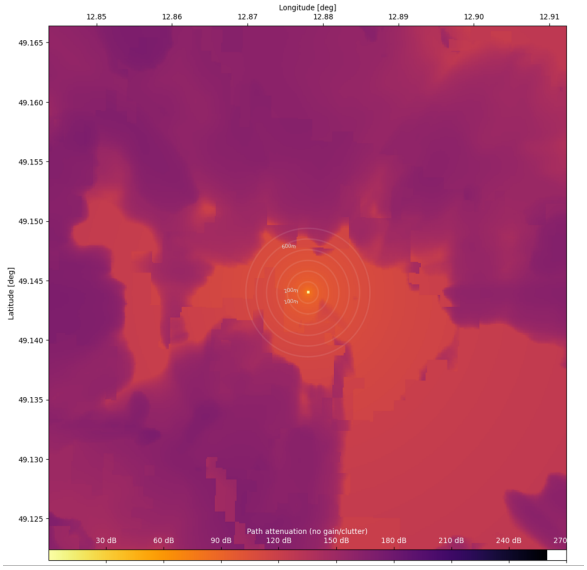

Fig. 1 Attenuation map applied to the topographic representation of Wettzell. The yellow/orange/red colors indicate areas with strong illumination (low attenuation) from the radio telescope and are not recommended for a DORIS installation, while the dark violet areas show a high degree of attenuation and may serve for an installation. The concentric rings around the center are spaced by 100 m as a scale. This figure demonstrates that the topography should be considered for the definition of locations for new transmitters in the surroundings of a radio telescope.

In a second computational step, the attenuation map is used to compute the exclusion zones for the three different threshold levels given in Tab. 2, namely for (1) the LNA saturation case (no VLBI results possible), (2) the VLBI/VGOS observation mode, (3) the single-dish/calibration mode (see Fig. 2). The minimum coupling loss (MCL) is the difference between the transmitted power and the RAS threshold. The margin is obtained by the difference of the attenuation and the MCL. A negative margin indicates that this attenuation is not enough to achieve the threshold. A positive margin indicates the attenuation is higher than the MCL (the threshold is overpass) and a zero margin provides the contour area that determines the exclusion zones (attenuation is equal to the MCL).

From Fig. 2 (1) the LNA threshold case can be concluded that the no-go area for a DORIS installation stretches up to 300m around the radio telescope (if both techniques shall be operated simultaneously). Due to the topographic situation of hills and valleys around Wettzell several mountain chains in the distance of up to 5 km for the VLBI-threshold level and up to 50 km (and a few spots up to 100 km) distance for the single-dish/calibration threshold level may have an impact on the observational activities of a radio telescope site for VLBI.

In a third step, the topographic terrain model with the determined threshold level lines can be overlaid with geographic map information (Fig. 3. For the case of Wettzell, the information of the (1) the LNA threshold case is of interest, as its simulated results can be compared with real measurements which had been made earlier at the station in search of a suitable DORIS site (Kluegel et al. , 2017). The results found by Klügel et al. coincide well with the simulation, so that the pycraf tools for these type of studies are helpful for future investigations; they are especially advantageous for the larger area up to 100 km around a radio telescope site.

This study considered only the carrier frequency of 2 GHz of the DORIS beacon, but also the higher order harmonics at 4 and 8 GHz should be analyzed in the same way as they may conflict with observation bands.

4 Conclusion

Compatibility studies for European geodetic radio telescope sites for DORIS installation in their vicinity have been conducted (Compatibility Study DORIS-VGOS , 2023). In this article the methodology using the pycraf

DORIS parameter	Value	Remarks
EIRP level @ 2 GHz towards zenith	46 dBm	extracted from document: DORIS beacon RF characteristics
EIRP level @ 2 GHz at 90° from zenith	38 dBm	maximum level of DORIS towards the VGOS radio telescope
Antenna height @ 2 GHz	2 m	general assumption, may vary at stations due to local situation
Duty cycle	100%	Percentage of active DORIS signal broadcast time

Table 1 DORIS input parameters for pycraf simulation.

VLBI System	Value	Remarks
Minimum elevation angle	10°	minimum elevation angle during VGOS session
Side lobe gain at minimum VGOS elevation angle, G_r	0 dBi	VGOS gain at 10° elevation angle, extracted from Fig. 8 (s. (Compatibility Study DORIS-VGOS , 2023))
Threshold interference levels **(1) LNA threshold case**	-50 dBm	1. worst case scenario, maximum input power level for linear regime of LNA,
(2) VLBI threshold case	-133 dB(W/m²)	2. maximum spectral density power for VGOS VLBI operation (ITU-R RA.2507)
(3) SD threshold case	-170 dB(W/m²)	3. maximum spectral density power for VGOS single dish operation/calibration (ITU-R RA.2507)
antenna height, h_{rx}	$D/2 + 2.5m$	D = diameter of reflector, 2.5 m is the offset between ground and reflector lower edge

Table 2 VGOS radio telescope input parameters for pycraf simulation (Winkel , 2023).

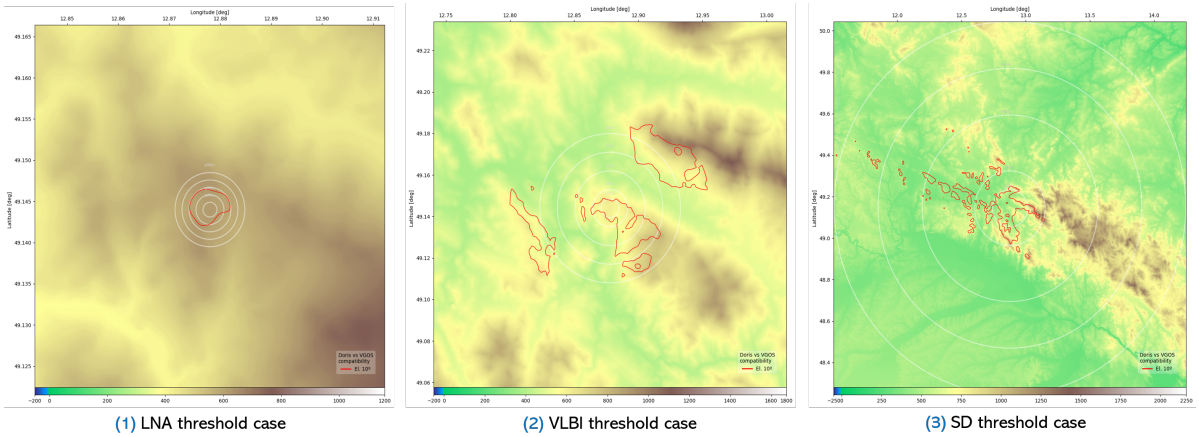

(1) LNA threshold case (2) VLBI threshold case (3) SD threshold case

Fig. 2 Exclusion zones for three different threshold levels indicated in Tab. 2. The left map indicates a zone of about 300 m in which harmful interference from DORIS would make VLBI results impossible. The map in the middle shows with the red-line marked areas (the outer rings are spaced by 1 km as scale), where a DORIS system would have an impact on the geodetic VLBI observations, while the right map shows the same but for the single dish/calibration threshold criteria (the largest circle has a 100 km radius for scale).

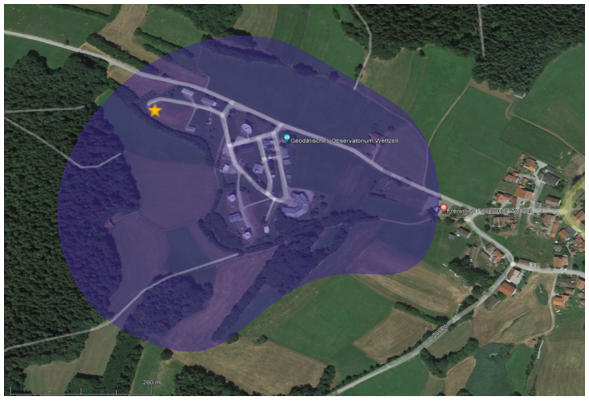

(1) LNA case exclusión zone (purple) and real location of DORIS (yellow star) at the Geodetic Observatory Wettzell

Fig. 3 Exclusion zone for DORIS computed by simulation and projected over a remote sensing image with geographic details. This information helps to identify the areas which are critical for an installation of DORIS. However, the digital terrain model does not provide high-resolution details on the local situation with constructions which could provide additional shielding and improve the situation. These investigations remain for local, real-condition studies.

software tool has been demonstrated for the case of Wettzell. The results from the simulations coincide with previous investigations by local measurements at the Wettzell site. Hence, the method is validated. The pycraf tool enables guidance in case of intended installation of any kind of terrestrial transmitters near a radio telescope site. To avoid harmful radiation of the DORIS system to the VLBI receivers, a minimum distance of about 300 m is suggested. Considering the threshold levels of ITU-R Report RA.2507 to provide undisturbed conditions for geodetic VLBI measurements, DORIS should be outside areas up to 5 km for VLBI observation mode and up to 50 km for single dish/calibration mode for the case of Wettzell. These results cannot be used for other sites and a case-by-case study is mandatory. However, local blockage of direct line-of-sight is crucial for the co-location of the DORIS transmitter near a VLBI radio telescope. Another option for the coexistence of both techniques at one site is the alternating operation in less than 100% duty cycles of each technique.

References

CRAF-Handbook for Radio Astronomy, 2005
https://craf.eu/wp-content/uploads/2015/02/CRAFhandbook3.pdf

CRAF-VGOS group: Compatibility Study Between DORIS And VGOS Systems
https://www.craf.eu/wp-content/uploads/2023/05/DORIS_VGOS_compatibility_study.pdf

ITU-R Recommendation P.452-16: Prediction procedure for the evaluation of interference between stations on the surface of the Earth at frequencies above about 0.1 GHz, 07/2015, [superseded by P.452-17, 09/2021]
https://www.itu.int/dms_pubrec/itu-r/rec/p/R-REC-P.452-16-201507-S!!PDF-E.pdf

ITU-R Recommendation RA.1513 : Levels of data loss to radio astronomy observations and percentage-of-time criteria resulting from degradation by interference for frequency bands allocated to the radio astronomy service on a primary basis
https://www.itu.int/dms_pubrec/itu-r/rec/ra/R-REC-RA.1513-2-201503-I!!PDF-E.pdf

ITU-R Report RA.2507: Technical and operational characteristics of the existing and planned Geodetic Very Long Baseline Interferometry, 10/2022
https://www.itu.int/dms_pub/itu-r/opb/rep/R-REP-RA.2507-2022-PDF-E.pdf

Klügel, T., Schüler, T., Phogat, A., Mähler, S., Plötz, C., Kronschnabl, G., Bertarini, A., Neidhardt, A., Saunier, J., Didelot, F., Walter, J.-M.: VLBI-DORIS Interference Investigation at Wettzell, In 23rd European VLBI Group for Geodesy and Astrometry Working Meeting 2017 (Vol. 23, pp. 24-28).
https://www.oso.chalmers.se/evga/23_EVGA_2017_Gothenburg.pdf

Winkel, B.: pycraf
https://github.com/bwinkel/pycraf

SRTM data source:
http://viewfinderpanoramas.org/panoramas.html

Lidar sources for the different RAS stations used in this Report, based on a compilation by Open Data Portal, Austria: Wettzell, G: Bayerische Vermessungsverwaltung (www.geodaten.bayern.de): DTM 50 Meter
https://opendata.bayern.de/detailansicht/datensatz/digitales-gelaendemodell-50-m-gitterweite

The VGOS High Road: From Inception and Prototyping to Operations to Maturation and Beyond

D. Behrend, C. Ruszczyk, P. Elosegui, A. Neidhardt

Abstract Legacy S/X has been the production system of the IVS since the inception of the service. VGOS was declared operational in 2020 after a visionary journey that involved designing, prototyping, and demonstrating the feasibility of the new observing system to generate high-quality geodetic products. And a fledgling VGOS network of between 8 and 10 stations has been contributing to IVS products operationally ever since. That VGOS network had further increased by the end of 2022 to 12 stations, and counting. Currently, the VGOS observing program encompasses the 24-hour VGOS-OPS and VGOS-RD session series; further, a weekdaily VGOS Intensive series has been established (with other VGOS Intensives being set up). In addition to the network, VGOS correlation capabilities have also expanded to try to keep pace with the increased VGOS correlation load, morphing into a multi-center distributed correlator. In this paper, we provide a status overview of the infrastructure realization efforts of the VGOS station network and the correlation centers as well as plans for a bright VGOS future.

Keywords VGOS, infrastructure, correlator

Dirk Behrend
NVI, Inc./NASA Goddard Space Flight Center, 7257 Hanover Parkway, Suite D, Greenbelt, MD 20770, USA

Chet Ruszczyk · Pedro Elosegui
MIT Haystack Observatory, 99 Millstone Rd, Westford, MA 01886, USA

Alexander Neidhardt
TU Munich, Geodetic Observatory Wettzell, Sackenrieder Str. 25, D-93444 Bad Kötzting, Germany

1 Introduction

When the IVS was established in 1999, the VLBI production system was—and had been for almost two decades—the legacy S/X system. In the early 2000s, studies were started that looked into the creation of a next-generation VLBI system using smaller, faster antennas and a wide bandwidth. This was the start of a journey to design, prototype, and demonstrate the VLBI Global Observing System (VGOS).

Following an extended development period, the new system was declared operational in 2020. High-quality geodetic and astrometric results were obtained from VGOS data and started to contibute to IVS products (including to ITRF2020). The fledgling VGOS network was limited in size (8 to 10 stations) and geographic distribution (northern hemisphere) but continued to grow, reaching some 12 stations by mid-2023. The network growth is expected to continue in the next few years (in particular in the southern hemisphere) and will help to improve overall data quality.

The larger network as well as the anticipated increase in observing cadence necessitated an expansion of the VGOS correlation capabilities. The correlator network saw an expansion from initially one to now seven centers to handle the correlation load (one 24-hour VGOS session per week or fortnight plus 5 to 10 1-hour VGOS Intensive sessions on various baselines). In the following, we give an overview of the infrastructure realization efforts of the VGOS station network and the correlation centers. We summarize the history of VGOS using some of the milestones and making reference to essential publications. Finally, we point out some of the system's current limitations (e.g., data transfer rates, storage capacities) and provide an outlook on a bright VGOS future.

2 VGOS: Some History

In the early 2000s, the IVS Directing Board recognized that the VLBI equipment of the legacy S/X system, developed in the 1970s and 1980s, was approaching the end of its lifetime and formed a working group to formulate a vision for a next-generation VLBI system. Over the time period from September 2003 to September 2005 IVS Working Group 3 on VLBI2010 examined current and future requirements for VLBI geodetic systems and summarized its findings in a final report (see Figure 1). This vision paper forms the basis for the subsequent developments.

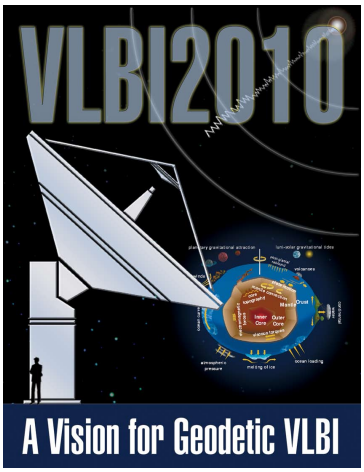

Fig. 1 *Vision document:* Final Report of IVS Working Group 3 on VLBI2010 "A Vision for Geodetic VLBI" (Niell et al., 2005).

To encourage the implementation of the recommendations of WG3, among other things, the Board then established the VGOS Technical Committee (VTC; formerly known as VLBI2010 Committee, V2C) in September 2005. As a committee the VTC is a permanent body in the IVS (unlike the temporary WG3). The primary function of the VTC is to promote and guide research into the improvement of the "technique" of geodetic VLBI. The committee saw as the most urgent issue the need to define the specifications for the VGOS antenna and accomplished this task with the publication of a progress report in 2009 (see Figure 2) which focused on the design aspects of the VGOS system. The VTC continues to work on improving the VLBI technique to this day.

With the specifications defined, it was possible to start work on prototyping a VGOS system. Two

Fig. 2 *Definition of specifications:* Progress Report of the VGOS Technical Committee (VTC, formerly VLBI2010 Committee) "Design Aspects of the VLBI2010 System" (Petrachenko et al., 2009).

proof-of-concept broadband signal chain systems were developed and installed at antennas in Westford and Goddard. The baseline was used between 2014 and 2017 to demonstrate the feasibility of VGOS. In addition to the developments on the station side, also new correlation and analysis procedures for the four-band, dual-linear-polarization data had to be created. A summary of the successful demonstration of the VGOS technique was eventually published in 2018 (see Figure 3).

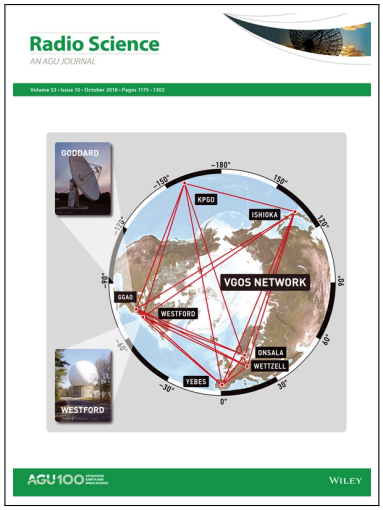

Fig. 3 *Demonstration of VGOS technique:* technical report in Radio Science (Niell et al., 2018).

3 Status and Growth of the VGOS Station Network

As of mid-2023, the VGOS observing network consists of 12 stations (see Figure 4). The addition of three further stations to this network is imminent. The network will further grow in 2024 and 2025 to about 25 stations. Recent milestones and the state of individual VGOS station projects are summarized in Table 1. Additional growth with a smaller number of stations is anticipated towards the end of this decade.

Table 1 Individual VGOS station projects with recent milestones and projected broadband readiness.

Station	Recent milestone	VGOS broadband
GGAO	VGOS-OPS, VGOS-RD	ready
Westford	VGOS-OPS, VGOS-RD	ready
Wettzell (Ws)	VGOS-OPS, VGOS-RD	ready
Yebes (Yj)	VGOS-OPS, VGOS-RD	ready
Ishioka	VGOS-OPS, VGOS-RD	ready
Kokee Park (K2)	VGOS-OPS, VGOS-RD	ready
Onsala (Oe, Ow)	VGOS-OPS, VGOS-RD	ready
McDonald	VGOS-OPS, VGOS-RD	ready
Hobart	VGOS-OPS, VGOS-RD	ready
Katherine	VGOS-OPS, VGOS-RD	ready
Ny-Ålesund (Nn)	VGOS-OPS, VGOS-RD	ready
Santa Maria	VGOS-RD	imminent
Sheshan	VGOS tagalong	imminent
Yarragadee	S/X observing	imminent
Wettzell (Wn)	VGOS fringe tests	2024
Ny-Ålesund (Ns)	S/X observing	2024
HartRAO	signal chain work	2024
Metsähovi	signal chain work	2024
Matera	RT built	2024
Chiang Mai	site preparation	2024
Songkhla	site selected	end 2024
Gran Canaria	RT stored, land purchase	2025
Fortaleza	RT and signal chain built	2025
Flores	RT design, RFI surveys	2025
Kanpur	proposal	2025
Badary	fixed broadband system	2017 [S/X/Ka]
Zelenchukskaya	fixed broadband system	2017 [S/X/Ka]
Svetloe	fixed broadband system	2019 [S/X/Ka]
Tahiti	site selected, RFI survey	beyond 2027

Beyond the projects listed, there are also efforts underway in other parts of the world. This includes undertakings in India (for three stations), Malaysia, and Indonesia. Please do let the authors know of any other projects that may be in the discussion stage.

In general, the observing network reaches levels of a mature buildout, but there remain gaps in Africa, South America, and Antarctica—that is, there is a level of scarcity in the southern hemisphere overall.

4 VGOS Correlation Capabilities

The VGOS correlation capabilities have evolved from a single correlator (until 2019) to a network of (up to seven) distributed correlators that can process VGOS sessions operationally (see Figure 5).

TSUK has processed VGOS Intensive data but does not have sufficient resources yet to handle 24-hour sessions. UTAS handles AUS mixed-mode sessions. Other correlation centers (e.g., at Yebes) may evolve over time to full-blown VGOS correlators. The correlator group regularly meets to have knowledge exchange and to refine the VGOS processing chain.

5 VGOS Observing: Current Limitations

Cadence of VGOS-OPS sessions. In 2022 and early 2023, the turnaround time for 24-hour VGOS sessions (end of observing to vgosDB creation) was 2+ months. With 4–5 correlators processing 24-hour sessions, a turnaround time of 30 days or better is needed to avoid a backlog of sessions. The last few VGOS-OPS sessions of 2023 were closer to this target time.

Data storage. Both stations and correlators need sufficient storage capacity for Level-0 data (raw station data). Several have upgraded their capacities recently. A subset of the correlators can handle physically shipped Mark 6 modules, while some only support e-transfers.

e-transfer rates. For transferring Level-0 data electronically, sufficiently large data transfer rates are needed. For stations sustained rates of 5–10 Gbps are sufficient, whereas correlators need multiples of these rates (20 Gbps or better for one 24-hour session per week; 140 Gbps at full VGOS maturity when observing continuously and assuming a monolithic correlator).

Hardware availability. Several hardware parts—such as masers, digitizers, and feed system components (e.g., LNAs)—are produced by small companies with small production series. Some parts have become unavailable ("unobtainium"), while other parts have high costs or long purchase order lead times associ-

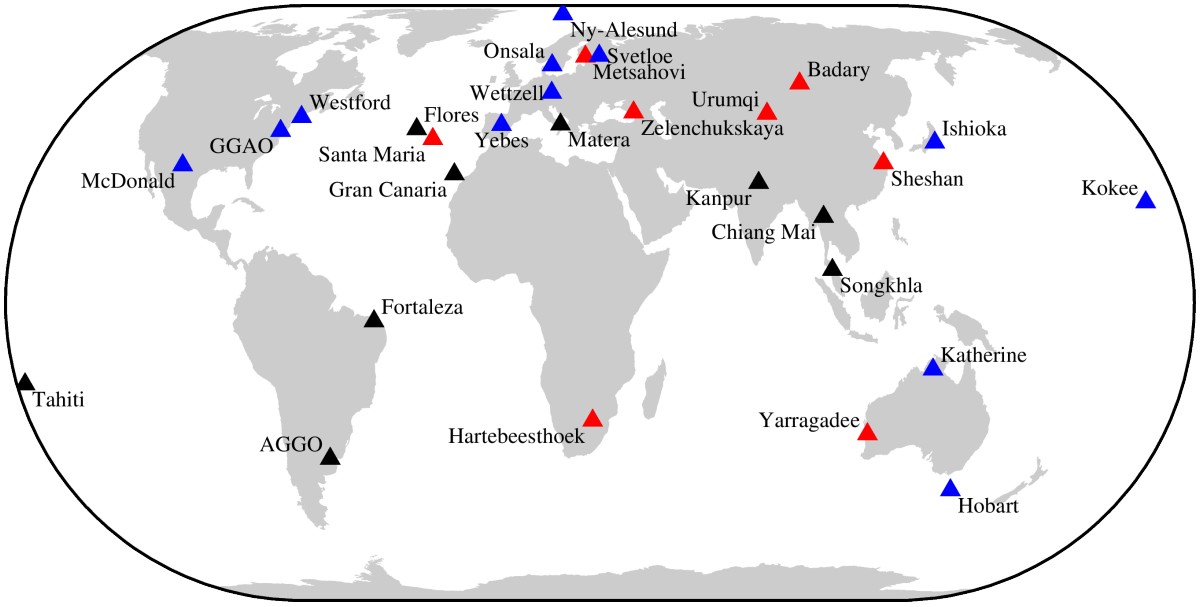

Fig. 4 Geographic distribution of the operational VGOS antennas (▲), built antennas with signal chain work in progress (▲), and VGOS projects in the planning stage (▲).

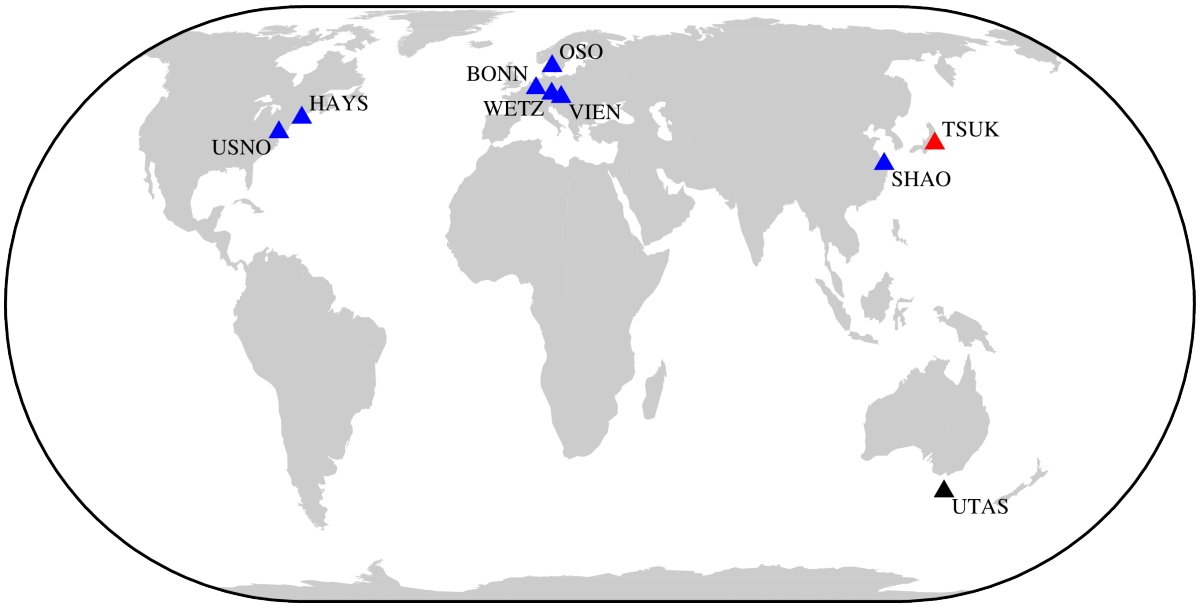

Fig. 5 Geographic distribution of the operational VGOS correlators (▲), correlators under verification (▲), and future correlation centers (▲).

ated with them. An inherent risk is a slowdown in the signal chain buildout or difficulties in maintaining the existing ones.

RFI impact. Both ground-based and space-borne radio emissions from active services can impact the station operations. Unwanted frequencies at one (or several) of the VGOS bands can cause radio frequency interference with possible loss of data or the need to install tailor-made notch filters into the signal chain. The latter situation was the case, for instance, for the VGOS antennas at Ishioka and Santa Maria.

6 Conclusions and Outlook

In 2022, the VGOS observing program encompassed about 265 Intensive (1-hour) sessions and 50 (24-hour) sessions. However, data transport and storage as well as correlator time are the main resources that limit the current program. It is expected that data transfer rates both at the stations and correlators will be improved over time resulting in an increased cadence of observing sessions. This needs to go hand in hand with enhancements of storage capacity.

There is still work to be done to be able to transition from the legacy S/X system to the VGOS system as the production workhorse of the IVS. Having two systems in parallel, of course, also means that they compete for resources. It is however essential that the nascent VGOS time series are rigorously integrated with the existing S/X time series so that the long-lasting S/X series can be carried forward by VGOS without real lapse. The tie of the S/X and VGOS systems can be accomplished by mixed-mode sessions as well as local tie sessions at sites with co-located legacy S/X and VGOS stations.

With a VGOS network of 25+ stations in the mid-2020s and the possibility of having 9–10 VGOS correlation centers processing operational VGOS sessions, we see the makings of the VGOS system reaching maturity. The VGOS Intensive series VGOS-INT-A furnishes dUT1 results by a factor of two better than the equivalent legacy S/X series. The IERS Rapid Service/Prediction Center has started to use the results operationally. Further VGOS Intensives are in the process of being validated. In short, the process has begun to phase in VGOS as a production tool.

References

Niell A, Barrett J, Burns A, Cappallo R, Corey B, Derome M, et al. (2018) Demonstration of a Broadband Very Long Baseline Interferometer System: A New Instrument for High-Precision Space Geodesy. *Radio Science*, 53, 1–23, doi: 10.1029/2018RS006617.

Niell A, Whitney A, Petrachenko B, Schlüter W, Vandenberg N, Hase H, Koyama Y, Ma C, Schuh H, Tuccari G (2005) VLBI2010: Current and Future Requirements for Geodetic VLBI Systems. In: *IVS 2005 Annual Report*, D. Behrend and K.D. Baver (eds.), NASA/TP-2006-214136, 13–40, https://ivscc.gsfc.nasa.gov/publications/ar2005/spcl-vlbi2010.pdf or https://ivscc.gsfc.nasa.gov/about/wg/wg3/IVS_WG3_report_050916.pdf.

Petrachenko B, Niell A, Behrend D, Corey B, Böhm J, Charlot P, Collioud C, Gipson J, Haas R, Hobiger T, Koyama Y, MacMillan D, Nilsson T, Pany A, Tuccari G, Whitney A, Wresnik J (2009) Design Aspects of the VLBI2010 System. Progress Report of the VLBI2010 Committee. *NASA Technical Memorandum*, NASA/TM-2009-214180, 58 pp., https://ivscc.gsfc.nasa.gov/technology/vgos-docs/TM-2009-214180.pdf.

Earth orientation parameters estimated from recent Australian mixed-mode and Southern Intensive sessions

S. Böhm, L. McCallum

Abstract The sensitivity of Very Long Baseline Interferometry (VLBI) measurements toward single Earth orientation parameters (EOP) and the resulting accuracy strongly depends on the network extension. We can expect high-quality estimates from sessions with a well-distributed observation network designed for EOP determination, such as the R1 and R4 sessions. The 24-h sessions observed within the Australian mixed-mode program (AUA/AUM) do not provide a globally extended network of stations. Still, they involve the future potential to deliver results with a short latency. Under this aspect, we investigate the possibilities to determine different sets of or single EOP from the AUA and AUM sessions observed since 2020. By fixing source and station positions and estimating the EOP as one offset each, we can derive all EOP from most of the examined AUA/AUM sessions with acceptable quality. A subset of the telescopes have been or are involved in observing the so-called Southern Intensive sessions since 2020. In addition to the results of the 24-h sessions, we present the UT1−UTC estimates derived from the latest Southern Intensives, now designated IVS-INT-S (IVS: International VLBI Service for Geodesy and Astrometry). Our assessment shows an accuracy of the IVS-INT-S comparable to that of other IVS Intensive sessions.

Sigrid Böhm
TU Wien, Department of Geodesy and Geoinformation, Wiedner Hauptstrasse 8-10, 1040 Vienna, Austria

Lucia McCallum
University of Tasmania, School of Natural Sciences, Physics, Private Bag 37, Hobart, Tasmania, 7001 Australia

Keywords Earth orientation parameters, Australian mixed-mode program, Southern Intensives

1 Introduction

We can determine all five Earth orientation parameters (EOP) within the adjustment process of geodetic very long baseline interferometry (VLBI) data, provided that there is a sufficient number and spatial and temporal distribution of observations. These parameters are the celestial pole offsets (CPO), the polar motion parameters, and the difference of universal time 1 to coordinated universal time, from now on referred to as dX, dY, xPol, yPol, and UT1−UTC.

In this study, we challenge the Australian mixed-mode sessions AUA/AUM (McCallum et al., 2022) regarding EOP determination. Due to their limited network extension, these sessions are not optimal for deriving EOP. Hence, we test different strategies imposing variable constraints.

Furthermore, we explore the UT1−UTC quality of the recent Southern Intensive sessions IVS-INT-S (Böhm et al., 2022).

2 Data and analysis

The considered periods are 2020–2023 for the AUA/AUM sessions and 2022–2023 for the IVS-INT-S. For both session types, the parameter estimation is carried out with the VLBI module of the Vienna VLBI and Satellite Software VieVS (Böhm et al., 2018).

2.1 Australian mixed-mode sessions

To evaluate the AUA/AUM EOP performance, we selected 84 AUA/AUM sessions from January 2020 to March 2023 and 91 R1 and R4 sessions close to the AUA/AUM sessions. The stations participating in the sessions in different constellations are shown in Fig. 1. Since the R1/R4 sessions are specially designed

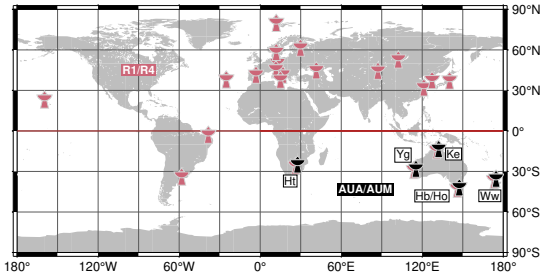

Fig. 1 Possible network stations of the AUA/AUM (black) and R1/R4 (red) sessions from 2020–2023.

for EOP determination, we regard the derived EOP results as the standard and investigate different processing strategies for the AUA/AUM to get EOP of comparable quality. For the R1/R4 sessions, we use our standard parameterization for EOP determination. We fix sources given in the International Celestial Reference Frame, ICRF3 (Charlot et al., 2020) and estimate non-ICRF sources. The coordinates of the stations are calculated, imposing no-net-rotation and no-net-translation conditions on the positions of the ITRF2020 catalog (International Terrestrial Reference Frame 2020, Altamimi et al., 2023). The parameters xPol, yPol, and UT1−UTC are estimated as piece-wise linear offsets at mid-nights, while dX and dY are estimated as offsets, referring to the middle of the sessions. Because of the spatial limitations of the AUA/AUM session networks, we did not apply the standard approach but fixed ICRF3 and ITRF2020 source and site positions. For EOP, we test three scenarios: estimation of all five parameters as offsets (*EOP*), fixing of CPO and estimation of polar motion and UT1−UTC as offsets (*ERP*: Earth rotation parameters), and an intensive-like setting with only UT1−UTC estimated (*UT1*).

2.2 Southern Intensive sessions

The IVS-INT-S are a series of Intensive sessions observed on baselines in the southern hemisphere. The results of the sessions from the years 2020 and 2021 are discussed in detail in Böhm et al. (2022). Here, we present the UT1−UTC results of 50 IVS-INT-S from January 2022 to April 2023 compared to 50 IVS-INT-1/3/00 observed close to the INT-S epochs. Fig. 2 shows

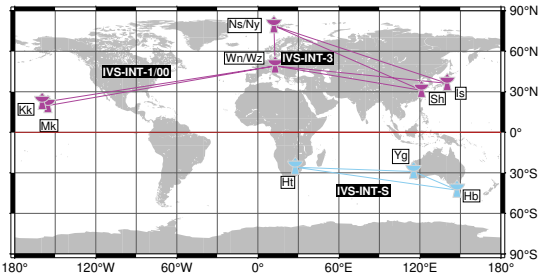

Fig. 2 Stations and baselines of the INT-S (light blue) and INT-1, INT-3, and INT-00 (purple) sessions from 2022–2023.

the networks of the different types of Intensive sessions analyzed here. As for the AUA/AUM sessions, the coordinates of stations and sources are fixed to the ITRF2020 and ICRF3 positions.

3 Results

The different analysis strategies applied for the AUA/AUM sessions are compared among each other and with the EOP results of the R1/R4 sessions using so-called boxplots. The statistical measures provided with a boxplot are illustrated in Fig. 3. All EOP results

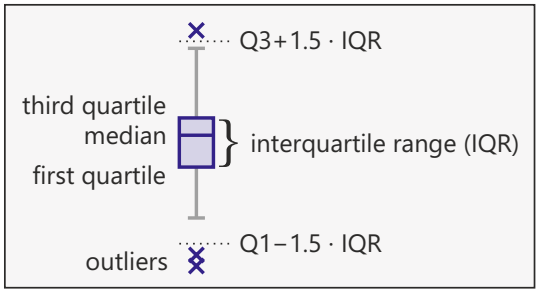

Fig. 3 Illustration of the boxplot concept.

are plotted as differences to the reference EOP time series JPL EOP2 (Chin et al., 2009). Sessions with differences to the reference EOP or formal errors larger than one milliarcsecond are excluded from the comparison and regarded as unsuitable for EOP determination. In the case of the R1/R4, this criterion does not apply to any session. When estimating all EOP or only ERP from the AUA/AUM sessions, 23 sessions are excluded from the comparison. Many deselected sessions are observed without the Ht telescope and, therefore, lack long baselines. If we do an Intensive-like analysis and estimate only UT1−UTC, only one session has to be dropped.

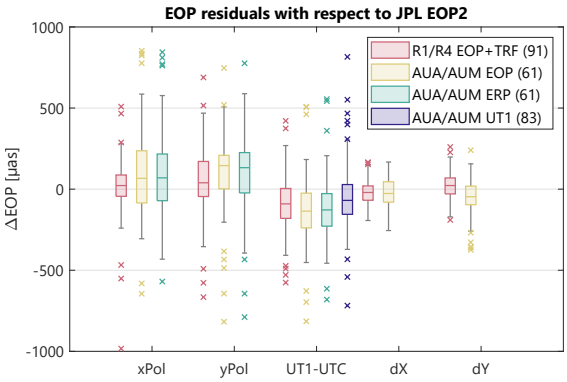

Fig. 4 Boxplots of EOP results (differences to JPL EOP2) from the 24-h sessions in µas. The number of sessions included in the comparison is given in parentheses.

The results of the examined 24-h sessions are displayed in Fig. 4. With the additional constraints added to the standard EOP estimation, the results produced by the different processing scenarios (*EOP*, *ERP*, and *UT1*) can keep up with those of the R1/R4 sessions. However, especially in the case of the xPol-component, the spread of the differences to JPL EOP2 is significantly larger. The reason is probably the poor north-south extension of the AUA/AUM session networks. Interestingly, we do not see much difference between the *EOP* and *ERP* scenarios. Not estimating CPO does not improve the quality of the other EOP results (xPol, yPol, and UT1−UTC), nor does it lead to the inclusion of more sessions. By applying the Intensive-like strategy (UT1), we can keep all but one session in the comparison. The quality of the UT1−UTC estimates is similar to that of the R1/R4 sessions. Yet, with this strategy, we can derive UT1−UTC only. So, it might be more beneficial to use the *EOP* strategy for the 61 sessions where it works and apply the *UT1* approach merely to the 22 sessions where the *EOP* strategy fails.

In Fig. 5, the UT1−UTC results of the different 24-h sessions and processings are shown together with the results of the Intensives IVS-INT-S and IVS-INT-1/3/00, again as differences to the JPL EOP2. The values are presented in µas like in Fig. 4 for better comparability with polar motion and celestial pole offsets. The *UT1*

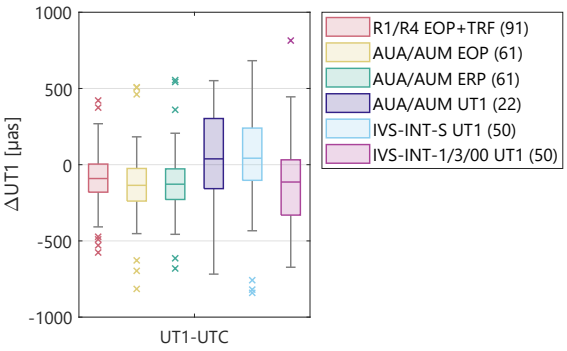

Fig. 5 Boxplots of UT1−UTC results (differences to JPL EOP2) from the 24-h and Intensive sessions in µas. The number of sessions included in the comparison is given in parentheses.

approach is only used for the 22 sessions where the geometry is insufficient for estimating all EOP. Compared with the performance of the southern Intensives and the other IVS Intensives shown here, the Intensive-like analysis yields results with Intensive-like accuracy, which is still better than not using these 22 sessions at all.

The differences to JPL EOP2 for the INT-S and the INT-1/3/00 are presented as individual values and in a histogram in Fig. 6.

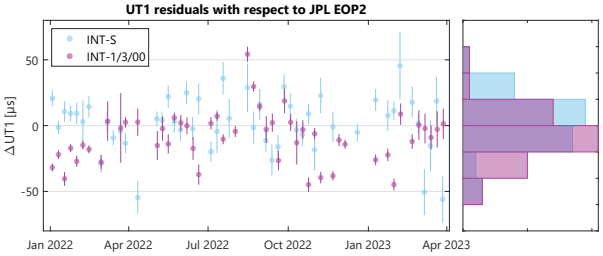

Fig. 6 UT1−UTC results (differences to JPL EOP2) from the IVS-INT-S (light blue) and IVS-INT-1/3/00 (purple) sessions with errorbars in µs.

As can also be read from Tab. 1, the UT1 residuals w.r.t. JPL EOP2 are mainly in the range of about ± 20 µs and rarely over 50 µs absolutely, for all Intensive types. We see a significant negative bias for the IVS-INT-1/3/00 sessions that could be due to the choice of the reference EOP series. The INT-S have a slightly lower weighted standard deviation w.r.t. JPL EOP2 but slightly larger formal errors than the other investigated Intensives during the study period.

Table 1 Statistics of UT1−UTC estimates from Intensive sessions with respect to JPL EOP2.

Statistical quantity [µs]	**INT-S**	**INT-1/3/00**
Weighted standard deviation	16	20
Weighted mean	2	−12
Interquartile range	23	24
Mean formal error	11	7
Median formal error	9	6

4 Conclusions and outlook

Although the AUA/AUM sessions are not designed for deriving EOP, they can be employed for that if certain constraints are imposed. Out of 84 AUA/AUM sessions from 2020–2023, 61 can be used to estimate all five EOP with acceptable accuracy if source and station positions are fixed to a priori values. The deviations w.r.t. a reference time series are slightly higher than those obtained from R1/R4 sessions, especially in the case of polar motion, xPol. We did not find a significant influence on polar motion or UT1−UTC if CPO are estimated or fixed. Sessions that fail when determining all EOP can be analyzed in an Intensive-like mode to retrieve at least UT1−UTC, with the drawback of a reduced accuracy.

The IVS-INT-S sessions from 2022 to April 2023, also assessed in this study, deliver stable UT1−UTC results, able to compete with the results of IVS-INT-1/3/00 Intensives from the same period. The Southern Intensives are operated every Monday at 6:30 UTC on the baseline Ht-Hb (South Africa - Tasmania), as a permanent component of the IVS observing program.

References

McCallum L, Chuan L, Krásná H, McCallum J, Böhm J, McCarthy T, Gruber J, Schartner M, Quick J, Rogers A (2022) The Australian mixed-mode observing program. *J Geod*, 96(67), doi: 10.1007/s00190-022-01657-2.

Böhm S, Böhm J, Gruber J, Kern L, McCallum J, McCallum L, McCarthy T, Quick J, Schartner M (2022) Probing a southern hemisphere VLBI intensive baseline configuration for UT1 determination. *Earth Planets Space*, 74(118), doi: 10.1186/s40623-022-01671-w.

Böhm J, Böhm S, Boisits J, Girdiuk A, Gruber J, Hellerschmied A, Krásná H, Landskron D, Madzak M, Mayer D, McCallum J, McCallum L, Schartner M, Teke K (2018) Vienna VLBI and Satellite Software (VieVS) for Geodesy and Astrometry. *Publ Astron Soc Pac*, 130(986), doi: 10.1088/1538-3873/aaa22b.

Charlot P, Jacobs C S, Gordon D, Lambert S, de Witt A, Böhm J, Fey A L, Heinkelmann R, Skurikhina E, Titov O, Arias E F, Bolotin S, Bourda G, Ma C, Malkin Z, Nothnagel A, Mayer D, MacMillan D S, Nilsson T, Gaume R (2020) The third realization of the International Celestial Reference Frame by very long baseline interferometry. *Astron Astrophys*, 644(A159), doi: 10.1051/0004-6361/202038368.

Altamimi Z, Rebischung P, Collilieux X, Métivier L, Chanard K (2023) ITRF2020: an augmented reference frame refining the modeling of nonlinear station motions. *J Geod*, 97(47), doi: 10.1007/s00190-023-01738-w.

Chin T M, Gross R S, Boggs D H, Ratcliff J T (2009) Dynamical and Observation Models in the Kalman Earth Orientation Filter. *The Interplanetary Network Progress Report*, 42-176.

Imaging ICRF3 sources at 0.2 mas resolution with the European VLBI Network at K band

P. Charlot, M. E. Gómez, R. M. Campbell, A. Collioud, A. Keimpema, M. Kettenis

Abstract We explore the capabilities of the European VLBI Network (EVN) to image radio reference frame sources observed through geodetic-style experiments at K band (22 GHz). The EVN includes long East-West and North-South baselines (from Europe to Asia and from Europe to South Africa) along with baselines of shorter and intermediate lengths within Europe, making it worthwhile to study the potential of the network for imaging in such observing mode. To this end, we use a 22-telescope experiment carried out as part of the EC-funded JUMPING JIVE project in October 2020. The experiment targeted a total of 80 sources from the third realization of the International Celestial Reference Frame (ICRF3), all of which selected from the pool of ICRF3 defining sources. Scheduling of the observations was accomplished by using sub-netting because the primary scope of the experiment was geodesy. Despite this geodetic-style approach, it was possible to image all of the sources, hence demonstrating the capability of the EVN for such work. The resulting images may be used to further assess the source compactness, and hence their astrometric suitability, at a frequency and a resolution higher than probed by the standard S/X observations that formed the basis for selecting those sources as ICRF3 defining sources.

Patrick Charlot · Arnaud Collioud
Laboratoire d'Astrophysique de Bordeaux, Université de Bordeaux, CNRS, Bât. B18N, Allée Geoffroy Saint-Hilaire, CS 50023, 33615 Pessac Cedex, France

Maria Eugenia Gómez
Universidad Nacional de La Plata, MAGGIA and CONICET, Av. 7 N° 776, La Plata (CP 1900), Buenos Aires, Argentina

Robert M. Campbell · Aard Keimpema · Mark Kettenis
Joint Institute for VLBI ERIC, Oude Hoogeveensedijk 4, 7991 PD Dwingeloo, The Netherlands

Keywords VLBI, EVN, radio sources, celestial reference frame, ICRF, imaging

1 Introduction

The work reported in this paper was carried out as part of the JUMPING JIVE project[1], an EC funded project for the period 2016–2021 whose objective was to enhance the profile of the Joint Institute for VLBI ERIC (JIVE). In this project, Work Package 6 "geodetic capabilities" (Colomer et al., 2019) was aimed to implement a fully operational geodetic path at the European VLBI Network (EVN) software correlator (SFXC) at JIVE and measure the geodetic position of the non-geodetic EVN telescopes. For the latter, two 24-hour experiments have been carried out using the EVN at K band, one in June 2018 (EC065) and one in October 2020 (EC076) (Gómez et al., 2020). Based on these data, geodetic positions at the cm level have been derived for the relevant telescopes (Gómez et al., 2023).

In the following, we explore the use of the same data, more specifically those from EC076, to image the sources targeted in these observations. Section 2 describes the VLBI observing network, source selection scheme, scheduling strategy, correlation and post-processing of the data, while Sect. 3 presents the imaging results. The latter includes plots of the resulting images for a few sources, including some for low-declination sources. Comparisons with independent VLBI images obtained with the Very Long Baseline array (VLBA) at K band are also provided to qualify the quality of the EVN images. Conclusions and future prospects are drawn in Sect. 4.

[1] See the web page of the project at https://jumping.jive.eu/

2 Observations

The observing network used to acquire the data involved in this work includes all EVN radio telescopes that have the capability to observe at K band, namely 17 telescopes in Europe, Asia and South Africa. The network was further augmented with the four e-MERLIN out-stations with K band capability (Cambridge, Darnall, Knockin and Pickmere in the UK) and the 26 m antenna in Hobart (Australia). In all, this forms a large network of 22 telescopes (Fig. 1). The e-MERLIN outstations provide short baselines which help with the recovery of extended structure, while the Hobart telescope helps with North-South resolution.

A total of 80 sources from the third realization of the International Celestial Reference Frame (Charlot et al., 2020) were observed during the experiment. Because the primary scope of the project was to determine the geodetic positions of the EVN telescopes, all sources were chosen among the pool of ICRF3 defining sources. This selection should limit potential effects due to source structure since the defining sources are deemed to be more compact. We arranged for these 80 sources to be well spread in right ascension and declination, as reflected by the sky distribution plotted in Fig. 2. No sources below -30° declination were selected because the network would then be reduced to the single baseline between Hartebeesthoek and Hobart, which would make imaging impossible.

The scheduling of the observations was achieved using NASA's SKED software. While the sky coverage above each telescope was optimized in the usual way to allow for the estimation of tropospheric parameters for geodesy, we also arranged for the observations to be reasonably well spread over all sources and forced each scan to include at least four telescopes. The number of scans per source was between 2 and 10, with a mean value of 5.6, while the number of observations ranged from 30 to 546, with a mean value of 257. Due to the large network, one-third of the scans had more than 10 telescopes and 10% had 16–18 telescopes, a very favorable situation for imaging.

The data were correlated with the SFXC correlator and post-processed in a standard way using AIPS based on the calibration information (system temperatures and gain curves) attached to the data. Fringes were found for all stations but Cambridge and Jodrell Bank, thus leaving a set of 20 stations for the analysis.

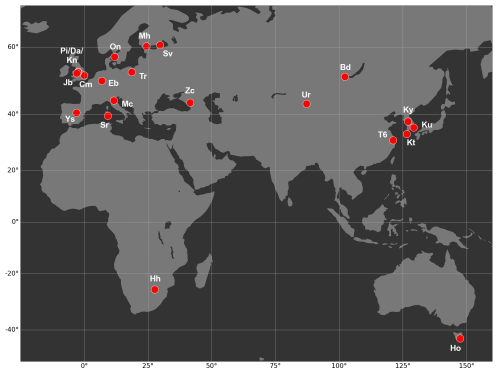

Fig. 1 Geographical location of the 22 radio telescopes involved in the EC076 experiment.

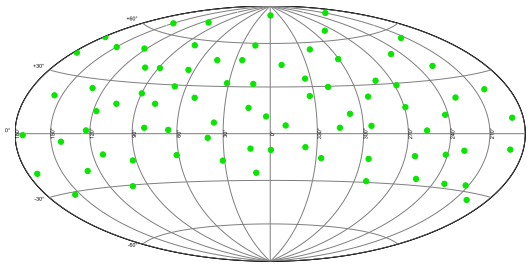

Fig. 2 Sky distribution of the 80 ICRF3 defining sources observed in the course of the EC076 experiment.

3 Imaging results

The imaging was accomplished using DIFMAP in a fully-automatic mode after averaging the visibilities over 10-second periods of time. Outliers were discarded in an automatic way using a homemade DIFMAP routine. Based on this procedure, all of the 80 sources have been successfully imaged, demonstrating the potential of the EVN for such work. The images produced for three of the observed sources are shown in Fig. 3 as examples. Apart from a few exceptions (see below), the sources are found to be mostly very compact at the EVN resolution, therefore confirming that they qualify well as defining sources for the celestial reference frame. The dynamic range of the images (defined as the ratio of the peak brightness to the rms of the brightness in the residual map) is up to 1300, with a median value of 490. Interestingly, nearly circular or moderately elongated restoring beams are obtained for sources at low declinations (see Fig. 4), a unusual but favorable situation which results from the network

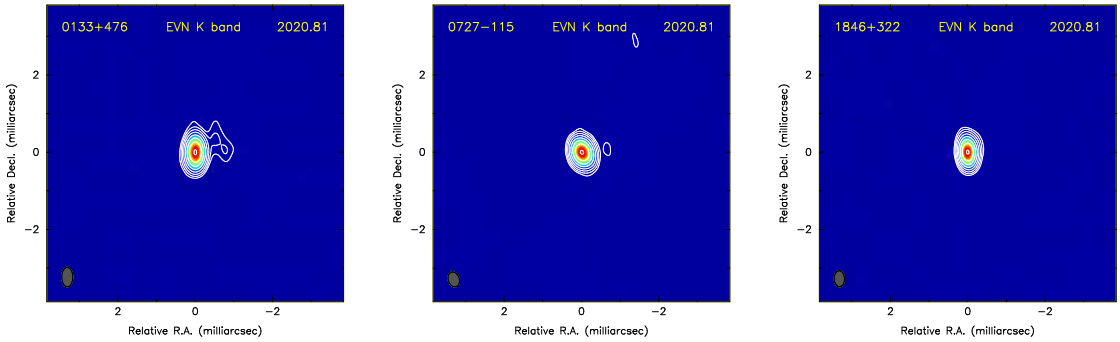

Fig. 3 VLBI images at K band for three ICRF3 defining sources (0133+476, 0727−115, 1846+322) observed in the EVN experiment EC076 conducted on 23 October 2020. Contour levels are drawn at ± 0.75, 1.5, 3, 6, 12, 24, 48 and 96% of the image peak brightness.

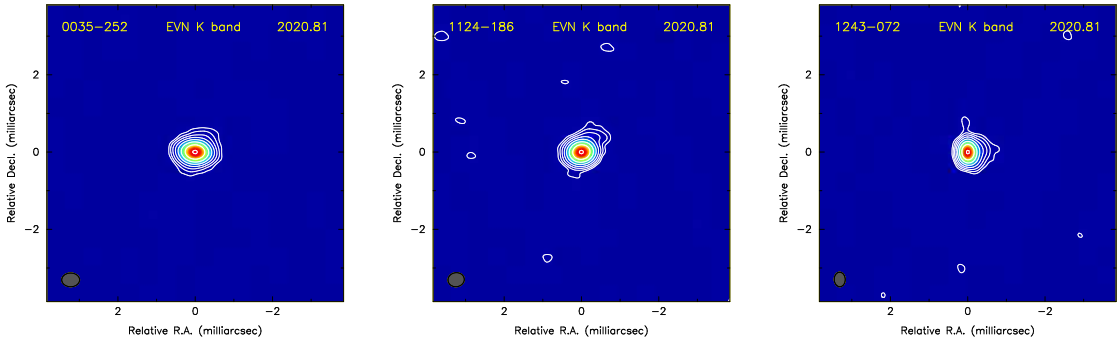

Fig. 4 VLBI images at K band for three low-declination sources (0035−252, 1124−186, 1243−072) observed in the EVN experiment EC076 conducted on 23 October 2020. Contour levels are drawn at ± 0.75, 1.5, 3, 6, 12, 24, 48 and 96% of the image peak brightness.

including long North-South baselines between Hartebeesthoek and Europe and between Hobart and Asia.

Figure 5 compares our EVN images for two sources that are not point-like (0552+398 and 1418+546) with previously published VLBA images of the same two sources, also at K band (de Witt et al., 2023). Though not at the same epoch, the EVN and VLBA images compare well, indicating similar jet-like structure elongated in the same direction in both cases. The comparison also shows that the EVN provides somewhat higher resolution compared to the VLBA. Considering our entire set of 80 images, the minor axis of the restoring beam ranges from 0.15 mas to 0.43 mas, with a median value of 0.28 mas. In comparison, the maximum resolution that the VLBA can reach is about 0.3 mas. Such increased resolution should help to probe source structure even closer to the core, which would be of interest for the K band celestial reference frame but also for understanding the physics of the sources.

4 Conclusions and outlook

Imaging of a sample of 80 ICRF3 defining sources observed during a geodetic-style EVN experiment conducted at K band demonstrates the capabilities of the EVN for such imaging work. The images compares well with VLBA images produced independently and have about 30% higher resolution. Southern stations (Hartebeesthoek, Hobart) are essential to image low-declination sources. Beyond their use for astrophysics, such high-resolution images are also useful to assess the continued astrometric suitability of the sources for the development and maintenance of the ICRF at K band. In the future, we plan to pursue further such observations with the EVN for mixed geodetic, astrometric and imaging goals. Along this line, an initial 48-hour experiment that observed another 166 ICRF3 defining sources was conducted early June 2023. Later on, we plan to go to weaker sources, taking

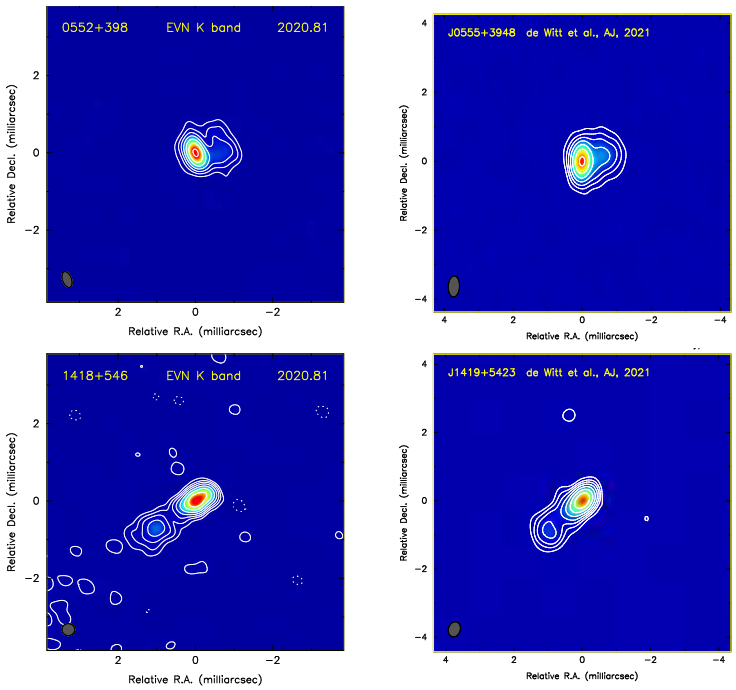

Fig. 5 Comparison of EVN (left) and VLBA (right) images at K band for the sources 0552+398 (J0555+3948) and 1418+546 (J1419+5423). The VLBA images are from de Witt et al. (2023) and are for epoch 2015.55 (case of 0552+398) and 2017.02 (case of 1418+546). Contour levels are drawn at ± 1.03, 2.75, 5.50, 10.99, 21.98, 43.97 and 87.94% of the image peak brightness for 0552+398 and at ± 0.64, 1.70, 3.41, 6.82, 13.63, 27.26 and 54.53% of the image peak brightness for 1418+546.

advantage of the large sensitivity of the EVN. The VLBI images presented here will be made publicly available through the Bordeaux VLBI Image Database[2].

Acknowledgments

The European VLBI Network (EVN) is a joint facility of independent European, African, Asian, and North American radio astronomy institutes. The results presented in this paper were derived from EVN data with project code EC076. We are indebted to the Hobart team at the University of Tasmania for agreeing to join this experiment, which strengthened significantly the geometry of the network. We are also grateful to Alet de Witt for making available K band VLBA images prior to publication. This research received funding from the European Union's Horizon 2020 Research and Innovation Programme, under grant agreement No. 730884. We also thank RadioNet for its support.

[2] See https://bvid.astrophy.u-bordeaux.fr/.

References

P. Charlot, C. S. Jacobs, D. Gordon, et al. (2020) The third realization of the International Celestial Reference Frame by very long baseline interferometry. A&A, **644**, A159.

F. Colomer, M. Kettenis, R. M. Campbell, P. Charlot, A. Szomoru (2019) Geodetic capabilities of the JIVE SFXC correlator. Proceedings of the 10th IVS General Meeting, Eds. K. L. Amstrong, K. D. Baver, and D. Behrend, NASA/CP-2019-219039, p. 117–120.

A. de Witt, C. S. Jacobs, D. Gordon, M. Bietenholz. M. Nickola, A. Bertarini (2023) The Celestial Reference Frame at K band: Imaging. I. The First 28 Epochs. AJ, **165**, 139.

M. E. Gómez, P. Charlot, R. M. Campbell, M. Kettenis, A. Keimpema (2020) Geodesy at K band with the European VLBI Network. Proceedings of the Journées 2019, Ed. C. Bizouard, Observatoire de Paris, p. 185–188.

M. E. Gómez, P. Charlot, R. M. Campbell, A. Keimpema, M. Kettenis (2023) Geodetic positions of radio telescopes from the European VLBI Network. A&A (in preparation).

Bonn Correlator Status

Y. K. Choi[1,2,3], S. Bernhart[1,2,3], H. Rottmann[3] and J. Wagner[3]

Abstract We report on the status of the Bonn Correlation Center focusing on geodesy. As well as technical aspects of the cluster and its performance, we summarize our duties as one of the IVS correlators and recent progress.

Keywords VLBI correlation, DiFX, VGOS

1 Introduction

The Bonn correlator, located in Bonn, Germany, is operated jointly by the Max Planck Institute for Radio Astronomy (MPIfR) in Bonn and the Federal Agency for Cartography and Geodesy (Bundesamt für Kartographie und Geodäsie, BKG) in Frankfurt. The MPIfR hosts the correlator facility and shares with the BKG the the investment and operational costs of the cluster. Since January 2017 the personnel responsible for the correlation of geodetic sessions are employed by the BKG via a private contractor, the Reichert GmbH.

2 Correlator Capabilities

The Distributed FX software correlator (Deller et al. 2011) in various versions is used at the Bonn correlator. For geodetic production, we currently use DiFX-2.6.3 for S/X Legacy sessions and DiFX-2.5.5 for VGOS observations.

The correlator is running on a high-performance computing (HPC) cluster, which was renewed in 2015 to match both VGOS and mm-VLBI requirements. It consists of

1) 68 nodes with 20 compute cores each, for a total of 1360 cores
2) three head nodes which allow execution of several correlations and postprocessing in parallel
3) 2.8 PB disk space in RAID units and combined in a BeeGFS parallel cluster file system
4) 14 Mark 5 playback units
5) 11 Mark 6 playback units each with four and some with six bays.

The raw data are recorded at the stations either on modules (Mark 5 or Mark 6) or on storage servers, usually referred to as Flexbuffs. For geodetic experiments the data are mostly e-transferred to the HPC cluster. Various raw data formats have already been correlated in Bonn: Mark IV, Mk5, DVP, and various flavors of VDIF.

The correlator output data (SWIN files) can be exported to FITS and HOPS (Mark IV) formats. For post-processing the following software packages are available: AIPS, CASA, PIMA, and HOPS (Haystack Observatory Postprocessing System), the latter of which is the standard tool for geodesy. The correlator outputs and other important files (e.g., VEX and v2d files) are backed up daily on the HPC cluster. The final products are archived on the MPIfR archive server, where they will be kept for at least ten years. The EXPAD and COMEDIA tools are used for bookkeeping of experiments and corresponding media correlated in Bonn. They are the frontends to a local database that records all relevant information such as the

1. Reichert GmbH
2. Bundesamt für Kartographie und Geodäsie
3. Max-Planck-Institut für Radioastronomie

observation date, participating stations, modules, and status of the experiment.
In 2022 correlator operations were switched to using SLURM for scheduling and executing correlations on the HPC cluster. The main motivation for this change was using SLURMs ability to automatically suspend and resume compute nodes depending on the current cluster workload in order to substantially reduce the energy consumption in idle time periods. On average 11000 kWh of power equivalent to about 10t of CO2 can be saved per month.

3 Activities in Bonn

3.1 IVS correlation

Our duties include the correlation of the following legacy S/X sessions:

- Weekly INT3 sessions observed every Monday with three to five participating stations and a duration of one hour. 34 sessions were processed in 2022, 37 sessions are scheduled for 2023.
- The R(apid)1 series also observed on Mondays with 10 to 15 participating station. 52 sessions were correlated in 2022, 52 sessions are to be processed in 2023. Since January 2023, the Australian VGOS stations participate in the R1 observations, making these so-called mixed-mode sessions in which legacy antennas equipped with right circular polarisation receivers observe along with antennas that record data in dual linear polarisation with a VGOS broadband receiver.
- Bimonthly observed T2 sessions to monitor the TRF: 7 sessions were worked on in 2022, 7 sessions are also scheduled for 2023. The T2s are currently the largest sessions in terms of participating antennas. The number of envisaged stations ranges between 14 and 25.
- The bimonthly OHG series focusing on southern hemisphere stations with a duration of 24 hours including five to seven stations. 6 sessions were processed in 2022, all of which having been observed in 2021, another 6 sessions are scheduled for 2023. The participation of the Antarctic stations Syowa and O'Higgins usually delays the processing for one year due to the late arrival of the data at the correlator which implies that the sessions, that will be processed in 2023, are those observed in 2022.

Moreover, the Bonn correlator regularly processes IVS VGOS (24 hours) sessions: 11 sessions were processed in 2022, 10 sessions are currently scheduled in 2023 with 8 to 11 stations. Since the processing time of VGOS experiments is on average quite long compared to the Rapid (R1 and R4) sessions, which are usually processed within two weeks, the experiments are still scheduled with a biweekly cadence. In the medium term, the observing cadence is planned to be shifted to a weekly interval.

3.2 DiFX-2.5.4 and 2.5.5

The Bonn correlator started correlating 24-hour IVS VGOS sessions in autumn 2020. Each correlator had their own local patches and different versions of DiFX and difx2mark4 to correlate and convert the data.
In August 2021, to regain a consistent DiFX-2.5 installation for VGOS correlation at all sites, Jan Wagner gathered the accumulated patches and also backported certain features from mainline DiFX-2.6. Combined with Haystack-provided HOPS 3.22, these were released to the DiFX community as DiFX 2.5.4.
In October 2022, to fix an issue in correlation of multi-datastream Ishioka data that affects the handling of IF-specific LO and clock offsets (*loOffsets*, *freqClockOffs*), he released DiFX 2.5.5 which is still the default DiFX version for VGOS correlation and has been used along with the Haystack Observatory Postprocessing System (HOPS) version 3.24 at the Bonn correlator.

3.3 DiFX-2.6

At the Bonn correlator, the established DiFX version for the correlation of legacy S/X sessions is currently 2.6.3 along with HOPS v3.24 (v3.25 in October 2023).
Correlation and fringe fitting are performed by means of batch job submission (SLURM) via 'difxslurm' for better sharing of the cluster compute nodes with other users (EHT/GMVA/pulsar/simulation/...).

3.4 DiFX-2.8

When the astronomers started testing DiFX 2.8.0, they noticed that the auto-correlation was not produced. This bug was reported and fixed in the meantime.
The geodetic VLBI group began testing the latest DiFX release 2.8.1 on two geodetic experiments, one of which was a mixed-mode session (r11094) where two stations (Hb, Ke) observed in dual linear polarisation (X, Y) mode and the others in single circular polarisation (R).
When checking the mixed-mode session fringe plots, it was noticed that scans with mixed baselines (i.e. linear-circular) show much higher amplitudes (factor of 4.7) and higher SNR than with DiFX-2.6.3 whereas baselines with only circular or only dual linear polarisation show the same numbers as with DiFX-2.6.3. This bug was reported to the DiFX developers and still awaits a fix before we can continue further testing.

3.5 Multi-datastream correlation

Recorded bands are spread across several files and previously these VGOS data should be vmux-ed to "merge" them for single-datastream correlation under DiFX-2.5.3. This procedure doubles the occupied disk space and substantially increases the processing time. In Bonn we carry out DiFX multi-datastream correlation, possible under DiFX-2.5.4 and 2.6.3 using multi-datastream configuration. Onsala Oe/Ow, Ishioka and Ny-Alesund north now observe with multi-files and e-transfer their files without prior "merging".

3.6 Upgraded Internet connection

Previously, we used two 1 Gbps links to the German Research Network (Deutsches Forschungsnetz - DFN), servers BONN and RZBONN. In October 2021, we upgraded to a commercial 10 Gbps link (NetCologne) for e-VLBI and replaced the BONN server. RZBONN as part of the DFN is still working. Transfer protocols we use are JIVE jive5ab/m5copy[1], and JIVE e-transfer etc/etd[2]. After the upgrade, the transfer speed is much faster than before. For example, the transfer of a typical VGOS data set from Onsala (≈23 TB) now takes two days instead of two weeks.

3.7 VGOS correlation (VO3124)

In order to meet the medium-term goal of a weekly observing cadence for the VGOS sessions, the IVS started to monitor the processing time at the correlators more closely. The aim is to deliver the database to the analysts not later than 30 days after the observation.
One of the more recent sessions correlated in Bonn was VO3124. Ten stations (Gs, Hb, Is, K2, Nn, Oe, Ow, Wf, Ws, Yj) participated in the observation, seven of which e-transferred their data and three shipped Mark6 modules to the correlator, the process of which took around two week. During fringe search, however, it turned out that one of the data sets had a problem in that the data of band D had been shifted by one second. This had to be fixed prior to correlation in order not to lose the band for the whole session. Fortunately, Jan Wagner managed to create a short program which shifted the 16-channel portion of the sample data to the correct time.
The fix was applied at the correlator, because the data transfer had already been completed, but could also have been executed at the station. This is an example of why a quick inspection of the data prior to correlation or even a complete transfer is essential.
The correlation itself took another 60 hours due to parallel processing of other sessions. Nevertheless, the time between observation and the submission of the correlation report and database took the targeted 30 days in total.

4 Future Plans

In 2023 we are assigned to correlate 39 INT3 sessions, 52 R1 sessions, regularly planed for mixed-mode with the Australian VGOS stations, seven T2, six OHIG and ten VGOS sessions. The Australian stations are regu-

[1] https://github.com/jive-vlbi/jive5ab

[2] https://github.com/jive-vlbi/etransfer

larly included in the network for the VGOS sessions since 2023. There are new VGOS intensive series Int-M sessions with three VGOS antennas (Is, Nn, Ws) starting from October 21, 2023 to be correlated in Bonn.
Furthermore, the geodesy group will continue testing the latest DiFX version (currently DiFX-2.8) before applying it for normal operation. After comparing the SWIN files as well as the resulting observables of the presently used DifX version (2.6.3) and the upcoming release, we will switch to the latter one as soon as possible - its stability presupposed.

References

A. T. Deller, W. F. Brisken, C. J. Phillips, J. Morgan, W. Alef, R. Cappallo, E. Middelberg, J. D. Romney, H. Rottmann, S. J. Tingay & R. Wayth (2011) DiFX-2: A More Flexible, Efficient, Robust, and Powerful Software Correlator *PASP*, 123, 275—287, doi: 10.1086/658907.

Digital Identifiers and Metadata for the IVS

G.L. Coetzer, Y. Takagi, M. Nickola

Abstract The International VLBI Service for Geodesy and Astrometry (IVS) is committed to providing quality data and scientific products in support of geodetic, astrometric and geophysical research through effective Research Data Management (RDM) practices. Innovative new data services, tools, applications and support approaches, such as Persistent IDentifiers (PIDs), descriptive metadata and repositories, have been developed to assist users in discovering, analysing and visualising IVS data and products. The use of Digital Object Identifiers (DOIs) and suitable metadata can contribute significantly to making IVS data and products Findable, Accessible, Interoperable and Reusable (FAIR). An exploratory study was initiated to determine the best practices for the attribution of DOIs to IVS data and products. We report on progress with the investigation and provide some recommendations.

Keywords Data management, Data repositories, Digital object identifiers, DOI, Information systems, Metadata, Metadata repositories

Glenda Coetzer · Marisa Nickola
South African Radio Astronomy Observatory (SARAO), Hartebeesthoek Radio Astronomy Observatory (HartRAO), PO Box 443, Krugersdorp 1740, South Africa

Glenda Coetzer
University of Pretoria (UP), Private bag X20, Hatfield 0028, Pretoria, South Africa

Yu Takagi
Geospatial Information Authority of Japan (GSI), 1, Kitasato, Tsukuba 305-0811, Japan

1 Introduction

The realisation of the importance of unique Persistent IDentifiers (PIDs), supported by Wilkinson's Findable, Accessible, Interoperable and Reliable (FAIR) data principles, led to the attribution of Digital Object Identifiers (DOIs) to data. Together with DOIs, the discovery of data largely depends on proper and encompassing descriptive metadata, the use of metadata standards and data repositories.

The International VLBI Service for Geodesy and Astrometry (IVS), established in 1999, is an international collaboration of organisations which operate or support Very Long Baseline Interferometry (VLBI) components (IVS, 2023). It is a member of the World Data System (WDS). Geodetic and astrometric data and science products of the IVS require structured and well-documented mechanisms towards enabling citability, scientific recognition and reward. This can be achieved with the attribution of DOIs, which is best practice for FAIR data, to data and products (GGOS, 2023). The use of DOIs, accompanying descriptive metadata and metadata repositories can significantly contribute towards making IVS data and products FAIR.

2 Digital Object Identifiers

A DOI is a unique persistent identifier or handle, used to identify various types of resources, e.g. journal articles, research data and products, instruments, etc. DOIs fit within the Uniform Resource Identifier (URI) system and follow the International Organisation for Standardisation (ISO) (ISO, 2012). They differ from other types of identifiers (e.g. International

Standard Book Numbers [ISBN]) in that they are also actionable and interoperable. DOIs are permanent and can therefore always be used to locate the data object to which it refers. The use of DOIs to identify datasets allows peer reviewers to more easily validate research methods and verify research results. When the data used in a project can be identified, then fellow researchers can duplicate results or expand on initial findings (Novacescu, J. et al. 2018).

A DOI consists of three components, namely the resolver information, prefix (identifies provider) and suffix (internal unique opaque name for the data source). The resolver and prefix are provided by Registration Agencies (RAs) and the suffix by clients (Wanchoo et al., 2017) (see Figure 1).

Fig. 1 Structure of a DOI (Wanchoo et al., 2017).

In 2000, the International DOI Foundation (IDF) introduced DOIs for unambiguous identification and linking of online articles. Four years later, the first DOI for digital datasets was registered (Paskin, 2010). Since its introduction, DOI usage has grown considerably. In 2016 the usage peaked at over 600 000 000 DOIs resolved. Seven years later more than 1 400 000 000 DOIs were resolved. This number is increasing daily (Figure 2).

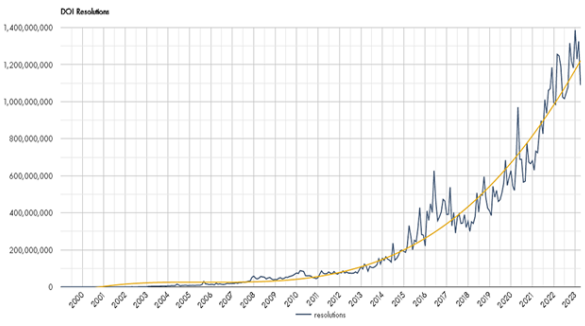

Fig. 2 Growth of DOI usage over time (DOI Foundation. 2023).

Different approaches, driven by the needs of the client, are followed for the processing of DOIs. A simplistic depiction of a DOI processing workflow and the various role-players is provided in Figure 3. Data providers/clients initiate the process by obtaining information/metadata of a dataset and submitting the metadata for review/quality check and validation. In some cases, this part of the process is conducted by the data providers themselves or other relevant people, such as data scientists, managers and librarians. The reserving or registering of a DOI follows with a request being sent to a Registration Agency (RA). Outcomes from the RA are communicated to the data provider/client. Should the request be accepted by the RA, the outcome is a DOI for that particular dataset.

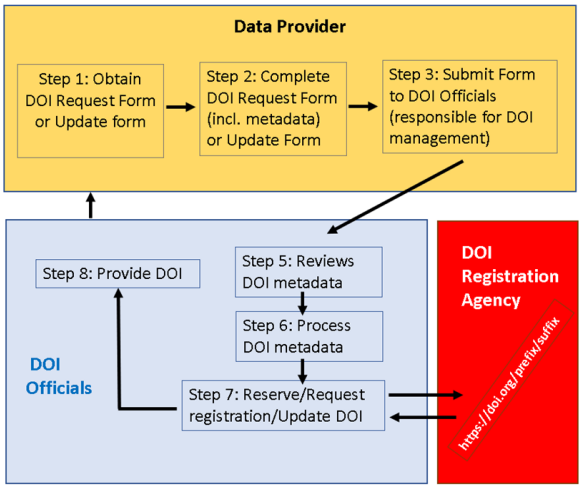

Fig. 3 Workflow for the processing of DOIs (Wanchoo et al., 2017).

A DOI resolves to its target, the information object to which the DOI refers. This is achieved by utilising a Uniform Resource Locator (URL) to link to where the object is located (Wanchoo et al., 2017). The URL ties the DOI to metadata about the dataset. It is also mandatory for each DOI to have its own landing page.

3 Metadata and metadata repositories

The discussion of DOIs cannot be concluded without mentioning metadata and the repositories which store the metadata. FAIR data are largely dependent on suitable and encompassing descriptive metadata as well

as Metadata Repositories (MR). When clients register their digital object content with an RA, a metadata record for the digital object is created. The metadata within that record become an enduring, widely distributed connection to the data (Crossref, 2023). A DOI's metadata are machine-readable, exchangeable and citable in scholarly literature.

Metadata records have requirements for the inclusion of mandatory and optional elements. These elements define data for accurate and consistent identification, description and citation. An example of mandatory and optional metadata elements on a DOI landing page is provided in Figure 4.

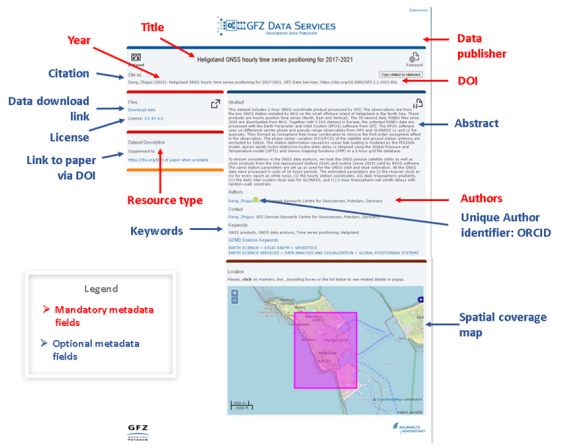

Fig. 4 Occurrence of mandatory and optional metadata attributes on a DOI landing-page (adapted from Deutsche GeoForschungsZentrum (GFZ) Data Services, 2023).

At its most basic level, a digital repository, for example an MR, is a database or file storage and retrieval mechanism created to store metadata (Bugaji & Chowdhury, 2018). An MR typically contains metadata far beyond simple definitions of the various data structures. MRs provide physical storage space and contain software that can be used for the cataloguing of metadata. Metadata in an MR must be generic, integrated, current and historical (Marco & Jennings, 2004).

The Crustal Dynamics Data and Information System (CDDIS) provides IVS data, products and the accompanying metadata. Various types of metadata are catalogued and stored in a relational database/repository which is accessible to the scientific community via the CDDIS platform (Noll, 2010). The CDDIS makes use of data type-specific formats, created in-house, for the metadata. The metadata include metadata elements, such as file name, source, arrival time, observing station identification, spatial and temporal attributes, iinstrument parameters, etc.

4 DOIs for the IVS community: project timeline

Members of the IVS community, with support from the IVS Directing Board (DB), initiated a project to determine best practices for attribution of DOIs for IVS datasets and products. A timeline of the study is presented in Figure 5.

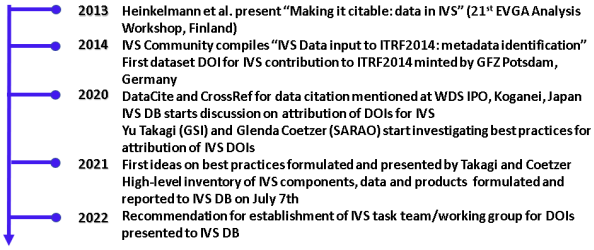

Fig. 5 DOIs for the IVS project timeline.

During the project, basic structures for IVS infrastructure, data and products were defined. An inventory of all IVS data and products was compiled and an assessment was conducted to determine which data and/or products should be minted first. It was agreed that DOIs for IVS products should be minted first. A few issues, such as who will be responsible for DOI minting for the IVS (i.e. which member institution or body) as well as the limited human resources (at the moment only two members are involved in a project that includes many institutions, etc.), were identified.

The following recommendations were proposed:

- Establish a task team or working group to manage the minting of DOIs.
- Determine which member institution will be responsible for the funding and administration of DOI minting.
- Use controlled vocabularies and ontologies for metadata standardisation.
- Harmonise metadata across all data centres.

- Include other persistent identifiers (PIDs), e.g. Open Researcher and Contributor IDdentifiers (ORCIDs), Research Organization Registries (RORs), Fundref, etc., as mandatory metadata elements.
- The term 'IVS' should be the descriptor in the DOI itself (e.g. 'IVS' tagged in DOI suffix).
- Establish a methodology and workflow for DOI minting, for example:
  - follow a hierarchical approach for PID allocation, e.g. a single PID for an entire IVS infrastructure with several children-PIDs for telescopes, etc.;
  - mint IVS products for ITRF2020 first, followed by minting of Level 2 data observations for ITRF2020 computations and conduct trial runs for minting of Level 2 data);
  - create DOI landing pages and investigate DOI automation;
  - implement GeodesyML for geodetic datasets and products.

5 Conclusions and outlook

Basic structures for IVS infrastructure, data and products were identified. The use of PIDs, such as DOIs, ORCIDs and RORs as well as suitable metadata can contribute to making IVS data and products more FAIR. Going forward, discussions with IVS members need to be conducted to determine which body will be managing the attribution of DOIs and to implement best practices for DOI minting.

6 Acknowledgement

Our thanks go to Robert Heinkelmann, Axel Nothnagel, Dirk Behrend and the IVS DB for their guidance and support, and also to Kirsten Elger (Chairperson of the GGOS Working Group on DOIs for Geodetic Datasets) for her much appreciated leadership.

References

Clark BG (2003) A review of the history of VLBI. *Radio Astronomy at the Fringe*, 1–8, https://articles.adsabs.harvard.edu/pdf/2003ASPC..300....1C

Crossref. (2023) Metadata principles and practices. https://www.crossref.org/documentation/principles-practices/

Deutsche GeoForschungsZentrum (GFZ) Data Services (2023) Heligoland GNSS hourly time series positioning for 2017–2021. https://doi.org/10.5880/GFZ.1.1.2023.001

DOI Foundation (2023) DOI System exceeds 50 million assigned identifiers. https://www.doi.org/

Global Geodetic Observing System (GGOS) (2023) Working group on Digital Object Identifiers (DOIs) for geodetic datasets. https://ggos.org/about/org/co/dois-geodetic-data-sets/

International Organisation for Standardisation (ISO) (2012) International Organisation for Standardisation. https://www.iso.org/obp/ui/#iso:std:iso:26324:ed-1:v1:en

International VLBI Service for geodesy and astrometry (IVS) (2023) IVS - International VLBI Service for geodesy and astrometry. https://ivscc.gsfc.nasa.gov/

Marco D, Jennings M (2004) *Universal Metadata Models*, 36–43, Wiley, ISBN 0-471-08177-9.

Noll C (2010) The crustal dynamics data information system: A resource to support scientific analysis using space geodesy. *Advances in Space Research*, 45:1421–1440, doi: 10.1016/j.asr.2010.01.018.

Novacescu J et al. (2018) A model for data citation in astronomical research using Digital Object Identifiers (DOIs). *The Astrophysical Journal Supplement Series*, 236, 20, doi: 10.3847/1538-4365/aab76a.

Paskin N et al. (2010) Digital Object Identifier (DOI) System. *Encyclopedia of Library and Information Sciences*, 1586–1592, 3rd ed. Taylor and Francis.

Wanchoo N, James N, Ramapriyan H.K. (2017) NASA EOSDIS Data identifiers: approach and system. *Data Science Journal*, 16:5, 1–11, doi: 10.5334/dsj-2017-015.

Imaging, Modelfitting, and Source Structure Corrections for the K-band (24 GHz) Celestial Reference Frame

A. de Witt, C. Jacobs, D. Gordon, M. Bietenholz, H. Krásná, M. Johnson, L. Hunt, N. Mwiya, M. Nickola

Abstract The K-band (24-GHz) celestial reference frame (K-CRF) program, supported through the United States Naval Observatory's (USNO) 50% timeshare allocation of the Very Long Baseline Array (VLBA), has so far provided high-resolution VLBA images for more than 800 Active Galactic Nuclei (AGN) at up to 81 epochs, as part of extending the International Celestial Reference Frame (ICRF) to K-band. A comprehensive analysis of these images has yielded metrics that serve as indicators for the suitability of each source as a calibrator or reference point. Additionally, our modelling efforts provide crucial insights into the overall dimensions and orientation of the source structure. Although AGN such as the Celestial Reference Frame (CRF) sources typically appear more compact at K-band than at X-band (8.4 GHz), they can, on occasion, still display noticeable extended emissions at K-band. We therefore initiated a project aimed at modelling structure effects in the astrometric analysis process. This involves utilizing readily available K-CRF VLBI images and up-to-date source structure models. This paper offers an overview of our image analysis efforts and outlines our plans to investigate the impact of source structure using all available K-CRF sources.

Keywords VLBI imaging, astrometry, celestial reference frame, AGN, K-band, 24 GHz

Aletha de Witt · Michael Bietenholz · Marisa Nickola
South African Radio Astronomy Observatory (SARAO), P.O. Box 443, Krugersdorp 1740, South Africa

Chistopher Jacobs
Jet Propulsion Laboratory (JPL), California Institute of Technology (CIT), 4800 Oak Grove Drive, Pasadena, CA 91109, USA

David Gordon · Megan Johnson
U.S. Naval Observatory (USNO), 3450 Massachusetts Ave NW, Washington, DC 20392, USA

Hana Krásná
Technische Universität Wien, Wiedner Hauptstraße 8-10/E120.4, Vienna, 1040, Austria

Lucas Hunt
National Radio Astronomy Observatory (NRAO), 800 Bradbury SE, Suite 235, Albuquerque, NM 87106, USA

Namakau Mwiya
University of Lusaka, P.O. Box 36711, Lusaka, Zambia

1 Imaging Status

The K-band celestial reference frame (K-CRF) program[1] has recently published high-resolution Very Long Baseline Interferometer (VLBI) images of 732 Active Galactic Nuclei (AGN) spanning up to 28 epochs per source, totalling an impressive 5078 images (de Witt et al., 2023b). All these images have been derived exclusively from monthly/bi-monthly 24-hour Very Long Baseline Array (VLBA, Napier, 1995) sessions observed from July 2015 to July 2018. The sessions were all observed in right circular polarization (RCP) using a data rate of 2 Gbps. Approximately 250 sources were observed in each session.

Building on this achievement, we have further expanded our imaging efforts by completing imaging for an additional 5 VLBA sessions observed from September 2018 to November 2018. As a result, we have now successfully captured images of 817 sources at up to 33 epochs, resulting in a total of 6095 images (available from our K-band imaging database[2]).

[1] K-band AstroGeo VLBI Project webpage
[2] K-band Imaging Database

The imaging for observations between December 2018 and January 2023 is completed and will be accessible in our database in December 2023, once modelfitting is finalized. This will increase the number of sources to more than 820 and will add 48 additional epochs (11 epochs at 2 Gbps RCP and 37 epochs at 4 Gbps dual-polarization), totalling 81 epochs. The imaging process for all VLBA sessions up to August 2023 is in its final stages and will result in a database of over 16,000 images.

2 Imaging, Analysis and Results

For imaging purposes, the correlated visibility data from our K-CRF VLBA observations are calibrated using the NRAO's Astronomical Imaging Processing System (AIPS, Greisen, 2003) via a semi-automated approach. The data calibration largely follows the VLBA calibration pipeline, utilizing standard AIPS utilities. An automated pipeline is employed for self-calibration, imaging, and deconvolution with the Caltech Difference Mapping software (DIFMAP, Shepherd, 1997). Custom Python routines generate images, u, v-coverage plots, and scan-averaged calibrated visibility amplitude plots. For example, such plots for the source NRAO140 (J0336+3218) from our K-CRF VLBA observations on 27 Oct 2018, are shown in Figure 1.

From each final K-band image, we extract various image parameters, including the peak brightness, total CLEAN flux density and the weighted average correlated flux density for four baseline length ranges (as shown in Figure 2), the background rms brightness level over the entire residual image and the image signal-to-noise-ratio (SNR), the quality of the fit between the observed and model visibilities after self-calibration, the maximum absolute brightness value in the residual map, the clean beam minor and major axes FWHM and position angle, an estimate of the residual rms phase calibration error, and a file with the flux density and position of each of the image CLEAN components. A comprehensive description of these image parameters can be found in de Witt et al. (2023b).

It is well-established that source structure and its variability can introduce significant errors in astrometric VLBI delay measurements and destabilize source positions (e.g., Charlot, 1990). While sources at K-band generally appear more compact than they do at S- and X-band as demonstrated by recent near-simultaneous S- (2.3 GHz), X- (8.4 GHz), K- (24 GHz), and Q-band (43 GHz) VLBA images (de Witt et al., 2022), they can still exhibit measurable extended emission (see Figure 3). We have therefore embarked on a project to apply source structure corrections directly to our K-band data during the astrometric analysis process, using updated source models obtained from our dedicated K-CRF observing campaigns on the VLBA (e.g., de Witt et al., 2023b).

3 Modelfitting

Source characteristics are estimated by fitting models directly to the visibility data through least squares. We use the MODELFIT task within DIFMAP to fit a model consisting of two circular Gaussian components to the calibrated visibilities. This process allows us to determine the flux density and FWHM angular size of the brightest and second brightest components, as well as the vector offset between the two components. To efficiently handle the substantial volume of data, we have developed an automated pipeline dedicated to modelfitting.

In addition to the modelfitting in DIFMAP, we also fit a line through the locations of image CLEAN components using a custom Python routine. This approach provides an effective means of gauging the source's angle of elongation and validating the robustness of the modelfitting in DIFMAP. Both unweighted and flux-density-weighted fits are performed. The outcomes of our modelfitting for the source NRAO140 (J0336+3218) from VLBA observations on 27 Oct 2018 are shown in Figure 4. More detailed information about the modelfitting process is available in de Witt et al. (2023b).

4 Structure Quantities and Source Variability

For a source to be considered a suitable VLBI calibrator or reference source, it should ideally be bright and compact at the frequency of observation and exhibit minimal variation over time. To assess source suitabil-

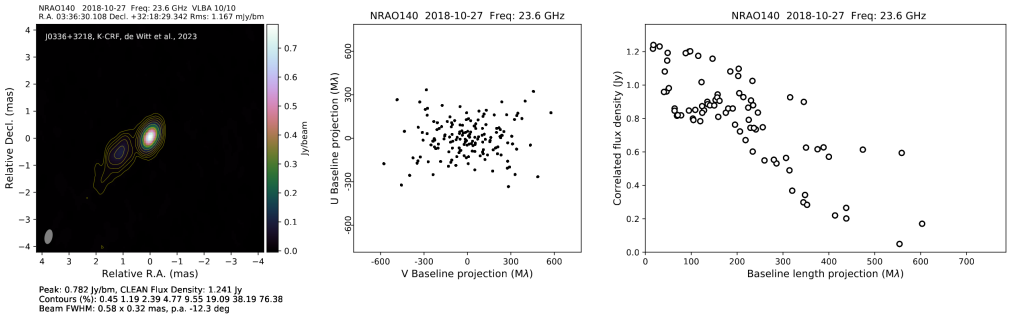

Fig. 1 Example plots for NRAO140 (J0336+3218). Left: image with both contours and colour scale showing brightness. The contour levels are listed below the image, and start at $3\times$ the background rms brightness level and increase by factors of 2 thereafter. Center: the u, v-coverage plot. Right: the scan-averaged visibility amplitudes plotted against the baseline length.

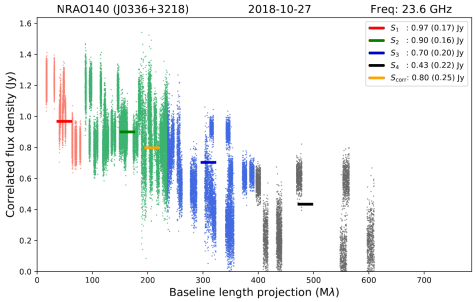

Fig. 2 The correlated visibility amplitude versus baseline length plot for the source NRAO140 (J0336+3218) from 27 Oct 2018. The colours indicate the correlated visibility amplitude and corresponding weighted average over baseline lengths < 1000 km (shown in red), between 1000 and < 3000 km (shown in green), between 3000 and < 5000 km (shown in blue), and 5000 km or more (shown in black). Also shown is the weighted average over all baselines (in orange). For each, the weighted average value is presented alongside the corresponding standard deviation in parentheses.

ity, we utilize the parameters and CLEAN component models derived from our VLBA images. These assessments include the analysis of flux density variability, source structure quantities and their variability, and image quality.

Source structure quantities comprise (1) a measure of source compactness or core domination, (2) radial extent, indicating the extent of source structure and overall angular size, and (3) a structure index (SI) quantifying the astrometric quality of a source, defined as $SI = 1 + 2 \times \log_{10}(\tau_{\rm median})$, where $\tau_{\rm median}$ represents the median value of the structure delay corrections, i.e. the additional phase terms due to source structure computed for each CLEAN component and each VLBI baseline for a particular image, in units of picoseconds (ps). An SI value between 0 and 2 indicates compact structure or faint extended emission, while values closer to 3 imply more substantial structural features and values of 4 or more signify pronounced extended emission or intricate structural elements. More detailed information about the structure metrics is available from de Witt et al. (2023b).

Time-series plots of fluctuations in peak brightness, core flux density, CLEAN flux density, and weighted average correlated flux densities for the source NRAO140 (J0336+3218), across 73 distinct epochs of VLBA observations conducted between July 2015 and January 2023, are shown in Figure 5. Time-series plots of the structure metrics, including source compactness, flux-density-weighted radial extent, and SI, for the source NRAO140 (J0336+3218), are shown in Figure 6. These plots reveal trends for this source such as increasing flux density over time, accompanied by a transition toward slightly more core domination. The images themselves show a fading of weak extended emission as the flux density increases.

5 Conclusions and outlook

We are actively working on numerous initiatives to enhance, maintain, and refine the K-CRF. Our roadmap includes completing the imaging of all VLBA astrometric K-band sessions from 2019 onwards and characterizing source structures and their temporal variations. Our primary goal is to maintain a dynamic database of high-resolution, multi-epoch K-band images, allowing us to evaluate source strength and morphology contin-

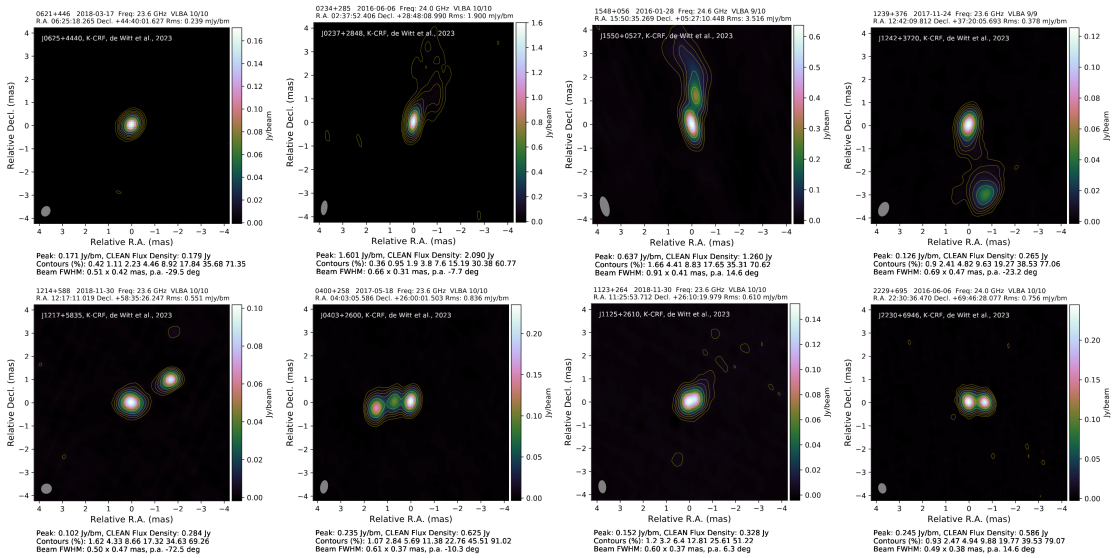

Fig. 3 Images for a selection of K-CRF sources. Both the colour scale and contours show brightness. For each image the colour scale is given at right, and the contour levels listed below. Our images show that the majority of K-CRF sources have a compact structure with no or weak extended emission, similar to that of the first two sources in the top panel. However, some sources do show significant structural features, such as bright extended emission, bright secondary components, or a more complex structure, such as those shown in the remaining six images.

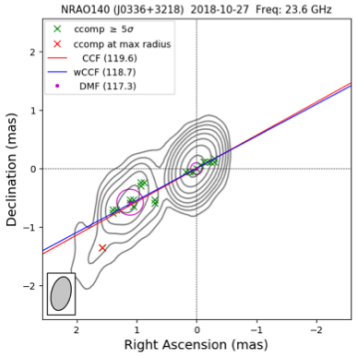

Fig. 4 Contour image of the source NRAO140 (J0336+3218) from 27 Oct 2018. The contours are in grey. The locations of the CLEAN components, ccomp, are shown with green crosses except for the component farthest from the phase centre which is indicated with a red cross. The diagonal red and blue lines are those fitted through the ccomp locations, measuring the overall orientation of the source, with CCF, in blue, being the unweighted fit and wCCF the flux-density weighted one. The position angles of these lines in degrees N through E are given in the legend. Finally, the positions and sizes of the DIFMAP modelfit components (DMF) are shown using magenta circles, also with the position angle in parentheses in the legend.

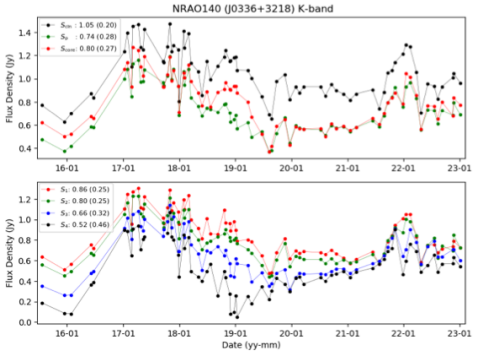

Fig. 5 Time-series plots of the source NRAO140 (J0336+3218) across 73 distinct epochs of VLBA observations between July 2015 and January 2023. The top panel shows the peak brightness, $S_{\rm p}$, core flux density, $S_{\rm core}$, and CLEAN flux density, $S_{\rm cln}$. The bottom panel shows the weighted average correlated flux density for each of the baseline length ranges shown in Figure 2. The corresponding mean value for each quantity, followed by the corresponding variability index in parentheses, are given in the Figure legends at top left in each panel

uously. Our objective is to study the impact of source structure on the K-CRF by modelling the structure effects in our astrometric and geodetic analyses. The outline of our plan is to:

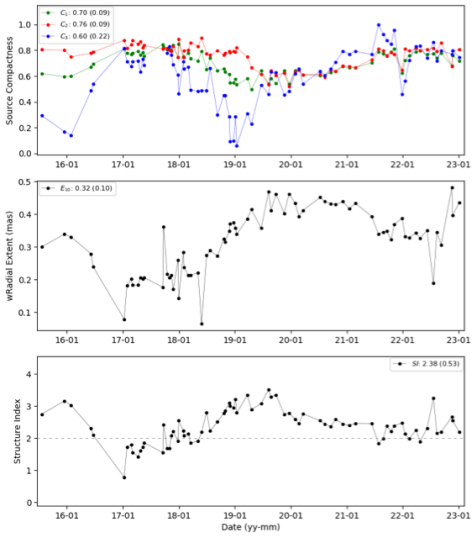

Fig. 6 Time-series plots of the source NRAO140 (J0336+3218) across 73 distinct epochs of VLBA observations between July 2015 and January 2023. These plots show the evolution of source structure metrics over time. The top plot shows the source compactness measures, where $C_1 = S_{\rm p}/S_{\rm cln}$, $C_2 = S_{\rm core}/S_{\rm cln}$, and $C_3 = S_4/S_1$. The middle plot shows the flux-density weighted radial extent, E_{10}, in units of mas. The bottom plot shows the structure index, SI. In each plot, the mean values for each line, followed by the corresponding standard deviations in parentheses, are given in the plot legends.

1. Quantify the structure and variability of all K-CRF sources.
2. Assess the impact of source structure on the K-CRF.
3. Implement a model to correct for source structure in the astrometric and geodetic analysis software VieVS (Böhm et al., 2018).

The ultimate aim is to produce a CRF with structure corrections applied to all sessions, which would be a significant achievement in the field of absolute astrometry!

Acknowledgements

 This research was carried out in part at the Jet Propulsion Laboratory, California Institute of Technology, under a contract with the National Aeronautics and Space Administration (80NM0018D0004). The VLBA is managed by NRAO, funded by the National Science Foundation, and operated under cooperative agreement by Associated Universities. The authors gratefully acknowledge use of the VLBA under the USNO's time allocation. This work supports USNO's ongoing research into the celestial reference frame and geodesy. This work was supported by the South African Radio Astronomy Observatory (SARAO,) a facility of the National Research Foundation (NRF) of South Africa.

References

Böhm J., et al. (2018) Vienna VLBI and Satellite Software (VieVS) for Geodesy and Astrometry. *PASP*, 130, 986, 044503.

Charlot P. (1990) Radio-Source Structure in Astrometric and Geodetic Very Long Baseline Interferometry. *Astron. J*, 99, 1309–1326.

Charlot P., et al. (2020) The third realization of the International Celestial Reference Frame. *A&A*, 644, A159.

de Witt A., et al. (2022) Multi-Frequency Imaging Results of 453 Extragalactic ICRF-3 Radio Sources. *15th EVN Symposium & Users Meeting*, 11-15 July 2022, Cork, Ireland.

de Witt A. (2023) The Growing Potential for K-band (24 GHz) Geodesy. *GGOS Days 2023*, 20-23 September 2023, Yebes, Spain.

de Witt A., et al. (2023b) The Celestial Reference Frame at K Band: Imaging. I. *AJ*, 165, 4, 139.

Greisen S. W. (2003) AIPS, the VLA, and the VLBA. *Information Handling in Astronomy - Historical Vistas*, 285, 109–125.

Napier P. J. (1995) VLBA Design. *Astronomical Society of the Pacific Conference Series*, 82, 59.

Shepherd M. C. (1997) Difmap: an Interactive Program for Synthesis Imaging. *Astronomical Data Analysis Software and Systems VI*, 125, 77.

Radiometry performance of the VGOS receivers of the Onsala twin telescopes

G. Elgered, P. Forkman, R. Haas, E. Varenius

Abstract We have assessed to stability of the present VGOS receivers in the Onsala twin telescopes (OTT) in order evaluate the possibility to use them to estimate the wet propagation delay of the atmosphere. As expected the highest possible frequencies that can be used in the present OTT receivers, 15.3 to 15.6 GHz, are too far from the centre of the water vapour emission line at 22.2 GHz in order to be meaningful for critical assessments of the wet delays estimated from the VLBI data themselves. However, we do find clear correlations between the wet delays estimated from the VGOS receivers with those provided by a traditional stand-alone microwave radiometer.

Keywords microwave radiometry, VGOS, wet delay

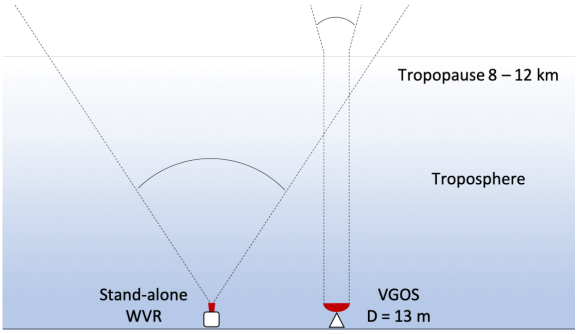

Fig. 1 The geometry of the sensed atmosphere. The typical dimension of the feed of the stand-alone WVR implies that almost all water vapour will be present in the far field of the antenna pattern (Balanis, 2005). On the other hand, for the VLBI telescope and elevation angles above 15° most of the water vapour is in the near field (from Forkman et al., 2021).

1 Introduction

An important difference when using a stand-alone water vapour radiometer (WVR) for calibration, or assessment, of the wet propagation delays estimated from geodesy VLBI data is the different air masses sampled by the telescope and the WVR (see Fig. 1). Petrachenko et al. (2009) suggested to use VGOS receivers also as a radiometers to observe the sky emission simultaneously with the VLBI source, provided that the observed frequency was close enough to the water vapour emission line at 22.2 GHz.

A simulation was performed by Forkman et al. (2021) in order to study the accuracy of the estimated wet delay. The simplest approach is to use one frequency only, to be used when no liquid water is present in the atmosphere. Fig. 2 summarise these results, presented as the expected standard deviation (SD) for three different levels of white noise of the observed sky temperature.

When clouds containing liquid water are present, there is a need to observe the sky emission at two different frequencies, with different emission properties due to water vapour and liquid water. That means two observations and two unknowns, the wet delay and the liquid water content in the direction of the observation. The concept that has been used since several decades is to have one frequency close to the water vapour emission line and one frequency around 31 GHz (Wu, 1979). In the work by Forkman et al. (2021) the range of frequencies were, however, restricted to the 14–24 GHz interval, assuming that a similar range

Gunnar Elgered, Peter Forkman, Rüdiger Haas, Eskil Varenius
Chalmers University of Technology, Onsala Space Observatory, SE-439 92 Onsala, Sweden

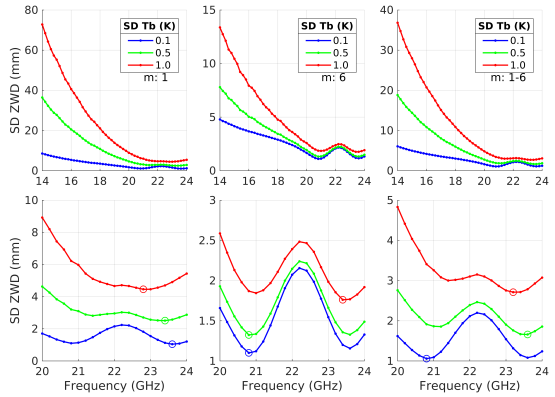

Fig. 2 The expected accuracy in the equivalent zenith wet delay (ZWD). Left: 1 airmass, middle: 6 airmasses, and right: 1–6 airmasses. The lower plots zoom in on the frequency range giving the lowest standard deviation (SD). The circles mark the lowest SD at the optimal frequency (from Forkman et al., 2021).

could be used in a future generation of VGOS receivers. The corresponding simulated results are presented in Fig. 3.

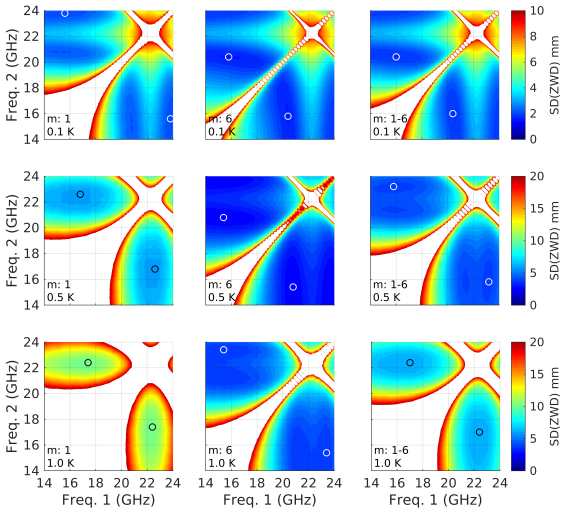

Fig. 3 The expected ZWD rms error (SD) for a two-frequency algorithm (one frequency at each axis in the graphs) for 1 (left), 6 (middle) and 1–6 (right) airmasses. The receiver noise is simulated as 0.1 K (top), 0.5 K (middle), and 1.0 K (bottom) for each row. The white areas correspond to rms errors larger than the upper limit of the scale and the circles mark the lowest rms error obtained for the optimal frequency pair (from Forkman et al., 2021).

2 Observations

The Onsala twin telescopes are equipped with different receivers. The northeast telescope (OE) has a QRFH feed and the southwest telescope (OW) has an Eleven feed (see Fig. 4). Fig. 5 depicts the receiver noise temperatures measured using the Y-factor method. For more details on the OTT receivers see Pantaleev et al. (2017).

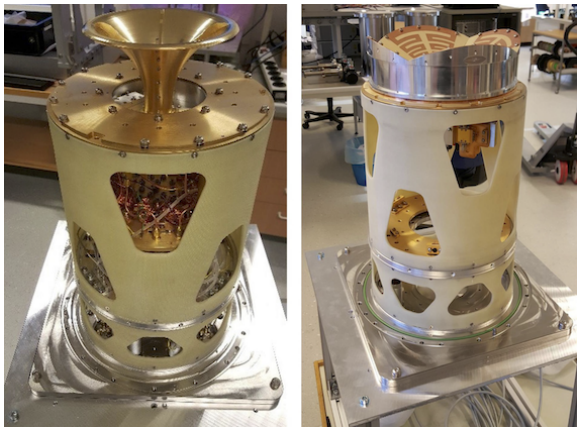

Fig. 4 Receivers in the Onsala twin telescopes. The receiver with the QRFH feed is in the OE telescope (left) and the receiver with the Eleven feed is in the OW telescope (right) (from Pantaleev et al., 2017).

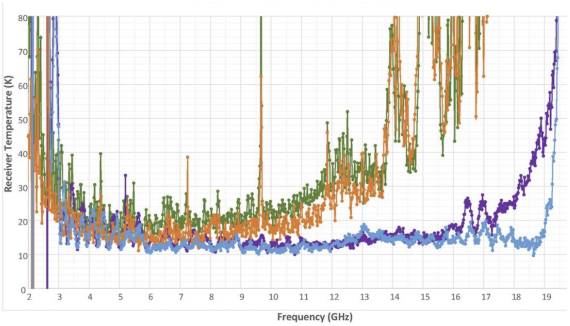

Fig. 5 Lab measurements of the receiver temperatures for the two different polarizations (vertical and horizontal), OE: blue/purple and OW: orange/green (from Pantaleev et al., 2017).

2.1 OTT radiometric data sets

Because our approach was to use radiometry data from the VGOS receivers in one frequency band only, the observations had to be acquired during periods with no liquid water in the atmosphere. This together with the fact that OTT also were scheduled to carry out regular geodesy VLBI observations during the winter-spring period of 2023, resulted in two measurement campaigns:

- OW was used from 28 February to 2 March 2023. Elevation angles: 8°, 20°, and 90°.
- OE was used from 8 to 12 May 2023. Elevation angles: 10°, 20°, and 90°.

During both periods the azimuth angle of the OTT was 220°, where the horizon is defined by the sea surface, in order to minimise the ground noise pickup.

2.2 OTT measurement sequence

The system temperature was measured every 1 s for 1 min at the three different elevation angles. Measurements were carried out in 8 frequency bands, 32 MHz wide, from 15,344 to 15,600 GHz, and for both horizontal and vertical polarizations. The mean value was calculated for each channel for every 1 min period. Because of intermittent interference the value was ignored if the SD was > 1 K (1.5 K at the lowest elevation angle to allow for more atmospheric variability). Thereafter, the mean value of all 16 channels was calculated, and for every 3 min period a tip curve analysis and the method of least squares was used to estimate the equivalent zenith sky brightness temperature due to the atmosphere, including the cosmic background radiation of 2.7 K, and the receiver temperature, assuming a horizontally homogeneous atmosphere.

2.3 Stand-alone WVR Konrad

In order to assess the quality of the estimated sky brightness temperatures and the ZWD from the VGOS receivers, we used the 20.64 GHz channel of the Konrad WVR. The second channel, usually utilized for correction of liquid water in the atmosphere, was not used, because both data sets were acquired during conditions without liquid water clouds. Konrad was scanning the sky in 17 different directions (varying both the azimuth and the elevation angles) in a repeating duty cycle of approximately 2 min. For more details on the Konrad WVR observations and the corresponding data reduction, see Ning & Elgered (2021) and Elgered & Ning (2023).

3 Results

The system temperatures, at the three elevation angles, are shown in Fig. 6. The larger scatter in February–March with OW is expected, given the higher system temperatures of that receiver (see Fig. 5).

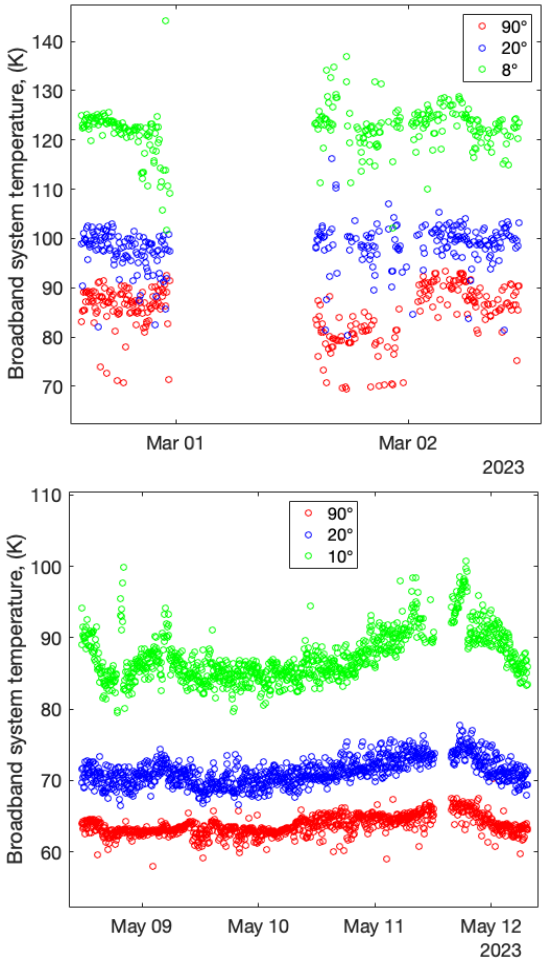

Fig. 6 Average system temperature over 1 min and over the 16 frequency bands (both polarizations) from February–March (OW top) and May (OE bottom).

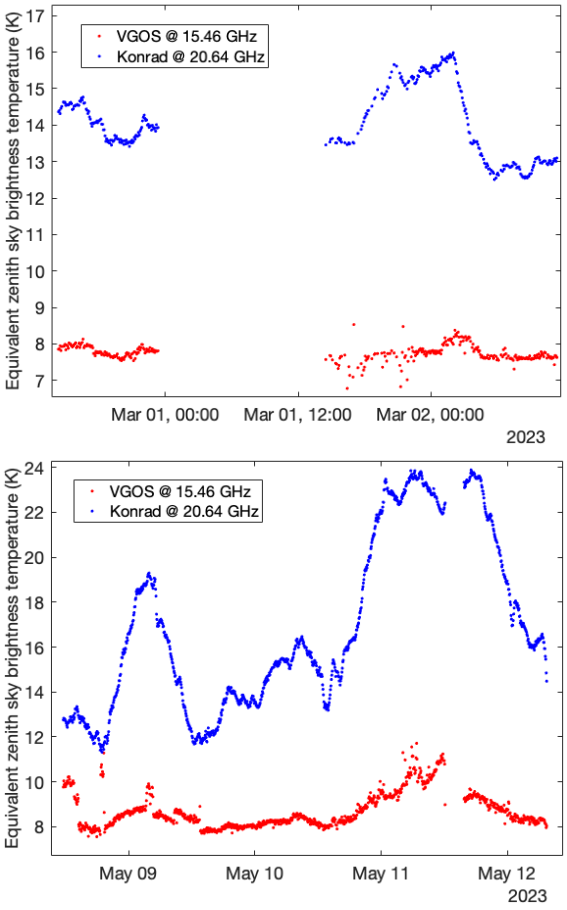

Fig. 7 Equivalent zenith sky brightness temperatures, (February-–March (OW top) and May (OE bottom).

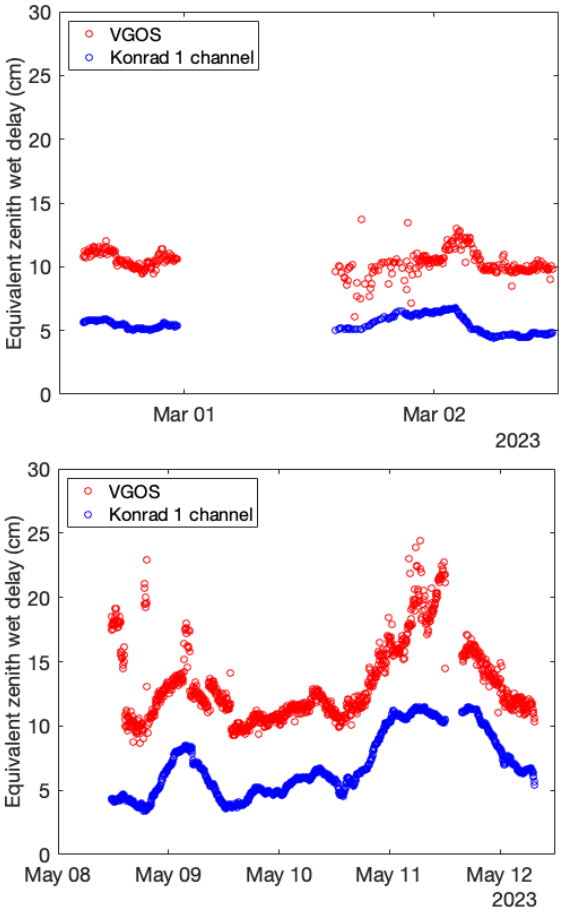

Fig. 8 Equivalent zenith wet delays, February–March (OW top) and May (OE bottom).

The equivalent zenith sky brightness temperatures are shown in Fig. 7 together with the zenith brightness temperatures from the Konrad WVR. These graphs clearly illustrate the lower sensitivity for water vapour at a frequency of 15.46 GHz and, therefore, there is a demand for a very high accuracy of the estimated sky brightness temperatures from VGOS. For the Konrad WVR channel at 20.64 GHz, an error of 1 K in the zenith sky brightness temperature corresponds to an error in the ZWD of 0.6 cm, whereas a 1 K error at the VGOS centre frequency of 15.46 GHz corresponds to a ZWD error of 5.4 cm.

The equivalent ZWD from Konrad, the stand-alone WVR, and estimates from the VGOS receivers are presented in Fig. 8. They were obtained as described by Forkman et al. (2021). Table 1 summarizes the ZWD comparison. Statistics are shown for the two complete sessions and for one selected period from each session when the VGOS receivers were more stable. We immediately notice a very large bias, of the order of 5 cm for both experiments. We speculate that there are two obvious causes.

The first being an increased ground noise pick up by VGOS with a decreasing elevation angle. No model for the ground-noise pickup was applied in our analysis. Due to the high demand on accuracy, 0.1 K or better, such a model will be difficult to produce given that the emission from the ground is not constant as a function of time and azimuth angle.

The second possible cause is an error in the absolute value of the equivalent noise temperature inserted by the noise diode. Because the 15 GHz frequencies are normally not used in VGOS experiments we carried out a quick calibration of the noise diode us-

Table 1 ZWD comparison VGOS radiometry – Konrad WVR

Time period	Bias (cm)	SD (cm)	Correlation coefficient
28 Feb–2 Mar (OW)	4.9	0.9	0.42
28 Feb (OW)	5.2	0.4	0.84
8–12 May (OE)	6.3	2.1	0.73
10–12 May (OE)	5.9	1.6	0.87

ing CasA as the calibration source. Assuming an uncertainty of 10 % in the noise-diode output we find that this introduces an error in the equivalent zenith sky brightness temperature of 0.5 K. This corresponds to a ZWD error of 2.7 cm.

Together these error sources could explain a bias of 5 cm in the ZWD. The effect due to ground-noise pickup could be reduced significantly if the tip-curve method based on the least square fit was not carried out. Instead one could use the individual observations of the brightness temperatures without any averaging. For these frequencies that would, however, pose unrealistic demands on the accuracy of the receiver temperature and the equivalent temperature inserted by the noise diode.

When the biases are removed we observe standard deviations (SD) of the differences of the order of 0.4 cm for a selected period in February when the atmosphere was stable, and 1.6 cm for a more variable period in May. This is roughly in agreement with the simulations in Fig. 2. It is clear that the accuracy of wet delay estimates from geodetic analysis of VLBI observations is usually much higher. Formal errors of less than 2 mm have been reported, e.g. by Elgered et al. (2019), from the analysis of legacy S/X experiments.

4 Conclusions and outlook

We conclude that even a frequency as low as 15 GHz can provide radiometric information about the wet delay, but it requires a careful screening of the data for receiver instabilities and interferences.

Nevertheless, observations at 15 GHz are too far away from the water vapour emission line in order to be useful for an assessment of the ZWD estimates from standard VGOS geodetic processing. The quality (uncertainty) of the estimated ZWD from a geodetic analysis pf S/X legacy VLBI data is less than 2 mm (formal error) (Elgered et al., 2019). The ZWD uncertainty from a geodetic analysis of VGOS data will be even lower, given the increased number of observations compared to legacy S/X. This uncertainty is significantly lower than our observed standard deviations obtained when comparing the ZWD from VGOS radiometry to those from the stand-alone WVR Konrad.

Future VGOS radiometry at frequencies closer to the water vapour emission line at 22.2 GHz will still require improvements in the stability and the calibration of the noise diode and hence the receiver noise temperature. Furthermore, the ground-noise pickup shall be investigated in detail, possibly resulting in a model for the corrections needed.

References

Balanis C A (2005). *Antenna Theory: Analysis and Design (3rd ed.)*, Chap. 2, John Wiley & Sons, New York, p. 34.

Elgered G, Ning T, Forkman P, & Haas R (2019) On the information content in linear horizontal delay gradients estimated from space geodesy observations *Atmos. Meas. Tech.*, 12, 3805–3823, https://doi.org/10.5194/amt-12-3805-2019.

Elgered G & Ning T (2023) On the use of water vapour radiometry for assessment of wet delay estimates from space geodetic techniques, *these proceedings*.

Forkman P, Flygare J, & Elgered G (2021). Water vapour radiometry in geodetic very long baseline interferometry telescopes: assessed through simulations, *J. Geodesy*, 95:117, https://doi.org/10.1007/s00190-021-01571z

Ning T, & Elgered G (2021) High-temporal-resolution wet delay gradients estimated from multi-GNSS and microwave radiometer observations *Atmos. Meas. Tech.*, 14, 5593–5605, https://doi.org/10.5194/amt-14-5593-2021.

Pantaleev M, Helldner L, Haas R, et al. (2017). Design, implementation and tests of the signal chain for the twin telescopes at Onsala Space Observatory, *Proc. of the 23rd European VLBI Group for Geodesy and Astrometry Working Meeting*, eds. R Haas and G Elgered, Gothenburg, 15–19.

Petrachenko B, Niell A, Behrend D, et al. (2009). Design aspects of the VLBI2010 system. In: *Progress report of the IVS VLBI2010 committee*, NASA/TM-2009-214180.

Wu S C (1979). Optimum frequencies of a passive microwave radiometer for tropospheric path-length correction, *IEEE Trans. Ant. Propagat., AP-27, 233–239, https://doi.org/10.1109/TAP.1979.1142066.*

On the use of water vapour radiometry for assessment of wet delay estimates from space geodetic techniques

G. Elgered, T. Ning

Abstract We have studied the impact of liquid water drops in the atmosphere on the retrieval accuracy of the wet propagation delay using microwave radiometry through a comparison with the corresponding results from ground-based GPS observations. Using all data available acquired at the Onsala Space Observatory during 2022 we find, as expected, the best agreement for the conditions with no, or a very small, liquid water content (LWC). For the LWC interval 0.0–0.1 mm the bias and the standard deviation of the equivalent zenith wet delay (ZWD) agreement between the WVR and the GPS estimates are 3.3 mm and 4.2 mm, respectively.

Keywords microwave radiometry, wet delay, GPS

Fig. 1 The GNSS station ONSA (left, at the end of the cable tray) and the Water Vapour Radiometer (WVR) Konrad (in the foreground). The twin telescopes, and the 25 m radio telescope, are seen in the background. A new WVR (to the right), manufactured by RPG, was installed in May 2023, but has not been used in this study.

1 Introduction

During the development of the Mark III VLBI system in the seventies, water vapour radiometers (WVR) were envisaged to provide independent observations of the signal propagation delay due to water vapour along the line of sight. The standard design of the WVR is to measure the atmospheric emission at two frequencies, close to and further away from the centre of the water vapour emission line at 22.2 GHz (Wu, 1979). These measurements are used to estimate two unknowns, the amount of water vapour, or the wet delay, and the liquid water content (LWC) along the line of sight.

We have assessed the retrieval accuracy of the equivalent zenith wet delay (ZWD) from WVR data and its dependence on the estimated LWC by comparing them to those estimated from data acquired by the GNSS station ONSA. Fig. 1 depicts the ONSA station and the WVR Konrad.

The main drawback of using a WVR is that the retrieval algorithm requires that any liquid water drops in the sensed volume of air are much smaller than the wavelength observed by the WVR, i.e., ≈ 1 cm (Westwater & Guiraud, 1980). Therefore, the algorithm more or less breaks down during rain, meaning that the WVR cannot be relied on for 100 % of time, unless it never rains on, or close to, the site. The method generally used is to avoid using WVR data with poor accuracy by ignoring observations obtained during rain and when the inferred equivalent zenith LWC is above a specific

Gunnar Elgered
Chalmers University of Technology, Onsala Space Observatory, SE-439 92 Onsala, Sweden

Tong Ning
Lantmäteriet (Swedish Mapping, Cadastral and Land Registration Authority), SE-801 82 Gävle, Sweden

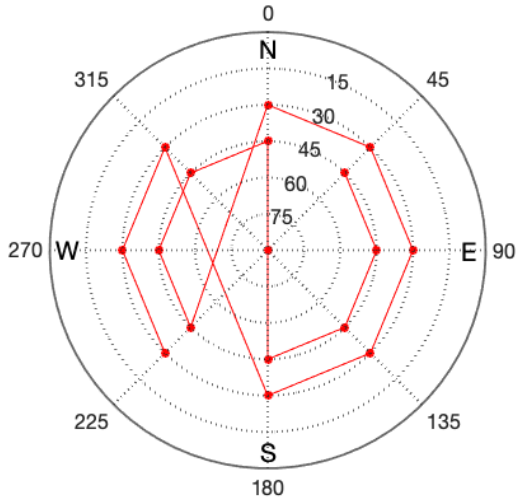

Fig. 2 The observational cycle of the Konrad WVR.

threshold. This method is, however, subject to some uncertainties: (i) There may be rain drops in the sensed volume of air in spite of the fact that no drops are detected at the ground on the site; (ii) there may still be drops of water on the WVR instrument many minutes after the rain has stopped, such as on the protective covers of the horn antennas and on the mirrors; and (iii) a low density of large drops may result in a smaller liquid water content than many small drops.

2 Data

The WVR observes the thermal emission from the sky in two different frequency channels: 20.64 GHz and 31.60 GHz. Each channel has a double sideband mixer and a total RF bandwidth of 320 MHz.

The WVR was operated continuously from mid-January to the end of 2022. The data were acquired using the same procedure mapping the sky. The observations were distributed on the sky covering the full range of azimuth angles at elevation angles above 30°. The different observational directions are illustrated in Fig. 2. These 17 samples took approximately 2 min and this cycle was repeated continuously.

Periods with rain and all individual observations resulting in an equivalent zenith LWC larger than 0.7 mm were deleted. Thereafter, for each 5 min period, having more than 30 observations, the equivalent zenith wet delay (ZWD), its time derivative, and the linear horizontal gradients in the east and in the north directions were estimated using the four parameter model described by Davis et al. (1993). This resulted in 78,814 data points, corresponding to a time coverage of 75 % of the year. After synchronising with the available GPS data, there were 77,972 data points.

The GNSS data were processed with the GipsyX software, using satellites in the GPS constellation and an elevation cutoff angle of 10°. The ZWD and the east and the north horizontal gradients were estimated every 5 min, with constraints equal to 10 mm/$\sqrt{\mathrm{h}}$ and 0.3 mm/$\sqrt{\mathrm{h}}$, respectively.

For more details about the WVR specifications and the GPS data processing, see Elgered et al. (2023).

3 Results

The ZWD estimates for the ONSA GPS data are shown together with the ZWD differences between the WVR and the GPS in Fig. 3. The ZWD differences shown in Fig. 3 are also shown in Fig. 4 but here vs. the LWC. The seasonal dependence and the large variability in the ZWD is clear and well known. It can also be noted that because first all individual observations with an LWC larger than 0.7 mm are ignored and, thereafter, an average is calculated for each 5 min period, the number of data points in Fig. 4 with an LWC larger than say 0.5 mm becomes relatively small. This would of course change if the temporal resolution is higher, but in this study we are limited by the 5 min temporal resolution for the GPS estimates.

For a large LWC we note a positive bias (WVR−GPS) for the ZWD. In Fig. 4 we also include a small negative LWC (LWC $>$ −0.05 mm) in order to allow for some noise in the sky brightness temperatures. However, observations implying a negative LWC will also introduce a positive bias in the ZWD because it indicates that we have either a positive error in 20.64 GHz channel, or a negative error in the 31.60 GHz channel, or a combination of these.

In June, July, and August there are a few occasions with large negative differences (see Fig. 3). Most of these are associated with a large and rapid change in the ZWD and a time delay between the WVR and the GPS. We assume that the WVR ZWD are more correct because of the constraint used in the estimation pro-

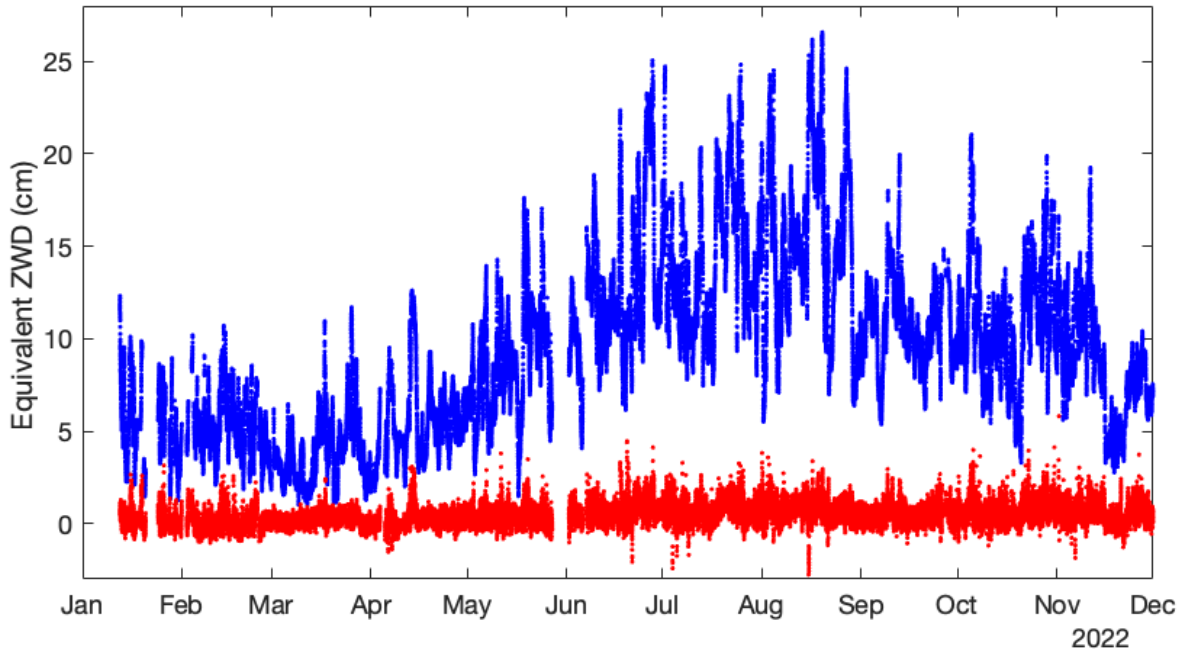

Fig. 3 ZWD using GPS data from ONSA (blue dots) and the ZWD difference WVR–GPS (red dots). The data are synchronized and most data gaps are periods of rain and LWC vaues larger than 0.7 mm. One exception is in the beginning of May when WVR data were lost due to a local network failure.

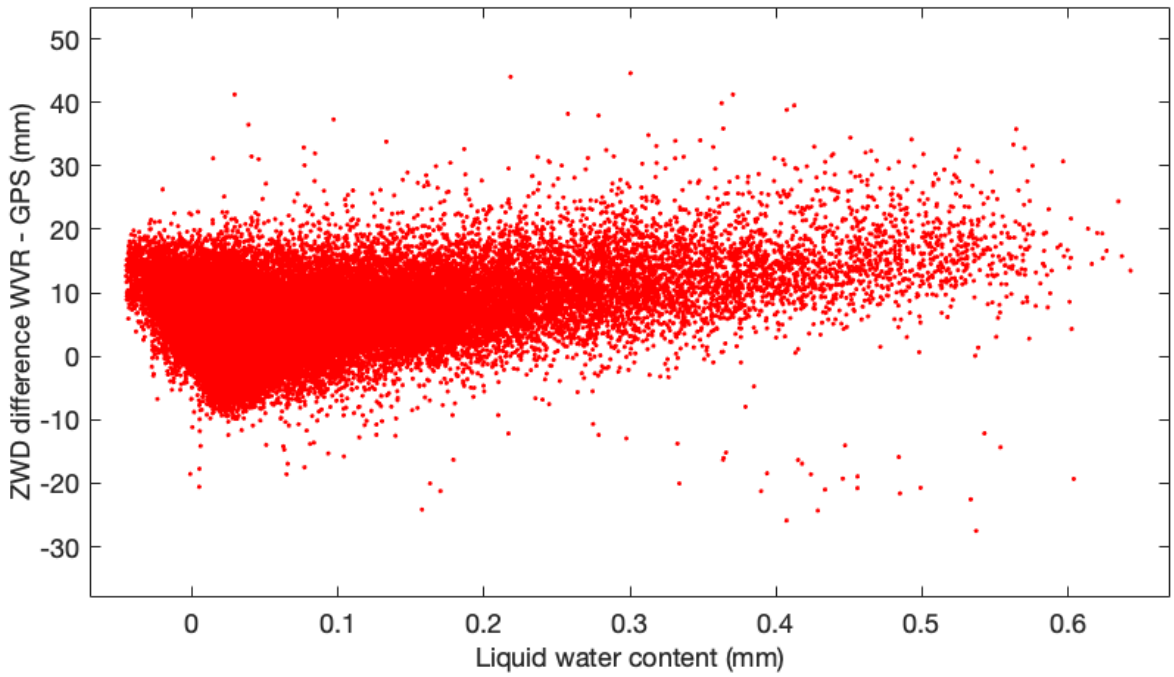

Fig. 4 Equivalent ZWD differences: WVR–GPS. The small amount of data for high LWC is is a bit misleading. The reason is that the graph contains 5 min averages that were calculated after that all individual LWC values larger than 0.7 mm in the equivalent zenith direction were removed.

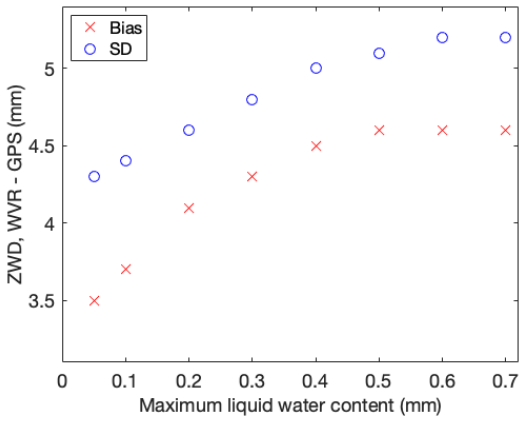

Fig. 5 The bias and the SD for the WVR–GPS differences of the ZWD vs the maximum LWC for the data used, inferred from the WVR observations. The number of data points is reduced from 77,966 for LWC < 0.7 mm to 56,176 for LWC < 0.05 mm.

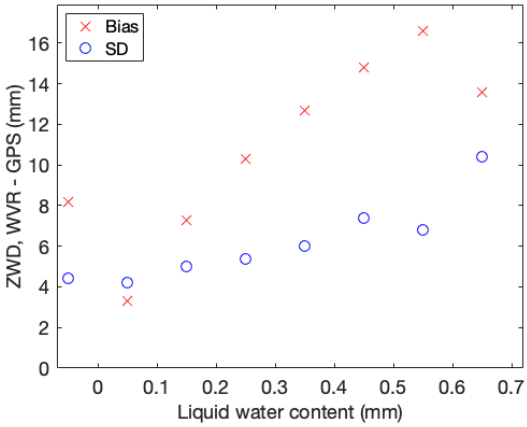

Fig. 7 The bias and the SD for the WVR–GPS differences of the ZWD for different intervals of the inferred LWC from WVR observations. Note the different scale compared to Fig. 5. The values are also presented in Table 1.

cess of the GPS data, whereas adjacent values in the WVR time series are independent. On 15 August the large differences are caused by unexplained high sky temperatures observed by the 31.4 GHz channel.

We investigate how the bias and the standard deviation (SD) of the ZWD and the gradients depend on the allowed LWC. Two different approaches are used to illustrate the dependence. Figs. 5 and 6 illustrate how the WVR ZWD and the gradients are improved compared to the GPS results when the maximum LWC is reduced. The minimum LWC is at -0.05 mm in all cases. The second approach is motivated because the number of data points are very different in the different LWC intervals. In this case we calculate the bias and the SD for different LWC intervals. These results are illustrated for the ZWD and the gradients in Fig. 7 and Fig. 8, respectively. The specific values are also presented in Table 1.

The improvement is larger for the ZWD compared to the gradients when the maximum LWC is reduced. The small improvement for the gradients is because the differences are dominated by the different sampling of the sky for the WVR and the GPS.

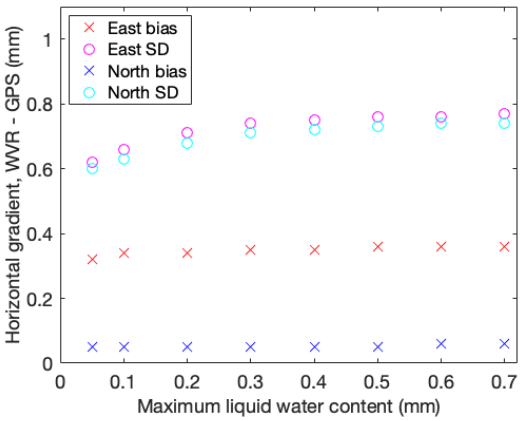

Fig. 6 The bias and the SD for the WVR–GPS differences of the linear horizontal gradients vs the maximum LWC for the data used, inferred from the WVR observations. The number of data points are the same as in Fig. 5

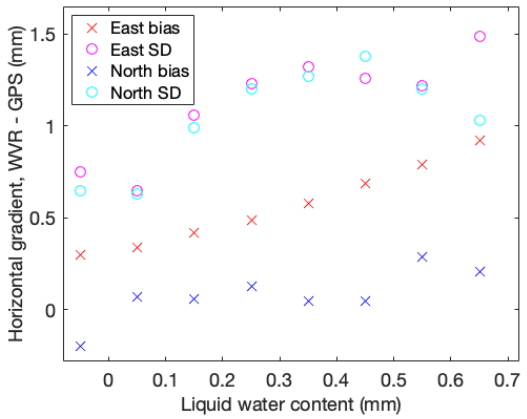

Fig. 8 The bias and the SD for the WVR–GPS differences of the linear horizontal gradients for different intervals of the inferred LWC from WVR observations. Note the different scale compared to Fig. 6. The values are also presented in Table 1.

Table 1 ZWD and horizontal gradient comparison between the Konrad WVR and GPS estimates

Interval of LWC	No. of data points	Relative amount of all data	ZWD		Horizontal gradient			
					East		North	
(mm)		(%)	Bias (mm)	SD (mm)	Bias (mm)	SD (mm)	Bias (mm)	SD (mm)
−0.05–0.0	4 979	6.39	8.2	4.4	0.30	0.75	−0.20	0.65
0.0–0.1	59 990	76.96	3.3	4.2	0.34	0.65	0.07	0.63
0.1–0.2	7 363	9.45	7.3	5.0	0.42	1.06	0.06	0.99
0.2–0.3	3 065	3.93	10.3	5.4	0.49	1.23	0.13	1.20
0.3–0.4	1 477	1.89	12.7	6.0	0.58	1.32	0.05	1.27
0.4–0.5	752	0.96	14.8	7.4	0.69	1.26	0.05	1.38
0.5–0.6	312	0.40	16.6	6.8	0.79	1.22	0.29	1.20
0.6–0.7	14	0.02	13.6	10.4	0.92	1.49	0.21	1.03

In the ZWD graphs (Figs. 5 and 7) it is clear that both the bias and the SD increase with increasing LWC. Note that the values for the two intervals with the highest LWC (Fig. 7) are more uncertain because of the low amount of data points. The increasing bias seen for the ZWD estimates confirm earlier results that the WVR tends to overestimate the ZWD when the LWC is increasing (Elgered et al., 1991).

For the gradients (Figs. 6 and 8) the SD also increase with an increasing LWC. This is expected since more liquid water clouds imply a less homogeneous atmosphere and the different sampling directions will have a greater impact. We do not expect that the bias in the gradients will increase with the LWC. However, we do see such a trend for the east gradient. We can speculate that because the WVR in general overestimates the wet delay for high LWC, and given that the location is at the coastline, oriented roughly in the south-north direction, more clouds with a higher LWC over land compared to over the sea could be the cause. More work is, however, needed in order to confirm such an explanation.

4 Conclusions and outlook

Using WVR data for validation of ZWD estimates in space geodesy means that data must not necessarily be available for all time periods. We can ignore more or less data with a high LWC, meaning that there is a balance between how much data we want to have available and the data accuracy.

As a consequence, a future application, for time periods when no liquid water is present in the atmosphere, would be to develop a one-frequency radiometer with high stability and accuracy.

References

Davis J L, Elgered G, Niell A E, and Kuehn C E (1993), Ground-based measurement of gradients in the "wet" radio refractive index of air, Radio Sci., 28(6), 1003–1018. https://doi.org/10.1029/93RS01917

Elgered, G. Davis J L, Herring T A, Shapiro I I (1991), Geodesy by radio interferometry: water vapor radiometry for estimation of the wet delay, J. Geophys. Res., 96, 6541–6555. https://doi.org/10.1029/90JB00834

Elgered G, Ning T, Diamantidis P K, Nilsson T (2023). Assessment of GNSS stations using atmospheric horizontal gradients and microwave radiometry, Adv. Space Res. https://doi.org/10.1016/j.asr.2023.05.010

Westwater E R, Guiraud F O, (1980). Ground-based microwave radiometric retrieval of precipitable water vapor in presence of clouds with high liquid content. Radio Sci., 15, 947–957. https://doi.org/10.1029/RS015i005p00947

Wu S C (1979). Optimum frequencies of a passive microwave radiometer for tropospheric path-length correction, *IEEE Trans. Ant. Propagat., AP-27, pp. 233–239*, *https://doi.org/10.1109/TAP.1979.1142066*.

Enhancing the Bernese GNSS Software for multi-technique analysis at BKG - Focus on the VLBI implementation

C. Flohrer, A. Walenta, D. Thaller, C. Gattano, R. Dach, U. Hugentobler

Abstract The Geodesy Group of the BKG (Federal Agency for Cartography and Geodesy) has been involved in IVS analysis and combination activities for many years. It successfully operates an IVS Analysis Center (AC), using NASA's software packages νSolve and Calc/Solve, and the IVS combination centre, using the DGFI-TUM software package DOGS-CS. BKG also operates an ILRS AC and is a partner in the CODE consortium, which operates the IGS AC "CODE". The IGS AC as well as the ILRS AC use the Bernese GNSS Software, which is developed by AIUB (Astronomical Institute of the University of Bern) and continuously adapted to changing requirements and user needs. In summary, BKG currently has different software packages in use for different geodetic analyses. However, our focus is not only on the individual techniques, but also on the combination of the different observation techniques, in particular to improve the Earth rotation parameters. We would like to continue the multi-technique combined analysis using a single software package, namely the Bernese GNSS Software. Ultimately, this will allow us to combine GNSS, VLBI and SLR data not only at the SINEX level, but also at the observation level in the near future. We present the current status of the Bernese GNSS Software enhancements for multi-technique analysis, with particular focus on the VLBI implementation.

Claudia Flohrer[1], Anastasiia Walenta[1], Daniela Thaller[1], César Gattano[2], Rolf Dach[2], Urs Hugentobler[3],
(1) Federal Agency for Cartography and Geodesy (BKG), Department Geodesy, Frankfurt am Main, Germany
(2) Astronomical Institute of the University of Bern, Bern, Switzerland
(3) Institute for Astronomical and Physical Geodesy, Technical University of Munich, Munich, Germany
Corresponding author: claudia.flohrer@bkg.bund.de

Keywords Bernese GNSS Software, VLBI, GNSS, combination at the observation level

1 Introduction

BKG's geodesy group has a long-standing experience in the analysis of the three space-geodetic techniques VLBI, SLR and GNSS. We operate an IVS data center (Walenta and Goltz, 2023), an IVS analysis center (AC) (Engelhardt et al., 2023), and an IVS combination center (Bachmann et al., 2023). In addition we are running an ILRS AC (König et al., 2020) and are partner of the CODE (Center for Orbit Determination in Europe) consortia. The CODE consortia consists of the four institutions - Astronomical Institute of the University of Bern (AIUB) located in Switzerland, Federal Office of Topography swisstopo in Switzerland, Federal Agency of Cartography and Geodesy in Germany, and Institute for Astronomical and Physical Geodesy at the Technical University of Munich (IAPG, TUM) in Germany. CODE operates an IGS AC (Dach et al., 2023) using the Bernese GNSS Software (BSW). The BSW, which is developed at AIUB, is a scientific, high-precision, multi-GNSS data processing software, which today is able to process the various GNSS as well as SLR observations (Dach et al., 2015). Since 2010 BKG has been using the BSW for its ILRS AC activities. As the BSW cannot yet be used for operational VLBI analysis, we are currently using NASA's software packages νSolve and Calc/Solve for our IVS AC activities.

Our research interest is not only in individual techniques but also in the combination of different observation techniques with particular focus on the

improvement of reference frames including Earth rotation parameters. The BSW has been used in the past for GNSS and SLR combination studies (e.g., Thaller et al., 2011). The extension of the BSW with the capabilities for processing SLR data in view of reference frame determination has been intensively carried out by a cooperation between BKG and AIUB for many years (Thaller et al., 2012). For the combination of VLBI and GNSS we are currently using the DOGS-CS software package (Gerstl et al., 2004) provided by DGFI-TUM (Lengert et al., 2023; Klemm et al., 2023).

At the last EVGA meeting in 2021, we already reported about an effort of BKG together with AIUB and TUM for the enhancement of the BSW for VLBI processing capabilities (Flohrer et al., 2021). The goal is to enable the combination of all three techniques (VLBI, SLR, GNSS) at the observation level within one single software package. This work is ongoing. Our current paper presents a status update of the BSW implementation for multi-technique analysis with particular focus on the VLBI enhancement. We also discuss the comparison of VLBI analysis results derived from other software packages with those derived from the Bernese GNSS Software. This approach is based on the so-called SINEX-NEQ-loop. Finally we highlight the advantages of using one single software package such as BSW for multi-technique analysis.

2 Bernese GNSS Software - VLBI implementation status

We begin with a brief overview of the BSW structure in order to better explain afterwards the current software developments for the multi-technique analysis.

The flowchart in Fig. 1 shows a very simplified and high-level structure of the BSW and is limited to the needs of this paper. Various external data formats can be read (as GNSS RINEX files, SLR normal point files, and VLBI vgosDB files) and are converted into an internal BSW observation file format in a first step. The observations pass through a preprocessing module, which releases cleaned observations.

As the geodetic data processing of the BSW is based on least-squares adjustment by solving normal equation systems, the normal equations (NEQ) are set-up in the next step, involving the observation modeling and parameter setup. As a result one obtains NEQs, which are free of any constraints. These NEQs are input to the "NEQ stacking" step. If there is more than one NEQ, these are accumulated, i.e. stacked. A priori parameter values are transformed to an agreed set of a priori values. The parameterization can also be adjusted by a linear parameter transformation in order to enable parameter stacking. Finally, geodetic datum constraints, such as minimum network constraints, as well as parameter-specific constraints are added to the accumulated NEQ, which allows to solve it and to obtain a solution for the desired parameters. The BSW provides the solution (a priori and estimated parameters, statistics) as well as the accumulated unconstrained NEQ as output of the processing. This information is written to both, internal and external format. The external format to exchange normal equations is called SINEX (IERS, 2006).

The white box "converter" on the right in Fig. 1, represents a BSW program that converts solutions and NEQs, which are provided via SINEX files, into the BSW internal NEQ format. This allows to process external input and use it for further stacking at the NEQ level and combined parameter estimation.

The current implementation status allows us to use the BSW for VLBI analysis based on a normal equation input (using SINEX files). In order to process actual VLBI observations several implementation steps have to be completed. The following milestones have been achieved so far:

- Implementation of VLBI-specific observation model.
- Implementation of a converter for VLBI observations provided in vgosDB format (version 4) into the internal BSW observation format [1]. The implementation is kept flexible to allow for further extension to the processing of the individual observations instead of using the preprocessed version 4.
- Redesign of the generic observation file for multi-technique handling with one ore more base objects

[1] We thank the IVS for providing tools to communicate with vgosDB, which uses the netCDF format (vgosDB, 2023). The source code of these tools was used as a starting point for our converter.

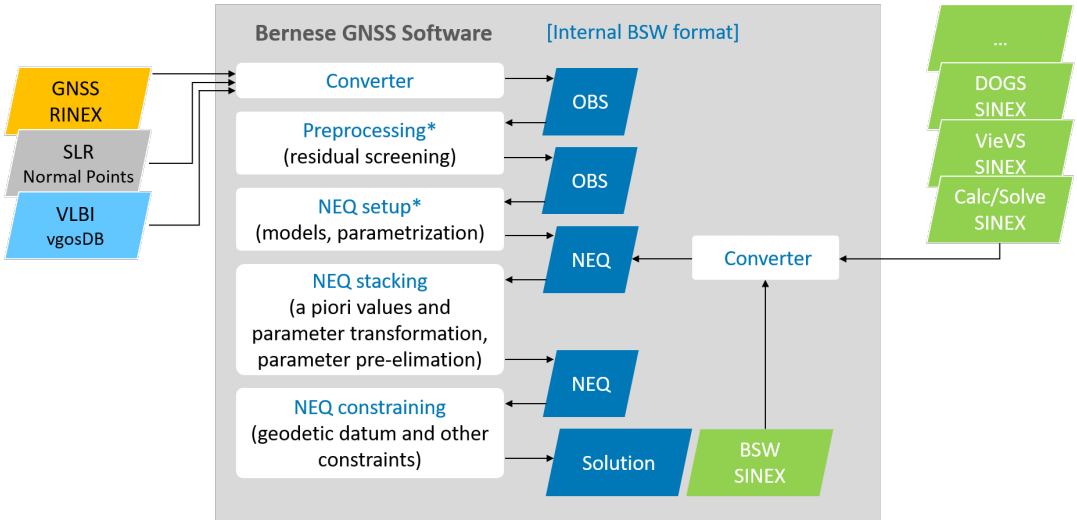

Fig. 1 High-level structure of the Bernese GNSS Software, simplified to the needs of this paper. Elements labelled with (*) still need to be adapted for VLBI capabilities.

(sensors collecting the observations, e.g., GNSS antennas or VLBI telescopes) and partner objects (the origin of the signal or the end of the measured distance, e.g., GNSS satellites or quasars) for one file.
- Design of an observation file handling object for the selection of observations.
- Design of the "space geodetic object class", covering satellites, quasars and ground objects. These objects can act as either base or partner objects in the observation files, depending on the observation type.
- Design of a dynamic space geodetic object database, which is build up during run-time and provides general information for the processed base and partner objects.
- Introduction of new parameter type "quasar coordinate".

Major effort was put in the redesign of the observation handling and the implementation of a more flexible space geodetic object class to cope with the new requirements for a multi-technique software. A significant part of the software development is devoted to unit testing. After the implementation phase it has to be ensured that the existing software functionalities and performance requirements are not affected, which also means a lot of additional effort, e.g., by sometimes keeping in parallel old and new source code until every change in the software design is pulled through all programs and modules. As the time frame of the software development is several years, parallel software developments for the GNSS and SLR technique are on-going as well and have to be merged constantly in order to keep consistency.

The current state of implementation does not yet allow a VLBI data processing starting from the observation level. There are still a number of steps to be achieved, which is indicated by the asterisk mark in the two affected boxes in Fig.1. The use of the space geodetic object class has to be spread across the existing modules, which will in turn also relax some of the current restrictions of the BSW regarding the GNSS and SLR implementation. Another major work package is the station clock handling, i.e. the automated detection and the introduction of clock breaks. Finally, VLBI specific corrections have to be added, e.g., due to cable calibration delays, thermal and gravitational antenna deformations, and galactic aberration effect. We are confident that we will achieve basic levels of these steps within the next two years, although we recognise that software development times are difficult to predict.

3 Validation of software implementation

In parallel with the technical testing we conducted some functional testing to ensure that the software developments meet our needs and expectations. We

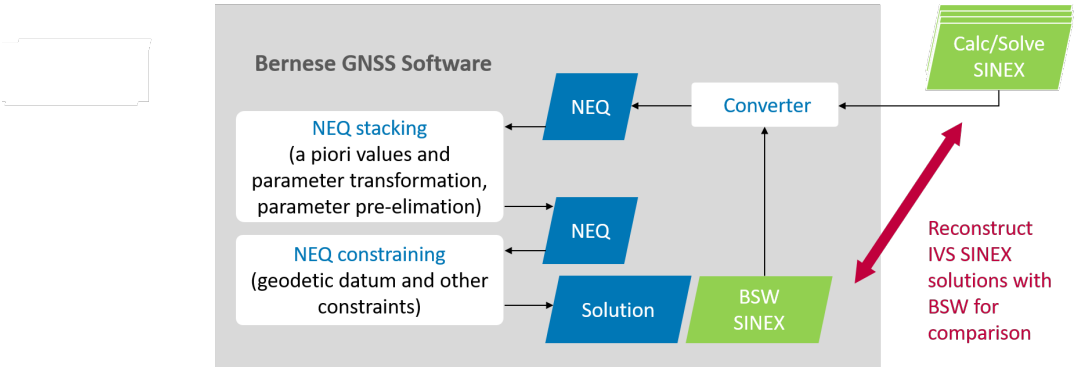

Fig. 2 SINEX-NEQ-loop as used for reproducing external VLBI solutions.

made some comparisons with other IVS ACs solutions and tried to reconstruct the solutions by starting from SINEX level. Figure 2 shows the testing approach, which we call the SINEX-NEQ-loop. External SINEX files from other software packages (like Calc/Solve, DOGS, VieVS, Where, Ascot) are converted into the BSW NEQ format, containing unconstrained NEQs. Then we apply the necessary transformations to use identical a priori information and parameterizations. Finally, we try to add identical geodetic datum constraints and solve the NEQ. The estimated parameters can be compared with the external estimates provided as well in the SINEX files. In order to generate identical solutions exact knowledge of the used a priori values and constraints is essential. Not all external solutions provide the constraint information as part of the SINEX file, as this information is optional. However, the software Calc/Solve delivers this constraint information and was thus the solution, which we could reconstruct the best.

When comparing a classical 24h-VLBI session solution from a Calc/Solve SINEX file (generated by our IVS AC operated at BKG) with the corresponding BSW solution, we reach consistency for quasar coordinates at the level of $0.5\,mas$, for station coordinates at the level of $0.3\,mm$, for polar motion and celestial pole offsets at the level of $0.01\,mas$, for dUT1 at the level of $0.5\,\mu s$, and for LOD at the level of $0.05\,\mu s$. One problem, which is not yet understood by the authors, has to do with the reported a priori information in the Calc/Solve SINEX files. This a priori information does not seem to be exactly the same as that used to generate the corresponding NEQ, reported in the very same SINEX file. One possible explanation relates the problem to the correction of quasar coordinates by the galactic aberration effect. We will follow up this issue with the Calc/Solve developers.

We also tested other VLBI solutions from other IVS ACs using Calc/Solve but also other software packages and achieved lower or similar levels of consistency. This was to be expected, since in most cases the constraint information used by the other software packages is not given, but it is essential to reconstruct the solution for such software tests. Other potential inconsistencies could be caused by different approaches to handle numerical instabilities for matrix operations within each software package. In addition we found that there are at least two approaches to apply minimum network constraints. For the case of no-net-rotation (NNR) conditions on the quasar coordinates the BSW uses the full constraint equation:

$$\mathbf{Hx} = (\mathbf{B^T P B})^{-1}\mathbf{B^T P x} = 0 \qquad (1)$$

with the rotation parameters $\mathbf{x}$ on which the constraints shall be applied. The Matrix $\mathbf{P}$ is specifying the constraints of the quasar coordinates. $\mathbf{B}$ is the transformation matrix converting a coordinate set $\mathbf{k}$ to $\mathbf{k}'$ by applying infinitesimal rotations $\mathbf{x}$ through $\mathbf{k}' = \mathbf{k} + \mathbf{Bx}$. Alternatively a simplified constraint equation can be used to constrain the infinitesimal rotation $\mathbf{x}$ to zero too:

$$\mathbf{Hx} = \mathbf{B^T P x} = 0 \qquad (2)$$

The strict Eqn. (1) assures that the constraints are applied to the rotations around the coordinate axes, while Eqn. (2) effectively constrains a linear combination of the rotations, which may however be favourable in case of non-homogeneously distributed

sources. For homogeneously distributed sources the two constraining options are equivalent, up to a factor of the order n, where n is the number of quasars considered for the NNR condition. For Eqn. (2) the constraint has to be scaled with the number of quasars. This equation type is implemented in Calc/Solve, according to our knowledge. It remains an open scientific question which of the two equations is favourable in terms of a stable celestial reference frame realization with non-homogeneously distributed quasars.

4 Outlook on using BSW for multi-technique analysis

We see a wide range of potential benefits from using the BSW for multi-technique analysis. The most obvious one is the combination of space-geodetic observation techniques at the observation level. Since the different techniques are processed by the very same software it is ensured that, by going through the same source code, the same underlying models are used. The combination at observation level is also beneficial for the observation screening, which is no longer possible at the NEQ level. The observations can be screened for outliers based on the combination and a consistent observation weighting can be applied. All parameters are derived from the very same analysis taking into account all correlations.

The BSW offers a nice tool for automated processing, called the BPE (Bernese Processing Engine), which makes it easy to process huge data sets. The software typically runs in session mode, where observations of one session are processed and the resulting NEQs are stored. The NEQ stacking module then allows the accumulation of multiple NEQs, enabling frequent updates of multi-year solutions. As a result the user gets not only the parameter estimates from the stacked NEQs but also those from the individual session-wise NEQs involved in the solution. Thus, one can easily compare the differences between the individual and the stacked solutions for parameters valid over the entire interval, e.g., to derive station coordinate repeatabilities.

Advantageously, a multi-technique analysis with the BSW offers access to all parameters from the different techniques, in contrast to a combination on NEQ level using SINEX files. Parameters common to the different space-geodetic techniques are the key to combine the techniques. Such technique connections are called "ties", like local ties (connecting on the ground through station coordinates), space ties (connecting in space through orbit parameters, see, e.g., Thaller et al. (2011)), and atmospheric ties (connecting in the atmosphere through troposphere parameters, see, e.g., Thaller (2008)). If the combination of techniques is done at the NEQ level using SINEX files, one looses access to entire parameter groups, like orbit or troposphere parameters, as they get pre-eliminated and cannot be stacked anymore. Parameter pre-eliminations are done for different reasons. For example, orbit parameter information cannot be stored in the SINEX format, and troposphere parameters are often pre-eliminated to speed up the processing and save disk space.

A new geodetic satellite mission GENESIS is now on the horizon. This mission would allow for the first time a co-location of the four main space-geodetic techniques VLBI, SLR, GNSS and DORIS by using the satellite as a space tie. This development is encouraging us in our efforts to make the BSW "VLBI-ready" within the next few years.

References

Bachmann S, Hellmers H, Modiri S, Schneider-Leck S, Bloßfeld M, Thaller D (2023) BKG/DGFI-TUM Combination Center. In: *International VLBI Service for Geodesy and Astrometry 2021+2022 Biennial Report*, eds. Armstrong KL, Behrend D, Baver KD, NASA/TP-20230014975, 2023.

Dach R, Lutz S, Walser P, Fridez P (Eds) (2015) Bernese GNSS Software Version 5.2. *User manual*, *Astronomical Institute, University of Bern*, *Bern Open Publishing*, doi: 10.7892/boris.72297.

Dach R, Schaer S, Arnold D, Kalarus M, Prange L, Stebler P, Villiger A, Jäggi A, Brockmann E, Ineichen D, Lutz S, Willi D, Nicodet M, Thaller D, Klemm L, Rülke A, Söhne W, Bouman J, Hugentobler U (2023) Center for Orbit Determination in Europe (CODE) Analysis Center Technical Report 2022. *IGS Central Bureau and University of Bern*, *Bern Open Publishing*, 45–64, doi: 10.48350/179297.

Engelhardt G, Walenta A, Ullrich D, Flohrer C (2023) BKG VLBI Analysis Center. In: *International VLBI Service for*

Geodesy and Astrometry 2021+2022 Biennial Report, eds. Armstrong KL, Behrend D, Baver KD, NASA/TP-20230014975, 2023.

Flohrer C, König D, Thaller D, Gattano C, Meyer U, Dach R, Hugentobler U (2021) VLBI enhancement of the Bernese GNSS Software for multi-technique analysis at BKG. In: *Proceedings of the 25th European VLBI for Geodesy and Astrometry (EVGA) Working Meeting*, eds. Haas R, Elgered G, e-book, 56–60, ISBN: 978-91-88041-41-8.

Gerstl M, Kelm R, Müller H, Ehrnsperger W (2004) DOGS-CS: Kombination und Lösung großer Gleichungssysteme. *DGFI (Deutsches Geodätisches Forschungsinstitut) MG/01/1995/DGFI*.

IERS (2006) SINEX – Solution Independent Exchange Format. `https://www.iers.org/IERS/EN/Organization/AnalysisCoordinator/SinexFormat/sinex.html`. Accessed 10 October 2023.

Klemm L, Thaller D, Flohrer C, Walenta A, Ullrich D, Hellmers H (2023) Intra-technique combination of VLBI Intensive and Rapid data to improve the temporal regularity and continuity of the UT1-UTC series. In: *International Association of Geodesy Symposia*, eds. Freymueller J and Sánchez L, Springer International Publishing (in press).

König D, Thaller D, Grahsl A, Meyer U (2020) ILRS Analysis Activities - BKG (Bundesamt für Kartographie und Geodäsie), Germany. In: International Laser Ranging Service (ILRS) 2016-2019 Report, eds. Noll C, Pearlmann M. *NASA/TP-20205008530; NASA Goddard Space Flight Center, Greenbelt, MD, USA*, 7-6–7-9.

Lengert L, Thaller D, Flohrer C, Hellmers H, Girdiuk A (2023) On the Improvement of Combined EOP Series by Adding 24-h VLBI Sessions to VLBI Intensives and GNSS Data. In: *Geodesy for a Sustainable Earth, Proceedings of the 2021 Scientific Assembly of the International Association of Geodesy, Beijing, China*, June 28 – July 2, 2021, eds. Freymueller J and Sánchez L, Springer International Publishing, 245–252, doi: 10.1007/978-3-031-29507-2.

Thaller D (2008) Inter-technique combination based on homogeneous normal equation systems including station coordinates, Earth orientation and troposphere parameters. *Scientific Technical Report STR08/15, GFZ, Potsdam, Germany*.

Thaller D, Dach R, Seitz M, Beutler G, Mareyen M, Richter B (2011) Combination of GNSS and SLR observations using satellite co-locations. *Journal of Geodesy*, 85(5), 257–272, doi: 10.1007/s00190-010-0433-z.

Thaller D, Sosnica K, Dach R, Jäggi A, Beutler G (2012) LAGEOS-ETALON solutions using the Bernese Software. In: *Proceedings of the 17th International Workshop on Laser Ranging "Extending the Range"*, Mitteilungen des Bundesamtes für Kartographie und Geodäsie, 48, 333–336.

vgosDB (2023) Files related to vgosDB. `https://ivscc.gsfc.nasa.gov/IVS_AC/IVS-AC_vgosDB.htm`. Accessed 10 October 2023.

Walenta A, Goltz M (2023) BKG Data Center. In: *International VLBI Service for Geodesy and Astrometry 2021+2022 Biennial Report*, eds. Armstrong KL, Behrend D, Baver KD, NASA/TP-20230014975, 2023.

Investigating the datum parameters of new solutions by IVS AC DGFI-TUM

M. Glomsda, M. Seitz, M. Bloßfeld, D. Angermann

Abstract In 2022 and at the beginning of 2023, the three latest realizations of the International Terrestrial Reference System (ITRS) became available: ITRF2020, JTRF2020, and DTRF2020. Among others, the data contribution by the International VLBI Service for Geodesy and Astrometry (IVS) to these reference frames contains new models for the gravitational deformation of six VLBI antennas. In particular, these models affect the estimated heights of the corresponding stations. In 2023, the IVS Analysis Centers (ACs) reprocessed their session series from 1979 to the present. The respective series of the AC at DGFI-TUM is *dgf2023a*. The main changes w.r.t. the previous series *dgf2020a*, which served as input data for the ITRS 2020 realizations, are a) the usage of ITRF2020 as a priori reference frame, and b) the corrections for the gravitational deformation of another seven antennas. Thereby, the choice of stations used for the no-net-translation and no-net-rotation conditions is a crucial issue. Furthermore, the additional deformation models will likely influence the scale parameter of similarity transformations (including the respective stations) between VLBI single-session solutions and the ITRS realizations. Three of the corresponding seven antennas belong to the next generation VLBI Global Observing System (VGOS). In this presentation, we examine the effects of the above mentioned novelties in solution *dgf2023a*. In particular, we take a look at the similarity transformations, i.e., the time series of datum parameters, and we put special emphasis on the scale parameter. Above all, a drift in the VLBI scale was observed for sessions after about 2013.75 during the computation of the ITRF2020. Not least to investigate this finding, we also apply the other two ITRS 2020 realizations, JTRF2020 and DTRF2020, as a priori reference frames.

Keywords VLBI, IVS, ITRS realization, similarity transformation, scale

Matthias Glomsda · Manuela Seitz · Mathis Bloßfeld · Detlef Angermann
Deutsches Geodätisches Forschungsinstitut, Technische Universität München (DGFI-TUM), Arcisstrasse 21, 80333 München, Germany

1 Introduction

The latest realizations of the International Terrestrial Reference System (ITRS) contain geodetic space observations up to the end of the year 2020, and several new geophysical and technique-specific models have been incorporated. In the case of Very Long Baseline Interferometry (VLBI), gravitational deformation (GD) has been modelled for six antennas (EFLSBERG, GILCREEK, MEDICINA, NOTO, ONSALA60, YEBES40M), for instance. The corresponding VLBI solution by DGFI-TUM is called *dgf2020a*, and the a priori antenna positions have been taken from the previous ITRF2014 (Altamimi et al., 2016).

Three ITRS 2020 realizations (terrestrial reference frames, TRFs) are available: *ITRF2020* (Altamimi et al., 2023) by the Institut national de l'information géographique et forestière (IGN, France), *JTRF2020* (*https://jpl.nasa.gov/site/jsgt/jtrf/category/jtrf2020/*) by NASA's Jet Propulsion Laboratory (JPL, USA), and *DTRF2020* (Seitz et al., 2023) by DGFI-TUM (Germany). ITRF2020 is a secular TRF which has been combined at the solution level, and the station positions have been reduced for post-seismic deformation (PSD) as well as

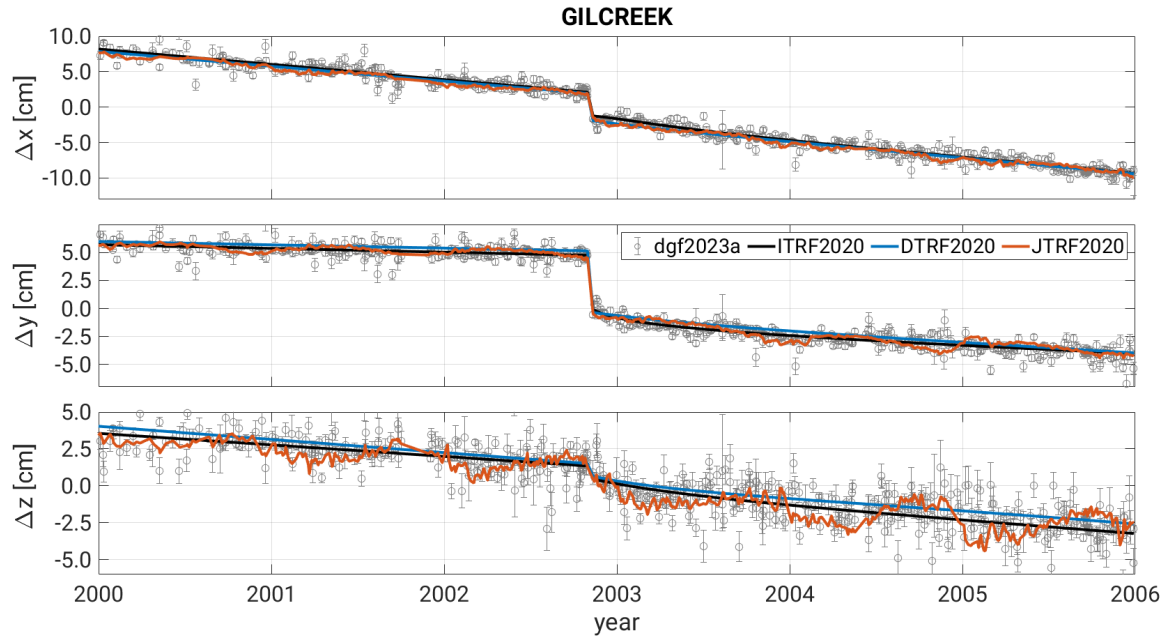

Fig. 1 Time series (reduced by some mean value per coordinate) of station positions for the VLBI antenna GILCREEK in the ITRS 2020 realizations (only linear and PSD parts for ITRF2020 and DTRF2020) and in DGFI-TUM's new solution *dgf2023a*.

(semi-) annual and draconitic (for selected stations) signals. DTRF2020 also is a secular TRF in which PSD has been reduced. However, it was calculated by a combination of normal equations (NEQs) after the additional reduction of geophysically modelled non-linear station motions, i.e., non-tidal loading displacements, at NEQ level. JTRF2020, on the other hand, is an epoch reference frame which has been computed sequentially with a square-root information filter. Corresponding position time series for the VLBI antenna GILCREEK are shown in Figure 1.

In addition, Fig. 1 shows the time series of estimated GILCREEK positions from DGFI-TUM's new VLBI solution *dgf2023a*. The a priori TRF used for this solution is the ITRF2020 (linear plus PSD parts), and new GD models for another seven antennas are considered. In this study, we investigate the impact of these changes on the estimated antenna coordinates and the corresponding similarity transformations between the single-session solutions and the (a priori) TRFs. Thereby, we put special emphasis on the choice of datum stations (affecting translations and orientation) and the scale parameter (affected by the choice of stations for the transformations).

Table 1 The distinct setups investigated in this study. *Old* refers to the original six antennas with a GD model in the ITRS 2020 input series, and *new* to the additional seven antennas with subsequent GD models. The asterix (*) highlights datum station lists not recommended by Gipson (2019) (compare text).

solution	a priori TRF	GD models	datum stations
dgf2020a	ITRF2014	old	excluding old
*dgf2023a old**	ITRF2020	old	excluding old
dgf2023a old	ITRF2020	old	all
*dgf2023a**	ITRF2020	old + new	all
dgf2023a	ITRF2020	old + new	excluding new
dgf2023a JTRF	JTRF2020	old + new	excluding new
dgf2023a DTRF	DTRF2020	old + new	excluding new

2 Method

We analyse the transition from our ITRS 2020 contribution *dgf2020a* to the new solution *dgf2023a* by introducing the distinct modifications successively. The resulting setups are listed in Table 1. In particular, we switch the a priori TRF and the amount of models for GD. The latter are empirical excess delay functions depending on the antenna elevation ε (see Figure 2). Since the estimated antenna height is proportional to $-\sin\varepsilon$, which is a function of elevation, too, the GD models will mainly affect the heights of the

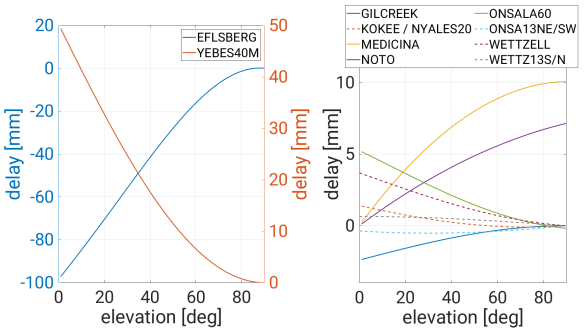

Fig. 2 Empirical excess delay models accounting for gravitational deformation. The dashed lines refer to the seven new models.

respective antennas. According to Gipson (2019), for example, these vertical changes have an impact on no-net-translation (NNT) and no-net-rotation (NNR) conditions. Hence, if we apply an a priori TRF that has not yet been computed with certain GD models, the corresponding antennas should not be part of the datum stations for the single-session solutions, either. To investigate this, we include solutions with different lists of datum stations, and the asterix (*) in Tab. 1 highlights those setups with lists not following the recommendation by Gipson (2019). The seven antennas with GD models only available after the 2020 realizations of the ITRS are the legacy antennas NYALES20, KOKEE, WETTZELL, and WETTZ13N, and the next generation VLBI Global Observing System (VGOS) antennas ONSA13NE, ONSA13SW, and WETTZ13S.

3 Results

3.1 A priori TRF

First, we replace the a priori ITRF2014 with the ITRF2020 (linear and PSD parts) but do not introduce the new GD models. The estimated antenna network geometries (i.e., the baseline lengths) do not change with a new a priori TRF. However, the application of NNT and NNR constraints w.r.t. this TRF affects the final coordinate estimates. If the list of datum stations remains constant (*dgf2023a old**), the impact is comparatively small if the a priori coordinates in a session network do not change much. The largest position deviations occur after 2014, since the ITRF2014 is only extrapolated for this period, while the ITRF2020 contains actual observation data and provides significantly different secular positions for antennas with only short observation histories before 2015. The addition of datum stations, on the other hand (*dgf2023a old*), creates additional noise for the entire time span.

Second, the new GD models are included and the corresponding antennas are removed from the datum stations, but we compare the effects of using the three different ITRS 2020 realizations as a priori TRFs (only linear plus PSD parts for DTRF2020, too). Namely, we compute 7-parameters similarity transformations between the ITRS realizations and the respective single-session solutions. As expected, the three translation and three rotation parameters are all closely distributed around 0 due to the NNT and NNR constraints (not shown here). The session-wise scale parameters, which can be realized by VLBI, are plotted in Figure 3. They contain a seasonal signal and are significantly different from 0. The scale drift for the ITRF2020 after about 2013.75, which was reported by Altamimi et al. (2023), is also revealed by our solution. A similar drift is obtained for the JTRF2020, but not for the DTRF2020. The reason for this apparent drift is still under investigation by a working group. An obvious difference between the realized scales is the choice of techniques used for its realization within ITRF2020/JTRF2020 (VLBI and Satellite Laser Ranging, SLR) and DTRF2020 (VLBI and Global Navigation Satellite Systems, GNSS). We further observe that the antenna heights are generally smaller in the ITRF2020 compared to the DTRF2020 (see Fig. 4). And when restricting ourselves to the VGOS sessions (bi-weekly sessions starting in 2019), basically all scales are positive for ITRF2020 and JTRF2020.

3.2 Gravitational deformation

Now, we stick with the a priori ITRF2020 and switch the GD models. As shown by Gipson (2019) and Glomsda et al. (2020), the change in estimated heights for the respective antennas generally depends on the maximum model excess delay and the sign of its slope w.r.t. elevation ε: a strictly positive [negative] slope induces an increase [decrease] in height. This is due to the aforementioned connection of height with

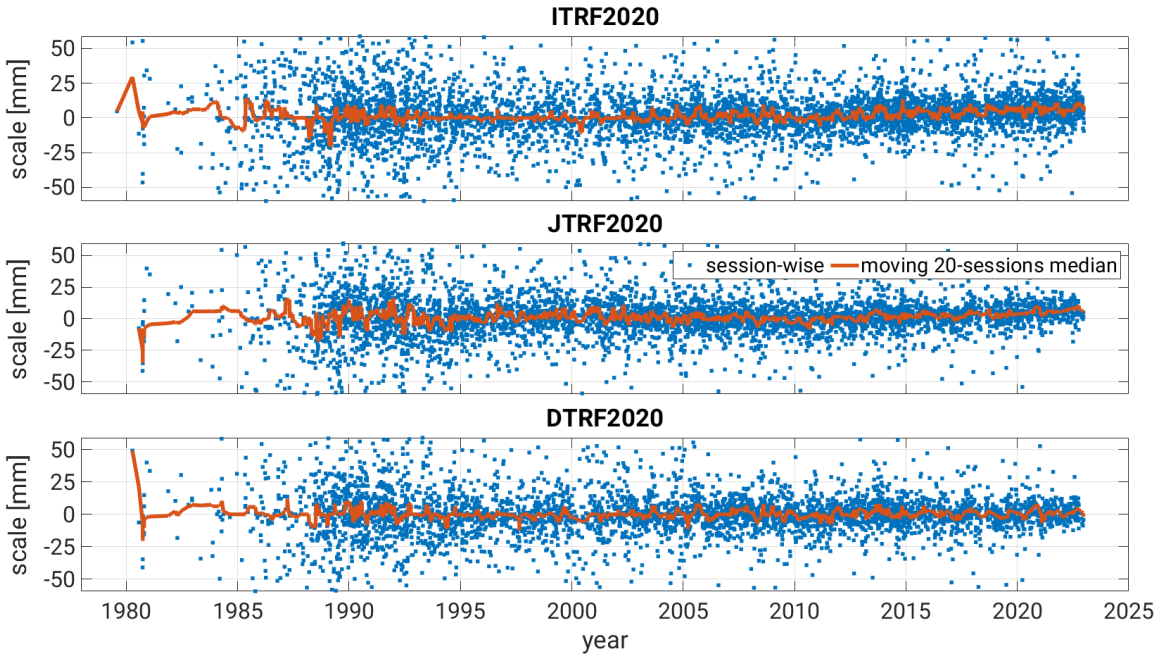

Fig. 3 Time series (blue) and moving 20-session medians (red) of the scale parameter in 7-parameters similarity transformations between an a priori TRF and the corresponding single-session solutions.

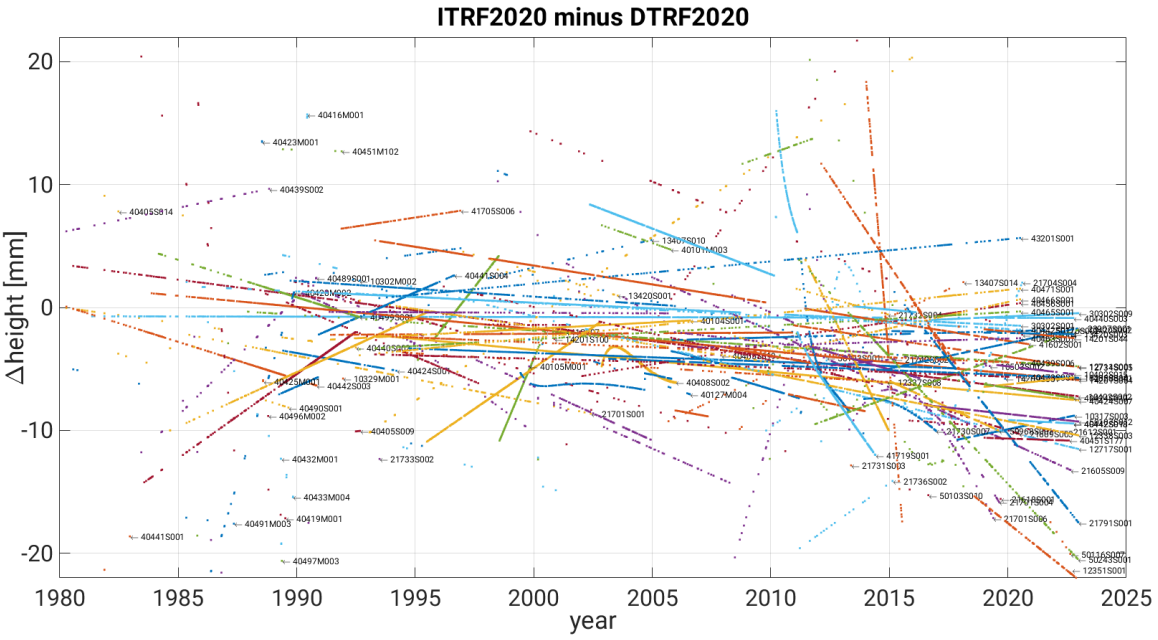

Fig. 4 VLBI antenna heights according to DTRF2020 (linear part plus PSD) subtracted from the corresponding heights according to ITRF2020. Each dot refers to a session in which the antenna (each represented by a different color) was actually observing.

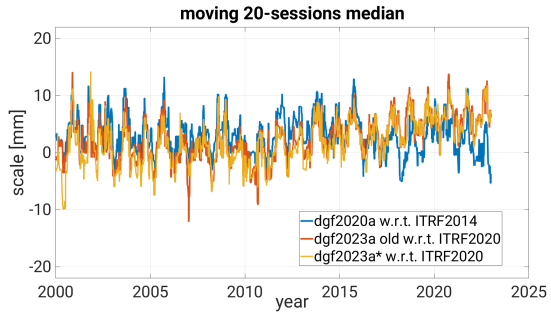

Fig. 5 The moving 20-sessions medians of the scale parameters for similarity transformations between various single-session solutions and their respective a priori TRFs.

$-\sin\varepsilon$. Hence, we expect an increase in height for the new Onsala twin telescopes only, and a decrease for the other five antennas (compare Fig. 2). The question remains whether these seven antennas should be removed from the datum station list. Unfortunately, KOKEE, NYALES20, and WETTZELL have remote locations and/or long observation histories, so they are very beneficial for the NNT and NNR constraints. Likewise, the current VGOS network is still very small, and neglecting ONSA13NE, ONSA13SW, and WETTZ13S would mean neglecting about a third of the network. In both setups, *dgf2023* and *dgf2023**, the median changes in antenna height have the expected sign, except for WETTZ13N when the seven antennas are removed from the list of datum stations. In this case, the overall scatter in height changes is also larger, since the list of datum stations is altered (compare the previous subsection). However, this list seems to not impair the general effect of the correction for GD. The largest impact for both setups is obtained for WETTZELL and KOKEE, which have the largest maximum excess delay (see Fig. 2).

Finally, we check the scale parameters after the introduction of the additional GD models. In Fig. 5, the moving 20-sessions medians of the scale are shown for the setups *dgf2023a old* and *dgf2023**, which both use the full list of datum stations but differ w.r.t. the antennas that are corrected for GD. In either case, the similarity transformation w.r.t. the ITRF2020 incorporates the seven antennas with a new GD model. The figure reveals that the scale parameters are hardly affected by the latter, and the scale drift is still existing.

Fig. 5 also contains the moving medians for the scale parameters of the similarity transformations between the session-wise solution *dgf2020a* and its a priori ITRF2014. Before 2016, they agree well with the medians for ITRF2020 (with and without the new GD models), but they do not show the drift afterwards.

4 Conclusions

The impact of replacing the a priori ITRF2014 with any of the new ITRS 2020 realizations on the final, NNT- and NNR-aligned coordinates is naturally largest for antennas with a short observation history before 2015. If the list of datum stations is altered as well, the differences are enlarged for all estimated coordinates of all epochs. Reasons for modifications of this list are, e.g., the availability of longer observation periods for particular (young) stations, or the introduction of antenna-specific GD models that have not been applied in the computation of the a priori TRF. We found that, on average, the changes in estimated heights due to GD had the expected sign and magnitude for the respective antennas, independent from their appearance in the datum station list.

The scale parameters of similarity transformations between the single-session solutions and their a priori TRFs still need to be investigated in more detail. We could replicate a scale drift w.r.t. ITRF2020, and we also found one w.r.t. JTRF2020 but none w.r.t. DTRF2020 and ITRF2014. Furthermore, we did not observe a significant impact of the new GD models on the scale.

References

Altamimi Z, Rebischung P, Metivier L, and Collilieux X (2016) ITRF2014: A new release of the International Terrestrial Reference Frame modeling nonlinear station motions. *J. Geophys. Res., Solid Earth*, Vol. 121, doi: 10.1002/2016JB013098.

Altamimi Z, Rebischung P, Collilieux X, et al. (2023) ITRF2020: an augmented reference frame refining the modeling of nonlinear station motions. *J. Geod.*, Vol. 97 (47), doi: 10.1007/s00190-023-01738-w.

Gipson J (2019) Impact of Gravitational Deformation of VLBI Antennas on Reference Frame. *Presentation at UAW 2019*.

Glomsda M, Seitz M, Gerstl M, Kehm A, Bloßfeld M, and Angermann A (2020) Impact of new models for the ITRF2020 in VLBI analysis at DGFI-TUM. *Presentation at AGU 2020*.

Seitz M, Bloßfeld M, Angermann D, Glomsda M, Rudenko S, Zeitlhöfler J, and Seitz F (2023) DTRF2020: ITRS 2020 realization of DGFI-TUM (data). *Zenodo*, doi: 10.5281/zenodo.8220524.

Current Status at BKG IVS Data Center

M. Goltz, A. Walenta, D. Thaller

Abstract Last year has brought several changes for IVS Data Center at BKG. By introducing the new software 'ingest' for processing uploaded files, the unified file validation among the IVS Data Centers is enforced. The next significant steps in the routine operations have been related to our own service: discontinuity of FTP in favour of FTPS and HTTPS. We have arranged a personal account for every uploader on request and supported the old user 'ivsincoming' during the protocol transition. At the end, user 'ivsincoming' has been removed as well. Corresponding mapping of user accounts and uploads simplifies the data center maintenance. In particular, an automatic feedback loop is planned to improve our user support. Also, we monitor the uploads and downloads by the users on a daily basis in a straight forward manner. The related illustrations are available on our website. The security measures are implemented as required by our internal IT. It means, that we provide proper supervision to secure sensitive data. Also, each incoming file is checked with a virus scanner, where only the SWIN files are treated separately because of their large file size. According to the IVS guidelines and rules for the Data Centers, we keep our Data Centers in sync with the other IVS Data Centers by mirroring them as well as running a consistency check to guarantee the data acquisition. Additionally, before activating new changes in the ingest software, we perform a test with sample data. For these operations, we distribute the incoming files to a white and a black list, which are updated continuously. Our server setup allows introducing software updates and tests without inflicting the productive environment. For instance, the last activities were regarding the validation of the EOP3.0 format from several ACs and proper acceptance of the new file name convention for the Level 2 Data Analysis in vgosDb format and SINEX files. These data comprise the major part of files uploaded to the Data Center, as a consequence, their validation impact the IVS Community at most. We will illustrate, how incoming data is validated at the example of EOP, SINEX and SWIN files, where the latter is slightly different.

Keywords IVS Data Center, status report, data management, ingest software

Federal Agency for Cartography and Geodesy, Division G1 - General Issues, Combination of Space Techniques, Richard-Strauss-Allee 11, 60598 Frankfurt a.M, Germany

1 General Information

The German Federal Agency for Cartography and Geodesy (BKG) is hosting a Data Center (DC) for the International VLBI Service for Geodesy and Astrometry (IVS). BKG's DC is one of altogether three primary IVS Data Centers. According to the IVS rules we are responsible to accept the recognized VLBI data from all IVS components: other Data Centers, Operation Centers, Network Stations, Correlators, Analysis Centers and Combination Centers, and provide them as open access. At this moment, access to our server is supported by File Transfer Protocol over Secure Socket Layer (FTPS) and Hypertext Transfer Protocol Secure (HTTPS). The principle of the open access is empowered by anonymous downloads over both protocols. The IVS users are offered to receive an account as described at our web-page (https://ivs.bkg.bund.de/) to upload data. In July 2022, FTPS and HTTPS access

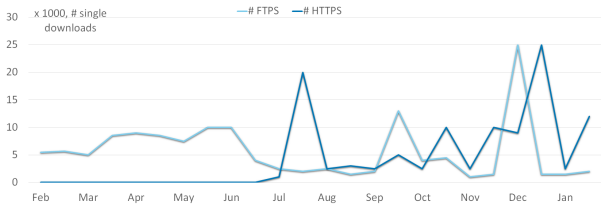

Fig. 1 Monthly Downloads of Files

have been arranged as the available data access. As it can be seen in Figure 1, the amount of downloads has dropped at first. But after a few months, the sum of FTPS and HTTPS downloads has reached approximately the same level as before the switch. In order to sync the data sets with the other official IVS DCs, mirroring procedures are set up. The exchange between the official DCs is established by providing new data in a designated directory (i.e., labelled RECENT) in scheduled intervals. The entire data center is reviewed weekly by comparing the file lists between BKG DC and CDDIS.

2 Set-Up and Testing of the Ingest Software

For the data management of the IVS DC, the ingest software is used (D. Behrend et al, 2022, D. Behrend et al(2022)).

Every received file is recognized in the same way: either uploaded by a user or retrieved from the other IVS DC as arranged in the incoming area for the external access environment shown in Figure 2.

The ingest software is continuously developed in cooperation with its developer and user – CDDIS. The use of the ingest software is extended to OPAR as well. Once the necessity of a change in the ingest software appears, it is reported and discussed at the regular IVS DC Meetings. The course of actions to fix the change in the software is defined at the meetings as well: from understanding how to handle the change to the moment when the IVS DCs should make an update. In order to introduce updates, internal and external environments are set up at BKG. Set-up and testing are implemented at BKG by making use of the same ingest software. In the internal access environment, a new version of ingest is tested against a black and a white list of files to verify the changes based on the test data as shown in Figure 2. After successful testing, the new ingest version is incorporated in the internal access integration environment as shown with the left arrow in Figure 2, where the same data as in the production environment is in place for testing. Finally, the new version is released in the external access production environment as shown with the right arrow in Figure 2 at the moment as defined at IVS DC meetings, so that a simultaneous update of the ingest software is implemented at all three IVS DCs.

3 File Processing

The file processing is structured in three major steps, which will be performed after the file is uploaded and moved into a dedicated working directory. After the very first security check (step 1), some basic formal checks are performed (step 2). Finally, a more specific formal validation is run (step 3) before the file is stored in the archives. As soon as the single file is placed in the appropriate location of our archive, it is available for the user access.

Both formal check routines are governed by the ingest software as shown in Figure 3:

(1) Each file is scanned to check for suspicious content as shown in the orange block in Figure 3, and will be quarantined (red block) if required. A separate workflow is added for Level 1 Data (i.e., SWIN files) due to the huge file size: an archived data can be extracted securely and quarantined if a single file is marked as suspicious. In the current data set of about 13 TB, a small amount of SWIN archives had to be checked manually because of false positive detections.
(2) Next, some basic and sanity checks shown in blue box in Figure 3 are run by the ingest software. Each file is verified: if it is already available at the DC and its name matches the Name Convention. The file content is marked as erroneous, if invalid characters are found or the content is empty. In addition to these basic checks, some more sanity checks are made, i.e., checks against the master file content and internal keywords. In particular, it is ensured that the file names of vgosdb and SINEX files as given by the master file version 1 are accepted for

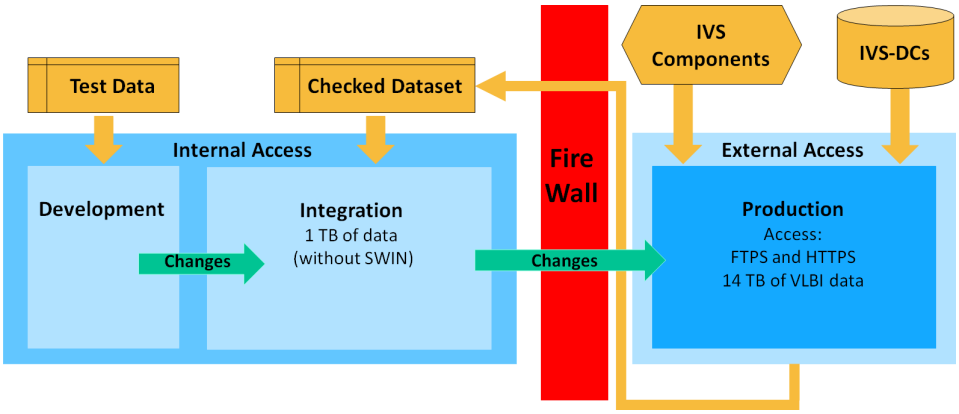

Fig. 2 Scheme of IVS-DC Set-Up, testing and production. The data are received and processed in production within the external access environment as shown on the right side of the firewall. The data testing part is maintained behind the firewall in the internal test environment (left side of the firewall). The approved updates are pushed to the production area.

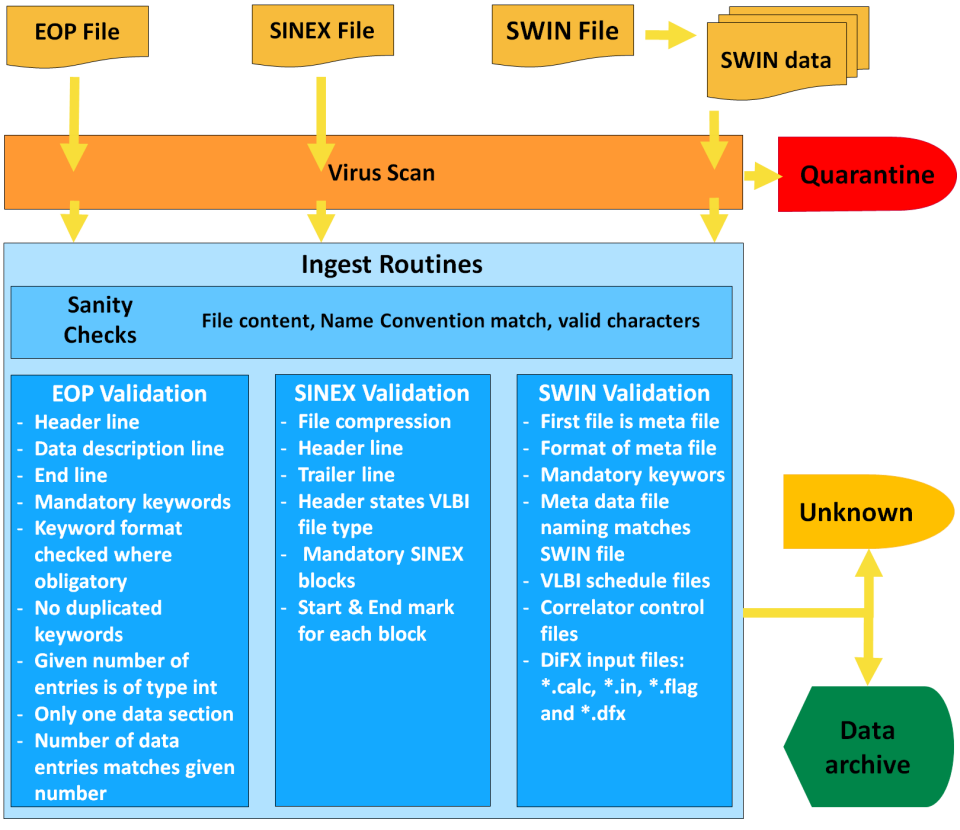

Fig. 3 File Processing is unified with ingest software. The procedure scheme is shown in detail for EOP, SINEX and SWIN files.

name	code	start	DOY	DUR	stations	sked	corr	status	DBC	SUBM	vdc_vgos	asi2023a
ivs-r4	r41104	2023-05-25 18	145	24:00	HbHtKeKkMaNsNyWwWz -Ft	usno	wash	wt_med	xe	usno	--	--
ivs-r1	r11104	2023-05-22 17	142	24:00	AgHbHtKeKvMcNsNyOn -FtNt	nasa	bonn	in_prog	xa	nasa	--	--
ivs-r4	r41103	2023-05-18 18	138	24:00	HtKeKkSvUrWwZc -Ft	usno	wash	ready	xe	usno	2023-05-31 23	2023-06-05 15
ivs-r1	r11103	2023-05-15 17	135	24:00	BdHbHtKeKkNsNySvWzZc -AgFt	nasa	bonn	20230530	xa	nasa	2023-05-30 12	2023-06-05 15

Fig. 4 The prototype of the table for monitoring the entire production chain within the IVS is shown. The column "asi2023a" is an example to illustrate the fact, that the SINEX file was uploaded for this session by ASI AC. A SINEX file of another AC will be presented in the additional column on the right once it is available.

sessions observed prior to 2023, and by version 2 only for the files afterwards (Ch. Dieck., 2023, Ch. Dieck.(2023)), e.g., vgosDB:
version 1 for 20FEB01XA.tgz
version 2 for 20230101-i23001.tgz

(3) The final processing step is strictly dependent on the file type. The file content is validated, e.g., the verification of EOP, SINEX and SWIN files is shown in Figure 3. Generally, the content is checked to have a proper file format and particular entries: header and end lines, keywords or certain files, if it is SWIN format. In more detail, the three blocks in Figure 3 describe the specific validation aspects of EOP, SINEX and SWIN files accordingly.

4 Outlook

Aside from the continuously updated ingest software, our further development is committed to the information service. For this reason, an automated email notification is sent in the test mode in that cases only, in which the ingest software has raised an issue.

Additionally, we design an enrichment of the information contained in the master file, e.g., the availability status of each data file and corresponding product at our data center. An overview of each session from scheduling to the final IVS products are intended to be accessible on the interactive basis, i.e. down to the level of all files provided by all ACs as the IVS combined products. The corresponding prototype is rather limited as seen in Figure 4 at this earlier stage and available for internal use only. The prototype table is shortened in this preview in Figure 4, where the column "asi2023a" represents only one IVS Analysis Center (AC), which delivers SINEX, while the whole prototype table tracks the SINEX files of each IVS AC showing which files are available at the data centers for the corresponding session.

Besides, the consistency check is planned to be executed on a daily basis instead of the weekly cadence that is applied at the moment. In order to enhance the performance of this process, the comparison by means of hash sums is to be implemented.

References

Behrend, D. (2022) Data Ingest at the IVS Data Centers, https://space-geodesy.nasa.gov/docs/2022/GM2022_behrend_ingest.pdf.

Dieck, Ch. (2023) IVS-analysis mail: Implementing the change to the new vgosDB naming convention, 07 January 2023.

A. Girdiuk, M. Goltz, D. Thaller (2022), IVS Data Center at BKG, IVS General Meeting 2022 Proceedings.

Close-Range photogrammetry for antenna deformation measurements

A. Greiwe, R. Brechtken, M. Lösler, C. Eschelbach, G. Kronschnabl, C. Plötz, A. Neidhardt

Abstract The knowledge of gravitational deformations at the receiving unit of VLBI antennas is one of the crucial components in achieving the GGOS accuracy goal of 1 mm in position on a global scale. Various geodetic methods for measuring the object geometry of the antenna's receiving unit are known such as terrestrial laser scanning (TLS) or close-range photogrammetry to cite but a few. The advantage of a photogrammetric approach compared to surface measurements by a single TLS station is the complete coverage of the surface by varying camera positions. Unlike the TLS-approach, surface points potentially shaded by structural elements are also captured in a photogrammetric survey.
Moreover, for signalized targets and under optimal conditions, close-range photogrammetry achieves an accuracy of up to 5 μm + 5 ppm. Due to the high accuracy requirements, a photogrammetric approach was chosen for the deformation measurements of the legacy 20 m Radio Telescope Wettzell (RTW) for the first time. To realize an advantageous photogrammetric block geometry configuration, a remote controlled unmanned aerial vehicle (UAV) was used as sensor platform. Signalized targets mounted at the receiving unit of the RTW were measured in ten elevation positions to investigate elevation dependent deformations. In each elevation position, image data were captured at least twice to obtain redundant and almost independent data sets. Up to five flights were performed in selected elevation positions using different camera systems. This contribution presents the results of the photogrammetric analysis of this extensive data material.

Keywords Close-range photogrammetry, Gravitational deformation, Radio telescope, VLBI

Ansgar Greiwe · Rainer Brechtken
Laboratory for Photogrammetry, Department of Geodesy, Bochum University of Applied Sciences, Am Hochschulcampus 1, 44801 Bochum, Germany

Michael Lösler · Cornelia Eschelbach
Laboratory for Industrial Metrology, Faculty 1: Architecture, Civil Engineering, Geomatics, Frankfurt University of Applied Sciences, Nibelungenplatz 1, 60318 Frankfurt am Main, Germany

Gerhard Kronschnabl · Christian Plötz
Geodetic Observatory Wettzell, Federal Agency for Cartography and Geodesy, Sackenrieder Straße 25, 93444 Bad Kötzting, Germany

Alexander Neidhardt
Geodetic Observatory Wettzell, Forschungseinrichtung Satellitengeodäsie, Technical University of Munich, Sackenrieder Straße 25, 93444 Bad Kötzting, Germany

1 Introduction

The goal of the Global Geodetic Observing System (GGOS) is a positional accuracy of 1 mm on global scales (Rothacher et al., 2009). For that purpose, the sources of error limiting the global results must be quantified. In addition, appropriate strategies must be developed to avoid or at least to reduce these errors. The knowledge of gravitational deformations at the receiving unit of VLBI antennas is one of the crucial components in achieving the GGOS accuracy goal. To emphasize this topic, the International VLBI Service for Geodesy and Astrometry (IVS) has adopted the resolution "Surveys of radio telescopes for modeling of gravitational deformation" in 2019. Investigations at radio telescopes participating in the VLBI Global

Observing System (VGOS) network show only minor deformations at the receiving unit (Lösler et al., 2019). In contrast, studies on legacy radio telescopes show significant deformations of up to several centimeters, which lead to systematic errors (Sarti et al., 2009). Therefore, investigations on legacy radio telescopes should be priorised. To compensate for gravitational deformations, the elevation-dependent deformation behaviour must be determined with a suitable measurement procedure.

For this study, the deformation behavior of the Radio Telescope Wettzell (RTW) at the Geodetic Observatory in Wettzell, which was commissioned in 1983, was investigated for the first time. The main reflector is designed as a rotationally symmetric paraboloid and has a diameter of 20 m. The apex of the main reflector is located at about 12 m above the ground. The aim was to investigate the geometry of the receiving unit under different load case changes, i.e. when the telescope orientation changes between 5° and 90° in elevation.

2 Method

To estimate the deformation of the main reflector surface at different elevation positions of the telescope, a terrestrial laser scanner (TLS) could be gimbaled near the subreflector on its struts (Holst et al., 2017; Bergstrand et al., 2019). By this measurement method, the surface of the main reflector is captured with an accuracy of about 1.5 mm (Holst et al., 2017). However, the subreflector is shaded by the instrument and additional equipment is required to obtain its variations.

As an alternative measurement method, close-range photogrammetry offers the possibility of measuring individual, signalized targets (Luhmann et al., 2019). Here, the targets are captured in several images from different camera positions. By applying a bundle adjustment the coordinates of the measuring targets are determined. Additionally, the camera parameters of the interior orientation are estimated by a simultaneous calibration. A local coordinate system is defined by a reference body with predefined targets as control points. The scaling of the individual local coordinate system is realized by scalebars.

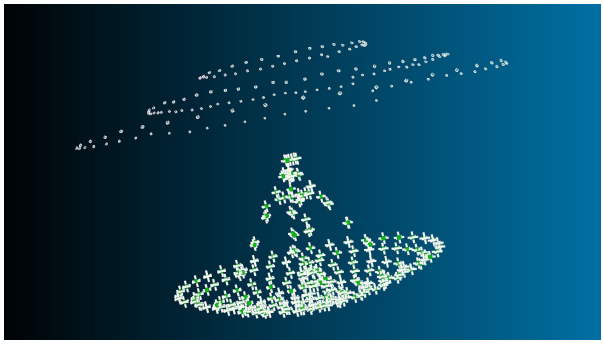

Fig. 1 Image block configuration with three concentric circles of varying camera positions around the main reflector.

Under optimal conditions and depending on the measurement volume, single point accuracies can be up to 5 µm+5 ppm (Luhmann et al., 2019).

2.1 Image Block Configuration

Prerequisite for a successful and accurate photogrammetric determination of measurment targets is the complete enclosure of the measuring volume by varying imaging positions. For imaging the surface of the main reflector and the subreflector, regulary distributed imaging positions are advantageous in which the camera moves on a circular path concentrically around the main axis of the telescope (see figure 1). Different radii of the concentric circles and varying distances of the individual circles (see table 1) from the main reflector also improve the resulting image block geometry.

This image block configuration are logistically difficult to realize with a crane as camera platform in positions of more than 40° elevation of the telescope due to the pickup height above ground and the circular path around the telescope. In order to be able to realize the required circular image block configuration for the entire elevation range of the telescope, an Unmanned Aerial Vehicle (UAV) was used at Wettzell for the first time instead of a crane as a camera platform.

The flight trajectory of the UAV was planned with three concentric circles (see figure 1). In addition to the distances to the apex of the main reflector, the radii and flight speeds were chosen in a way to meet the flight time of about 12 minutes. The number of images taken during a single flight was limited by the frame

rate of the cameras which were up to five seconds (see table 1).

Table 1 Image block configuration

Circle	Radius [m]	Distance [m]	# Images	Speed [m/s]
1	16	25	48	0,4
2	11	22,5	64	0,2
3	6	20	36	0,2

In this measurement campaign an individually configured hexacopter with a diameter of 1.8 m and a take-off weight of about 10 kg was used (see figure 2). This custom made UAV is a modular system and thus has individual gimbals that allow changing the camera systems to be used. Equipped with two 10,000 mAh batteries, the UAV's flight time is between 12 minutes (1,500 g) and 15 minutes (400 g), depending on the weight of the camera system.

In addition to manual control by the pilot, the UAV has a semi-autonomous flight mode, which is essentially supported by GNSS and a barometric altitude measurement. A flight trajectory can be defined by a waypoint script. For each waypoint, a flight speed, dwell time at the waypoint, camera triggering and UAV orientation can be specified by an ASCII file. During the flight, the UAV is continuously aligned to a Point of Interrest (POI), which in this case is located approximately at the position of the subreflector. In this way, the horizontal alignment of the camera and the triggering of the images is automated, only the vertical alignment of the camera has to be controlled manually by the pilot.

2.2 Camera System

During flight, the UAV generates high-frequency vibrations, which affect the gimbal and thus also the camera. To avoid a rolling shutter effect which results in an image blur, the use of lenses with a central shutter is obligatory. Systems with an electronic or a hardware rolling shutter are unsuitable. In addition, prime lenses with a fixed focal length are preferable to zoom lenses with a variable focal length, as these have a higher optical imaging quality, which has a positive effect on the point measurement accuracy in the images.

Fig. 2 UAV with Sigma camera (foreground, left) and Sony a7R (mounted in gimbal)

UAV-suitable camera systems do not have the geometric stability of a metric camera due to their modular design. Thus, the parameters of the interior orientation have to be determined by a simultaneous calibration within the bundle adjustment. In order to stabilize the focal length and the principal point position at least for a short time, a stable mounting of the used lens, a deactivated image stabilizer and a manual focus adjustment are mandatory.

Table 2 Camera systems used

Camera	Lens	Sensor Size	Footprint@15m	GSD@15 m
Sony a7R	50 mm	24 mm x 36 mm	7,2 m x 10,8 m	1,1 mm
Sigma DP2	30 mm	16 mm x 24 mm	8,0 m x 12,0 m	2,5 mm
Sigma DP3	50 mm	16 mm x 24 mm	4,8 m x 7,2 m	1,5 mm

Three camera systems that fulfill the above criteria were available for the present study (see figure 2). The requirement for a fixed sensor-lens combination is best met by the Merrill series from Sigma. The Sigma Merrill comes with different prime lenses, each permanently mounted. Thus, each focal length leads to its own model (see table 2). Due to this concept, the lenses of this camera series have no variable components except for the focusing lens, and the cameras also lack an image stabilizer.

In contrast, the Sony a7R has a bayonet mount and thus allows the selection of suitable prime lenses. For this study, a Carl Zeiss Loxia prime lens was used (see table 2). This particular lens has neither image stabilizer nor autofocus; aperture and focus are set man-

ually. Additionally, the image stabilizer of the camera sensor was deactivated during photogrammetric imaging.

2.3 Photogrammetric measurements

For photogrammetric imaging, the object was equipped with 169 targets, which were evenly distributed on the main reflector surface. 14 bit coded black and white targets were used for an automated recognition of the unique point ID. The targets were arranged in seven concentric circles on the main reflector. 16 targets were placed on the tube in the center of the main reflector and six targets were placed on the subreflector.

In addition, a cross with six targets was mounted on the subreflector as a reference body. On the struts of the subreflector 44 targets and the scale bars were fixed (see figure 3). The telescope elevation positions were then changed from 5° to 90° in 10° increments, and each of these elevation positions was observed at least twice. Frame rate and the weight of the camera system were considered for individual flight time calculation to ensure capturing at least 200 images.

Fig. 3 Coded targets on the telescope (main and subreflector as well on struts and tube in the center)

Within the measurement campain 37 flights were carried out at the telescope, here the flights were numbered chronologically. Up to flight number 5 the Sony a7R was used, followed by 19 flights with the Sigma DP3. From flight number 25 the Sigma DP2 was used. Flight number 3 and 4 with the Sony a7R have too few images for a successfull bundle adjustment. Thus 35 data sets were available for further analysis.

3 Results

3.1 Effects of camera change and image block configuration

The reason for the change of the camera systems during the measurement campaign was the different image measurement accuracy (Sony a7R 200 µm, Sigma DP3 100 µm and Sigma DP2 50 µm), which led to a different standard deviation in line of sight of the telescope (z-axis). In Figure 4 it can be seen that the Sony a7R was able to realize the most image shots per flight. Consequently, there are the most image measurements per point compared to the other cameras. This usually leads to a high geometric stability of the image composite. However, due to the low image measurement accuracy of the camera system, the reliability of the points is not satisfactory.

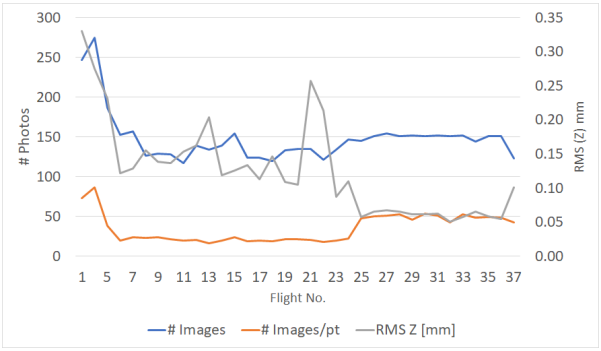

Fig. 4 Effect of the camera selection on the image block accuracies (flight 1-5 Sony a7R, 6-24 Sigma DP3, from 25 Sigma DP2)

As an alternative, the Sigma DP3 was used in the further course of the measurement campaign, which realizes an identical sampling rate on the object surface due to the same focal length as the Sony a7R. However, due to the considerably smaller sensor compared to the Sony a7R, the footprint on the object is smaller. A point on the main reflector is thus imaged in significantly fewer images of the Sigma DP3 than in case of the Sony a7R. Nevertheless, the better image measurement accuracy leads to a better RMS(Z) (see figure 4).

However, taking a closer look at flights 6 to 24, it shows that the RMS(Z) varies greatly from image block to image block in different elevation positions. It is assumed that the image block configuration of the Sigma DP3 has a slightly unstable geometry and thus cannot be reliably evaluated.

In contrast to the Sigma DP3, the Sigma DP2 uses the same sensor size (APS-C) but a smaller focal length (30 mm instaed of 50 mm, see table 2). Thus, the sampling rate at the object is lower and the image measurement of a point is less accurate. However, the image blocks 25 to 37 show a much better RMS(Z). Only the results of the last flight (37), which was performed in the elevation position 5°, are worse. Here the influence of the incomplete block configuration is clearly visible. According to Greiwe et al. (2020), in the upright position of the main reflector of the telescope the UAV cannot fly the planned full circles shown in figure 1. Thus, the resulting configuration is suboptimal and leads to a larger RMS(Z).

3.2 Combined processing of image blocks

Due to the change of camera, more than the planned two flights per elevation position of the telescope were available for the deformation analysis. In some elevation positions of the telescope, up to five flights were evaluated separately in order to derive the focal length of the paraboloid. The differences between the camera systems proof the previously determined single point accuracies (see figure 5).

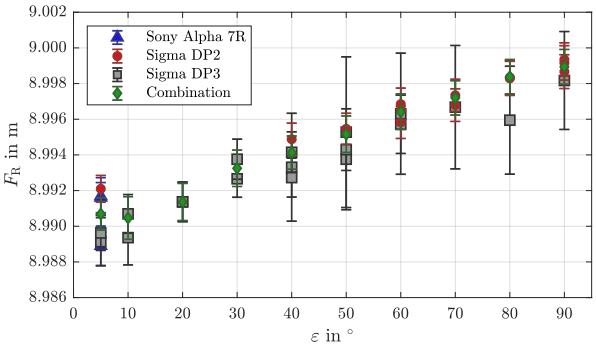

Fig. 5 Estimated focal lengths depending on the elevation position, marked according to the camera system used. The combined solution is shown in green.

For the determination of the elevation-dependent deformation behavior of the rotationally symmetric paraboloid, the data sets were combined on the observation level, i.e. during the bundle adjustment. For each elevation position, all available image sets were processed in a common bundle adjustment. The data of the different camera systems were modeled by the use of separate camera models. Here the parameters of the interior orientation were adjusted in a simultaneous calibration. The results of the combined evaluation is shown in the figure 5. The estimated focal length increases by about 9 mm while the telescope rotates upwards from 5° to 90°.

3.3 Movement of the subreflector

In this campaign, the subreflector was also equipped with targets (see figure 6). Since these were also coded, they were easily identified in further processing of the individual elevation positions and the movement of the subreflector was determined. A displacement of the subreflector relative to the apex of the rotation paraboloid was detected.

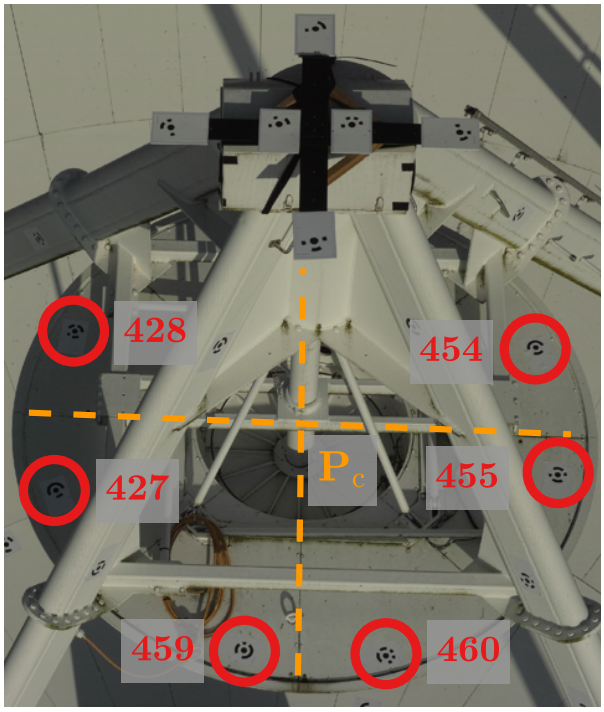

Fig. 6 Coded targets on the subreflector.

The subreflector moves along the main axis contrary to the focal length with increasing elevation position towards the vertex (see figure 7). In addition, however, a tilting of the subreflector also was detected.

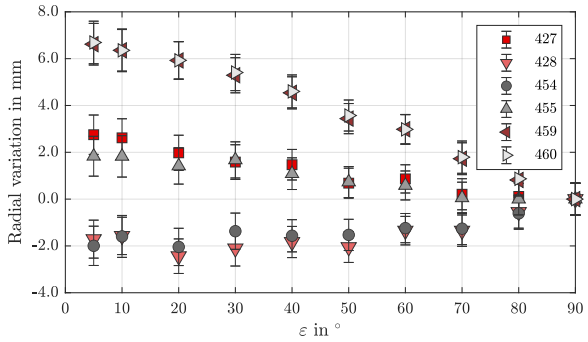

Fig. 7 Elevation-dependent variations i.e. tilt and shift of the subreflector.

4 Conclusions and outlook

Within the scope of the investigations it turned out that the selection of the camera has a large influence on the accuracy of the object points. The number of images and the image footprint, respectively the number of image measurements per object point are decisive. It is suspected that the block geometry (recording arrangement, see figure 1) also has an influence on the results and can be improved in future studies.

In previous studies, the achieved accuracies of the individual flights were much more constant over the different elevation positions (Lösler et al., 2019). Based on the results of the present investigation, Lösler et al. (2022) derived a correction function that compensates for gravitationally induced deformations of the RTW.

References

Bergstrand S, Herbertsson M, Rieck C, Spetz J, Svantesson C.G., Haas, R. (2019) A gravitational telescope deformation model for geodetic VLBI. *Journal of Geodesy*, 93(5), 669–680, doi: 10.1007/s00190-018-1188-1.

Greiwe A, Brechtken R, Lösler M, Eschelbach C, Haas R (2020) Erfassung der Hauptreflektordeformation eines Radioteleskops durch UAV-gestützte Nahbereichsphotogrammetrie. Kersten TP (ed.):*40. Wissenschaftlich-Technische Jahrestagung der DGPF*, 29, 346-357.

Holst C, Schunck D, Nothnagel A, Haas R, Wennerbäck L, Olofsson H, Hammargren R, Kuhlmann H (2017) Terrestrial Laser Scanner Two-FaceMeasurements for Analyzing the Elevation-Dependent Deformation of the Onsala Space Observatory 20-m Radio Telescope's Main Reflector in a Bundle Adjustment. *Sensors*, 17(8), 1833, 1–21, doi: 10.3390/s17081833.

Lösler M, Haas R, Eschelbach C, Greiwe A (2019) Gravitational Deformation of Ring-Focus Antennas for VGOS - First Investigations at the Onsala Twin Telescopes Project. *Journal of Geodesy*, 93(10), 2069–2087, doi: 10.1007/s00190-019-01302-5.

Lösler M, Eschelbach C, Greiwe A, Brechtken R, Plötz C, Kronschnabl G, Neidhardt A (2022) Ray tracing-based delay model for compensating gravitational deformations of VLBI radio telescopes. *Journal of Geodetic Science*, 12(1), 165–184 doi: 10.1515/jogs-2022-0141.

Luhmann T, Robson S, Kyle S, Boehm J (2019) Close-Range Photogrammetry and 3D Imaging. de Gryter, Berlin, 3. Edition.

Rothacher M, Beutler G, Behrend D, Donnellan A, Hinderer J, Ma C, Noll C, Oberst J, Pearlman M, Plag H-P, Richter B, Schöne T, Tavernier G, Woodworth P.L. (2009) The future Global Geodetic Observing System. *The Global Geodetic Observing System. Meeting the Requirements of a Global Society on an Changing Planet in 2020*, 237–272, doi: 10.1007/978-3-642-02687-49.

Sarti P, Luca Vittuari L, Abbondanza C (2009) Laser Scanner and Terrestrial Surveying Applied to Gravitational Deformation Monitoring of Large VLBI Telescopes' Primary Reflector. *Journal of Surveying Engineering*, 135(4), 136–148, doi: 10.1061/(ASCE)SU.1943-5428.0000008.

Atmospheric parameters derived from VGOS sessions observed with the Onsala twin telescopes

R. Haas, G. Elgered

Abstract We compare the atmospheric parameters derived from the analysis of VGOS sessions that were observed with the Onsala twin telescopes to the corresponding results derived from co-located GNSS stations and a ground-based microwave radiometer at Onsala. The focus is on the first four VGOS Research & Development sessions, observed in 2021 and 2022, aimed at testing scheduling strategies with short scan length in order to obtain a good local sky coverage. The data analysis of all three techniques allows a high temporal resolution of 5 min for the atmospheric parameters. We find high correlation (0.97) for the zenith total delays of the three techniques, and pair-wise weighted root mean square difference on the order of 4–10 mm. The linear horizontal delay gradients are less well correlated (0.4–0.5) and have pair-wise weighted root mean square differences in the sub-mm range.

Keywords VGOS, GNSS, WVR, ZTD, gradients

1 Introduction

The VLBI Global Observing System (VGOS) was designed to achieve one order of magnitude improvement in accuracy and precision for the derived geodetic parameters, compared to the legacy S/X system (Petrachenko et al., 2009). To reach this goal, a number of areas of improvement were identified in the VGOS design phase. One aspect of major concern was turbulence that is affecting the signal delay in the neutral atmosphere (Nilsson and Haas, 2010). One outlined strategy to address this effect is to improve the spatial and temporal sampling of the signal delay introduced by the atmosphere, i.e. more observations per unit of time and in many different local directions. This is implemented by using radio telescopes that move fast in azimuth and elevation, e.g. the Onsala twin telescopes (OTT) (Haas et al., 2019).

During 2021 and 2022 a series of VGOS Research & Development (VR) sessions were scheduled to address the aspect of high spatial and temporal sampling of the local atmosphere. Observatories that are equipped with VGOS stations and co-located instrumentation for other space geodetic and remote sensing techniques, such as Global Navigation Satellite Systems (GNSS) and ground-based microwave radiometers, often called water vapour radiometers (WVR), are perfect sites to assess this new VGOS strategy.

The Onsala Space Observatory (OSO) inaugurated the twin telescopes in 2017. They have been operational in the IVS VGOS observing program since 2019 (Haas et al., 2019). In the following we refer to these two stations as O13E for ONSA13NE and O13W for ONSA13SW. OSO operates also several co-located GNSS stations, including the two stations ONSA and ONS1 that are part of several networks, e.g. the IGS. Additionally, there is a continuously operating WVR at OSO. The VLBI, GNSS, and WVR instruments are co-located within about 600 m distance, thus sharing the local atmosphere at the site. A comparison of the atmospheric parameters derived from the different techniques therefore is a suitable way to assess the accuracy of VGOS when using high spatial and temporal resolution.

Rüdiger Haas · Gunnar Elgered
Chalmers University of Technology, Department of Earth, Space and Environment, Onsala Space Observatory, SE-439 92, Onsala, Sweden

2 Data set

We focus on the first four VR sessions that were observed in 2021 and 2022. These sessions were scheduled using the *VieSched++* software (Schartner and Böhm, 2019) with the aim to generate observing plans with as short as possible scan length in order to achieve as many as possible scans in as many as possible local directions. Doing so, a very dense sampling of the local atmosphere at the participating VGOS stations should be achieved.

Table 1 provides an overview of these first four VR sessions in 2021 and 2022, and the instrumentation operated during these sessions. While both VGOS stations were available for VR2101 and VR2202, unfortunately only one each could participate in VR2022 and VR2203. The two GNSS stations were operating during all four VR sessions, and the WVR was operating during three out of four VR sessions.

Table 1 Overview of the instrumentation operating at OSO during the first four VR sessions in 2021 and 2022.

Session	Date	O13E	O13W	ONSA	ONS1	WVR
VR2101	2021-07-29/30	√	√	√	√	√
VR2201	2022-01-20/21	√	√	√	√	
VR2202	2022-03-17/18	√		√	√	√
VR2203	2022-05-19/20		√	√	√	√

3 Data analysis

We analyzed the VGOS database of the above mentioned four VR sessions with the *ASCOT* software (Artz et al., 2016) using a least-squares analysis and following the analysis strategy used for the IVS ITRF2020 analysis (Gipson, 2020). We applied the VMF3 mapping functions (Landskron and Böhm, 2018) and included data to a minimum elevation cutoff of 5^{o}. The locally observed pressure, from the VLBI logfiles, was the basis for the Zenith Hydrostatic Delays (ZHD). Then Zenith Wet Delay (ZWD) corrections and total linear horizontal gradients (GRAD) were estimated with 5 min temporal resolution using loose constraints. The GRAD parameters were expressed as east (GRE) and north (GRN) components. The a priori ZHD and estimated ZWD were added to calculate the Zenith Total delays (ZTD). The results for O13E and O13W have basically the same formal errors, see Tab. 2.

The data recorded with the co-located GNSS stations ONSA and ONS1 were analysed with the GipsyX software (Bertiger et al., 2020). The analysis used multi-GNSS data, i.e. GPS, Galileo, and GLONASS, with the precise point positioning (PPP) approach (Zumberge et al., 1997). Two daily RINEX-files each were analysed together in order to achieve continuity of the results over day boundaries. A minimum elevation angle cutoff of 7^{o} was used and the VMF3 mapping functions (Landskron and Böhm, 2018) were applied. ZHD were modelled using standard pressure values, while ZWD corrections and total GRAD were estimated with 5 min temporal resolution using loose constraints. As for the VGOS case, the final ZTD were calculated by adding the a priori ZHD and the estimated ZWD. The formal errors of the result derived for both GNSS stations are very similar, see Tab. 2.

The WVR data were observed in a sky-mapping mode and analyzed with an in-house software. An elevation angle cutoff of 25^{o} was used for an unconstrained least-squares analysis (Elgered et al., 2019) with a 5 min temporal resolution. In contrast to VGOS and GNSS is the WVR not sensitive to hydrostatic delays. Thus, the derived atmospheric parameters from the WVR are pure ZWD and pure wet linear horizontal gradients (GRAD-W). In order to be able to compare the WVR results to the results from VGOS and GNSS, ZHD and hydrostatic horizontal gradients (GRAD-H) needed to be added to the WVR results of ZWD and GRAD-W so that the comparisons finally could be done on the basis of ZTD and GRAD. We calculated ZHD based on the locally recorded pressure data at Onsala and added these to the WVR-derived ZWD. For the gradients, we added VMF3-referred horizontal hydrostatic gradients (VMF data server, 2022) that are based on the ERA-Interim numerical weather model data to the WVR-derived gradients. Information on the formal errors for the WVR-derived parameters are provided in Tab. 2

Table 2 Median formal errors of the ZTD (σ_{ZD}) and GRAD (σ_{GE}, σ_{GN}) results derived from VGOS, GNSS, and WVR analysis.

Session	VGOS			GNSS			WVR		
	σ_{ZD}	σ_{GE}	σ_{GN}	σ_{ZD}	σ_{GE}	σ_{GN}	σ_{ZD}	σ_{GE}	σ_{GN}
VR2101	1.61	0.35	0.35	1.42	0.23	0.26	0.37	0.15	0.16
VR2201	1.13	0.24	0.23	1.44	0.24	0.28	–	–	–
VR2202	1.15	0.23	0.25	1.43	0.23	0.25	0.20	0.09	0.10
VR2203	1.08	0.22	0.24	1.42	0.26	0.27	0.30	0.13	0.15

To do a meaningful comparison of the ZTD from VGOS, GNSS and WVR, their values need to be referred to the same reference height. We chose the common reference height to be the GNSS reference point of the station ONSA. Thus, we applied corresponding height corrections (Rothacher et al., 2011), since the reference points of the different instruments are at different heights. However, for the GRAD parameters, no further corrections were needed.

4 Comparisons of atmospheric parameters

OSO operated its VGOS twin telescopes, several GNSS stations, and a WVR, during the four VR sessions. However, only during VR2101 all five instruments were operated, while for the other VR sessions only four out of five could not be operated, see Tab. 1. Nevertheless, we had the possibility to compare all three techniques, VGOS, GNSS and WVR, for three out of the four VR sessions.

In the following, we present several steps of comparisons. We start with the VGOS-internal comparison using VR2101 and VR2201. Then we present the GNSS-internal comparison using all four VR sessions. Finally, we perform the three-technique comparisons with the VR sessions where all three techniques were operated. Here we focus on one station each for VGOS and GNSS, respectively, to be representative for the corresponding technique and to be compared to the WVR results.

4.1 VGOS-internal comparisons

Both VGOS stations, O13E and O13W, participated in VR2201 and VR2202. The derived ZTD and GRAD results agree well. Statistical information in terms of correlation coefficient ρ, offset δ, and standard deviation σ, after subtracting the offset, is provided in Tab. 3. The correlation coefficients are 0.99 for the ZTD, and at least for VR2101 also above 0.93 for the gradients. The low GRAD correlation for VR2201 is simply because there were no significant variations in the gradients during the session. The offsets and standard deviations are all less than or on the order of the formal errors.

Table 3 Statistical information on the agreement of the results derived from VGOS stations O13E and O13W in terms of correlation coefficient ρ, offset δ (O13E-O13W), and standard deviation σ after subtracting the offset.

Session	ZTD			GRE			GRN		
	ρ	δ mm	σ mm	ρ	δ mm	σ mm	ρ	δ mm	σ mm
VR2101	0.99	-0.59	0.73	0.93	-0.05	0.20	0.94	-0.05	0.17
VR2201	0.99	-0.51	0.98	0.54	0.02	0.24	0.53	-0.07	0.34

4.2 GNSS-internal comparisons

The GNSS stations ONSA and ONS1 were operated during all four VR sessions. As for VGOS, the level of agreement between the results derived from the two stations is as expected very high. Statistical information in terms of correlation coefficient ρ, offset δ (ONSA-ONS1), and standard deviation σ after subtracting the offset, is provided in Tab. 4. The correlation coefficients for ZTD are all 0.98 or higher. The ZTD offsets on the order of 2–3 mm are detected, which might indicate that the correction for the height difference between the stations needs to be revisited. The remaining standard deviations after removing the offsets are slightly larger than the formal errors. The correlation coefficients of the GRAD parameters are not as high and vary between the VR sessions. Values of up to 0.79 are seen, and the lowest ones relate to VR2201, the same VR session where the GRAD parameters had low correlation coefficients. Offsets for GRAD parameters are insignificant, and the remaining standard deviation after removing the offsets are about twice as large as the formal errors.

Table 4 Statistical information on the agreement of the results derived from GNSS stations ONSA and ONS1 in terms of correlation coefficient ρ, offset δ (ONSA-ONS1), and standard deviation σ after subtracting the offset.

Session	ZTD			GRE			GRN		
	ρ	δ mm	σ mm	ρ	δ mm	σ mm	ρ	δ mm	σ mm
VR2101	0.99	-1.92	1.78	0.79	0.03	0.47	0.70	0.01	0.42
VR2201	0.99	-2.94	2.06	0.26	-0.12	0.44	0.39	0.04	0.44
VR2202	0.98	-3.42	1.83	0.56	-0.04	0.41	0.75	0.04	0.46
VR2203	0.99	-2.64	1.81	0.67	-0.01	0.44	0.65	0.01	0.49

4.3 VGOS-GNSS-WVR comparisons

For three out of the four VR sessions all three techniques, i.e. VGOS, GNSS, and WVR, could be compared. The ZTD times series are presented in Fig. 1. These graphs show that the VGOS and GNSS results for ZTD follow each other very nicely, including small features variations. It also is visible that the WVR for some periods deviated a bit, e.g. in the second half of VR2101 (top plot) and around 21:00–00:00 during VR2203 (bottom plot), possibly due to high amounts of liquid water and/or less accurate calibrations. It appears that session VR2202 provided the most reliable results from the WVR. As an example, we therefore present the GRAD time series of VR2202 in Fig. 2. The GRAD parameters agree well and also here the small features are picked up by all three techniques.

Table 5 summarizes the average statistical agreement between the three techniques. This is expressed as average values for correlation coefficient (ρ) and the weighted root mean square (wrms) deviation. The average for the correlation coefficients for ZTD is 0.97 for all three pairwise comparisons. The average correlation coefficients for the gradient parameters are about 0.4 but do not reach 0.5 for any of the three pairwise comparisons. The highest value is seen for the north gradient for the comparison of VGOS and GNSS. Both space geodetic techniques reach just 0.42 and 0.44 as correlation coefficient for GRN and GRE when comparing to WVR. We see that the average ZTD wrms for the space geodetic techniques is of the order of 4 mm, while the ZTD wrms difference between the space geodetic techniques and the WVR are of the order of 10 mm. Also for the gradients we see lower wrms values for the comparison of the space geodetic techniques than when comparing the space geodetic techniques with the WVR. However, in all comparison cases, the wrms for the GRAD parameters are sub-mm.

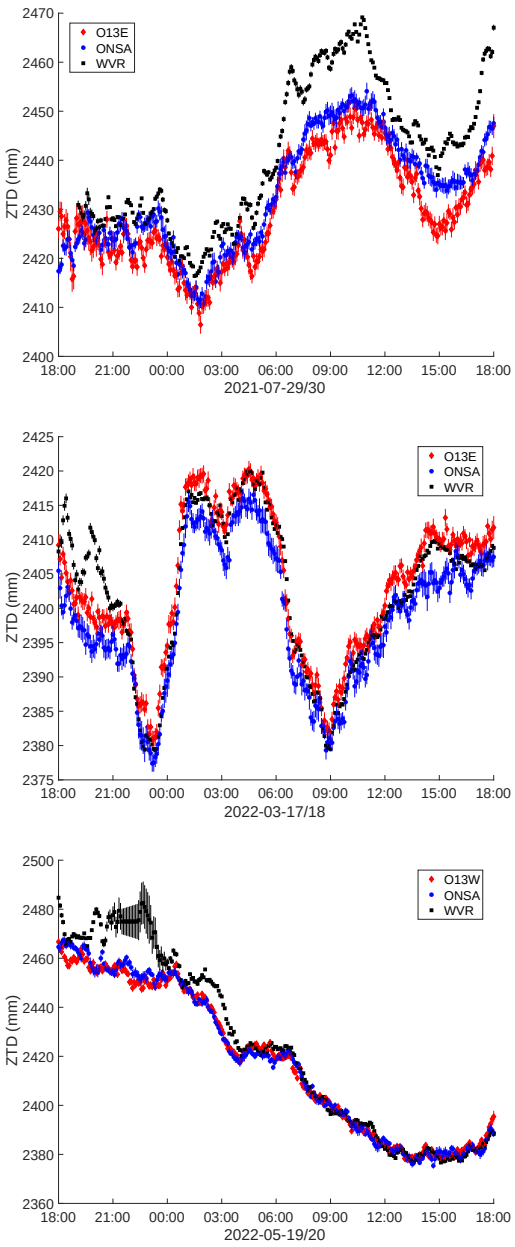

Fig. 1 Time series of ZTD derived from VGOS (red), GNSS (blue) and WVR (black) for VR2101 (top graph), VR2202 (middle graph) and VR2203 (bottom graph).

5 Conclusions and outlook

We compared atmospheric parameters in terms of ZTD and GRAD results for four VR sessions observed in 2021 and 2022. The focus was on simultaneous observations with the co-located instrumentation at Onsala, including two VGOS stations, two GNSS stations, and a WVR. Results for ZTD and GRAD could be determined from independent analyses with an identical temporal resolution of 5 min. To achieve such a high sampling with VGOS was possible thanks to the special scheduling of the VR sessions, aiming as short scan length and high number of well distributed observations. The comparison of the results reveals that the ZTD of all three tech-

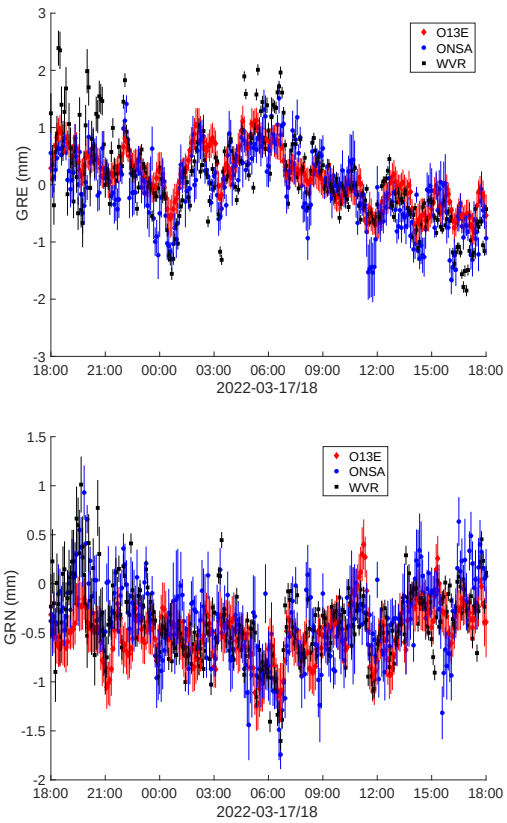

Fig. 2 Time series of gradients GRE (top) and GRN (bottom) derived from VGOS (red), GNSS (blue) and WVR (black) for VR2202.

Table 5 Statistical information on the agreement of the results derived from VGOS, GNSS and WVR. Listed are average values for correlation coefficient (ρ), and average weighted root-mean square (wrms) deviation.

	ρ	WRMS (mm)	ρ	WRMS (mm)
ZTD	GNSS		WVR	
VGOS	0.97	4.04	0.97	10.47
GNSS	–	–	0.97	9.89
GRE	GNSS		WVR	
VGOS	0.44	0.58	0.44	0.87
GNSS	–	–	0.44	0.95
GRN	GNSS		WVR	
VGOS	0.47	0.50	0.42	0.87
GNSS	–	–	0.42	0.87

niques show very high correlation, but still suffer from so-far unexplained offsets on the order of 5–10 mm. The results for gradient parameters are less well correlated and have offsets in the sub-millimetre range. As expected the two space geodetic techniques agree in general slightly better than each one of them agrees with the WVR.

We focused on only four VGOS sessions and thus suffer from a low number of data points. A larger data set is needed in order to draw further conclusions. Thus, we plan to perform similar analyses with as many as possible VGOS sessions observed at Onsala. Also different analysis approaches need to be tested, e.g. different temporal resolutions and constraints.

References

Artz T et al. (2016) ivg::ascot: Development of a new vlbi software package. In: Behrend, Baver, Armstrong (eds) *IVS 2016 General Meeting Proceedings*, **NASA/CP-2016-219016**, 217–221, https://ivscc.gsfc.nasa.gov/publications/gm2016/045_artz_etal.pdf

Bertiger W et al. (2002) GipsyX/RTGx, a new tool set for space geodetic operations and research. *ASR*, 66(3), 469–489, doi:10.1016/j.asr.2020.04.015

Elgered G et al. (2019) On the information content in linear horizontal delay gradients estimated from space geodesy observations, *AMT*, 12, 3805–3823, doi:10.5194/amt-12-3805-2019

Gipson J (2020) IVS Checklist for ITRF2020. https://ivscc.gsfc.nasa.gov/IVS_AC/ITRF2020/ITRF2020_checklist_v2020Jan13.pdf

Haas R et al. (2019) Status of the Onsala twin telescopes – two years after the inauguration. In: Haas, Garcia-Espada, Lopez Fernandez (eds) *Proc. 24th EVGA working meeting*, ISBN: 978-84-416-5634-5, 5–9.

Landskron D, Böhm J (2018) VMF3/GPT3: refined discrete and empirical troposphere mapping functions. *J Geod*, 92, 349–360, doi:10.1007/s00190-017-1066-2

Nilsson T, Haas R (2010) Impact of atmospheric turbulence on geodetic very long baseline interferometry. *JGR* 115(B3), doi:10.1029/2009JB006579

Ning T, Elgered G (2021) High-temporal-resolution wet delay gradients estimated from multi-GNSS and microwave radiometer observations. *AMT*, 14, 5593–5605, doi:10.5194/amt-14-5593-2021

Petrachenko B et al. (2009) Design aspects of the VLBI2010 system. **NASA/TM-2009-214180**

Rothacher M et al. (2011) GGOS-D: homogeneous reprocessing and rigorous combination of space geodetic observations. *J Geod*, 85(10):679–705, doi:10.1007/s0019 0-011-0475-x

Schartner M, Böhm J (2019) VieSched++: A New VLBI Scheduling Software for Geodesy and Astrometry. *PASP*, 131:084501, doi:10.1088/1538-3873/ab1820

re3data.org: VMF Data Server; editing status 2020-12-14; re3data.org - Registry of Research Data Repositories, doi:10.17616/R3RD2H

Zumberge J F et al. (1997) Precise Point Positioning for the efficient and robust analysis of GPS data from large networks. *JGR*, 102(B3), 5005–5017, doi:10.1029/96JB03860

Investigating software specific dependencies within the intra-technique VLBI combination

H. Hellmers, S. Modiri, S. Bachmann, D. Thaller, M. Bloßfeld, M. Seitz

Abstract The IVS Combination Centre generates and releases combined VLBI products for the International VLBI Service for Geodesy and Astrometry (IVS). The solutions are generated session-wise by applying an intra-technique combination of the individual contributions provided by multiple IVS Analysis Centres (AC). For the twice-per-week R1/R4 combination, typically eleven different ACs provide 24-h VLBI sessions with station coordinates, source positions and Earth Orientation Parameters (EOP) in form of datum-free normal equations (NEQ) stored in SINEX files. As the same software packages are used by various ACs (e.g. Calc/Solve by five ACs), the question arises whether the combined solution is potentially dominated by these contributions. Consequently, the software specific modelling might impact the estimated EOP and station coordinates. In this contribution, we study the impact of such software dependencies on combined parameters due to identical software packages.
Therefore, the developments of the accuracies of individual and combined solutions have been investigated. In addition, an alternative weighting strategy based on a software specific sub-combination is established. In order to assess the quality of the individual components of the combination, the internal comparisons of the estimated EOP with respect to various combination scenarios are performed.

Hendrik Hellmers · Sadegh Modiri · Sabine Bachmann · Daniela Thaller
Federal Agency for Cartography and Geodesy (BKG), Department Geodesy, Frankfurt am Main, Germany

Mathis Bloßfeld · Manuela Seitz
Deutsches Geodätisches Forschungsinstitut – Technische Universität München (DGFI-TUM), Munich, Germany

Keywords VLBI, Combination Centre, analysis software, Earth Orientation Parameter, VLBI combination

1 Introduction

The Combination Centre of the International VLBI Service for Geodesy and Astrometry (IVS; Nothnagel et al (2017)) is operated in cooperation between the Federal Agency of Cartography and Geodesy (BKG) and the Deutsches Geodätisches Forschungsinstitut at TU München (DGFI-TUM; Bachmann et al (2019)). Its tasks comprise the generation of a combined VLBI product using individual contributions of different Analysis Centres (AC), accompanied by a quality control (Bachmann et al (2012)) of the resulting parameters (Earth Orientation Parameters, station coordinates), and, finally, the release of the combination results as official IVS products.

In this context, the IVS Combination Centre performs a combination of session-based contributions of the IVS Analysis Centres on the level of normal equations (NEQ; Böckmann et al (2010b); Vennebusch et al (2007)). The tasks at BKG include format checking, outlier detection as well as comparisons with products provided by the International Earth Rotation and Reference Systems Service[1] (IERS). The official combination products are submitted to the IERS and released on the official website of the IVS Combination Centre.

For the routinely performed IVS combination, typically up to eleven different ACs provide individual contributions as datum-free NEQs in SINEX file format[2]. At

[1] https:www.iers.org

[2] Solution (Software/technique) INdependent EXchange Format Version 2.02 (December 01, 2006)

the moment, six different software packages are used by the IVS ACs.

As one of the software packages is used by various ACs (Calc/Solve[3]), this paper focuses on potential software specific dependencies that influences the corresponding combined solution. In this context, earlier studies already tried to find a conclusive answer: an investigation about assumed correlations between the contributions of individual IVS ACs have been carried out by Böckmann et al (2010a). In addition, Kutterer et al (2009) and Schmidt et al (2015) investigated the impact of identical observation data within an intra-technique combination process. In extension to these studies, we would like to investigate the following questions within this paper:

- Is the combined solution dominated by the Calc/Solve software package?
- Does specific modelling and solution setup (i.e., the so-called "'operator impact"') lead to independent Calc/Solve contributions?
- Is a software specific downscaling of each contribution necessary?

In order to assess the quality of the individual parameters of the combination, internal comparisons of various combination scenarios of the estimated EOP are carried out.

2 Contributions by the IVS Analysis Centres

For the operational IVS combination, the individual ACs provide 24-hour session-wise VLBI data twice per week, i.e. for the so-called R1 and R4 sessions. The contributions are provided in SINEX format containing datum-free normal equations with a parameterisation of all five EOP as well as station coordinates. Most of the ACs additionally provide source positions in their SINEX files. The atmospheric and clock specific parameters have been reduced previously. The guidelines for the homogeneous analysis are provided by the IVS Analysis Coordinator[4].

In the recent years, the different ACs provide re-processed data for the ITRF2020 computation (Hellmers et al, 2022). This includes all 24-hour sessions from the year 1979 until the end of 2020 as well as 39 VGOS sessions within the time span 2017 until 2020. Allover about 6,600 sessions were provided to the IVS Data Centre, which stores all published VLBI data and solutions. For this reprocessing effort, altogether eleven ACs took part.

Table 1 Analysis Centres contributing to IVS combination in the framework of the reprocessing for ITRF2020.

AC	Name	Software
ASI	Italian Space Agency	CALC/SOLVE
BKG	Federal Agency for Cartography and Geodesy	CALC/SOLVE
DGF	Deutsches Geodätisches Forschungsinstitut at TU München	DOGS-RI
GFZ	German Research Centre for Geosciences	PORT
GSF	Goddard Space Flight Center	CALC/SOLVE
NMA	Norwegian Mapping Authority	Where
OPA	Observatoire de Paris	CALC/SOLVE
OSO	Onsala Space Observatory	ASCOT
USN	United States Naval Observatory	CALC/SOLVE
VIE	Vienna University of Technology	VieVS

Table. 1 summarizes the different ACs and the applied software packages, respectively. The goal of the combination is to benefit from the diversity of contributions and improve the quality of estimated parameters compared to the individual solutions provided by the ACs.

Within the combination process, a variance component estimation (VCE) leads to individual weighting factors for scaling each contribution to the same variance level. This method takes into account the individual and the combined solution and delivers global variance factors as estimates for the a priori variance factor. The weighting factors are then defined as the inverse values of the resulting variance factors. The final combination is performed by stacking each individual re-weighted NEQ.

However, as the Calc/Solve software package is represented five times, it might potentially dominate the combined solution. In the following, an analysis of software specific dependencies is carried out, which investigates in detail the impact of the Calc/Solve based contributions on the combination. For that, data of the most recent 16 years have been considered consisting of two parts: the reprocessed ITRF2020

[3] https:spacegeodesy.nasa.govtechniquestools calc_solvecalc_solve.html

[4] https:ivscc.gsfc.nasa.govIVS_ACIVS-AC_contact.htm

contributions (covering the years 2007–2020), and the newly processed sessions for the years 2021 and 2022.

3 Results

For our investigations on software-specific dependencies, the datum free NEQs provided via SINEX files for the years 2007 until the end of 2022 have been taken into account. From Table 1 it becomes clear, that the corresponding combination includes five Calc/Solve based and five non-Calc/Solve based contributions, so that the AC contributions can be grouped into two subsets.

Table 2 Subsets of combination scenarios.

Subset	Analysis Center	Software
1	ASI, BKG, GSF, OPA, USN	CALC/SOLVE
2	DGF, GFZ, NMA, OSO, VIE	different

For that, Fig. 1 and Fig. 2 depict the internal consistency of each AC subset, which describes the amount of deviation of each individual solution w.r.t. the corresponding combination.

The WRMS values of dUT1 and polar motion are in the range of 2 μs and 40 μas, respectively, for the Calc/Solve scenario, and in the range of 4 μs and 50 μas for the non-Calc/Solve scanario. Hence, the individual solutions of the Calc/Solve based contributions are closer to each other than the solutions

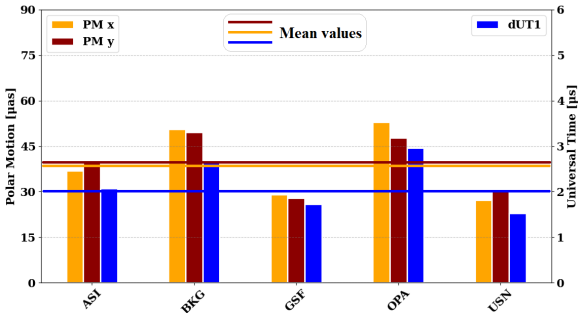

Fig. 1 WRMS of Calc/Solve based individual AC contributions w.r.t. the corresponding combined solution (based on this subset of ACs only).

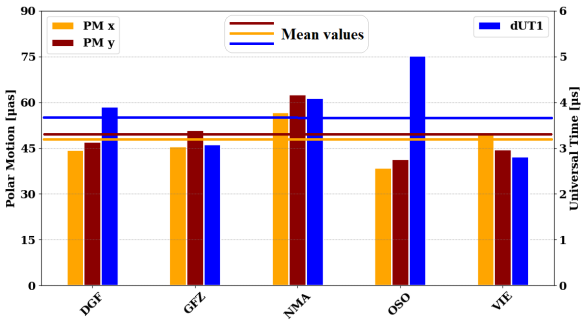

Fig. 2 WRMS of non-Calc/Solve based individual AC contributions w.r.t. to corresponding combined solution (based on this subset of ACs only).

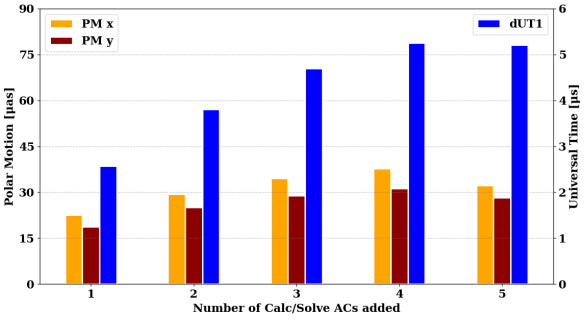

Fig. 3 WRMS of IVS combination depending on the number of Calc/Solve contributions. The combined solution of non-Calc/Solve based contributions serves as reference.

of the different software packages. This behaviour is expected.

In order to get more detailed information about the impact of Calc/Solve based contributions on the combined solution, we investigate different combination scenarios where the number of Calc/Solve based AC contributions are added step-by-step to the combination of the five non-Calc/Solve contributions. The combination scenarios are listed in Table 3. Fig. 3 shows how the consistency w.r.t. the combined solution evolves for the different combination scenarios. It can be seen that the WRMS values depend on an increasing number of Calc/Solve ACs w.r.t. the non-Calc/Solve based combined solutions.

Scenario 1 is characterized by a WRMS of approx. 20 μas for polar motion and 2.5 μs for dUT1. Contrary, when adding four Calc/Solve based AC contributions, the WRMS values rise up to 30–40 μas for polar motion and 5 μs for dUT1. This means an increase of 60–

Table 3 Combination scenarios. The number of Calc/Solve contributions is increased.

number	added ACs
ref	DGF, GFZ, NMA, OSO, VIE
1	+ ASI
2	+ ASI, BKG
3	+ ASI, BKG, GSF
4	+ ASI, BKG, GSF, OPA
5	+ ASI, BKG, GSF, OPA, USN

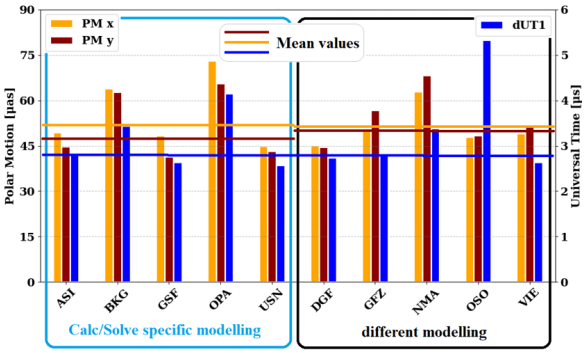

Fig. 4 WRMS of the individual solutions w.r.t. the internal combined solution.

70 %, showing the impact of including an ascending number of Calc/Solve based contributions within the combination.

In addition to that, Fig. 4 depicts the internal consistency of the individual solutions w.r.t. the entire combined solution. It shows a similar level of accuracy for the Calc/Solve-only and the non-Calc/Solve based contributions. For both types of AC selections, the mean WRMS values are in the range of 50 μas for polar motion and 3 μs for dUT1.

However, although variations of the different error bars can be recognized within both AC subsets, a significant impact of Calc/Solve-based contributions cannot be recognized. Obviously, the impact of the individual setup and modelling from the operator leads widely to independent Calc/Solve-based contributions for the session SINEXes investigated here.

This conclusion can also be confirmed by looking at the consistency between the combinations of both AC subsets. Fig. 5 shows the ERP differences between the Calc/Solve-only and the non-Calc/Solved based combination results. The 90-days-moving-median filter leads to a more smooth waveform. A summary of offsets

Table 4 Offsets and drifts between Calc/Solve-only and non-Calc/Solve combination.

parameter	offset	drift
dUT1	-3.1 μs	0.5 μs/y
PM x	-5.5 μas	0.1 μas/y
PM y	0.7 μas	2.5 μas/y

and drifts is given in Table 4. The offsets between both types are in the range of μs and μas and are hence not significant. Merely a small drift can be recognized for dUT1 and the y-direction of polar motion. This manifests the statement, that both types of AC subsets lead to similar combination results. Even the drifts must be focused on in further works.

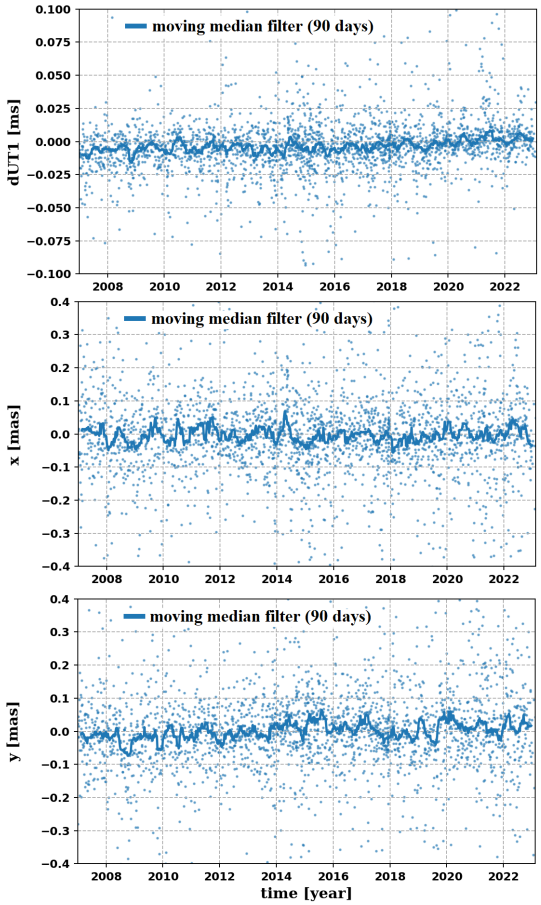

Fig. 5 Calc/Solve-only combination vs. non-Calc/Solve combination.

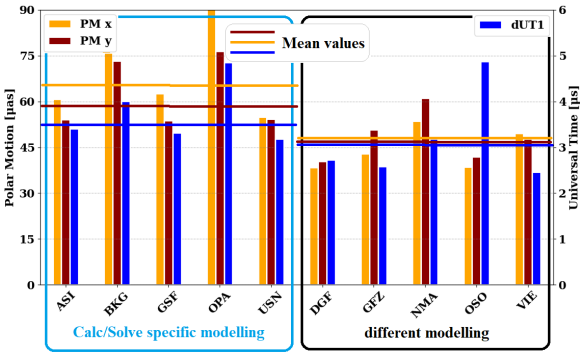

Fig. 6 WRMS of all individual contributions by applying a software-specific downscaling.

In order to complement the study on potential software dependencies, we wanted to investigate whether a dedicated downscaling of the contributions based on the identical software package is necessary and / or beneficial. In this scenario the Calc/Solve based contributions have been scaled equally by:

$$\sum_{AC} \frac{SC_{AC}}{n} = Calc/Solve \tag{1}$$

with $AC = \{ASI, BKG, GSF, OPA, USN\}$.

This procedure leads to a unique Calc/Solve contribution with weight one. This strategy is based on a weighted pre-combination of the Calc/Solve-based contributions before the actual combination process. The resulting pre-combined NEQ is then considered as a contribution of one single AC, and - in addition to the remaining NEQs - subject to a VCE. This alternative weighting strategy down-scales the Calc/Solve-based contributions proportionally to their appearance within the combination.

The effect of such a software-specific downscaling is shown in Fig. 6. It can be seen that this scenario leads to a higher level of WRMS values for the Calc/Solve-based contributions. In summary, this behaviour confirms that the "operator impact" leads widely to independent Calc/Solve contributions, so that a downscaling is not necessary.

4 Conclusions and outlook

In this contribution, we investigated the impact of software specific modelling and setup on the combined solution within the intra-technique VLBI combination. For generating official IVS products, at the current state ten Analysis Centres deliver SINEX files containing NEQs to the IVS Data Centre, where five of the ACs are applying the Calc/Solve software package for their VLBI analysis. Hence, the combined solution is in danger of being dominated by these contributions. Thus, the question arises whether the dominance of one software package really biases the combination or whether the contributions can be treated as independent even if they ares based on the same software package.

Investigating a potential impact on the combined product, different combination scenarios have been carried out with a subset of sessions covering the most recent 16 years. In the first step, a higher internal consistency of the Calc/Solve-based contributions in comparison to the different modelling could be demonstrated.

In addition to that, further scenarios confirm the impact of the Calc/Solve-based contributions. The WRMS values of the ERPs rise in the range of 60 - 70 % with an ascending number of Calc/Solve-based contributions added to the combination.

Finally, we show the WRMS values of the individual solutions within the overall combination. It could be shown that the internal consistencies for the Calc/Solve ACs and the non-Calc/Solve ACs are similar. The mean WRMS values are in the range of 50 μas and 3 μs for polar motion and dUT1, respectively, for both types of AC subsets. Consequently, the domination of Calc/Solve-based contributions within the combined solution could not be recognized. This statement could also be confirmed by comparing the combination of both AC subsets. The corresponding offsets are in the range of few μs and μas, thus, they are not significant. However, the appearing drifts must be investigated closer in further studies.

In addition, we showed that a software specific down-scaling leads to a lower level of accuracy for the Calc/Solve based contributions and is thus not recommended.

In conclusion, a software specific domination of the combined solution could not be proven. Fortunately,

the “operator impact” (modelling, setup) of the different ACs leads widely to independent Calc/Solve contributions.

In future studies, investigations about software specific dependencies will be extended. At the moment, two additional software packages (i.e., Where and VieVs) are used by more than one IVS AC for the operational contributions. Further studies will aim to look at the impact of these multiplication of software contributions. In addition, the appearing drifts between the Calc/Solve and non-Calc/Solve based combination will be focused on.

References

Bachmann S, Lösler M, Messerschmitt L, Schmid R, Bloßfeld M, Thaller D (2012) Ivs combination center at bkg - robust outlier detection and weighting strategies. International VLBI service for geodesy and astrometry pp 266–270

Bachmann S, Hellmers H, Schneider-Leck S, Geist S, Thaller D, Bloßfeld M, Seitz M (2019) Bkg/dgfitum combination center 2019+2020 biennial report. International VLBI Service for Geodesy and Astrometry 2020

Böckmann S, Artz T, Nothnagel A (2010a) Correlations between the contributions of individual ivs analysis centers. In: Proceedings of the Sixth General Meeting of the International VLBI Service for Geodesy and Astrometry

Böckmann S, Artz T, Nothnagel A (2010b) Vlbi terrestrial reference frame contributions to itrf2008. Journal of Geodesy 84(3):201–219

Hellmers H, Modiri S, Bachmann S, Thaller D, Bloßfeld M, Seitz M, Gipson J (2022) Combined ivs contribution to the itrf2020. Springer

Kutterer H, Krügel M, Tesmer V (2009) Towards an improved assessment of the quality of terrestrial reference frames. In: Geodetic Reference Frames: IAG Symposium Munich, Germany, 9-14 October 2006, Springer, pp 67–72

Nothnagel A, Artz T, Behrend D, Malkin Z (2017) International VLBI Service for Geodesy and Astrometry: Delivering high-quality products and embarking on observations of the next generation. Journal of Geodesy 91(7):711–721

Schmidt M, Göttl F, Heinkelmann R (2015) Towards the combination of data sets from various observation techniques. In: The 1st International Workshop on the Quality of Geodetic Observation and Monitoring Systems (QuGOMS'11) Proceedings of the 2011 IAG International Workshop, Munich, Germany April 13–15, 2011, Springer, pp 35–43

Vennebusch M, Böckmann S, Nothnagel A (2007) The contribution of very long baseline interferometry to itrf2005. Journal of Geodesy 81:553–564

VLBI signals transmitted from Earth orbiting satellites

Ö. Karatekin, H. Sert, V. Dehant, B. Ritter, H. Vasseur, U. Hugentobler

Abstract Creating an absolute space-tie where all the geodetic methods are onboard is the key for an improved and stable terrestrial reference frame as well as with various scientific applications. Such satellite concepts have already been proposed to achieve an accurate and stable terrestrial reference frame. Next generation Galileo satellites can provide a single well-calibrated platform for the colocation of the space-based geodetic techniques establishing precise and stable ties between the key geodetic techniques. One of the most crucial and novel aspect of such concepts is the VLBI transmitter (VT) which will emit quasar-like signals from the space to be observed by the VLBI ground stations. VT can directly link the terrestrial and celestial reference frames and bring the unique features of VLBI technique to an Earth orbiting satellite. In the context of call for future Galileo payloads a novel VT has been under development. Here, we present the progress on ongoing ESA study for VT for Galileo as well as for other future missions.

Keywords VLBI, VLBI transmitter, space-tie

Özgür Karatekin · Hakan Sert · Veronique Dehant · Birgit Ritter
Royal Observatory of Belgium

Huegs Vasseur
AntwerpSpace

Urs Hugentobler
Technical University of Munich

1 Introduction

Global Navigation Satellite System (GNSS), Doppler Orbitography and Radiopositioning Integrated by Satellite (DORIS), Satellite Laser ranging (SLR) and Very-long Baseline Interferometry (VLBI) are the main space-geodetic techniques to define accurate and stable International Terrestrial Reference Frame (ITRF). In addition, VLBI allows the realisation of International Celestial Reference Frame (ICRF) and Earth orientation parameters including the rotation angle (UT1 – UTC). Each geodetic technique is traditionally linked by so called 'local-ties'. Due to the scarcity of local-tie number as well as their accuracy (Altamimi et al. , 2016; Altamimi, Z. , 2008; Glaser et al. , 2015), combining the techniques onboard spacecraft is a promising candidate to create an accurate and continuous link between different geodetic techniques (Pollet et al. , 2023).

Galileo satellites allow already the use of GNSS and SLR methods and discussed in several studies (Thaller et al. , 2011, 2014; Zoulida et al. , 2016; Bury et al. , 2021). An additional VLBI transmitter onboard next generation Galileo satellites can offer an opportunity to benefit unique capabilities of VLBI technique to immediate referencing of the Galileo orbits to the ICRF through differential measurements with respect to quasars. VT would allow direct determination of the absolute orientation of the satellite constellation with respect to the ICRF and the improvement of the ITRF. It may also enable other scientific experiments such as improved relativity parameter determination, time-transfer experiments, ionospheric determination and modelling. Several mission concepts like GRASP (Nerem et al. , 2011) and E-GRASP (Biancale et al. , 2017) with VT have already been proposed to achieve

an accurate and stable terrestrial reference frame. Recently, ESA FutureNAV programme included one component to implement the GENESIS mission, consisting of the collocation, for the first time ever, of the four space-based geodetic techniques (GNSS, VLBI, SLR and DORIS) onboard a single well-calibrated satellite establishing precise and stable ties between the key geodetic techniques. This aims to result in a unique dynamic space geodetic observatory combined with the measurements of geodetic collocation techniques stations on Earth, would contribute to improving ITRF.

Feasibility of VT onboard earth orbiting satellites including the compatibility with existing VLBI network, traditional VLBI processing and scheduling have been the subject of several recent studies; frame transformations between GNSS and VLBI (Plank et al. , 2017; Anderson et al. , 2018), performance of onboard Galileo VT for scheduling and estimation of the ascending node of the orbit (Wolf et al. , 2022), transferring UT1-UTC (Sert et al. , 2022) and technical feasibility (Jaradat et al. , 2021).

A VT, compatible with the accommodation constraints onboard a Galileo satellite, performance of the receiving stations as well as with the ITU regulations in all transmission frequency bands is currently under development for consideration of Galileo second generation satellites. The VT prototype for G2G has been developed within the frame of the Call for Ideas “H2020-ESA-038 GNSS Evolutions Experimental Payloads and Science Activities”. The main objectives are:

- to improve the ties between different space geodetic techniques (GNSS, VLBI and SLR Retro-Reflectors.
- to contribute to the establishment of accurate and long-term stable reference frames (Inertial and Terrestrial) and to the absolute orientation of the Galileo constellation in inertial space, since VLBI is the only technique that has an access to International Celestial Reference Frame (ICRF).

In the next sections we provide the details of the VT mission concept, its design and technical specifications.

2 VT Mission Concept

The mission concept for the VT relies on the observations by the IVS (International VLBI Service) network stations. The IVS network currently consists of more than 30 stations with additional about 15 cooperating stations, mainly VLBA (Very Long Baseline Array) stations as well as DSS (Deep Space Station). The network is further extended in the framework of the VGOS (VLBI Global Observing System) project. The VGOS aims to extend IVS observation operations to 24 hours and 7 days per week in the future and to extend the observation bands from S and X to a band from 2 to 14 GHz to increase the accuracy of the products.

The Depth-of-Coverage (DoC) is shown in Figure 1. It displays the number of IVS stations that can be seen for a Galileo satellite located above a given geographical position for different networks. For all corresponding figures an elevation cutoff angle of 5° was used. The figures in the top are based on the CONT17 network of 14 stations (left) and on the typical R1 session with 9 stations (right). The bottom figures are based on all stations with more than 500,000 observations in the past 20 years (left): for a total of 27 stations, with cooperating VLBA stations included; (right): for only 17 IVS stations.

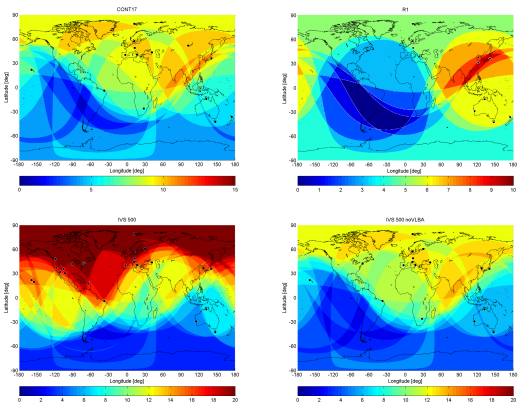

Fig. 1 (Top) Galileo Depth of Coverage (DoC) for different IVS networks: top left: CONT17, top right: typical R1 session, bottom left: all stations with more than 500,000 observations in 20 years, bottom right: same but without VLBA stations

it would be possible to schedule Galileo VT observations together with quasar observations in regular IVS sessions since all IVS telescopes are mechanically

capable to track Galileo satellites that are moving at an angular speed below 1 arcmin/sec. In operational mode the VT transmitter can be permanently switched on and can be scheduled by IVS for observation with high flexibility for experimental measurement campaigns and for routine sessions. Alternatively, the VT can be on only during time periods for which observations are scheduled by the IVS network.

3 VT Design

The VT instrument is designed to be:

- Compatible with the VLBI Global Observation System (VGOS) as well as legacy VLBI stations, in terms of frequency, bandwidth, signal type and power spectral flux density at ground level.
- Compliant with ITU Radio Regulations.
- Maximizing the transmitted bandwidth for better measurement resolution.
- Simultaneous transmission in ≥ 2 frequency bands for ionospheric correction

The basic function of the VT equipment is to broadcast of low power spectral density wideband signals at different frequencies between 2 and 14 GHz. It includes two main aspects: the transmitted waveforms and the simultaneous transmission at multiple frequencies.

The VT is designed to transmit simultaneously up to four wideband signals with a power spectral flux density of less than few Jansky ($1Jy = 10^{-26}W/m2/Hz$) at the surface of the Earth which is compatible with VLBI ground stations and compliant with ITU regulations. The ITU Radio Regulations limit quite drastically the power flux density (PFD) that can be generated either at the surface of the Earth or at the geostationary satellite orbit, in the frequency ranges available for the VT application or in adjacent frequency ranges. The VT is designed so that from switch on until switch off, it is capable to transmit RF signals continuously, with a duty cycle of 100%.

Table 1 shows the signal characteristics of the VT compliant with ITU Radio Regulations. The transmitted signals is designed to be as wideband as possible, because the bandwidth directly impacts the resolution of the VLBI measurements. The transmitted waveforms therefore occupy as much as possible the complete bandwidth available in each frequency band.

Frequency band	Frequency range $[MHz]$	Center Frequency $[MHz]$	Occupied bandwidth $[MHz]$
S-	3100-3300	3200	200
C-	5250-570	5410	320
Low X	8200-8400	8300	200
High X	9200-9700	9450	500

Table 1 Signal characteristics of the VT

4 VT Technical Specifications

The VT is composed of two subsystems: the Electronic Box that generates the RF signals and the Antenna Subsystem that ensures the transmission of the RF signals to the VLBI ground stations. The two subsystems are connected by coaxial cables.

The Electronic Box ensures the generation of the two different types of waveforms: the white noise or deterministic pseudo-noise signal, intended for "standard" VLBI measurements as with quasars and the spread spectrum signal with a pseudo random sequence based on the Galileo master clock and aligned with the Galileo PPS, intended to provide an additional clock tie on one hand and to enable single-station VLBI measurements on the other hand. The generation of the latter waveform type requires external input signals (Galileo master clock and Galileo PPS). The former type of quasar-like signals will allow to be captured by VLBI ground stations and be conveniently implemented into the traditional pipeline of VLBI correlating and processing chain. The white noise is identical to thermal noise at a high temperature.

The pseudo-noise datastream is generated in an FPGA (Field-programmable gate array) for reasons of flexibility and re-programmability in course of the activity. The polarisation of the emitting antenna is Left Hand Circular Polarization (LHCP, IEEE specification). The spurious emissions (spurs, harmonics, intermodulation products, redundant spectral images, etc.) generated by the VT shall be at least 60 dB below the relevant signal power, for each operating band. As most of the VLBI bands sit right next to ITU protected bands, it is necessary to ensure band protection via filtering. VT relies on the analogue filters to ensure suppression of out-of-band spurious emissions since the separations between VLBI and ITU bands demand steep filters digital filters with arbitrary steepness are also considered.

At time of preliminary design, the transmit output filters were assessed, looking at technology, manufacturing and their performance in terms of insertion loss, in-band return loss and adjacent frequency band protection. The purpose of these output filters is indeed to reject out-of-band spurious and harmonics. Figure 2 shows the insertion loss measurements for S- and X bands respectively where y- axis is magnitude in dB. The preliminary filter parameters here varies from the signal properties in Table 1 updated later during the project. Based on the preliminary tests, it was possible to adopt and refine the filter specification for transmit filters to be integrated in the updated design. For all of four bandwidths manufacturing repeatability were concluded to be satisfying.

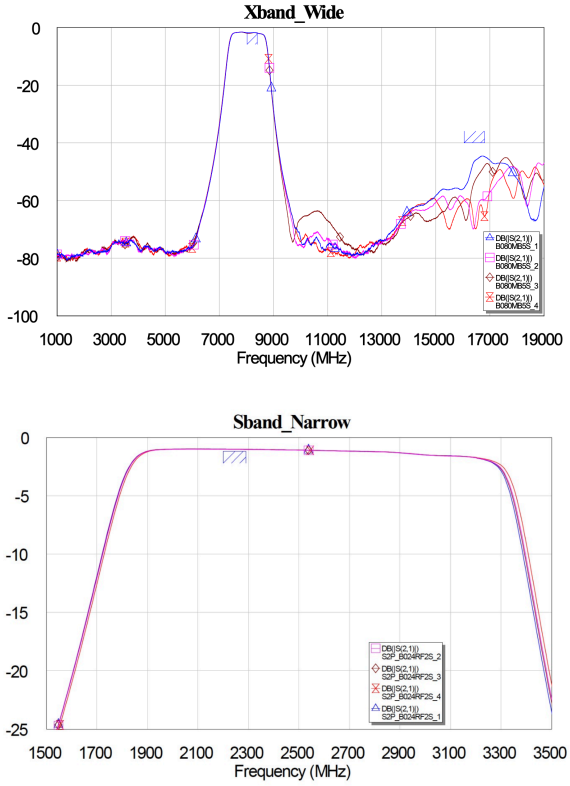

Fig. 2 (Top) X-band bandpass filter wideband insertion loss measurement of four different samples. Filter re-insertion will not attenuate third harmonic content, the amplifier is designed not to have gain higher than 15 GHz.(Bottom) S-band bandpass filter narrowband insertion loss measurement of four different samples.

The second waveform of VT is pseudo-random noise based on the onboard clock -master clock of Galileo satellite(s) in the context of the design- in addition to an internal clock. Having internal clock available, avoiding complete instrument incapability without an external clock dependency. Indeed, when an external clock signal is presented to the VT instrument, the internal clock source will automatically phase/frequency align to the master clock source and it can track the Galileo reference frequency with an Allan Deviation contribution better than 10^{-15} for $\tau = 1000s$. The pseudo-random noise generator is being implemented in an FPGA device. The pseudo-random sequence waveform consists of a spread-spectrum signal which mimics the autocorrelation property of white noise. Two types of waveforms are envisaged for this purpose: a BOC(40,20) signal or a Glonass signal.

The modulating waveform of the Glonass signal is a pseudo-random ranging code while BOC(m,n) is a binary offset carrier modulation. While the Glonass signal has most of its spectral energy concentrated around the carrier frequency (Top in Figure 3), the BOC-modulated signal has low energy around the carrier frequency and two main spectral lobes further away from the carrier, resulting in better flat spectrum characteristics (Bottom in Figure 3).

5 Summary and outlook

The development of an Elegant Breadboard prototype of the VT with its E-Box and its Antenna system has been ongoing within the framework of “H2020-ESA-038 GNSS Evolutions Experimental Payloads and Science Activities”. Technical specifications design and manufacturing of VT breadboard has been recently completed. The integrated tests are planned to verify the subsystem’s compliance to its technical requirements initially set in pursuit of Galileo enhancement and science objectives. An end-to-end ground subsystem demonstration to prove the compatibility of the VT with processing of its random noise and pseudo-noise at a VLBI Ground Station is foreseen in VLBI Ground station at the Geodetic Observatory of Wettzell. The VT designed for next generation Galileo satellites can be also tailored for other missions like ESA’s GENESIS mission consisting of the collocation, for

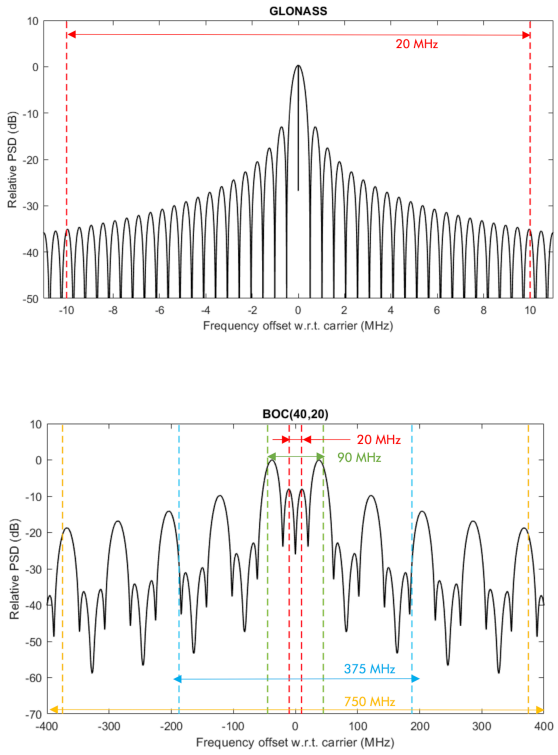

Fig. 3 (Top) Glonass spectrum.(Bottom) BOC(40,20) spectrum

the first time ever, of the four space-based geodetic techniques. It can also be positioned as an artificial radio source on the surface of the Moon to be tracked by VLBI antennas.

References

Altamimi Z., Rebischung P, Metivier L., Collilieux X (2016) ITRF2014: A new release of the International Terrestrial Reference Frame modeling nonlinear station motions. *Journal Of Geophysical Research: Solid Earth*, 121, 6109–61311.

Altamimi Z (2008) Importance of local ties for the ITRF (2008) *13th FIG Symposium On Deformation Measurement And Analysis*, pp. 12-15.

Glaser S., Fritsche M., Sośnica K., Rodrıéguez-Solano C., Wang K., Dach R., Hugentobler U., Rothacher M., Dietrich R. (2015) Validation of components of local ties. *REFAG 2014*, pp. 21-28.

Pollet A., Coulot D., Biancale R., Pérosanz F., Loyer S., Marty J., Glaser S., Schott-Guilmault V., Lemoine J., Mercier F. et al. (2023) GRGS numerical simulations for a GRASP-like mission: A way to reach the GGOS goal for terrestrial reference frame. *Journal Of Geodesy*, 97, 45.

Thaller D., Dach R., Seitz M., Beutler G., Mareyen M. & Richter B. (2011) Combination of GNSS and SLR observations using satellite co-locations. *Journal Of Geodesy*, 85, 257-272.

Thaller D., Sośnica K., Dach R., Jäggi A., Beutler G., Mareyen M. & Richter B. (2014) Geocenter coordinates from GNSS and combined GNSS-SLR solutions using satellite co-locations. *Earth On The Edge: Science For A Sustainable Planet*, pp. 129-134.

Zoulida M., Pollet A., Coulot D., Perosanz F., Loyer S., Biancale R. & Rebischung P. (2016) Multi-technique combination of space geodesy observations: Impact of the Jason-2 satellite on the GPS satellite orbits estimation. *Advances In Space Research*, 58, 1376-1389.

Bury G., Sośnica K., Zajdel R., Strugarek D. & Hugentobler U. (2021) Geodetic Datum Realization Using SLR-GNSS Co-Location Onboard Galileo and GLONASS. *Journal Of Geophysical Research: Solid Earth*, 126, e2021JB022211.

Biancale R., Pollet A., Coulot D. & Mandea M. (2017) E-GRASP/Eratosthenes: a mission proposal for millimetric TRF realization. *EGU General Assembly Conference Abstracts*, pp. 8752.

Nerem R., Bar-Sever Y. & Grasp Team (2011) The Geodetic Reference Antenna in Space (GRASP) - A Mission to Enhance the Terrestrial Reference Frame. *AGU Fall Meeting Abstracts*, 2011, pp. eG51B-04.

Plank L., Hellerschmied A., McCallum J., Böhm J. & Lovell J. (2017) VLBI observations of GNSS-satellites: from scheduling to analysis. *Journal Of Geodesy*, 91, 867-880.

Anderson J., Beyerle G., Glaser S., Liu L., Männel B., Nilsson T., Heinkelmann R. & Schuh H. (2018) Simulations of VLBI observations of a geodetic satellite providing co-location in space. *Journal Of Geodesy*, 92, 1023-1046.

Klopotek G., Hobiger T., Haas R. & Otsubo T. (2020) Geodetic VLBI for precise orbit determination of Earth satellites: a simulation study. *Journal Of Geodesy*, 94.

Wolf H., Böhm J., Schartner M., Hugentobler U., Soja B. & Nothnagel A. (2022) Dilution of Precision (DOP) factors for evaluating observations to Galileo satellites with VLBI. Springer, 2022.

Sert H., Hugentobler U., Karatekin O. & Dehant V. (2022) Potential of UT1–UTC transfer to the Galileo constellation using onboard VLBI transmitters. *Journal Of Geodesy*, 96, 1-13.

Jaradat A., Jaron F., Gruber J. & Nothnagel A. (2021) Considerations of VLBI transmitters on Galileo satellites. *Advances In Space Research*, 2021, https://doi.org/10.1016/j.asr.2021.04.048.

Kodet J., Plötz C., Schreiber U., Neidhardt A., Pogrebenko S., Haas R., Molera G. & Prochazka I. (2013) Co-location of space geodetics techniques in Space and on the ground. *Reports Of The Finnish Geodetic Institute, Proceedings Of The 21st Meeting Of The European VLBI Group For Geodesy And Astronomy, Ed. By N. Zubko And M. Poutanen*, 2013, 223-226.

Vienna Combination Software - VieCompy

L. Kern, H. Krásná, J. Böhm, A. Nothnagel, M. Madzak

Abstract The Vienna Center for VLBI (Very Long Baseline Interferometry) presents a new state-of-the-art combination software called *VieCompy* written in Python. *VieCompy* is a stand-alone tool of the Vienna VLBI and Satellite Software (*VieVS*) and can be used to estimate global parameters, such as terrestrial and celestial reference frames based on normal equations. Currently, solely VLBI-only solutions can be derived, but we plan on continuously expanding the functionalities of *VieCompy*. In this work, the general concept of the software is presented and further development is discussed. The software will be made freely available in the future.

Keywords Global solution, *VieVS*, *VieCompy* software

1 Introduction

In general, there are few software packages which have been developed specifically for the combination of different space geodetic techniques, e.g., *CatRef*[1], developed at the Institut Géographique National (IGN) (Altamimi et al., 2002), *DOGS-CS*[2], developed at DGFI-TUM (Deutsches Geodätisches Forschungsinstitut) (Gerstl et al., 2004) and *KALREF*[3], developed at the Jet Propulsion Laboratory (JPL) (Abbondanza et al., 2017). With these software packages, it is possible to derive catalogs of station coordinates and velocities from a combination of all space-geodetic techniques, including Very Long Baseline Interferometry (VLBI), Satellite Laser Ranging (SLR), Global Navigation Satellite Systems (GNSS), and Doppler Orbitography and Radiopositioning Integrated by Satellite (DORIS).

Single-technique analysis programs provide the input to these inter-technique combination packages via solution independent exchange (SINEX) files. In the case of VLBI, beyond many others, *nuSolve*, developed at the NASA Goddard Space Flight Center (Bolotin et al., 2014) and *VieVS*[4], developed at the Vienna Center for VLBI (Very Long Baseline Interferometry) (Böhm et al., 2018) exist for this purpose. Besides the possibility of providing single-session solutions, some VLBI packages, such as the submodule *vie_glob* within *VieVS*, are capable of generating multi-session/global solutions to derive global parameters based on datum-free and unconstrained normal equation (NEQ) systems.

Standard geodetic VLBI sessions last 24 hours and are observed by subsets of a global network of antennas. By combining thousands of these sessions in a global least squares adjustment, very precise terrestrial reference frames (TRF) with catalogs of coordinates and their velocities, as well as celestial reference frames (CRF) with catalogs of source positions, can be determined. For this purpose, the NEQs of the respective sessions are stacked. By an inversion of the resulting global NEQ, the global parameters are determined. As already mentioned, thousands of VLBI sessions are combined in the process of determining a global reference frame, e.g., over 6700 sessions consisting of ap-

Lisa Kern · Hana Krásná · Johannes Böhm · Axel Nothnagel · Matthias Madzak
TU Wien, Department of Geodesy and Geoinformation, Wiedner Hauptstrasse 8–10, Vienna, 1040 Austria

[1] Combination and Analysis of Terrestrial Reference Frame

[2] DGFI Orbit and Geodetic parameter estimation Software - Combination and Solution

[3] Kalman filter for Terrestrial Reference Frame determination

[4] Vienna VLBI and Satellite Software

proximately 20 million observations are combined in the VIE2022 solution (Krásná et al., 2023).

Despite *vie_glob* being a well-developed tool, this module is part of the *VieVS* software and cannot be used independently, nor can it be easily extended to include other techniques. Therefore, at the Vienna Center for VLBI, we are currently working on a new state-of-the-art and stand-alone combination software, called *VieCompy*, which is currently capable of deriving a VLBI-only solution based on datum-free and unconstrained NEQ from SINEX files. This modern and flexible software package will enable computing inter-technique solutions in the future.

In the following, the concept and most essential functionalities of *VieCompy* are explained (Section 2). In Section 3 the current performance of the software is presented and in Section 4 further developments and ideas are discussed.

2 Concept

VieCompy is written in Python and is a stand-alone software under the umbrella of the chain of *VieVS* developments (Böhm et al., 2018). It can be operated by a text control file or by a modern graphical user interface (GUI) generated using the PyQt5 library. Both invoke the corresponding Python script and control, beyond other details, the input data and the parameterization of the global adjustment.

Fig. 1 *VieCompy* logo

The input are standard SINEX files, which contain unconstrained and datum-free NEQ. The software currently works for SINEX files of version 2.02 (IERS, 2006). First, information on all sessions is collected, leading to a high data volume and memory usage. The bookkeeping is of great importance so that it is known which elements are stored within the NEQ and where. For this purpose, Pandas DataFrames are used and provided with multiple indices (MultiIndex), stating the type of parameter and the reference epoch. In the next step, additional information can be added to the individual NEQ systems by expanding the NEQ by the corresponding rows and columns. This makes it possible to estimate so far unaccounted-for parameters, such as station or source velocities. The NEQ systems are reduced in the next step to decrease the high data volume. Therefore, based on the user input, parameters can be fixed, reduced or estimated. In the case of fixing parameters, the corresponding rows and columns are simply removed from all NEQ systems. By reducing parameters, in comparison to fixing parameters, the parameters can be implicitly estimated in a so-called backward solution. In the process of reduction, the NEQ is divided into two parts, global parameters (1) and reduced parameters (2) and special restitution equations (see Equation 1, Bloßfeld (2015)) are performed for every session i. Typically reduced parameters depend on a finite amount of time and do not profit from longer observing periods, e.g., clock parameters, zenith wet delays or tropospheric gradient parameters. By default, clock parameters are not included in standard SINEX files but may be of interest in the future.

$$\begin{aligned} N_r^i &= N_{11} - N_{12}N_{22}^{-1}N_{21} \\ b_r^i &= b_1 - N_{12}N_{22}^{-1}b_2 \end{aligned} \tag{1}$$

The remaining parameters are the global parameters that are considered constant over several sessions, today mainly source positions as well as station coordinates and their velocities. Subsequently, the reduced NEQ systems are merged into one global NEQ system. This process is called *stacking* or *Helmert blocking* (Helmert, 1872) and it describes the summation of common parameters (see Equation 2, with N being the number of sessions). Since, as mentioned earlier, Pandas MultiIndex DataFrames are used, it is ensured that when stacking, common parameters are added up correctly.

$$N = \sum_{i=1}^{N} N_r^i, \qquad b = \sum_{i=1}^{b} b_r^i \tag{2}$$

Before the solution can be utilized, exterior information about the parameters is necessary. Since VLBI observations are relative and, therefore, do not provide an absolute position or orientation, constraints concerning the geodetic datum must be applied to

remedy the rank defect (Brockmann, 1997), making the NEQ invertible and, therefore, solvable.

In general, there are different methods of introducing a geodetic datum in VLBI analysis, including

- *Helmert rendering*, where constraints are forced to be fulfilled and
- *no-net-translation/no-net-rotation* (NNT/NNR) approaches, where formal errors for the constraints can be introduced.

For more details on the possibilities of datum definition and scaling, see Kern et al. (2023a,b,c,d). In *VieCompy*, the user can select between the different methods of datum definition and scaling and can define the formal errors in the NNT/NNR approach.

The most important step in the processing is the final inversion of this global NEQ system, which results in the determination of the global parameters (see Equation 3) and their variance information (see Equation 4, with s_0^2 being the a posterior variance of unit weight and C_{xx} the resulting covariance matrix).

$$x = N^{-1}b \tag{3}$$

$$C_{xx} = s_0^2 \cdot N^{-1} \tag{4}$$

As a standard, the software currently provides catalogs of station positions and velocities (TRF), source positions and, if selected, velocities (CRF). Estimates of session-wise reduced parameters, e.g., EOPs and tropospheric parameters, can be generated if the coefficients are carried over in the SINEX files and a backward solution is wanted. Furthermore, a set of plots showing the kinematics of stations and sources as well as the corresponding networks is provided.

3 Performance and validation

As mentioned before, thousands of VLBI sessions are typically combined in a global least squares adjustment making the matrices to be handled very numerous. Consequently, the process is computationally and memory expensive. For this reason, parallel computing was implemented in the following processing steps to improve the performance of *VieCompy*:

- reading of SINEX files,
- expansion of NEQ,
- application of constraints of parameters,
- reduction of NEQ,
- performing backward solutions.

Within *VieCompy*, the parallel processing is handled in a way that n processes are started, which are executed simultaneously. n represents the number of available logical cores on the executing device. This is applied to all of the steps listed above. The improvement in performance is dependent on the device's hardware. However, it can be said that the introduction of parallel computing has drastically reduced the processing time.

Besides that, since we plan to offer quarterly solutions soon, it is possible to save the stacked NEQ system from a previous solution and process and add only new NEQ information in the new solution. In this case, so-called pickle files are used to serialize the NEQ systems and thus reducing the computing time.

The results of *VieCompy* are validated by comparison with vie_glob. As already mentioned, in comparison to vie_glob, *VieCompy* is an independent program based on the NEQ of SINEX files and, therefore, not strictly coupled to a specific analysis package. Furthermore, performance optimization is a key element of *VieCompy* while its modular structure makes it easily extendable. In addition, many tests have already been implemented using the *pytest* framework to check the software and its individual functionalities automatically. This makes *VieCompy* a modern and flexible software package for the determination of global solutions.

4 Future plans

VieCompy is a software that is still under development. Currently, it can combine VLBI sessions for the determination of terrestrial and celestial reference frames on the NEQ level. We are continuously working on improving the performance and memory usage as well as implementing software tests that automatically check the code for bugs and correctness.

We also plan to introduce more functionalities in *VieCompy* in the near future, including the combination of VLBI with other space geodetic techniques, such as Satellite Laser Ranging (SLR) or data from ring lasers. Furthermore, the implementation of filter solutions, to ensure an optimal state estimation of

the dynamical system Earth, as in Abbondanza et al. (2017), is one of the next major goals.

We plan on making *VieCompy* freely available on GitHub in the future.

References

Abbondanza C, Chin TM, Gross RS, Heflin MB, Parker JW, Soja BS, van Dam T, Wu X (2017) JTRF2014, the JPL Kalman filter and smoother realization of the International Terrestrial Reference System. *Journal of Geophysical Research: Solid Earth*, 122(10), doi: 10.1002/2017JB014360.

Altamimi Z, Sillard P, Boucher C (2002) ITRF2000: a new release of the international terrestrial reference frame for Earth science applications. *Journal of Geophysical Research: Solid Earth*, 107(B10), doi: 10.1029/2001JB000561.

Altamimi Z, Rebischung P, Métivier L, Collilieux X (2016) ITRF2014: A new release of the International Terrestrial Reference Frame modeling nonlinear station motions. *Journal of Geophysical Research: Solid Earth*, 121(8), 6109--6131, doi: 10.1002/2016JB013098.

Bloßfeld M (2015) The key role of Satellite Laser Ranging towards the integrated estimation of geometry, rotation and gravitational field of the Earth. *PhD thesis*, *Technische Universität München*.

Bolotin S, Baver K, Gipson JM, Gordon D, MacMillan D (2014) The VLBI data analysis software *v*Solve: development progress and plans for the future. *IVS 2014 General Meeting Proceedings*, Science Press, Beijing, China, 253—257.

Böhm J, Böhm S, Boisits J, Girdiuk A, Gruber J, Hellerschmied A, Krásná H, Landskron D, Madzak M, Mayer D, McCallum J, McCallum L, Schartner M, Teke K (2018) Vienna VLBI and Satellite Software (VieVS) for Geodesy and Astrometry. *Publications of the Astronomical Society of the Pacific*, 130(986), doi: 10.1088/1538-3873/aaa22b.

Brockmann E (1997) Combination of Solutions for Geodetic and Geodynamic Applications of the Global Positioning System (GPS). *Geodätisch Geophysikalische Arbeiten in der Schweiz*, *Schweizerische Geodätische Kommission*, Vol. 55.

Charlot P, Jacobs CS, Gordon D, Lambert S, de Witt A, Böhm J, Fey AL, Heinkelmann R, Skurikhina E, Titov O, Arias EF, Bolotin S, Bourda G, Ma C, Malkin Z, Nothnagel A, Mayer D, MacMillan DS, Nilsson T, Gaume R (2020) The third realization of the International Celestial Reference Frame by very long baseline interferometry. *Astronomy & Astrophysics*, 644, A159, doi: 10.1051/0004-6361/202038368.

Gerstl M, Kelm R, Müller H, Ehrnsperger W (2004) DOGS-CS: Kombination und Lösung großer Gleichunsgsysteme. *Deutsches Geodätisches Forschungsinstitut*, MG/01/1995/DGFI.

Helmert FR (1997) Die Ausgleichungsrechnung nach der Methode der kleinsten Quadrate. *Teubner*, *Leipzig*.

IERS (2006) IERS Message No. 103 https://www.iers.org/.

Kern L, Krásná H, Böhm J, Madzak M (2023) Current status and future perspectives of VLBI global solutions. *European Geosciences Union (EGU) General Assembly 2023*, Vienna, Austria, April 23-28, 2023, doi: 10.5194/egusphere-egu23-13970.

Kern L, Krásná H, Nothnagel A, Böhm J, Madzak M (2023) Neglected issues of terrestrial datum definition in VLBI. *26th Meeting of the European VLBI Group for Geodesy and Astrometry (EVGA)*, Bad Kötzting, Germany, June 11-15, 2023.

Kern L, Krásná H, Nothnagel A, Böhm J, Madzak M (2023) Issues of terrestrial geodetic datum definition in VLBI data analysis. *International Union of Geodesy and Geophysics (IUGG) 28th General Assembly*, Berlin, Germany, July 11-20, 2023.

Kern L, Krásná H, Nothnagel A, Böhm J, Madzak M (2023) Terrestrial datum definition methods in VLBI global solutions. *Proceedings of the International Association of Geodesy (IAG) Symposia: International Union of Geodesy and Geophysics (IUGG) 28th General Assembly* [submitted].

Krásná H, Baldreich L, Böhm J, Böhm S, Gruber J, Hellerschmied A, Jaron F, Kern L, Mayer D, Nothnagel A, Panzenböck O, Wolf H (2022) VLBI Celestial and Terrestrial Reference Frames VIE2022b. *Astronomy & Astrophysics*, Forthcoming article, doi: 10.1051/0004-6361/202245434.

The benefits of the Australian mixed-mode program (2018 - 2023) for the celestial reference frame at S/X-band

H. Krásná, L. McCallum, T. McCarthy

Abstract The current realization of the International Celestial Reference Frame at 8.4 GHz, the ICRF3-SX, is computed from very long baseline interferometry (VLBI) measurements starting in 1979 through until March 2018. The concentration of the majority of VLBI telescopes in the Northern hemisphere reflects itself in the unequal distribution of observations to radio sources over declination, causing the ICRF3-SX to be weaker in the south. One of the current VLBI observing programs active in the Southern hemisphere is the Australian mixed-mode program (AUM) which started to be organized in July 2018. In this contribution, we show the benefits of the AUM for the celestial reference frame including observation until December 2022 and also discuss its current limitations. The individual sessions were scheduled for currently available VLBI telescopes (Hb, Ke, Yg for the first block, then also including Ht and Ww in the second block). In terms of scheduling, the sessions were scheduled geodetically, i.e. aiming for a high number of scans. In AUM049-058, five target sources were observed in 4-5 scans of 10 minutes duration. This setup still ensures about 25 scans/hr/station, which is seen as a foundation for good geodetic results.

Keywords Australian mixed-mode program (AUM), celestial reference frame (CRF)

Hana Krásná
TU Wien, Department of Geodesy and Geoinformation, Wiedner Hauptstrasse 8–10, Vienna, Austria

Lucia McCallum · Tiege McCarthy
University of Tasmania, Hobart, Australia

1 Introduction

Conventional celestial reference frames (CRF) are practical realizations of the international celestial reference system (ICRS; Arias et al., 1995). The ICRS was adopted by the International Astronomical Union (IAU) as the conventional system in 1997. At its XXX General Assembly in 2018, IAU resolved in Resolution B2, "On The Third Realization of the International Celestial Reference Frame" (ICRF3 working group , 2018) that from 1 January 2019, the fundamental realization of the ICRS shall be the Third Realization of the International Celestial Reference Frame (ICRF3; Charlot et al., 2020). The ICRF3 at S/X band consists of absolute positions of extragalactic radio sources that were estimated from geodetic and astrometric very long baseline interferometry (VLBI) sessions. These sessions were organized and made available mainly by the International VLBI Service (IVS) and the Very Long Baseline Array (VLBA) across several observing programs. The substantial dominance of the telescopes in the Northern hemisphere included in these programs reflects itself in the proportionally lower number of observed radio sources in the Southern hemisphere with a lower cadence for their re-observations. Petrov et al. (2011, 2019) organized calibrator surveys of southern compact radio sources (LCS1 and LCS2) using the Australian long baseline array (LBA), with one of the objectives being to match the density of calibrator sources in the Northern hemisphere with positions accurate to a few milliarcseconds. As the measurements were carried out at X band only, without a precise access to the ionospheric contribution on the delay, the LCSs are not included in the ICRFs. One of the IVS observing programs which focuses on the increase of density and precision of the southern radio sources

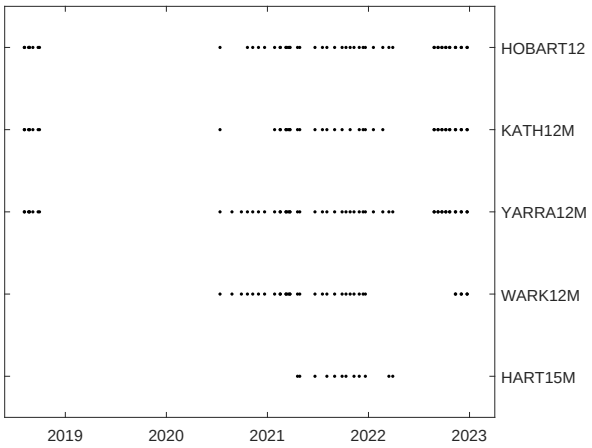

Fig. 1 Telescopes observing in the AUM001-064 sessions.

included in ICRF3, is the celestial reference frame deep south (CRDS; Weston et al., 2023) program.
The Australian mixed-mode program (AUM; McCallum et al., 2022) started in 2018 as a network of three Australian telescopes Hobart12 (Hb), Kath12m (Ke) and Yarra12m (Yg). In 2020 Wark12m (Ww) in New Zealand joined followed by Hart15m (Ht) in South Africa (Fig. 1). The mixed-mode configuration means that the upgraded VLBI Global Observing System (VGOS) stations (Hb, Ke) observe the legacy S/X configuration with the remaining telescope(s) in the network. In this paper we describe contribution of sessions AUM001-064 (2018-Jul-31 to 2022-Dec-17) to the CRF on basis of the VIE2022sx[1] solution (Krásná et al., 2023).

2 Method

The AUM sessions started to observe in July 2018 in the novel mixed-mode configuration to close the gap in the global IVS network as well as in the station time series which arised after the upgrade of Hb and Ke to VGOS telescopes. For sessions AUM049-058, we decided to exploit the potential of the strategic location of the AUM network to reobserve ICRF3 sources in the Southern hemisphere with a low number of prior observations. We scheduled dedicated sessions with 5 target sources. We included 10 min scans on each of them. We also scheduled 4 calibration blocks in each session, with 2 min scans. Still, sky coverage includes about 25 scans/hr/station, which gives similarly good geodetic results as described for sessions AUM001-033 in McCallum et al. (2022). Table 1 shows the scheduled target sources per session in detail.

Table 1 Overview of the dedicated AUM049-058 sessions.

session	start date	target sources
AUM049	2022-Aug-19	0035-534, 0407-658, 1030-590, 1352-632, 1839-486 (target1)
AUM050	2022-Aug-20	0125-484, 0700-465, 1204-613, 1343-601, 1722-554 (target2)
AUM051	2022-Sep-02	0219-474, 0809-493, 1253-590, 1600-489, 1830-589 (target3)
AUM052	2022-Sep-03	0252-712 , 0647-475, 1556-580, 1829-718 (target4)
AUM053	2022-Sep-16	target1
AUM054	2022-Sep-17	target2
AUM055	2022-Sep-30	target3
AUM056	2022-Oct-01	target4
AUM057	2022-Oct-14	target3
AUM058	2022-Oct-15	target1

3 Results

The analysis of these dedicated sessions showed that only several scheduled scans to the target sources could be successfully observed. The limitation factor was the low flux density of the radio sources. Nevertheless, the sessions even after the loss of several scans performed well and could be used for CRF estimation in a global solution.

The global solution VIE2022sx includes the AUM001-064 sessions by default. For this investigations, we computed another global solution that is identical to VIE2022sx but without the AUM sessions denoted as VIE2022sx_noAUM. The contribution of the AUM001-064 sessions to the VIE2022sx global solution, with the number of observations per source plotted over declination (δ), is depicted in top panel of Fig. 2. The lower plot shows the percentage of AUM observations to the respective sources coming from AUM in the VIE2022sx solution. It shows that even a small number of observations to sources below -45° declination represents a significant percentage of their observations in VIE2022sx. Fig. 3 depicts the sources in AUM001-064 with a mollweide projection

[1] https://vlbi.at/data/analysis/ggrf/crf_vie2022_sx.txt

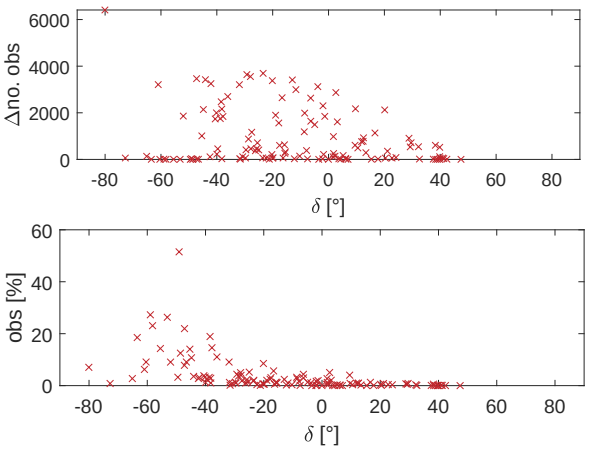

Fig. 2 Top panel: Difference in no. of observations between VIE2022sx and VIE2022sx_noAUM, i.e., no. of observations to respective sources in AUM001-064. Lower panel: Percentage of observations to sources in VIE2022sx coming from AUM001-064.

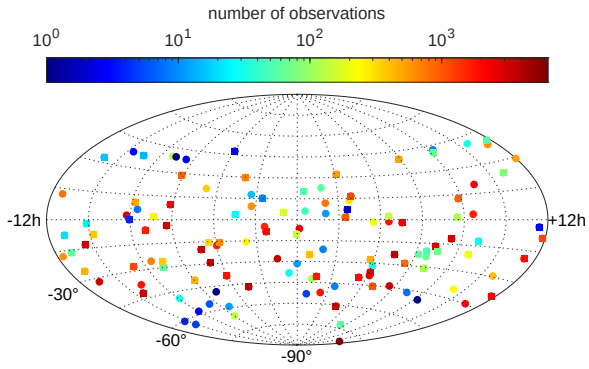

Fig. 3 No. of observations (logarithmic scale) to ICRF3 defining sources (squares) and ICRF3 non-defining sources (circles) in AUM001-064 sessions.

using a logarithmic heat color scale for the number of observations per source (ICRF3 defining sources are squares and other sources are circles).

Comparison of the two CRF catalogs (VIE2022sx_noAUM minus VIE2022sx) shows a slight systematic difference in the declination estimates plotted over declination of all southern sources included in VIE2022sx. The peak of the systematic difference in δ reaches about -10 μas at -40° declination (lower plot in Fig. 4) but is within the formal errors of the estimates. The differences in the estimated right ascension (α^*) and δ for sources observed in AUM001-064 sessions, are shown in

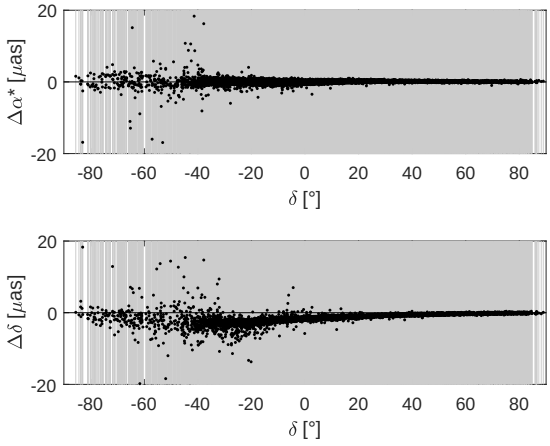

Fig. 4 Difference in right ascension (top panel) and declination (lower panel) computed as VIE2022sx_noAUM minus VIE2022sx for all sources in VIE2022sx. We use the designation α^* for right ascension scaled by declination of the source, i.e., $\alpha^* = \alpha \cdot \cos\delta$. Grey color indicates inflated formal error of the differences.

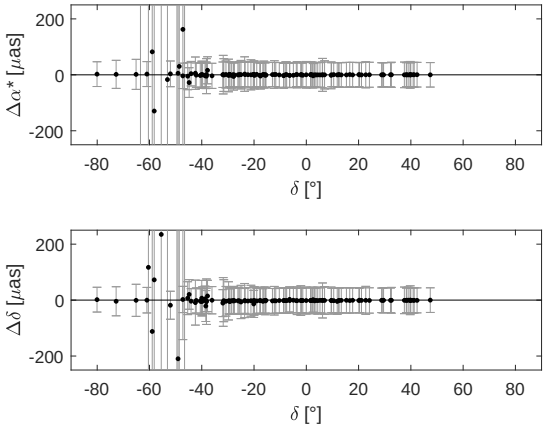

Fig. 5 Difference in right ascension (top panel) and declination (lower panel) computed as VIE2022sx_noAUM minus VIE2022sx for sources observed in AUM001-064 sessions. Grey color indicates inflated formal error of the differences.

Fig.5. The largest differences exceeding 50 μas in one or both coordinates appears for sources with declinations between -45° and -62°. Comparison with Fig. 2 yields that the amount of observations coming from AUM sessions for these sources exceeds 10%.

In Figs. 6 and 7 we show the difference in inflated formal errors ($\Delta\sigma_{\alpha^*}$ (left panels), $\Delta\sigma_\delta$ (right panels)) computed as VIE2022sx_noAUM minus VIE2022sx plotted with respect to the corresponding inflated

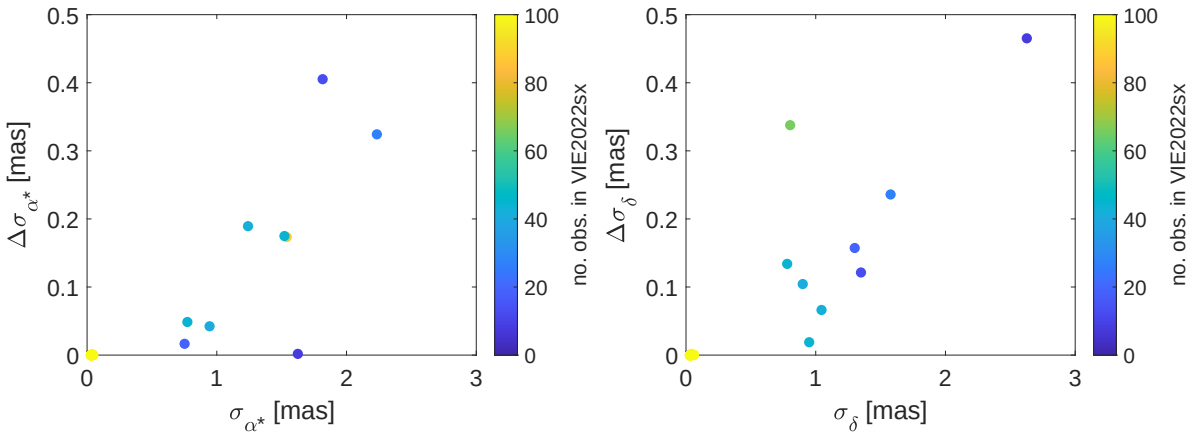

Fig. 6 Difference in inflated formal errors ($\Delta\sigma_{\alpha^*}$ (left panel), $\Delta\sigma_{\delta}$ (right panel)) computed as VIE2022sx_noAUM minus VIE2022sx w.r.t. the inflated formal error in VIE2022sx_noAUM. Color-coded is number of observations in VIE2022sx.

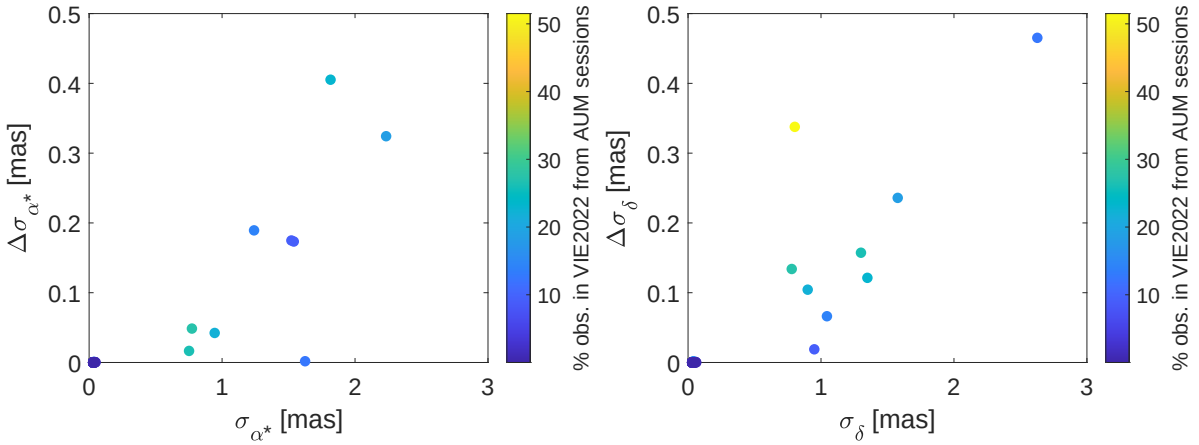

Fig. 7 Difference in inflated formal errors ($\Delta\sigma_{\alpha^*}$ (left panel), $\Delta\sigma_{\delta}$ (right panel)) computed as VIE2022sx_noAUM minus VIE2022sx w.r.t. the inflated formal error in VIE2022sx_noAUM. Color-coded is percentage of observations coming from AUM001-064.

formal error in VIE2022sx_noAUM. The inflation of errors was done following the recommendation given for ICRF3, i.e., multiplication of formal errors by scaling factor 1.5 and addition of noise floor 30 μas as RSS. The difference between Figs. 6 and 7 is in the information coded in the color scale. The color bar in Fig. 6 depicts the number of observations of the individual sources in VIE2022sx, and in Fig. 7 it shows the percentage of observations for the respective sources coming from AUM001-064 sessions in VIE2022sx. There are eleven sources which show a reduction of formal error larger than 100 μas in one or both coordinates: 0035−534, 0219−474, 0700−465, 0809−493, 1343−601, 1352−632, 1556−580, 1600−489, 1722−554, 1830−589, 1839−486. These sources have large formal error in VIE2022sx_noAUM (1–3 mas) mainly due to low number of observations (< 100) and the amount of extra observations coming from AUM sessions for these sources lays between 10% and 50% of observations in VIE2022sx.

4 Conclusions and outlook

The Australian mixed-mode program (AUM) supports the realization of the ICRS in the Southern hemisphere. We show that the dedicated AUM049-058 sessions improved inflated formal errors of eleven radio sources by $100 - 500$ μas in one or both coordinates. These sources had large formal error (1–3 mas) of their posi-

tion in CRF without AUM sessions primarily due to low number of observations (< 100).
The AUM program is ongoing with a double session (one weekend) per month. We expect Hobart26 to join the AUM sessions in 2023 which will increase the sensitivity of the baselines to the weaker radio sources.

References

Arias EF, Charlot P, Feissel M, Lestrade J-F (1995) The extragalactic reference system of the International Earth Rotation Service, ICRS. *Astron. Astrophys*, 303, 604–608.

Charlot P, Jacobs CS, Gordon D, Lambert S, de Witt A, Böhm J, Fey A, Heinkelmann R, Skurikhina E, Titov O, Arias EF, Bolotin S, Bourda G, Ma C, Malkin Z, Nothnagel A, Mayer D, MacMillan DS, Nilsson T, Gaume R (2020) The third realization of the International Celestial Reference Frame by very long baseline interferometry. *A&A*, 644, A159, doi: 10.1051/0004-6361/202038368.

ICRF3 working group (2018) IAU Resolution B2 on The Third Realization of the International Celestial Reference Frame. *Proceedings of the XXX IAU General Assembly*.

Krásná H, Baldreich L, Böhm J, Böhm S, Gruber J, Hellerschmied A, Jaron F, Kern L, Mayer D, Nothnagel A, Panzenböck O, Wolf H (2023) VLBI Celestial and Terrestrial Reference Frames VIE2022b. *A&A*, forthcoming, doi: 10.1051/0004-6361/202245434.

McCallum L, Chin Chuan L, Krásná H, McCallum J, Böhm J, McCarthy T, Gruber J, Schartner M, Quick J, Rogers A (2022) The Australian mixed-mode observing program. *J Geod*, 96, 67, doi: 10.1007/s00190-022-01657-2.

Petrov L, Phillips C, Bertarini A, Murphy T, Sadler E (2011) The LBA Calibrator Survey of southern compact extragalactic radio sources – LCS1. *Mon Not R Astron Soc*, 414, 3, 2528–2539, doi: 10.1111/j.1365-2966.2011.18570.x.

Petrov L, de Witt A, Sadler E, Phillips C, Horiuchi S (2019) The Second LBA Calibrator Survey of southern compact extragalactic radio sources – LCS2. *Mon Not R Astron Soc*, 485, 1, 88-–101, doi: 10.1093/mnras/stz242.

Weston S, de Witt A, Krásná H, Le Bail K, Hardin S, Gordon D, Shu F, Fey A, Schartner M, Basu S, Titov O, Behrend D, Jacobs CS, Hankey W, Salguero F, Reynolds JE (2023) On more than two decades of Celestial Reference Frame VLBI observations in the deep south: IVS-CRDS (1995–2021). *Publ Astron Soc Aust*, 40, e041, doi: 10.1017/pasa.2023.33.

A VGOS antenna for the Argentinean-German Geodetic Observatory

C. Kristukat, H. Hase

Abstract A new VGOS compatible radio telescope will be installed at the Argentinean-German Geodetic Observatory in Argentina. Its design will take into account local peculiarities of the site as well as new developments and experiences at other stations worldwide. With the erection of the new telescope AGGO aims at becoming a fully compliant GGOS site.

Keywords VGOS, GGOS, VLBI, Radioantenna

1 Introduction

AGGO is the Argentinean-German Geodetic Observatory. It is located in Argentina, South America, near the city of La Plata. It is run by the Argentinean research council CONICET and the German Federal Agency for Cartography and Geodesy BKG. AGGO is a geodetic fundamental station with three of the four geodetic space techniques, i.e. VLBI, SLR and GNSS, needed to establish the global geodetic reference frame (GGRF) and for the determination of the Earth Orientation Parameters (EOP). AGGO is part of the global infrastructure for geodesy and is unique of its category in Latin America.

The current VLBI antenna is a primary focus 6 m offset radio telescope with a legacy S/X cryogenic receiver. It was designed as part of a transportable geodetic station in the early 1990ies when the IVS station network was still rather sparse. It was desirable to be able to operate a transportable geodetic observatory at distinct points in the world and thus improve the precision of the GGRF and the determination of the EOP. With the growth of the IVS station network, the interest in stable reference points and time series became more important than the possibility to obtain multiple reference points by using a transportable observatory. In the end the observatory moved only twice, once from Germany to Chile and then to Argentina.

Now AGGO is to become a Global Geodetic Observing System (GGOS) site with the installation of a VLBI Global Observing System (VGOS) compatible radio telescope according to VGOS2010 (Niell et al. (2005)).

The key characteristics of a VGOS antenna are:

- Antenna diameter > 12 m
- Very fast slewing: 12 °/s in azimuth, 6 °/s in elevation axis
- Broad band observation in at least four frequency bands with up to 1 GHz bandwidth between 2-14 GHz
- Data rate ≥ 8 Gbps

The project is currently in its planning phase. The system is expected to be operative by 2030.

2 Motivation

Each new station added to the global VLBI network potentially increases the accuracy of the EOP parameter determination. As can be seen on the map in figure 2, the current VGOS site distribution is rather inhomogeneous and the network suffers from a lack

Christian Kristukat · Hayo Hase
Argentinean German Geodetic Observatory, Argentina
Federal Agency for Cartography and Geodesy, Germany

Fig. 1 Aerial photograph of the AGGO observatory. The area on the right side is reserved for the the new telescope.

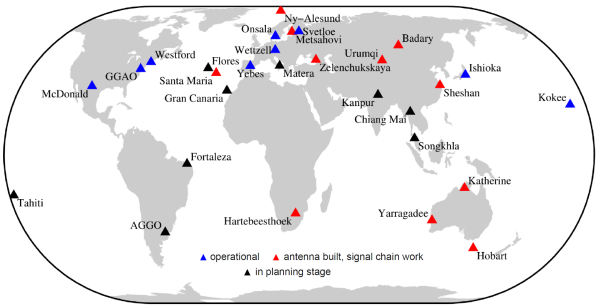

Fig. 2 VGOS antennas around the world (2022). From: D. Behrend, *Status of the VGOS Infrastructure Rollout*, 12th IVS General Meeting

of stations in the southern hemisphere. Schartner et al. (2015) carried out a theoretical study in order to determine the best locations for new antennas. They generated a large amount of schedules for the existing network plus around 500 possible stations, homogeneously distributed over land areas on the globe. They then simulated in which region an additional station would have the largest impact on the accuracy of geodetic parameters. They conclude that adding an antenna in the southern hemisphere, especially in South America, leads to better results for almost all EOP. Furthermore, considering plate tectonics, it is desirable to have at least three stations on each major plate in order to model the plates' rotation correctly.

These findings encourage us all the more to carry out the present project.

3 Characteristics of the radio telescope

The characteristics of the new telescope will resemble those of the TWIN telescopes at the Geodetic Observatory Wettzell, Germany: a gregorian type antenna with a ring focus sub-reflector. While writing down the specifications we consider the gained experience from the TWIN telescope project and also the latest experience from observing operations at other stations around the world.

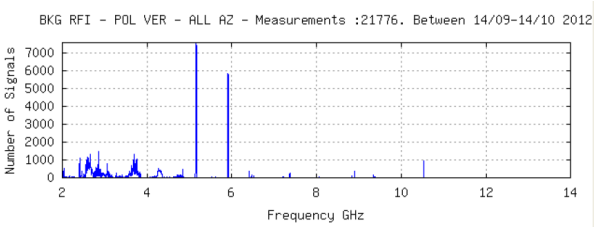

Fig. 3 Cumulative radio frequency intensity spectrum measured in the complete semi sphere during 24 hours at AGGO in 2012.

In particular, the radio frequency interference (RFI) load is on the rise worldwide and it is becoming increasingly difficult to observe without disturbance in the frequency range of 2 - 14 GHz. In the design of the receiver, we will foresee the possibility of incorporating notch filters to be able to block certain frequencies. Hopefully, within the next year or two, the VGOS technical committee (VTC) will commit to specific frequency bands for observation within the total frequency range and/or raise the lower frequency limit in order to operate outside of the mobile phone frequency ranges. A working group has been formed for this purpose within the IVS-VTC. If it turns out that it is feasible to reduce the full bandwidth to some specific frequency bands, we might initiate the development of a new receiver feed with adapted frequency characteristics.

When observing with AGGO's small radio telescope, RFI is not much of an issue, since its sensitivity is much lower than a VGOS type antenna. We are currently repeating a RFI study which has been done in 2012 at AGGO. At that time the RFI load was at a low level (see figure 3). Since then, terrestrial and satellite-based communications technology has evolved tremendously, and RFI exposure is expected to be significant today. Unfortunately, AGGO is located in a metropolitan area with 12 million inhabitants, in close proximity to airports and commercial shipping lanes.

The statutes of the AGGO Observatory foresee that the Argentine side will provide land, infrastructure and personnel, and the German side the equipment. As it is legally impossible for the German state to erect an

immovable structure on foreign territory, in this case a radio telescope, the base of the telescope will have to be dismountable and made from pre-fabricated steel elements rather than from concrete.

As AGGO lies within a natural reserve and is surrounded by high trees (see figure 1) which may not be cut down, the elevation axis will have to be at around 15 m above ground level in order to improve the horizon mask.

The higher the antenna base, the more the invariant point will move in the diurnal cycle due to thermal expansion of the antenna base. With the planned dimensions, the vertical movement will be about 3 mm considering the thermal amplitude within 24 hours. Asymmetric heating of the tower by solar irradiation will further produce a horizontal motion in the same order of magnitude. Monitoring the movement is therefore indispensable. An on-axis tube containing an invar-wire altitude measuring system connecting the reference point at the axes intersection with a ground marker at the telescope foundation shall be installed for that purpose.

The soil at AGGO consists basically of sand, slit and gravel, there are no rocks below the soil's surface. This has to be taken into account for the design of the foundation. The 6 m antenna is installed on a flat concrete platform with a large concrete cone pointing downwards in its center. The cone has the function of holding the platform in position while it literally floats on the soft ground. The same concept shall be used for the new antenna, adapted to its superior weight.

Besides the radio telescope additional space for maintenance of the receiver, workshops, an antenna control room and offices needs to be constructed.

4 Conclusions and outlook

A VGOS compatible radio telescope and its infrastructure shall be installed at AGGO during the next years. It is intended to hire a general contractor for the implementation of the project, including the design and fabrication of the radio telescope with all subsystems as well as for the local construction work. The purchase specifications will be finished until end of 2023 so that in 2024 the bidding process can start and the contract with the elected provider may be signed. After terminating the design phase the local infrastructure and the foundation for the antenna shall be built around mid of 2025. The delivery of all parts shall be done until end of 2028 so that in 2029 the assembly can start. We expect to start observing operations in 2030.

References

A. Niell, A. Whitney, B. Petrachenko, W. Schlüter, N. Vandenberg, H. Hase, Y. Koyama, C. Ma, H. Schuh & G. Tuccari (2005) VLBI2010: Current and Future Requirements for Geodetic VLBI Systems. https://ivscc.gsfc.nasa.gov/about/wg/wg3/IVS_WG3_report_050916.pdf.

M. Schartner, J. Böhm & A. Nothnagel (2015) Optimal antenna locations of the VLBI Global Observing System for the estimation of Earth orientation parameters. *Earth Planets Space*, 72, 87, doi: 10.1186/s40623-020-01214-1.

Impact of terrestrial datum on the estimation of Earth Orientation Parameters by geodetic VLBI

A. Laha, J. Böhm, S. Böhm, H. Krásná, N. Balasubramanian, O. Dikshit

Abstract The selection of terrestrial datum stations has a significant impact on the geodetic parameters. Continuous observation with precise a priori information is required in defining geodetic datum to avoid error propagation in the estimation of Earth orientation parameters (EOP) through VLBI. When estimating EOP, stable positions of the stations and sources are included in the respective datum. This study assesses the influence of station removal from the terrestrial datum on EOP. We removed three different stations- Wettzell, Sejong, and Kokee, individually. The study has utilized data from 2001 to 2022, derived from geodetic VLBI sessions, and analyzed them with VieVS. To understand the statistics, the EOP solutions, obtained after removing the stations from the datum are compared against standard Vienna, IERS 20 C04, and IGS finals solutions. The results reveal that celestial pole offsets (CPO) remain unaffected, regardless of the station's removal, while UT1-UTC and PM are influenced by station location and the presence of neighboring stations.

Keywords EOP, Datum, VLBI, ITRF

Arnab Laha · Nagarajan Balasubramanian · Onkar Dikshit
Geoinformatics, Dept. of Civil Engineering, Indian Institute of Technology Kanpur, India

Johannes Böhm · Sigrid Böhm · Hana Krásná
Higher Geodesy, Department of Geodesy and Geoinformation, TU Wien, Austria

(Correspondence: alaha@iitk.ac.in)

1 Introduction

Group delays in VLBI sessions, observed from baselines forming a polyhedron, are associated with a "free" network where the datum is defined by selecting a subset of points. According to Heinkelmann et al. (2007), the selection of points is contingent upon various criteria, including the objectives of the network or session, the type, quantity, and precision of measurements, as well as the attributes of the sources (such as structure and stability) or stations (encompassing ground properties, monumentation, episodic motions, etc.). These designated datum points substantially impact the Terrestrial Reference Frame (TRF) defined by geodetic Very Long Baseline Interferometry (VLBI).

United Nations highlighted the significance of the Global Geodetic Reference Frame (GGRF) for the benefit of society and the scientific community. As per Plag et al. (2009), GGRF is realized as the International Terrestrial Reference Frame (ITRF) with the intention to achieve mm-level accuracy to the geodetic products. To fulfill this goal, continuous observations with precise a priori information regarding station positions and velocities are required to avoid significant noise in the definition of geodetic datum that subsequently propagates in the determination of various geodetic parameters such as Celestial Reference Frame (CRF) and Earth Orientation Parameters (EOP) (Raposo-Pulido et al., 2016). Geodetic VLBI utilizes an interferometric technique, observing a catalog of distant radio sources to establish a quasi-inertial external reference frame, commonly referred to as CRF (Karbon at al., 2019). The determination of these two reference frames, TRF and CRF, is intricately interlinked and not mutually consistent. The transition between these reference frames is facilitated through

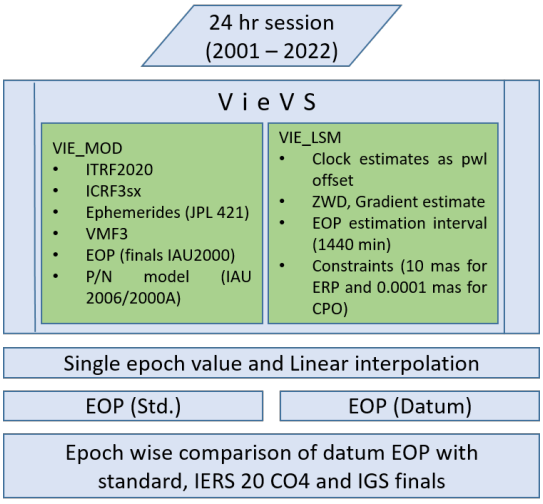

Fig. 1 Flowchart showing the models and steps involved in the estimation of EOP.

a set of five angles, collectively termed as EOP. These parameters encompass celestial pole offsets (CPO) (dX and dY), polar motion (x_p and y_p), and variations in universal time (UT1-UTC), all of together can exclusively be measured through geodetic VLBI.

In general, it can be imagined that the reliability of a terrestrial datum should improve as the number of stations used in its definition increases. However, for this to be true, the prerequisite is that all stations exhibit similar accuracy and stability. Paradoxically, in certain scenarios, both the addition and removal of stations can adversely affect the reliability of the terrestrial datum, consequently influencing other geodetic parameters such as the CRF and EOP. In the scope of this study, we quantify the impact of eliminating stations from the terrestrial datum on EOP. The central question we investigate is whether removing a single station from the terrestrial datum, regardless of its geographical location, produces a consistent impact on EOP. In anticipation of future scenarios necessitating the removal of stations from the terrestrial datum, our research aims to point out which station should be prioritized for removal to maximize the precision of EOP.

2 Parametrization and Analysis

In this study, we utilized VLBI 24-hour sessions observed by the International VLBI Service for Geodesy and Astrometry (IVS) from 2001 to 2022. These sessions were analyzed using VieVS (Böhm et al., 2018) to estimate the daily value of EOP. The a priori models employed in the routine analysis of IVS 24-hour sessions by the Vienna Analysis Center were implemented (Fig 1). The EOP values were estimated at 1440 min intervals with relative constraints of 10 mas for Earth Rotation Parameters (ERP) and 0.1 μas for Celestial Pole Offsets (CPO). Furthermore, piecewise linear offsets with 60 min interval and 1.3 cm relative constraint for the clocks, zenith wet delays with 30 min interval and 1.5 cm relative constraint, and troposphere gradients with 180 min and 0.5 mm constraint were also estimated. Additionally, station coordinates were also estimated and the datum was defined by applying no-net-translation (NNT) and no-net-rotation (NNR) conditions for stations with continuous observations in the ITRF2020.

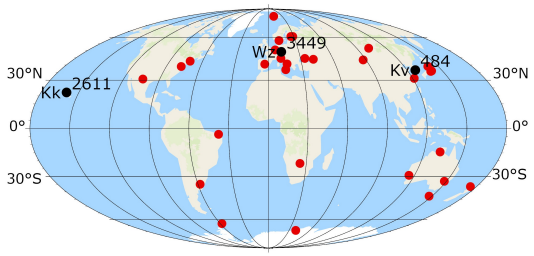

Fig. 2 Distribution of VLBI stations (red), whereas black represents the station removed one at a time from the datum. Numbers denote the participation in sessions (2001–2022).

To evaluate the impact of terrestrial datum on EOP, we removed different stations—Wettzell (Wz), Kokee (Kk), and Sejong (Kv)—one at a time from the datum (Fig 2). Four distinct EOP time series were estimated using VieVS in this study using the same a priori models and parameters: the standard EOP file (utilizing standard parameters), and three variations obtained after individually excluding Wz, Kk, and Kv. The estimated time series were not continuous, with some epochs having missing values, and in a few instances, multiple EOP values for the same epoch. To address this, we selected the EOP value with the minimum standard error when multiple values were present for the same epoch and applied linear interpolation to fill in missing values. The quality assessment of the three variations of the EOP time series (after excluding Wz, Kk, and Kv) was performed in terms of weighted mean (WM)

and weighted root mean square (WRMS) value with respect to standard Vienna, IERS 20 C04 and IGS final solution. However, the comparison with respect to IGS finals was limited to a subset of EOP directly observed from GNSS, specifically, x_p and y_p. IERS 20 C04 solution served as the reference epoch, and both VieVS solutions (CPO) and IGS finals were linearly interpolated to the IERS 20 C04 epoch, which is at 00 : 00 UTC.

3 Results and Discussion

3.1 Comparison w.r.t. standard Vienna solution

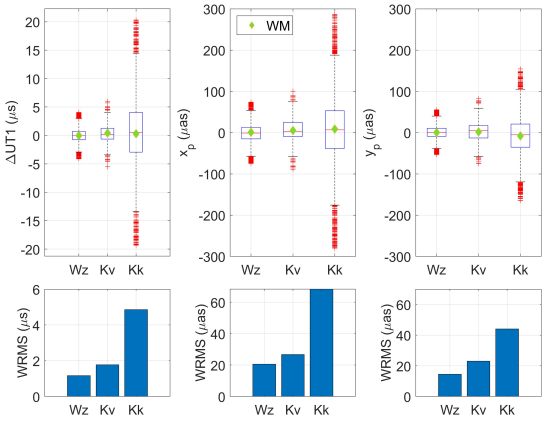

Fig. 3 Statistics showing the comparison of EOP solution, when stations are removed with respect to standard Vienna solution.

Our initial analysis focuses on comparing three different datum time series solutions with respect to the Vienna standard solution. Looking at Fig 3, it becomes apparent that the distribution of variations in UT1-UTC and PM exhibits significant dispersion when Kokee (Kk) is removed from the terrestrial datum, whereas the dispersion is reduced when Wettzell (Wz) is excluded. Notably, the WRMS values are found to be highest when Kk is removed from the terrestrial datum. Upon the removal of Wz, 3449 epochs were compared, while with the exclusion of Kv and Kk, the epochs compared were 484 and 2611, respectively, spanning from 2001 to 2022. Specifically, when Kk is removed, the WRMS value for x_p is 60 μas, compared to 40 μas for y_p. It can be because most of the session in the time frame is best suitable for the estimation of y_p. Nilsson et al. (2014) and Raposo-Pulido et al. (2016) stated that to have a good sensitivity for x_p, N-S long baseline close to 0° or 180° longitude is needed. Consequently, the significant distribution and higher WRMS value in x_p compared to y_p may be due to an insufficient number of N-S baselines after the removal of Wz and Kk. However, since only 484 epochs were compared after the removal of Kv, the difference in WRMS values for x_p and y_p is not as pronounced.

Wettzell (Wz) is located in the European region, surrounded by a cluster of nearby VLBI stations. Conversely, Sejong (Kv) is located in the eastern part with only a few neighboring VLBI stations, and Kokee (Kk) stands as the sole VLBI station in the western part. From Fig 2, it becomes evident that if we eliminate Wz from the datum, there are ten other neighboring stations that can effectively maintain the network geometry. However, removing Kk leaves no other station available to uphold the network geometry. Consequently, the sequential removal of Wz, followed by Kv and Kk, leads to progressively higher WRMS values (Fig 3). Moreover, it is observed that the removal of any station from the terrestrial datum does not have an impact on CPO.

3.2 Comparison w.r.t. IERS 20 C04 and IGS finals solution

In this section, we compare the EOP solutions derived from the removed datum with reference to the IERS 20 C04 and IGS finals solutions. Nilsson et al. (2014) mentioned that WRMS values are independent of the datum. Consequently, we focus our comparison on the WM values in this section.

The WM value for UT1-UTC is found to be highest when Kv is removed. However, it is noteworthy that WM values exhibit similarity regardless of which station is removed from the terrestrial datum. This uniformity in behavior may be attributed to the sensitivity of UT1-UTC, which relies on a long East-West (E-W) baseline, as indicated by Schartner et al. (2021). Consequently, the removal of any of the stations appears to impact the E-W baseline in a comparable manner. A similar pattern is observed for CPO, particularly in the case of dX, but the reason may be different. However, for PM, the WM values concerning the IGS fi-

Table 1 EOP solutions obtained after removing the stations from the datum are compared against IERS 20 C04/IGS finals solution in terms of WM. All units are in μas except for UT1-UTC (μs).

	Wz	Kv	Kk
$UT1-UTC$	−2.24	−2.09	−2.59
dX	1.32	1.3	1.33
dY	−0.83	−0.84	−0.96
x_p	−31.31	−31.3	−30.23
x_p (IGS)	−21.8	−21.38	−16.76
y_p	4.97	5.12	8.41
y_p (IGS)	8.99	9.02	13.67

nals are higher. This outcome aligns with expectations since Global Navigation Satellite Systems (GNSS) offer the most precise PM estimates. This is primarily attributed to the extensive and globally distributed IGS GNSS network, which encompasses hundreds of stations and operates continuously. In contrast, the ITRF data is derived from the combination of various space geodetic techniques. Notably, the removal of Kokee (Kk) has a more substantial impact on PM in comparison to Wettzell (Wz) and Sejong (Kv). This difference may be attributed to the unique geographical position of Kokee as the sole station in the western part.

4 Conclusions and Outlook

Our comparative analysis has examined the effects of removing three distinct stations, individually, from the terrestrial datum on EOP. Within the EOP, CPO exhibit no noticeable impact, regardless of which station is excluded from the datum. Conversely, the influence on UT1-UTC is relatively minor and seems to be contingent on the specific location of the station being removed. Significantly, we have observed a substantial impact on PM, which appears to depend not only on the station's geographical location but also on the density of neighbouring stations. This study highlights the importance of recognizing that the removal of a station from the terrestrial datum can have a significant impact on ERP, particularly when no other nearby stations are available to uphold the network geometry. The study also reveals that the precision of EOP doesn't depend on the number of sessions. It is emphasized that, for datum stability, stations should be strategically removed, only when alternative stations are available in the vicinity to maintain the integrity of the network geometry.

The effect of removing any station from the southern hemisphere has not been addressed in this study. Additionally, separate analyses for stations situated at different longitudes and that affect the E-W baseline, would contribute to a more comprehensive understanding of how station removal influences ERP. A separate analysis can be implemented on the intensive sessions to understand the effect on UT1-UTC.

Acknowledgement

The authors thank OeAD for providing financial support to AL through the Ernst Mach grant, facilitating his stay in Vienna. Additionally, AL extends his heartfelt appreciation to the research team at TU Wien for their valuable research insights and for providing computational resources. He also acknowledges the National Centre for Geodesy, IITK, for their support in covering expenses related to EVGA.

References

Heinkelmann, R., Böhm, J. and Schuh, H., 2007. Effects of geodetic datum definition on the celestial and terrestrial reference frames determined by VLBI.

Plag, H.P., Rothacher, M., Pearlman, M., Neilan, R. and Ma, C., 2009. The global geodetic observing system. In Advances in Geosciences: Volume 13: Solid Earth (SE) (pp. 105-127).

Raposo-Pulido, V., Kayikci, E.T., Heinkelmann, R., Nilsson, T., Karbon, M., Soja, B., Lu, C., Mora-Diaz, J. and Schuh, H., 2016. Impact of Celestial Datum Definition on EOP Estimation and CRF Orientation in the Global VLBI Session IYA09. In IAG 150 Years: Proceedings of the IAG Scientific Assembly in Postdam, Germany, 2013 (pp. 141-147). Springer International Publishing.

Karbon, M., Belda, S. and Nilsson, T., 2019. Impact of the terrestrial reference frame on the determination of the celestial reference frame. Geodesy and geodynamics, 10(1), pp.58-71.

Böhm, J., Böhm, S., Boisits, J., Girdiuk, A., Gruber, J., Hellerschmied, A., Krásná, H., Landskron, D., Madzak, M., Mayer, D. and McCallum, J., 2018. Vienna VLBI and satellite software

(VieVS) for geodesy and astrometry. Publications of the Astronomical Society of the Pacific, 130(986), p.044503.

Nilsson, T., Heinkelmann, R., Karbon, M., Raposo-Pulido, V., Soja, B. and Schuh, H., 2014. Earth orientation parameters estimated from VLBI during the CONT11 campaign. Journal of Geodesy, 88(5), pp.491-502.

Schartner, M., Kern, L., Nothnagel, A., Böhm, J. and Soja, B., 2021. Optimal VLBI baseline geometry for UT1-UTC Intensive observations. Journal of Geodesy, 95(7), p.75.

Exploring reasons for the ITRF2020 VLBI scale drift

K. Le Bail, M. Ishigaki, R. Haas, T. Nilsson, M. Mouyen

Abstract Since the release of the new realisation of the International Terrestrial Reference System, ITRF2020, one of the focuses of the IVS community is to understand the cause of the drift in the VLBI scale factor time series after 2013.75 that is detected by the ITRF team. In this work, we consider the official IVS combined solution, i.e. the IVS contribution to the ITRF2020 realisation, and calculate scale factors using the CATREF software with the single-technique combination strategy that was used to process the ITRF2020. The investigation of time series of Up components of specific IVS stations with the statistical tool BEAST reveals offsets and trends changes that are not taken into account in the ITRF2020. These changes are significant for five IVS stations: NYALES20, WETTZELL, ONSALA60, TSUKUB32, and MATERA. Adding discontinuities for these five IVS stations significantly decreases the VLBI scale drift.

Keywords ITRF, VLBI scale drift, CATREF, BEAST

1 Introduction

The scale of the International Terrestrial Reference Frame (ITRF) is defined by a combination of selected VLBI sessions and SLR weekly solutions. For the first time in the ITRF history, the selected VLBI sessions for the ITRF2020 are not covering the entire IVS observation time span but comprises only sessions up to 2013.75. The reason for this selection is the detection of a drift in the scale factor time series of the VLBI CATREF-combined solution after 2013.75. For more details, see Altamimi et al. (2023).

As a consequence, the IVS Directing Board initiated the creation of an IVS Task Force with the goal of identifying the reasons for this apparent VLBI scale drift. The IVS Task Force works on testing various potential reasons for the VLBI scale drift and on quantifying their impact on the VLBI scale factor time series. The Task Force shall assess the performance of analysis strategies and geophysical models, evaluate the impact of changes in the station network, and investigate local, stations-related issues.

This work focuses on the latter point: our purpose is to find out which stations of the IVS network are potentially affected by noisy data, mis-modeling or critical events that could affect their positions. In Section 2 we describe the data, the tools and the approach we used in this work. Section 3 presents the impact of adding discontinuities for five IVS stations on the VLBI scale factor, and Section 4 concludes this paper, including some recommendations to the IVS and perspectives on future work.

2 Data and analysis approach

We analysed the IVS combined solution that was considered in the calculation of the ITRF2020. We used the Combination and Analysis of Terrestrial REference

Karine Le Bail[1] · Masafumi Ishigaki[2,1] · Rüdiger Haas[1] · Tobias Nilsson[3,1] · Maxime Mouyen[1]
(1) Chalmers University of Technology, Department of Space, Earth and Environment, Onsala Space Observatory, SE–439 92 Onsala, Sweden
(2) Geospatial Information Authority of Japan, Japan
(3) Lantmäteriet – The Swedish mapping, cadastral and land registration authority, Lantmäterigatan 2C, SE-801 82 Gävle, Sweden

Frame (CATREF) software, applying the same analysis strategy as used by the ITRF team for the ITRF2020 production (Altamimi et al., 2023), except for estimation of seasonal components.

The first step was to go through the Up component time series of each of the IVS stations over the time span 2000.0–2021.0 and to extract possible offsets and trend changes that were not considered as discontinuities in the ITRF2020. To detect these, CATREF was run without estimating scale factors and we applied the statistical tool BEAST (Bayesian Estimator of Abrupt change, Seasonal change, and Trend) (Zhao et al., 2019) on the Up component residuals (IVS combined solution w.r.t. ITRF2020) time series for each IVS station. We obtained a list of possible offsets and trend changes that we converted into discontinuities. These discontinuities were not accounted for while computing the original ITRF2020.

The second step was then to add these discontinuities in the CATREF processing and to run the combination a second time. However, in this second run, the scale factors were estimated.

3 Adjusting additional discontinuities

Using the method described in Section 2, five IVS stations showed significant offsets in the time series of their Up component: NYALES20, WETTZELL, ONSALA60, TSUKUB32, and MATERA. The case of NYALES20 is shown separately in Subsection 3.1 since it can be related to a mis-modeling associated to present-day ice melting. The results for the other four stations are presented together in Subsection 3.2.

3.1 The case of NYALES20

When investigating the Up component residual time series of NYALES20 with the BEAST tool, three significant trend changes were detected. These are marked in Figure 1 with solid vertical lines.

The VLBI antenna NYALES20 is colocated at the geodetic site in Ny-Ålesund with several GNSS stations. In the ITRF2020 combination, the collocated GNSS station NYAL was implemented with five different velocities in the discontinuity file, while the VLBI station NYALES20 was considered with one constant velocity over the entire observation time span. We then added the three discontinuities for NYALES20 provided by the BEAST in the VLBI discontinuity file and ran CATREF with this new information. The scale factor drift for the period 2013.75–2021.0 decreased from 0.518 ± 0.066 mm/yr to 0.262 ± 0.065 mm/yr. Many studies show the impact of the present-day ice melting on various sites in the world. Kierulf et al. (2022) discussed the example of Ny-Ålesund, and their conclusions are consistent with our suggestion to model the Up component of NYALES20 with a piecewise linear model.

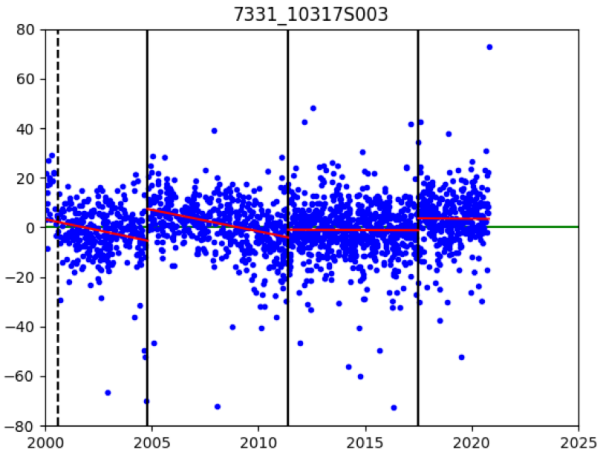

Fig. 1 NYALES20 (7331) Up component CATREF-residuals w.r.t. ITRF2020. CATREF was run using the same strategy than for the ITRF2020, except for seasonal and scale factors estimation. The solid vertical lines indicate epochs of trend changes as identified by the statistical tool BEAST.

Even though the scale drift is significantly decreased, it is not entirely explained. The next subsection looks at four additional stations.

3.2 The cases of TSUKUB32, WETTZELL, MATERA and ONSALA60

We used the BEAST tool also for all other IVS stations, following the approach described above. The BEAST tool detected significant offsets and trend changes for four additional stations: TSUKUB32, WETTZELL, MATERA, and ONSALA60. At TSUKUB32, we observe that

BEAST identifies a change of trend only a few months before the 2011 Tohoku earthquake (top plot in Fig. 2). Since the Tohoku earthquake affected the VLBI measurements at TSUKUB32 MacMillan et al. (2012), we speculate that this change of trend might be due to an imperfect modelling of the co- and post-seismic displacements at this site. However, the occurrence of another instrumental issue, independent from Tohoku earthquake, cannot be ruled out. Regarding ONSALA60 (bottom plot in Fig. 3), the trend change seems to correspond to maintenance work on the subreflector in January 2018, associated to the calculation of a new pointing model. No known reasons explain the detected trend changes for WETTZELL and MATERA.

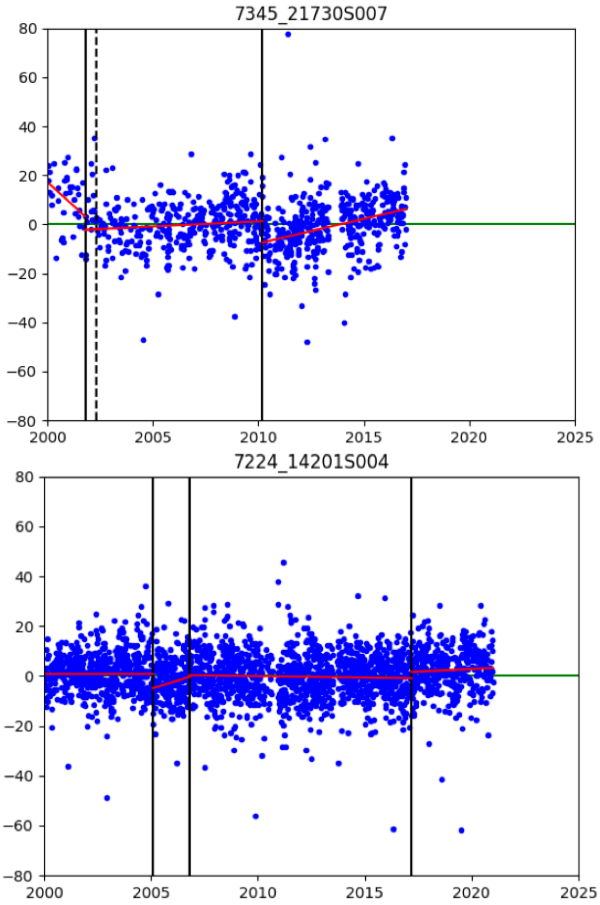

Fig. 2 TSUKUB32 (7345) and WETTZELL (7224) Up component CATREF-residuals w.r.t. ITRF2020. CATREF was run using the same strategy than for the ITRF2020, except for seasonal and scale factors estimation. The solid vertical lines indicate epochs of trend changes as identified by the statistical tool BEAST.

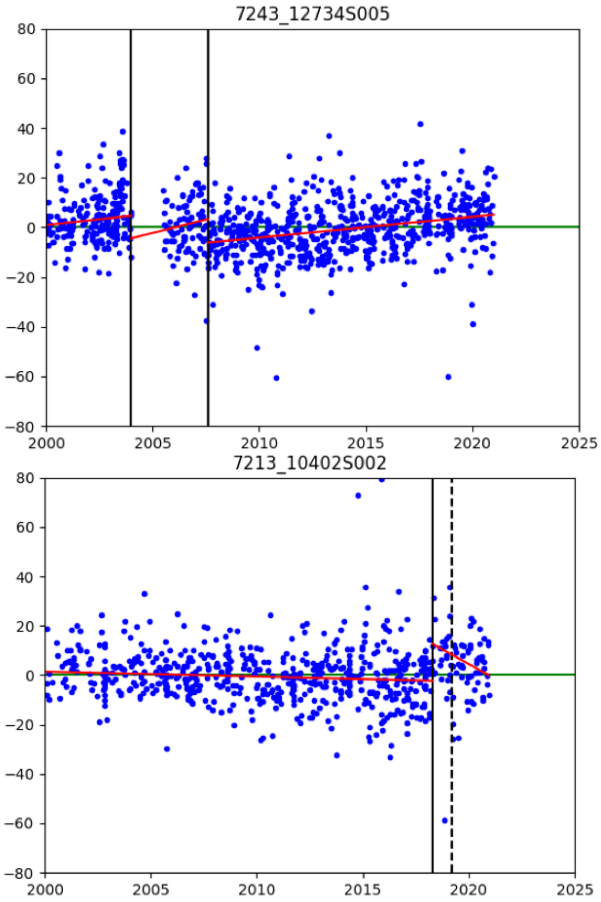

Fig. 3 MATERA (7243) and ONSALA60 (7213) Up component CATREF-residuals w.r.t. ITRF2020. CATREF was run using the same strategy than for the ITRF2020, except for seasonal and scale factors estimation. The solid vertical lines indicate epochs trend changes as identified by the statistical tool BEAST.

The discontinuities for the Up component of these four stations, as detected by BEAST and indicated as solid vertical lines in figures 2 and 3, were then added in the discontinuity file and CATREF was run again with this new information, in addition to the discontinuities added for NYALES20.

The scale factor drift for the period 2013.75–2021.0 decreased from originally 0.518 ± 0.066 mm/yr (no discontinuities added) to 0.262 ± 0.065 mm/yr (three discontinuities added for NYALES20 only), to 0.102 ± 0.064 mm/yr (eleven discontinuities added in total for the five stations NYALES20, TSUKUB32, WETTZELL, MATERA, and ONSALA60).

However, the reasons for the missing discontinuities for TSUKUB32, WETTZELL, MATERA and

Table 1 Scale factor drift over the time span 2013.75–2021.0 using three different discontinuity lists for the CATREF analysis. Original: the discontinuity list used was the origional ITRF2020 discontinuity list. NYALES20 adj.: the discontinuity list was the original discontinuity list plus three discontinuities added for NYALES20 (as determined in Subsection 3.1). 5 stations adj.: the discontinuity list was the original discontinuity list plus three discontinuities added for NYALES20 (as determined in SubSection 3.1), two for TSUKUB32, three for WETTZELL, two for MATERA, and one for ONSALA60 (all as determined in Subsection 3.2).

Scale factor	2013.75–2021.0	drift (mm/yr)
IVS_{ITRF}	Original	0.518 ± 0.066
IVS_{ITRF}	NYALES20 adj.	0.262 ± 0.065
IVS_{ITRF}	5 stations adj.	0.102 ± 0.064

ONSALA60 are not completely understood and are still under investigation.

4 Conclusions

Table 1 and Figure 4 provide a summary of the results. Our results are a demonstration that adding discontinuities significantly flattens the VLBI scale drift of the ITRF2020.

This work outlines the importance of keeping track of what happens at the IVS stations and of monitoring the changes in positions that can be due to change of equipment, service and maintenance events, or updates in models (e.g. pointing model), but may indicate also the necessity to take into account the present-day ice melting impact on station positions.

The next steps of this work are twofold. First, the objective is to find and collect information related to station events that could potentially change the positions of the station reference point, and to test the impact of these station events with the help of the ITRF team. Such a list of station events has to be regularly maintained over time within the IVS, and communicated to the ITRF team. Second, collaboration with geodynamics experts is needed to understand the impact of the present-day ice melting and earthquakes on station positions at specific places in the world.

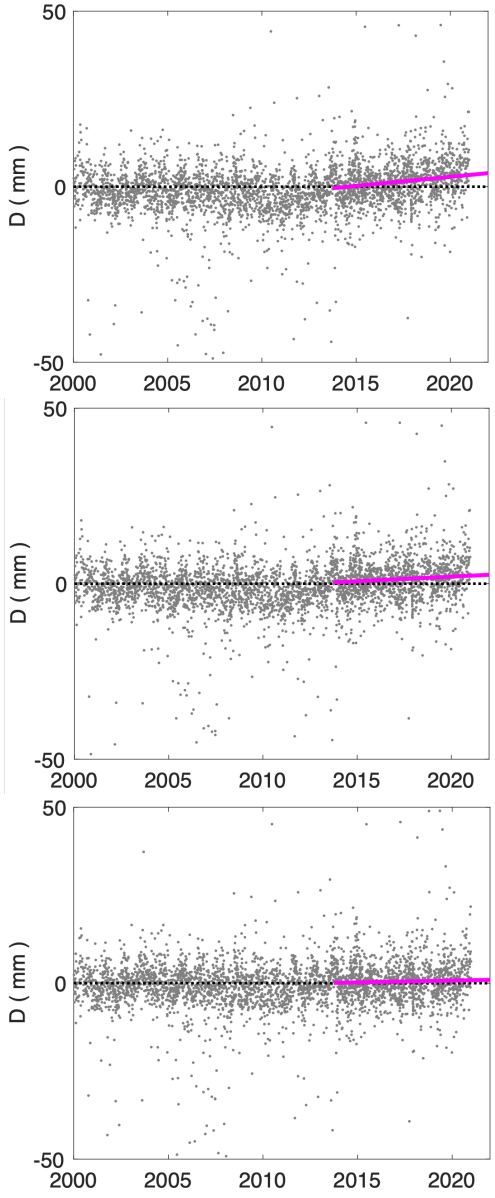

Fig. 4 Scale factor time series over the time span 2000.0–2021.0 using three different discontinuity lists. Top plot (Original): the discontinuity list was the ITRF2020 discontinuity list. Middle plot (NYALES20 adj.): the discontinuity list was the original discontinuity list plus three discontinuities added for NYALES20 (as determined in SubSection 3.1). Bottom plot (5 stations adj.): the discontinuity list was the original discontinuity list plus three discontinuities added for NYALES20 (as determined in Subsection 3.1), two for TSUKUB32, three for WETTZELL, two for MATERA, and one for ONSALA60 (as determined in Subsection 3.2). The solid magenta lines indicate the VLBI scale drift estimated over the 2013.75–2021.0 time span.

Acknowledgments

We are grateful to Zuheir Altamimi for giving us access to the CATREF software, and to the International VLBI Service for Geodesy and Astrometry (IVS) and the IVS Combination Center for providing the VLBI data used in this work.

References

Altamimi Z, Rebischung P, Collilieux X, Métivier L, Chanard K (2023). ITRF2020: an augmented reference frame refining the modeling of nonlinear station motions. *Journal of Geodesy*, 97(47), doi: 10.1007/s00190-023-01738-w.

Kierulf H P, Kohler J, Boy J P, Geyman E C, Mémin A, Omang O C D, Steffen H, Steffen R (2022) Time-varying uplift in Svalbard—an effect of glacial changes. *Geophysical Journal International*, 231(3):1518–1534, doi: 10.1093/gji/ggac264.

MacMillan D, Behrend D, Kurihara S (2012) Effects of the 2011 Tohoku earthquake on VLBI geodetic measurements, *Proceedings 7th International VLBI Service for geodesy and astrometry 2012 General Meeting*.

Zhao K, Wulder M A, Hu T, Bright R, Wu Q, Qin H, Li Y, Toman E, Mallick B, Zhang X, Brown M (2019) Detecting change-point, trend, and seasonality in satellite time series data to track abrupt changes and nonlinear dynamics: A Bayesian ensemble algorithm. *Remote Sensing of Environment*, 232:111–181, doi: 10.1016/j.rse.2019.04.034x.

On the consideration of frequency-dependent illumination functions in modelling signal path variations

M. Lösler, G. Kronschnabl, C. Plötz, A. Neidhardt, C. Eschelbach

Abstract Investigations on the deformation behaviour of the receiving unit of large radio telescopes used for Very Long Baseline Interferometry (VLBI) indicate several elevation-dependent deformation patterns. These include, for instance, elevation-dependent deformations of the main reflector dish, variations in the position of the sub-reflector or the main reflector, or tilts of the sub-reflector. The deformation of the receiving unit yields signal path variations and, if unconsidered, distorts the vertical station position and, hence, the scale of the obtained global geodetic reference frame.
Compensation models for considering signal path variations result from a weighted combination of the overlapping deformation patterns. The corresponding weights are obtained by the intrinsic illumination function of the radio telescope. However, the gain of the feed horn and, thus, the illumination of the aperture depends on the frequency used. Whereas the primary frequency band of legacy radio telescopes is the X-band at about 8.4 GHz, the new generation of radio telescopes participating in the VLBI Global Observing System (VGOS) is designed for broadband reception between 2 GHz and 14 GHz having corresponding illumination functions.
This contribution investigates the impact of frequency-dependent illumination functions on signal path variations for the first time. For that purpose, several data-sets obtained from different feed-horns are analysed, and the impact on the signal path variations is studied.

Keywords Illumination function, Radio telescope, Signal path variation, Deformation, VLBI, VGOS

Michael Lösler · Cornelia Eschelbach
Laboratory for Industrial Metrology, Faculty 1: Architecture, Civil Engineering, Geomatics, Frankfurt University of Applied Sciences, Nibelungenplatz 1, D-60318 Frankfurt am Main, Germany

Gerhard Kronschnabl · Christian Plötz
Geodetic Observatory Wettzell, G 5: Microwave Techniques, Federal Agency for Cartography and Geodesy, Sackenrieder Straße 25, D-93444 Bad Kötzting, Germany

Alexander Neidhardt
Geodetic Observatory Wettzell, Forschungseinrichtung Satellitengeodäsie, Technical University of Munich, Sackenrieder Straße 25, D-93444 Bad Kötzting, Germany

1 Introduction

The analysis of the impact of gravitational deformations of the receiving unit of radio telescopes used for Very Long Baseline Interferometry (VLBI) on global products has become an important topic for geosciences. The main reasons are improvements in radio interferometry and analysis techniques that have significantly improved VLBI results over the past decades. The increased accuracy allows the detection of errors that were previously considered as random noise. Gravitational deformations are systematic errors and limit the reliability and precision of VLBI results. For that reason, the International VLBI Service for Geodesy and Astrometry (IVS, 2019) recently adopted the resolution on the *surveys of radio telescopes for modeling of gravitational deformation*, to investigate the resulting signal path variations (SPV) and to provide appropriate compensation functions.

Based on the pioneer work of Clark and Thomsen (1988), SPV caused by gravity-induced deformations of VLBI radio telescopes are usually modelled by

a weighted sum. The proposed model reads

$$\Delta L(\varepsilon) = \sum_{j \in \mathscr{J}} \alpha_j \Delta_j(\varepsilon), \tag{1}$$

where ε is the elevation angle and Δ parametrizes the deformation of a specific part of the receiving unit. The corresponding weight is α, which depends on the intrinsic (normalized) illumination function I_n of the radio telescope under investigation. The elements of the set $\mathscr{J}$ refer to specific parts of the receiving unit.

According to Clark and Thomsen (1988), for prime focus VLBI radio telescopes, the set $\mathscr{J} = \{F, V, R\}$ consists of the focal length F and the vertex position V of the main reflector, respectively, as well as the receiver position R. The deformations Δ_j refer to the focal length variation Δ_F of the main reflector, the axial shift of the main reflector vertex Δ_V, and the receiver displacement Δ_R along the optical axis. For secondary focus VLBI radio telescopes, Δ_R corresponds to the subreflector displacement along the optical axis, as shown by Abbondanza and Sarti (2010). Nothnagel et al. (2019) extend the set $\mathscr{J}$ by a further component H, which describes the displacement of the feed horn Δ_H. This displacement is to be applied, if the distance between the feed horn and the elevation axis is independent of ε. The corresponding weight reads $\alpha_H = 1$. The great advantage of Eq. (1) is that all components act rotationally symmetrically and, thus, the original spatial problem can be simplified into a projected two-dimensional problem (Abbondanza and Sarti, 2010; Artz et al., 2014).

However, the total deformation of the receiving unit cannot be described exclusively by rotationally-symmetric deformation components. For instance, the main reflector surface may be affected by local deformations and shape-changing deformations. Whereas the first one results from, e. g., misaligned panels (Holst et al., 2015), the second one changes the geometric shape parameterizing the main reflector, e. g., the rotationally-symmetric paraboloid becomes an elliptical paraboloid (Lösler et al., 2018b). Moreover, the subrefector tilts and shifts radially and transversely (Fu et al., 2022; Lösler et al., 2022).

In order to account for all *modelable* deformations changing the path length ΔD, Lösler et al. (2022) propose a universal approach to spatial ray tracing, which evaluates the signal path variations by numerical integration, i. e.,

$$\Delta L(\varepsilon) = \frac{\sum_{\phi=0}^{2\pi} \sum_{r=0}^{\bar{r}} I_\mathrm{n}\left(\gamma_{\phi,r}\right) r \Delta D_{\phi,r}(\varepsilon)}{\sum_{\phi=0}^{2\pi} \sum_{r=0}^{\bar{r}} I_\mathrm{n}\left(\gamma_{\phi,r}\right) r}. \tag{2}$$

The polar coordinates of the incoming ray w.r.t. the frame of the receiving unit are the direction ϕ and the distance r as depicted in Fig. 1. The main reflector radius is $\bar{r}$, the aperture angle is 2γ, and I_n denotes the (normalized) illumination function. According to Lösler et al. (2022), Eq. (1) provides a sufficient first-order approximation, if rotationally-symmetric components dominate.

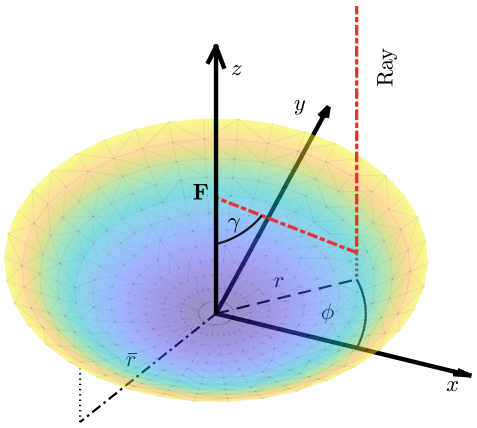

Fig. 1: Polar coordinates ϕ and r of the incoming ray w.r.t. the frame of the receiving unit. The main reflector radius of the depicted prime focus VLBI radio telescope is $\bar{r}$. The angle of incidence of the received ray is γ, and $\mathbf{F}$ denotes the focal point.

Common to both approaches is the introduction of the telescope's illumination function for zonal weighting. However, the gain of the feed horn and, thus, the illumination of the aperture depends on the frequency f. Whereas legacy radio telescopes observe in X-band at about $8.4\,\mathrm{GHz}$, the new generation of VGOS radio telescopes is designed for broadband reception between $2\,\mathrm{GHz}$ and $14\,\mathrm{GHz}$ having corresponding illumination functions $I(f)$. Thus, the signal path variation $\Delta L(\varepsilon, f)$ depends on the elevation angle ε and the frequency f. Whereas elevation-dependent deformations are undisputed and proven, the impact of frequency-dependent illumination functions on signal path variations has not yet been investigated in detail. This contribution

continuous the work of Abbondanza and Sarti (2010) and extends the investigation of Lösler et al. (2023).

2 Geodetic Observatory Wettzell

The Geodetic Observatory Wettzell (GOW) is jointly operated by the Federal Agency for Cartography and Geodesy and the Forschungseinrichtung Satellitengeodäsie (FESG; engl. Satellite Geodesy Research Facility) of Munich Technical University. The observatory is a core-station within the Global Geodetic Observing System (GGOS) and hosts instruments of all basic space geodetic techniques (Hugentobler et al., 2011). For VLBI, the legacy $20\,\mathrm{m}$ Radio Telescope Wettzell (RTW) as well as two modern $13.2\,\mathrm{m}$ VGOS-specified radio telescopes, the Twin Telescopes Wettzell (TTW), are operated.

In order to evaluate the signal path variations of these VLBI radio telescopes, a comprehensive measurement campaign was carried out in the fall of 2021. The RTW and the southern antenna TTW-2 were equipped with photogrammetric black and white coded targets as shown in Fig. 2. An unmanned aerial vehicle (UAV) was used to capture these targets in several elevation positions of the antenna. A detailed description of the measurement campaign is given by Greiwe et al. (2023). The photogrammetric data were analyzed by the in-house software package JAiCov (2021) and elevation-dependent deformations Δ were detected (Lösler et al., 2022). According to Eqs. (1) and (2) these deformations are weighted by means of telescope-specific illumination function.

For legacy S/X VLBI radio telescopes the illumination function should refer to the X-band because S-band observations are basically used to reduce the effect of ionospheric dispersion, and the X-band represents the primary observations in geodetic VLBI (Schuh, 1987, Ch. 6.2.2). However, VGOS radio telescopes are designed for broadband reception from $2\,\mathrm{GHz}$ to $14\,\mathrm{GHz}$ (Petrachenko et al., 2009, Ch. 4.1). Therefore, the question arises which frequency should be used for deriving the illumination function or whether a frequency-dependent parameterization is necessary.

Fig. 2: Unmanned aerial vehicle in front of the prepared legacy $20\,\mathrm{m}$ VLBI radio telescope RTW at GOW, which is equipped with coded photogrammetric targets at the whole receiving unit.

3 Illumination function

The illumination function introduced as a zonal weighting scheme in Eqs. (1) and (2) describes the exploited intensity of the areas of the aperture. Usually, the function is rotationally symmetric and reduces the influence of errors by downweighting regions of low intensity (Baars, 2007, Ch. 4.2). The aperture illumination of the VLBI radio telescope is an intrinsic property but usually undocumented, and the function has to be reconstructed from discrete samples. However, measuring the gain at several aperture angles is elaborated, and often only the relation along the optical axis at $\gamma_{\mathrm{min}} = 0^\circ$ and at the edge for γ_{max} are known. Due to such a small sample size, the evaluation of suitable functions is difficult or almost impossible, as already mentioned by Nothnagel (2020).

Currently, two functional models are primarily used to characterize illumination, namely the Gaussian function and the cosine-squared function (Lösler et al., 2023). The use of a Gaussian function is mainly physically motivated, because the best approximation of the field radiated by a circular feed horn represents a Gaussian beam. For that reason, Abbondanza and Sarti (2010) *strongly* recommend to model the illumination by a Gaussian function. A common Gaussian function having its maximum at $\gamma = 0^\circ$ reads

$$I^{\mathrm{g}}(\gamma) = g_0 + g_1 \exp\left(-\frac{\gamma^2}{g_2^2}\right), \tag{3}$$

where g_0 is the ordinate shift, g_1 scales the height of the peak, and g_2 parametrizes the width of the bell-shaped curve (Lösler et al., 2023)

The cosine-squared function is introduced by Artz et al. (2014). Even though this function is not based on physical principles, it is supposed to be commonly used in the radio astronomical community. According to Nothnagel et al. (2019), the functional model is given by

$$I^{\mathrm{c}}(\gamma) = c_0 + c_1 \cos^2(\gamma c_2), \tag{4}$$

where c_0 is the ordinate shift, c_1 is the amplitude, and c_2 is a damping coefficient scaling the angle of incidence γ.

Another heuristic approach to describe the functional relationship is to use n-th order polynomial functions. However, choosing a suitable order of such a polynomial function is challenging, because polynomial functions tend to large oscillations near the edge if n gets large. This effect is well-known as Runge phenomenon reported in 1901. In order to keep the number of coefficients small but identical w.r.t. Eqs. (3) and (4), a third order polynomial function is chosen. The functional model reads

$$I^{\mathrm{p}}(\gamma) = p_0 + p_1\gamma + p_2\gamma^2 + p_3\gamma^3. \tag{5}$$

To ensure the maximum in the aperture center, the necessary and sufficient conditions are

$$I^{\mathrm{p}'}(0^\circ) = p_1 = 0, \tag{6a}$$
$$I^{\mathrm{p}''}(0^\circ) = 2p_2 < 0, \tag{6b}$$

respectively. For that reason, the parameters to be estimated are p_0, p_2, and p_3, with $p_2 < 0$.

Hereinafter, a superscript $^{\mathrm{c}}$, $^{\mathrm{p}}$, and $^{\mathrm{g}}$ refers to the cosine-squared function, the polynomial function, and the Gaussian function, respectively.

4 Analyses and results

In order to evaluate the impact of frequency-dependent illumination functions on signal path variations, two data sets obtained from different feed horns are investigated. The first set is taken from the TTW-1, which is equipped with a Quadruple-Ridged Flared Horn (QRFH). The second one relates to the TTW-2, which uses the Eleven Feed. A set consists of seven series having ten sampling points each. The series refer to specific frequencies, i. e., 2 GHz, 3 GHz, 5 GHz, 6 GHz, 8 GHz, 10 GHz, and 11 GHz.

Eqs. (3)-(5) are used to specify the functional model of the illumination functions. The coefficients are obtained by means of least-squares adjustment, treading the sample points as observations. To serve as zonal weighting function in Eqs. (1) and (2), the illumination function has to fulfil the condition

$$\int_{\mathscr{A}} k I \,\mathrm{d}\mathscr{A} = 1 \tag{7}$$

over the entire aperture $\mathscr{A}$ of the antenna (Abbondanza and Sarti, 2010), where k is the normalization factor obtained from

$$\frac{1}{k} = 2\pi \int_{\gamma_{\min}}^{\gamma_{\max}} I(f,\gamma)\,\mathrm{d}\gamma. \tag{8}$$

Figure 3 compares the results of the estimated normalized illumination functions $I_{\mathrm{n}}(f,\gamma)$ of the Eleven Feed and the QRFH for different angles of incidence γ and frequencies f. The polynomial model $I_{\mathrm{n}}^{\mathrm{p}}$, the cosine-squared model $I_{\mathrm{n}}^{\mathrm{c}}$, and the Gaussian model $I_{\mathrm{n}}^{\mathrm{g}}$ are depicted in green solid, blue dashed, and red dashed-dotted style, respectively. For a single frequency, the curves obtained from different functional models are quite similar, and one can conclude that the choice of functional model has only a minor effect on the results. However, the dependence of the results on the frequency is evident for both feed horns under investigation.

The weights introduced in Eq. (1) are obtained from the normalized illumination function $I_{\mathrm{n}}(f,\gamma)$. As shown by Clark and Thomsen (1988), the weights are linearly dependent on α_R, i. e.,

$$\alpha_R(f) = \lambda \int_{\mathscr{A}} h(\gamma)\, I_{\mathrm{n}}(f,\gamma)\,\mathrm{d}\mathscr{A}, \tag{9a}$$
$$\alpha_F(f) = \lambda - \alpha_R(f), \tag{9b}$$
$$\alpha_V(f) = -1 - \alpha_R(f), \tag{9c}$$

where $\lambda = 1$ for prime focus telescopes and $\lambda = 2$ for secondary focus telescopes. The function $h(\gamma)$ describes the extra path length caused by a unit vertical shift $\Delta_R = 1$. Suitable functions $h(\gamma)$ for different telescope types are discussed by Lösler (2021, Ch. 5.3).

Figure 4 compares the resulting weights $\alpha_R(f)$ of the Eleven Feed and the QRFH for different frequen-

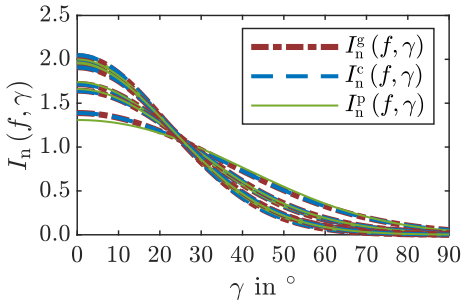

(a) QRFH (TTW-1)

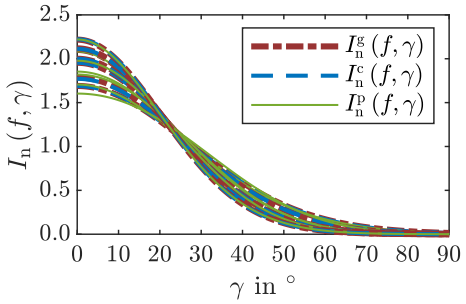

(b) Eleven Feed (TTW-2)

Fig. 3: Frequency-dependent normalized illumination functions $I_\mathrm{n}(f,\gamma)$ of the QRFH (a) and the Eleven Feed (b) using different functional models. Green, blue and red curves relate to the polynomial model, the cosine-squared model, and the Gaussian model, respectively.

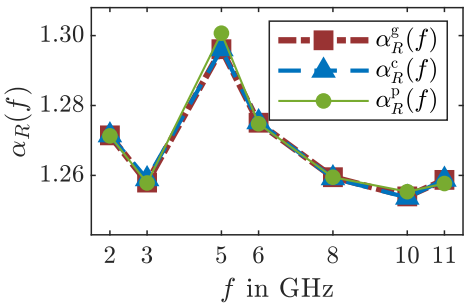

(a) QRFH (TTW-1)

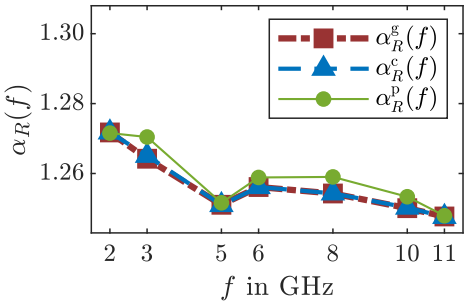

(b) Eleven Feed (TTW-2)

Fig. 4: Frequency-dependent weights $\alpha_R(f)$ of the QRFH (a) and the Eleven Feed (b) using different functional models. Green, blue and red curves relate to the polynomial model, the cosine-squared model, and the Gaussian model, respectively.

cies f. The weight of the Eleven Feed slightly decreases as the frequency increases. The sample points of the QRFH are more noisy and a similar behavior cannot be clearly identified.

Obviously, the weights are largely independent of the functional model used. In particular, the results obtained from the cosine-squared model and the Gaussian model are almost identical, as indicated by the corresponding mean values given in Table 1. Moreover, if the weights of the two feed horns are compared to each other, equivalent values are obtained.

According to Lösler et al. (2022), the elevation-dependent variation of the main reflector focal length Δ_F, the axial shift of the main reflector vertex Δ_V, and the sub-reflector displacement Δ_R are given by

$$\Delta_F(\varepsilon) = -1.07\,\mathrm{mm}\cos\varepsilon, \tag{10a}$$
$$\Delta_V(\varepsilon) = -0.08\,\mathrm{mm}\cos\varepsilon, \tag{10b}$$
$$\Delta_R(\varepsilon) = 1.16\,\mathrm{mm}\,(1-\sin\varepsilon), \tag{10c}$$

Table 1: Mean values of the weight α_R w.r.t. the Eleven Feed and the QRFH using different functional models. $\bar{\alpha}_R^\mathrm{g}$, $\bar{\alpha}_R^\mathrm{c}$, and $\bar{\alpha}_R^\mathrm{p}$ relate to the polynomial model, the cosine-squared model, and the Gaussian model, respectively.

Feed Horn	$\bar{\alpha}_R^\mathrm{g}$	$\bar{\alpha}_R^\mathrm{c}$	$\bar{\alpha}_R^\mathrm{p}$
Eleven Feed	1.257	1.257	1.259
QRFH	1.268	1.268	1.268

respectively. Combining the deformations given by Eqs. (10) and the weights obtained from Eqs. (9) yields the signal path variation $\Delta L(\varepsilon,f)$ via Eq. (1), which depends on ε and f. Due to the small variations of the weights, the deviations between the resulting SPV are small, as depicted in Fig. 5. The maximum deviation,

$$\delta = \max\Delta L(\varepsilon,f) - \min\Delta L(\varepsilon,f), \tag{11}$$

of the Eleven Feed and the QRFH is about $0.05\,\mathrm{mm}$ and $0.1\,\mathrm{mm}$, respectively, which corresponds to a time delay of less than $0.4\,\mathrm{ps}$. According to Petrachenko et al. (2009, Ch. 3.3), a delay measurement precision of about $4\,\mathrm{ps}$ is required, to achieve the GGOS goal of $1\,\mathrm{mm}$ in positions on global scales.

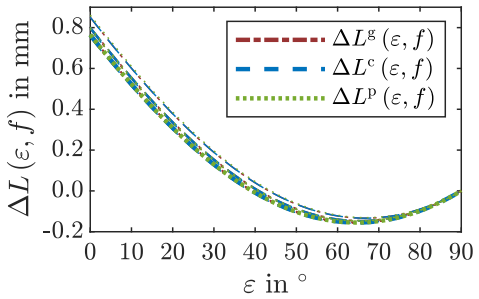

(a) QRFH (TTW-1)

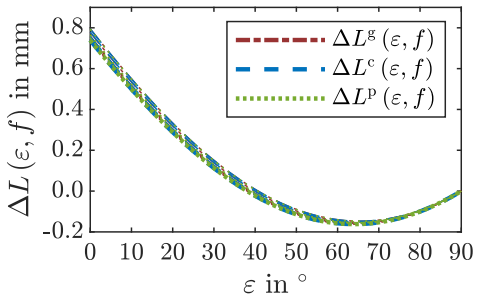

(b) Eleven Feed (TTW-2)

Fig. 5: Signal path variation w.r.t the elevation angle ε as well as the frequency f for the QRFH (a) and the Eleven Feed (b). Green, blue and red curves relate to the polynomial model, the cosine-squared model, and the Gaussian model, respectively.

Figure 5 depicts the SPV of the Eleven Feed and the QRFH, respectively. The range is about $0.9\,\mathrm{mm}$ and corresponds to a time delay of about $3\,\mathrm{ps}$. Obviously, the determined SPV are almost unaffected of the frequency and the functional model describing the illumination. The variations are mainly caused by deformations of components of the receiving unit of the VLBI radio telescope. Assuming a similar deformation behavior for both TTW, the SPV can be compensated by the same correction function.

5 Conclusion

Gravity-induced deformations of VLBI radio telescopes yield signal path variations and, thus, bias obtained global results. Particularly, the estimation of the vertical station position is significantly affected by signal path variations, as recently shown by Varenius et al. (2021). Different approaches are known for modeling SPV. The most commonly used approach is derived by Clark and Thomsen (1988), and is based on a weighted sum of the main deformations of the receiving unit. This approach is widely used for legacy VLBI radio telescopes, and is considered the current standard model (Nothnagel, 2020).

A more complex approach applies spatial ray tracing to the whole receiving unit. This approach outperforms the standard model, because it is able to consider any kind of modelable deformations. In contrast to the standard model, which reduces the computational burn by converting the spatial problem into a projected two-dimensional problem, ray tracing is applied to the original spatial problem (Lösler et al., 2018a, 2022). Common to both approaches is the introduction of the telescope-specific illumination as a zonal weighting function. Since the new generation of VGOS radio telescopes is designed for broadband reception, and the gain of the feed horn depends on the frequency, the question arises which frequency should be used for specifying the illumination function or whether a frequency-dependent parameterization is necessary.

In this contribution, the impact of frequency-dependent illumination functions on signal path variations was studied. In total 14 data sets obtained from an Eleven Feed and a Quadruple-Ridged Flared Horn used by the Twin Telescopes Wettzell were investigated in detail. Moreover, suitable functional models for parameterizing the illumination function were evaluated, namely the cosine-squared function, the polynomial function, and the Gaussian function. Previous studies imply a significant influence of the selected functional model on signal path variations, but are based on only a small sample size. Thus, an objective evaluation was not possible so far (Nothnagel, 2020).

The dependence between the results and the introduced functional model is negligible. All functions under investigation are suitable to model the illumi-

nation function. In particular, the results based on the cosine-squared function and the Gaussian function are almost identical. Whereas the cosine-squared function and the polynomial function are heuristic models, the Gaussian function is physically motivated (Abbondanza and Sarti, 2010). For that reason, the Gaussian function is preferred to any other function.

The frequency has also only a minor impact on the results. A slightly dependency of the frequency onto the modeled signal path variation was detected for the Eleven Feed. Due to the noisy data of the QRFH, a similar conclusion could not be seriously drawn. However, the effect is less than $0.4\,\mathrm{ps}$ and – at least – one order of magnitude smaller than the total variation. Compared to the uncertainty of the measured deformations, this impact is currently negligible. The structural deformation of the receiving unit is by far the most important contribution to the signal path variation.

References

Abbondanza C, Sarti P (2010) Effects of illumination functions on the computation of gravity-dependent signal path variation models in primary focus and Cassegrainian VLBI telescopes. *J Geod*, 84(8), 515–525. doi: 10.1007/s00190-010-0389-z

Artz T, Springer A, Nothnagel A (2014) A complete VLBI delay model for deforming radio telescopes: the Effelsberg case. *J Geod*, 88(12), 1145–1161. doi: 10.1007/s00190-014-0749-1

Baars JWM (2007) The Paraboloidal Reflector Antenna in Radio Astronomy and Communication – Theory and Practice. Springer, New York. doi: 10.1007/978-0-387-69734-5

Clark TA, Thomsen P (1988) Deformations in VLBI Antennas. NASA-TM-100696, Greenbelt.

Fu LB, Liu JJ, Yan W, Kong DQ, Ren X, Liu CD, Zhang HB (2022) Gravitational Deformation Measurement Method for the Main Reflector and Sub-reflector of the 70 m Antenna by Laser Scanner. *Res Astron Astrophys*, 22(9). doi: 10.1088/1674-4527/ac6e5a

Greiwe A, Brechtken R, Lösler M, Eschelbach C, Plötz C, Kronschnabl G, Neidhardt A (2023) Close-Range Photogrammetry for Antenna Deformation Measurements. *Proceedings of the 26th European VLBI for Geodesy and Astrometry (EVGA) Working Meeting*, Geodetic Observatory Wettzell, Federal Agency for Cartography and Geodesy.

Holst C, Nothnagel A, Blome M, Becker P, Eichborn M, Kuhlmann H (2015) Improved area-based deformation analysis of a radio telescope's main reflector based on terrestrial laser scanning. *J Appl Geod*, 9(1), 1–14. doi: 10.1515/jag-2014-0018

Hugentobler U, Neidhardt A, Lauber P, Ettl M, Schreiber KU, Dassing R, Klügel T, Riepl S, Herold G, Kronschnabl G, Plötz C, Hessels U (2011) The Geodetic Observatory Wettzell – A fundamental reference point. *Geological Field Trips in Central Western Europe: Fragile Earth International Conference*, Munich, 1–6. doi: 10.1130/2011.0022(01)

IVS (2019) Surveys of radio telescopes for modeling of gravitational deformation. *IVS-Res-2019-01*, International VLBI Service for Geodesy and Astrometry (IVS), Directing Board, https://ivscc.gsfc.nasa.gov/about/resolutions/IVS-Res-2019-01-TelescopeSurveys.pdf

JAiCov (2021) Java Aicon Covariance matrix – Bundle Adjustment for Close-Range Photogrammetry. https://github.com/applied-geodesy/bundle-adjustment

Lösler M (2021) Modellbildungen zur Signalweg- und in-situ Referenzpunktbestimmung von VLBI-Radioteleskopen. *Deutsche Geodätische Kommission*, Series C, 865, Munich.

Lösler M, Eschelbach C, Greiwe A, Brechtken R, Plötz C, Kronschnabl G, Neidhardt A (2022) Ray tracing-based delay model for compensating gravitational deformations of VLBI radio telescopes. *J Geod Sci*, 12(1), 165–184. doi: 10.1515/jogs-2022-0141

Lösler M, Eschelbach C, Haas R (2018a) Bestimmung von Messunsicherheiten mittels Bootstrapping in der Formanalyse. *zfv*, 143(4), 224–232. doi: 10.12902/zfv-0214-2018

Lösler M, Eschelbach C, Haas R (2018b) Zur Modellierung eines Ring-Focus-Paraboloids. In Luhmann T, Schumacher C (eds.), *Photogrammetrie – Laserscanning – Optische 3D-Messtechnik*, 222–234, Wichmann, Offenbach.

Lösler M, Kronschnabl G, Plötz C, Neidhardt A, Eschelbach C (2023) Frequenzabhängige Modellierung von Signalwegvariationen an VLBI-Radioteleskopen. *zfv*, 148(3), 177–187. doi: 10.12902/zfv-0429-2023

Nothnagel A (2020) Very Long Baseline Interferometry. In Freeden W, Rummel R (eds.), *Mathematische Geodäsie/Mathematical Geodesy*, 1257–1314, Springer, Berlin. doi: 10.1007/978-3-662-55854-6_110

Nothnagel A, Holst C, Haas R (2019) A VLBI delay model for gravitational deformations of the Onsala 20 m radio telescope and the impact on its global coordinates. *J Geod*, 93(10), 2019–2036. doi: 10.1007/s00190-019-01299-x

Petrachenko B, Niell A, Behrend D, Corey B, Böhm J, Charlot P, Collioud A, Gipson J, Haas R, Hobiger T, Koyama Y, MacMillan D, Malkin Z, Nilsson T, Pany A, Tuccari G, Whitney A, Wresnik J (2009) Design aspects of the VLBI2010 system. NASA/TM-2009-214180, Washington.

Runge CDT (1901) Über empirische Funktionen und die Interpolation zwischen äquidistanten Ordinaten. *Z Angew Math Phys*, 46, 224–243.

Schuh H (1987) Die Radiointerferometrie auf langen Basen zur Bestimmung von Punktverschiebungen und Erdrotationsparametern. *Deutsche Geodätische Kommission*, Series C, 328, Munich.

Varenius E, Haas R, Nilsson T (2021) Short-baseline interferometry local-tie experiments at the Onsala Space Observatory. *J Geod*, 95(5), 54. doi: 10.1007/s00190-021-01509-5

The Australia-Japan VGOS observation

S. Matsumoto, L. McCallum, J. McCallum, A. Jaradat, M. Ishigaki, H. Yoshifuji, T. Kobayashi

Abstract The final goal of VLBI Global Observing System (VGOS) is to get the initial results of station position and earth orientation parameters (EOPs) in less than 24h. However, it takes a lot of time to get the results at present because of the huge amount of the data. This is true for the actual results, as well as for initial performance feedback for new VGOS stations. The Australia-Japan VGOS observations were started with the purpose to (1) perform first intercontinental VGOS observations to the new Hobart VGOS station and (2) to develop expertise in VGOS processing. The AUJ program are VGOS observations between Ishioka (Japan), Hobart and Katherine (Australia). We performed eight sessions scheduled for 3 hours in the same time range of R1 sessions in 2022 and present first results.

Keywords VGOS, EOP

1 Introduction

The VLBI Global Observing System (VGOS) which has been promoted by International VLBI Service for Geodesy and Astronomy (IVS) (Nothnagel et al., 2017) is the new observation system designed to achieve the high accuracy by using the smaller and faster slewing antenna and observing broadband frequency. The final goal of the VGOS is continuous measurement of station position and EOP and get the initial results in less than 24h (Petrachenko et al., 2009). However, at the moment, it takes a minimum of about 30 days to get the results, mainly because of the huge amount of the data that needs to be transported to the correlators (Behrend et al., 2023).

We started the VGOS mode observations for EOP determination between Ishioka (Japan), Hobart and Katherine (Australia) called AUJ (Australia - Japan) session. These three stations have smaller and faster slewing antennas and are equipped with broadband receivers. Besides the operational aim of performing VGOS observations, a scientific goal of the AUJ sessions could be to determine the EOPs in less turnaround time, enabled through short sessions on a small station network with reasonable data connections. We performed eight sessions scheduled for 3 hours in the same time range of R1 sessions in 2022. Here we show the first results from the AUJ observations and the comparison with those of R1 sessions and discuss future plans for these observations.

2 Observation

2.1 Plans

The AUJ observations are conducted with IVS VGOS mode (3, 5, 6 and 10 GHz). To evaluate the results, we conducted the observations in the time range of the R1 sessions. Figure 1 shows the stations participating the AUJ observations. Table 1 shows the status of AUJ VGOS mode observations in 2022. In 2022, we held 3 hours observations 8 times totally, once in two weeks

Saho Matsumoto · Masafumi Ishigaki · Hiroyuki Yoshifuji · Tomokazu Kobayashi
Geospatial Information Authority of Japan, 1 Kitasato, Tsukuba, Ibaraki, Japan

Lucia McCallum · Jamie McCallum · Ahmad Jaradat
University of Tasmania, Private Bag 37, Hobart 7001, Australia

Fig. 1 Stations participating the AUJ observations.

basically. The Katherine station has been available in VGOS mode after a new sampler was ready, allowing observations between three stations.

2.2 Stations

The AuScope Geodetic VLBI array (Lovell et al., 2013; McCallum et al., 2021) is managed by the University of Tasmania (UTAS), contracted through Geoscience Australia. The 12 m telescope at the Mt. Pleasant Radio Astronomy Observatory (Hobart 12) has participated in IVS sessions since 2010. Since its upgrade in 2015 it has VGOS facility, which is able to observe the frequency range of 2.2 - 14 GHz and participates in the both of broadband and S/X sessions. The slew speed of the antenna is 5deg/sec for azimuth (AZ) and 1.25deg/sec for elevation (EL).

After the VGOS upgrade of Katherine, , it also joined the AUJ sessions. The telescope of the Katherine station is the same type as Hobart and finally the broadband observation became possible in the middle

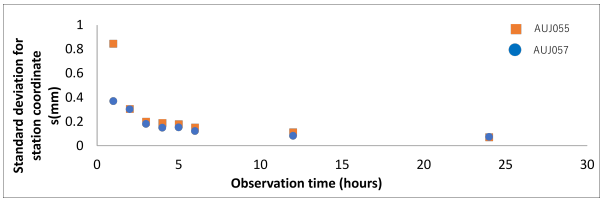

Fig. 2 Standard deviation for simulated station coordinate in difference observation time range.

of 2022.

Geospatial Information Authority of Japan (GSI) operates the 13 m telescope at the Ishioka geodetic observing station. The slew speed of the antenna is 12 deg/sec for AZ and 6 deg/sec for EL. It has the broadband receiver (2-14 GHz) and participate in both IVS VGOS observation and in S/X observation (see the details in Matsumoto et al. (2021)).

2.3 Scheduling and Simulation

We prepared the schedule files for AUJ sessions using "VieSched++" (Schartner and Böhm., 2019). For the VGOS mode observation, we made the schedules using fixed scanlengths of 30s. Further we made use of the optimization tool of the VieSched++ software, trialing multiple schedules with changing the weight for multi parameters, and selected the optimal one by trial and error which has high signal-to-noise (S/N) ratio and low formal errors for simulated EOPs.

We also run the simulations to see the expected accuracy of estimated values from the schedule file. This was used in order to get an idea of a suitable session length. We used the VieVS software (Böem et al., 2018) for the simulations. Figure 2 shows the standard deviation of station coordinates for simulated AUJ055 and AUJ057 for different observing times. Following this investigation, we selected a session duration of 3 hours for the AUJ sessions.

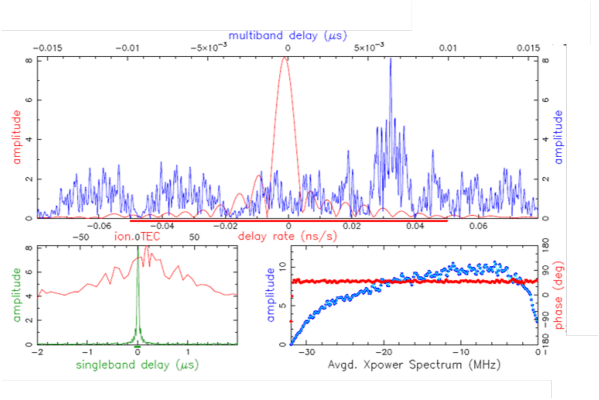

Fig. 3 Detected fringe between Ishioka and Katherine in AUJ068.

2.4 Observation, Correlation and Analysis

All stations which participate in the AUJ sessions can be operated remotely. We operated Hobart and Katherine from UTAS and for Ishioka from GSI remotely. We conducted all eight observations as planned in Table 1.

After the observation, the data for Ishioka was transferred to UTAS and correlated with the DifX software correlator (Deller et al., 2007). We used the software Fourfit to detect the fringe. We have detected the fringes for each session. Figure 3 shows the fringe between Ishioka and Katherine in AUJ068. It shall be noted here, that there was no working phasecal for these sessions and a manual phasecal solution was applied. Subsequent analysis was done using VieVS.

Table 1 AUJ VGOS mode observations in 2022

	Session	Day	Stations
1	AUJ055	June 14, 9:00–12:00	Hobart, Ishioka
2	AUJ057	June 28, 9:00–12:00	Hobart, Ishioka
3	AUJ059	July 12, 9:00–12:00	Hobart, Ishioka
4	AUJ061	July 26, 9:00–12:00	Hobart, Ishioka
5	AUJ064	August 17, 10:00–13:00	Hobart, Ishioka
6	AUJ066	August 30, 9:00–12:00	Hobart, Ishioka, Katherine
7	AUJ068	September 13, 9:00–12:00	Hobart, Ishioka, Katherine
8	AUJ070	September 27, 11:00–14:00	Hobart, Ishioka, Katherine

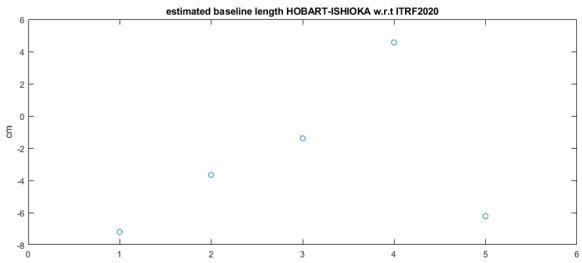

Fig. 4 Estimated baseline length Hobart – Ishioka.

3 Results

The most important result is the successful performance of those sessions. In particular, new expertise was developed at GSI to schedule and correlate VGOS observations. In terms of geodetic results, this first set of sessions has not performed as possibly expected. When looking at the estimated baseline length between Ishioka and Hobart12, we find a repeatability at the level of a few cm (see figure 4).

We will show the preliminary estimated EOP results in figure 5. Horizontal axis means the number of observations in the Table 1 and vertical axis shows the estimated parameters. The results from the AUJ sessions and R sessions at the same time of AUJ observation are plotted by blue and orange colored circles, respectively. In addition, simulated values from schedule files are also plotted by gray circles. The error bar shows the standard deviations of each estimated parameters for the AUJ sessions.

For some observations, we had experienced some instrumental problems during the observation, and thus it may affect the data quality. In addition, for the VGOS observation with short and fixed observation time range for one scan, the detectability of the fringe depends on the flux structure of the target source. To improve the quality of the results, we need to consider these things more carefully when we create the schedule file.

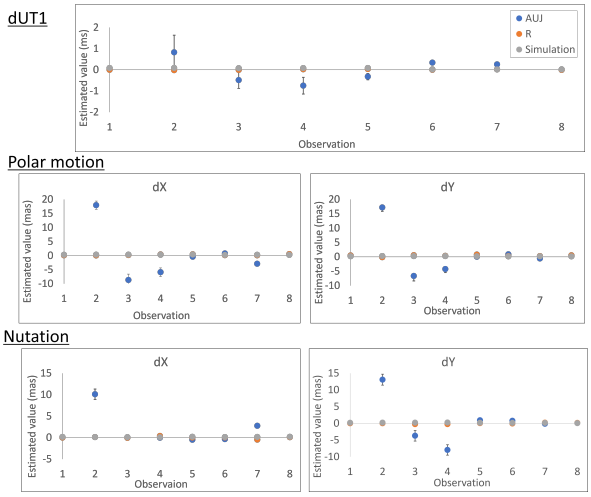

Fig. 5 Estimated EOP value for AUJ and R sessions.

4 Conclusions and outlook

We started the VGOS observation between Australia and Japan named “AUJ observation”. A scientific aim of these sessions could be to determine EOPs with VGOS in less turnaround time, enabled through short sessions on a small station network with reasonable data connections. Yet, the data quality needs to be improved in order to meet expected precision of the results. We conducted 8 observations in 2022, and succeeded in processing the VGOS sessions, all the way through geodetic analysis. We think we can expand the possibility for the use of VGOS observation (facility) if we can get the enough accurate results from the observation with less observations time and between less stations. We will continue the observation with reviewing scheduling, observation, correlation, and analysis method.

References

Behrend D, Ruszczyk C, Elosegui P, Weston S (2023) Status of the VGOS Infrastructure Rollout, in IVS 2022 General Meeting Proceedings, edited by Kyla L. Armstrong, Dirk Behrend, and Karen D. Baver, *NASA/CP-20220018789*.

Böhm J, Böhm S, Boisits J, Girdiuk A, Gruber J, Hellerschmied A, Krásná H, Landskron D, Madzak M, Mayer D, McCallum J, McCallum L, Schartner M, Teke K (2018) Vienna VLBI and Satellite Software (VieVS) for Geodesy and Astrometry. *Publications of the Astronomical Society of the Pacific*, 130, 044503, doi: 10.1088/1538-3873/aaa22b.

Deller A. T, Tingay S. J, Bailes M, West C (2007) DiFX: A Software Correlator for Very Long Baseline Interferometry Using Multiprocessor Computing Environments. *Publications of the Astronomical Society of the Pacific*, 119, 318, doi: 10.1086/513572.

Lovell J. E. J, McCallum J. N, Raid P. B, McCulloch P. M, Baynes B. E, Dickey J. M, Shabala S. S, Watson C. S, Titov O, Ruddick R, Twilley R, Reynolds C, Tingay S. J, Shield P, Adada R, Ellingsen S. P, Morgan J. S, Bignall H. E (2013) The AuScope geodetic VLBI array. *Journal of Geodesy*, 87, 527–538, doi: 10.1007/s00190-013-0626-3.

McCallum L, McCallum J, Chuan L. C, Hankey W, Jaradat A, McCarthy T, Calvés G. M, Reid B, Salarpour S (2021) AuScope VLBI Array and Hobart 26-m Antenna, in International VLBI Service for Geodesy and Astrometry 2019+2020 Biennial Report, edited by D. Behrend, K. L. Armstrong, and K. D. Baver, *NASA/TP-20210021389*.

Matsumoto S, Ueshiba H, Nakakuki T, Takagi Y, Hayashi K, Yutsudo T, Mori K, Nozawa K (2021) Ishioka Geodetic Observing Station – 13.2-m Radio Telescope, in International VLBI Service for Geodesy and Astrometry 2019+2020 Biennial Report, edited by D. Behrend, K. L. Armstrong, and K. D. Baver, *NASA/TP-20210021389*.

Nothnagel A, Artz T, Behrend D, Malkin Z (2017) International VLBI Service for Geodesy and Astrometry: Delivering high-quality products and embarking on observations of the next generation. *Journal of Geodesy*, 91, 711–721, doi: 10.1007/s00190-016-0950-5.

Petrachenko B, Niell A, Behrend D, Corey B, Böhm J, Charlot P, Collioud A, Gipson J, Haas R, Hobiger T, Koyama Y, MacMillan D, Malkin Z, Nilsson T, Pany A, Tuccari G, Whitney A, Wresnik J (2009) Design Aspects of the VLBI2010 System. *Progress Report of the IVS VLBI2010 Committee*.

Schartner M and Böhm J (2019) VieSched++: A New VLBI Scheduling Software for Geodesy and Astrometry. *Publications of the Astronomical Society of the Pacific*, 131, 084501, doi: 10.1088/1538-3873/ab1820.

RFI monitoring using “mark5access” spectra and Python programs

A. Neidhardt, R. Aktas, L. Rigon, Ch. Plötz

Abstract RFI monitoring is always an essential task. We made some experiments to monitor spectral power levels using the ”mark5access” spectra data from each scan in combination with Python code to generate spectrograms (waterfall plots). It is a straight forward method to present basic RFI information on-the-fly during or directly after a session.

Keywords ”RFI” monitoring, spectrograms, Python tools

1 Introduction

Radio frequency interference or related receiving of unwanted signals with radio telescopes is an increasing issue. With the coming of new authorized frequency bands for satellite Internet or mobile telecommunication, unpolluted frequency ranges become really rare. In combination with strong senders at the base stations sending into all directions, the situation is a critical point for VGOS setups with broad band over a large frequency range. The issue is not only a reduced quality. The over-saturated receiving units lead to complete blackouts of whole bands or in critical situations even to a destruction of low-noise amplifiers used in cryogenic dewar environments. The results are high costs or even the end of a service at some areas.

The knowledge of potential dangerous signals or changing scenarios around observatories resulting from new sending stations is important and a first step to adapt to a changing environment. While professional equipment like broadband spectrum analyzer and direction finders are expensive, so that continuous monitoring is not yet given at most network stations of the IVS, existing equipment can be used to get a first qualitative overview. Software like the ”mark5access” library of the DiFX correlation software (see Brisken (2023)), originally also installed on Mark5 data recorders to give a local possibility of data quality checks, can be used to create spectra plots. A selection of plot data over complete 24 hour sessions in combination with pointing information give a suitable basis to create sky plots showing directions of the strong sources.

The following paper describes a demonstrator written in Python which creates spectra plots and sky plots using the existing software packages.

A. Neidhardt
FESG Wettzell, Technical University of Munich, Geodetic Observatory Wettzell, Sackenrieder Str. 25, D-93444 Bad Kötzting, Germany

Rozerin Aktas, Luca Rigon
Technical University of Munich, Forschungseinrichtung Satellitengeodäsie Arcisstr. 21, D-80333 München Germany

Christian Plötz
Federal Agency for Cartography and Geodesy Geodetic Observatory Wettzell, Sackenrieder Str. 25, D-93444 Bad Kötzting, Germany

2 Test workflow

A first test with an elementary demonstrator was done during the project ”Joining up Users for Maximizing the Profile, the Innovation and Necessary Globalization of JIVE” (Jumping JIVE) funded by the European Union (see JIVE (2019)). The demonstrator was written in Python and was able to create single spectra plots

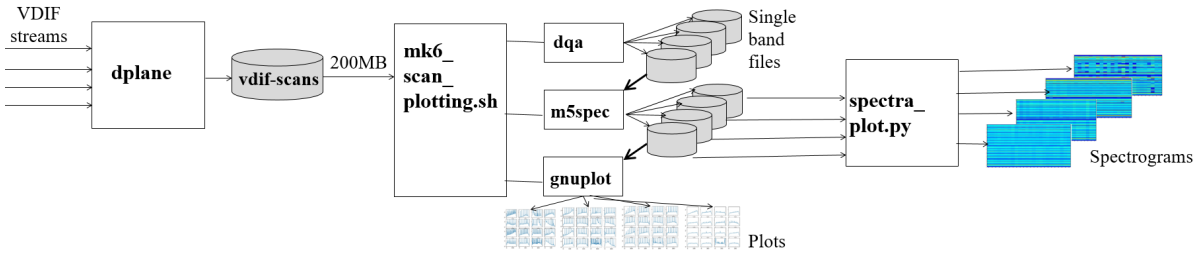

Fig. 1 Test workflow.

for each band of a scan (see Fig. 2) and spectrograms (waterfall plots) for predefined time intervals. Directions had to be added manually to the spectra plots using the information from session summary files generated by the VLBI Field System (originally NASA Field System, see Himwich (2023)).

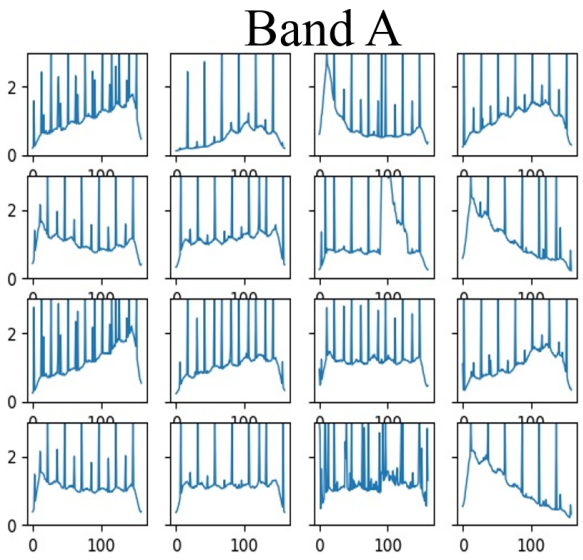

Fig. 2 Power spectra plot of a typical band A at Wettzell observatory with impacts of unwanted signals.

The workflow of the demonstrator is shown in Fig. 1. The focus was put on VGOS data, because they show broader bands and the impact of RFI is much worse. VDIF data from the DBBC/FILA10G systems were recorded on the Mark6 recorders. Each scan produces a corresponding file set on the disks of one or more modules. 200 MB of one of these multi-threaded files for each single scan was copied after each recording. Such a multi-threaded file chunk is a snapshots of the whole scan. The files were converted to single band files using the Mark6 tool "dqa", so that four different files were created representing band A (3032.4 - 3512.4 MHz), B (5272.4 - 5752.4 MHz), C (6392.4 - 6872.4 MHz), and D (10232.4 - 10712.4 MHz) (see Ming (2022)). Each band itself uses eight 32 MHz-channels for horizontal and eight 32 MHz-channels for vertical polarization, so that a selection of frequencies are represented within the band.

The separated files were used to create power spectra numbers using "m5spec" from the "mark5access" library of the DiFX software (see Brisken (2008)). Additionally, "gnuplot" was used to produce single spectra plots for each scan directly after each scan. These plots were used as real-time feedback for operators to evaluate the quality of the bands, e.g. if phase calibration tones with necessary signal power could be detected. The power spectra values were stored on separated directories for a later processing while the session was ongoing. All of the described steps were managed by a shell script "mk6_scan_plotting.sh", which was called each time after the recording in the "postob" procedure of the session schedule.

After completing of a session, a separate Python script was used to read the spectra values and produce waterfall plots (spectrograms). They show the time on the x-axis, the frequency range on the y-axis, and the power spectra numbers as qualitative "power counts" with a color range over x an y. The result is a sequence of color plots. The time interval can be selected, so that single hours or the complete 24 hour sesion can be printed.

These spectrograms give a qualitative level of signal power over time. Together with the pointing information of the telescope from the summary files generated by the VLBI Field System (see Fig. 4), pointing

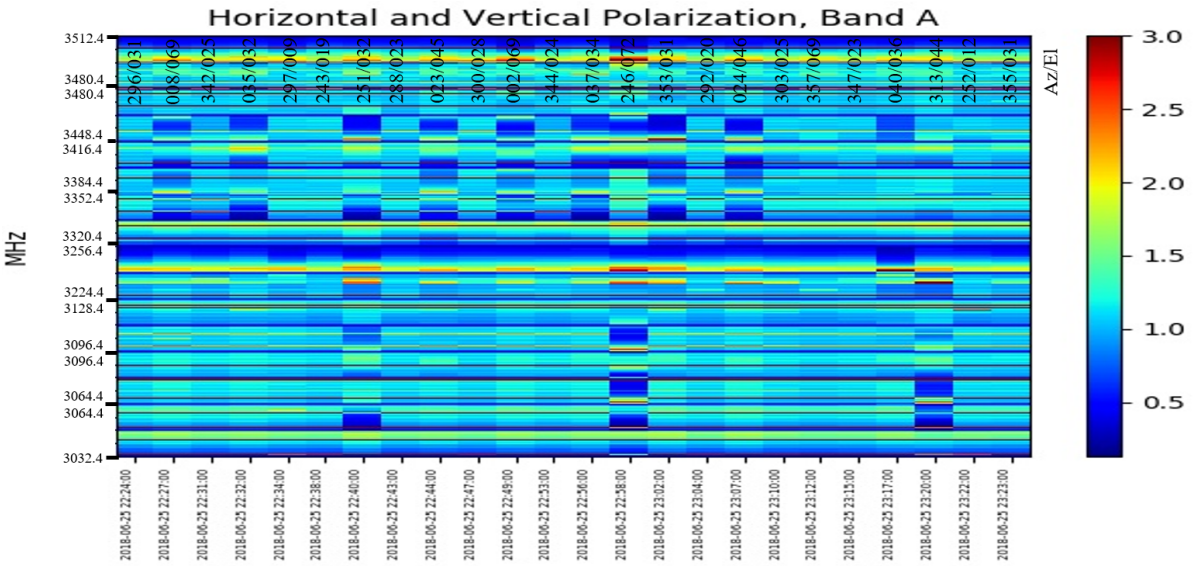

Fig. 3 First results of a spectrogram of band A with reference data using session "vt8175ws" of the year 2018.

```
176-2223  2078 0016+731  22 43 CW    22:23:12  22:23:42   0:30   3747.8
176-2224  2095 1144+402 296 31 CW    22:24:47  22:25:17   0:30   3778.6
176-2227  2112 3C371      8 69 CW    22:27:30  22:28:00   0:30   3809.3
176-2231  2129 0800+618 342 25 CW    22:31:26  22:31:56   0:30   3840.0
176-2232  2146 0059+581  35 32 CW    22:32:40  22:33:10   0:30   3870.7
176-2234a 2163 1040+244 297  9 CW    22:34:56  22:35:26   0:30   3901.4
176-2238  2180 1351-018 243 19 NEUTR 22:38:45  22:39:15   0:30   3932.2
176-2240  2197 0716+714 351 32 CW    22:40:28  22:40:58   0:30   3962.9
176-2243  2214 1156+295 288 23 CW    22:43:20  22:43:50   0:30   3993.6
176-2244  2231 0016+731  23 45 CW    22:44:57  22:45:27   0:30   4024.3
176-2247  2248 1144+402 300 28 CW    22:47:27  22:47:57   0:30   4055.0
176-2249  2265 3C371      2 69 CW    22:49:55  22:50:25   0:30   4085.8
176-2253  2282 0800+618 344 24 CW    22:53:50  22:54:20   0:30   4116.5
```

Fig. 4 Selection of a summary file describing the scans of a session in the NASA Field System giving information of antenna pointing (highlighted area).

directions can be added for each timestamp. This gives a first hint of directions with higher power received by the antenna.

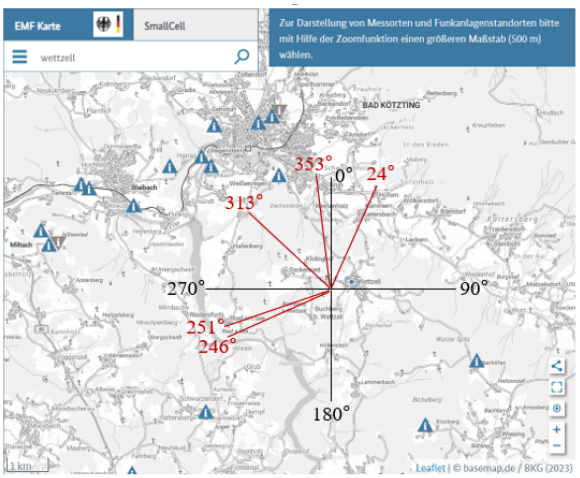

https://www.bundesnetzagentur.de/DE/Vportal/TK/Funktechnik/EMF/start.html

Fig. 5 Sample of manual analysis of the data from Fig. 3 using the EMF map of the German Bundesnetzagentur.

3 First results

Each test with a changed Python program is done using data session "vt8175ws" of the year 2018 because the first program was finished at this time and new results can always be compared to the original output. A spectrogram of band A for the time interval June 25th, 2018 22:24-23:24 UTC is shown in Fig. 3. The y-label with the frequency band were added manually. The new programs from 2023 do this automatically. Additionally, a first combination with azimuth and elevation values from the summary file were made. The values on top of the diagram were manually arranged to the right timestamp. This gives a first hint of directions with high power levels in the band.

Additionally, the German regulation authority for frequencies, the Bundesnetzagentur, offers an EMF

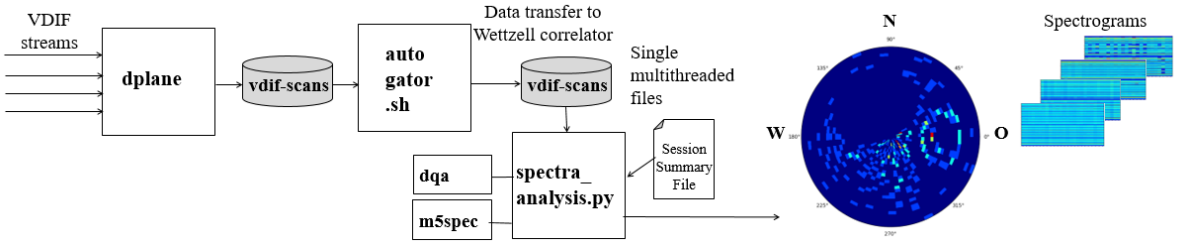

Fig. 6 Workflow of the planned, automated analysis.

map showing registered base station senders for mobile telecommunication (see BNETZA (2023)), which can be used to overlay the directional information from the spectrogram. A manual sample is shown in Fig. 5. The map shows the directions having the highest power levels within the defined hour. This gives a first good evaluation of the quality, because it is assumed that they will point to senders in the near environment of the observatory around Bad Kötzting.

While the first manual demonstrations do not yet offer a scientific accreditation, they are a first proof of concept, so that further tests are valuable.

4 Conclusions and outlook

Because of the benefit having such an on-the-fly approach to get RFI information directly as byproduct of the real VLBI data, the TUM finances a student position over half a year to stabilize and extend the software. Most of the manual parts should be automated, so that waterfall models and other plots can be controlled using program argument lists. The program should produce sky plots and other useful outputs. Additionally, the snapshots of each scan should be produced automatically on the Flexbuff storage after the recording and gathering of all scans of a complete observation. This avoids time delays and unwished influences during recording. This means an extension at different levels resulting in a workflow shown in Fig. 6.

The following further tasks are planned:

- Test of the software with current data sets from the year 2023
- Use of legacy S/X-data as well as VGOS data
- Implementation of utilities from a direction finder, like maps with arrows or zoom bands
- Stabilization of the software, so that it can be used at other antenna sites or eventually regularly at correlators
- Establishing as GitHub tool
- Evaluation of power levels to avoid influences of specific sources
- Evaluation to convert the qualitative power value counts to real quantitative power levels using continuous system temperatures

Acknowledgment: This project has received funding from the European Union's Horizon 2020 research and innovation programme under grant agreement No 730884 - JUMPING JIVE.

References

Brisken, W.: Walter Brisken's library for reading Mark5 and similar VLBI-format data. https://github.com/demorest/mark5access, Download 2023-10-31

Brisken W.: A Guide to Software Correlation Using NRAO - DiFX Version 1.0. NRAO-DiFX-UserGuide.pdf, NRAO, Tech.Rep., http://www.aoc.nrao.edu/ wbrisken/NRAO-DiFX-1.0/, 2008

Bundesnetzagentur: EMF Karte. https://www.bundesnetzagentur.de/DE/Vportal/TK/Funktechnik/EMF/start.html, Download 2023-06-01.

Himwich, E.: VLBI Field System. https://github.com/nvi-inc/fs, Download 2023-10-31

Ming H. Xu, Tuomas Savolainen, James M. Anderson, Niko Kareinen, Nataliya Zubko, Susanne Lunz, Harald Schuh: Impact of the image alignment over frequency for the VLBI Global Observing System. Astronomy and Astrophysics, Volume 663, https://www.aanda.org/articles/aa/full_html/2022/07/aa40840-21/aa40840-21.html#T3, July 2022

JIVE: JUMPING JIVE https://jive.eu/jumping-jive, Download 2021-06-29.

New features of the IVS Seamless Auxiliary Data Archive (IVS SADA) and the EVN Monitor

A. Neidhardt, S. Seidl, A. Keimpema

Abstract Auxiliary and meta data can be collected and offered seamlessly with the IVS Seamless Auxiliary Data Archive (IVS SADA). Some antennas supported the data injection and especially with the Wettzell antennas it is possible to test new features. A similar approach is made for the EVN with the EVN monitor. The presentation explains the functional principle of the IVS SADA and shows new features and possibilities.

Keywords Auxiliary data, data archive, meta data

1 Introduction

The IVS Seamless Auxiliary Data Archive (IVS SADA) and the EVN Monitor was explained in detail in "IVS Seamless Auxiliary Data Archive (SADA) and EVN Monitor" in IVS 2022 General Meeting Proceedings (see Neidhardt (2022)). Both are databases accessible from the Internet to receive auxiliary meta data from radio observatories containing status, health, and helpful information used for correlation and analysis. Data can be extracted from this database using a Python script on the basis of an Application Programming Interface (API) for the monitoring system ZABBIX, so that auxiliary data can be extracted seamlessly.

The benefits of such an archive are:

A. Neidhardt, S. Seidl
FESG Wettzell, Technical University of Munich, Geodetic Observatory Wettzell, Sackenrieder Str. 25, D-93444 Bad Kötzting, Germany

A. Keimpema
Joint Institute for VLBI ERIC, Oude Hoogeveensedijk 4, 7991 PD Dwingeloo, The Netherlands

- Continuous, auxiliary data are of high interest
- Additional data might be interesting for research
- A centralized data repository is easy to access
- A real-time overview of the observation network is valuable
- Preparations for dynamic observations might be possible

This paper gives a short overview of further and current ongoing developments.

2 Extended methods of data injection

The regular mechanism to inject data is to run a program "zabbix_sender" via an encrypted SSH call. The program expects a list of arguments containing the identifier of the data (key), the value, etc. The sampling rate is greater or equal to one second. But it automatically creates a local timestamp for the value without a consideration of delays generated by the sending over the Internet.

If a timestamp should be added by the sender holding the real date and time of creation of the data, a special table with UNIX timestamp, key and value must be created which is then piped ("forwarded") to the sender.

To simplify the injection without these troublesome process, a new program "datasender" was implemented at the EVN monitor (see Keimpema (2023)). The program simplifies the workflow so that the UNIX timestamp can be directly added as program argument with an own identifier.

Additionally, people at Wettzell observatory continuously extends the API script "ZabbixAPI.py" to not only support the extraction of data but also to send

data via the Zabbix API. This would mean that the script can be used for sending and receiving of data.

A disadvantage of this new script is that it requires the installation of the script and Python3 on the sending computer at the observatories, which is not necessary with the original method and the "datasender" by EVN. But the script would help to reduce the processor load on the server machines, because each SSH call of the SSH injection methods has a chain of activations of operating system programs as consequence (e.g. "sshd", "dbus", "polkitd", "postgresqld"). Benchmarks has shown that many injections with a repetition of one second can increase the processor load tremendously, which is not the case if the API via an Apache Web server is used.

3 Extensions for data extractions

#Date	Unixtime	Value
2022-03-15 18:29:01	1647368941	911.0114
2022-03-15 18:28:01	1647368881	911.0114
2022-03-15 18:27:01	1647368821	911.0114
2022-03-15 18:26:01	1647368761	911.0114
2022-03-15 18:25:02	1647368702	911.0114
2022-03-15 18:24:02	1647368642	910.9211
2022-03-15 18:23:01	1647368581	910.9211
2022-03-15 18:22:01	1647368521	910.9211
2022-03-15 18:21:01	1647368461	910.9211
2022-03-15 18:20:02	1647368402	910.9211
2022-03-15 18:19:01	1647368341	910.8493
2022-03-15 18:18:02	1647368282	910.8493
2022-03-15 18:17:02	1647368222	910.8493
2022-03-15 18:16:01	1647368161	910.8493
2022-03-15 18:15:02	1647368102	910.8493

Fig. 1 Resulting table of a data request to get seamless auxiliary pressure values.

Neidhardt (2022) describes the standard way to request data with the Python script "ZabbixAPI.py". The program currently understands the following arguments:

- -h, –help: show this help message and exit
- -ASC: Order values ascending (together with -K/-I and -L)
- -ALL: Print all hosts and not just enabled ones (in combination with -H and -L)
- -C CONFFILEPATH: Use specified Configuration file
- -DESC: Order values descending (together with -K/-I and -L)
- -f: Print output to file with standard filename
- -F FILENAMEOUT: Print output to file with individual filename
- -G: Show a list of graphs of a host (together with -H)
- -GID GRAPHID: Select a graph with graph-id and download PNG
- -GW GRAPHWIDTH: Width of graph-PNG
- -GH GRAPHHEIGHT: Height of graph-PNG
- -GF GRAPHFILE: Filepath of graph-PNG
- -H HOST: Select host with hostname or host ID
- -I ITEM: Select item with ID
- -K KEY: Select item with key
- -L: Show a list of hosts, items (together with -H), or values (together with -K/-I/-TS/-TE)
- -LIM LIMIT: Limit the number of requested records
- -P: Show a list of problems (also together with -H/-TS/-TE)
- -SIG SIGNLFOUR: Check problems and activate DERDACK SIGNL4 (https://www.signl4.com/de/) with team secret
- -TS STARTDATE: Start time of records ["YYYY-MM-DD HH:MM:SS"]
- -TE STOPDATE: Stop time of records ["YYYY-MM-DD HH:MM:SS"]
- -VL VERBOSITYLEVEL: Verbosity level [0=off, 1=basic, 2=detailled]

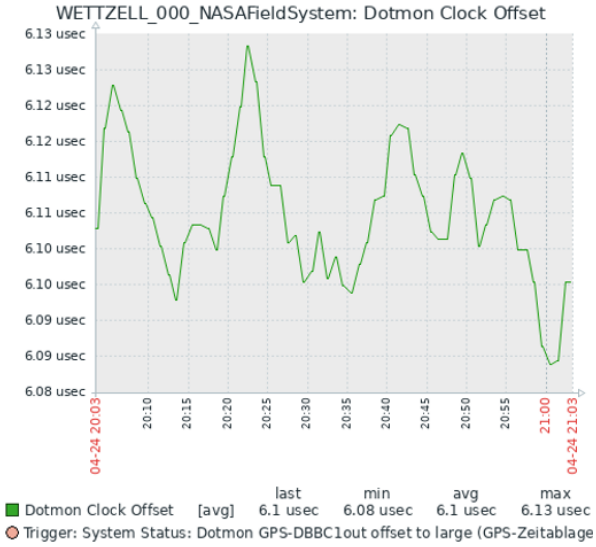

Fig. 2 Resulting sample PNG graph image of seamless auxiliary pressure values.

The standard request to get individual seamless data sets e.g. is `python.exe ZabbixAPI.py -C config_evn.ini -L -H YEBES_000_NASAFieldSystem -K ERC.PRESSURE -TS "2022-03-15 18:15:00" -TE "2022-03-15 18:30:00"`, which requests a list of pressure data for the time period March 15th, 2023 18:15 to 18:30 UT of antenna YEBES using the ZABBIX configuration in "config_evn.ini". The result is shown in Fig. 1. The data table can also be stored to a text

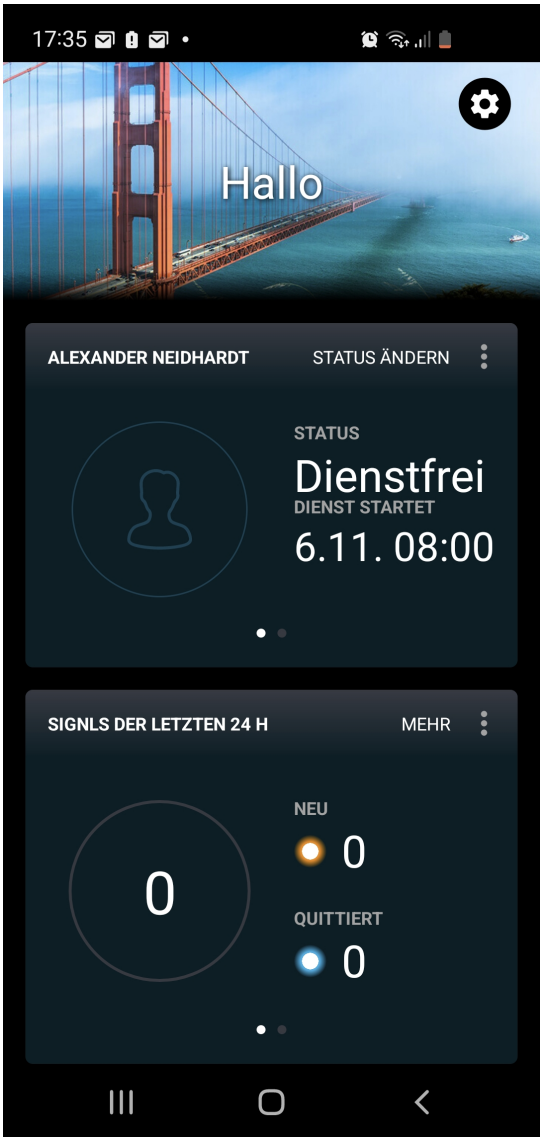

Fig. 3 Sample APP screen for DERDACK SIGNL4 showing the latest signals sent by the webhook of the ZabbixAPI script.

file, so that it can be read by another program to plot or process extracted data.

Very new is the feature to directly get plots as PNG files for specified time periods. The corresponding arguments are "-GID" (graph identifier in ZABBIX), "-GW" (width of resulting PNG), "-GH" (height of resulting PNG), and "-GF" (filepath to store PNG). A simple request e.g. is `python.exe ZabbixAPI.py -C config_evn.ini -GID 1237` and the result is shown in Fig. 2.

Another very new feature is the activation of a webhook to send alerts to DERDACK SIGNL4, a mobile alerting and anywhere incident management platform (see Derdack (2023)), using the argument "-SIG". The call checks the alarms of the latest full minute. If a new alert of a specific level is active, it sends a signal to DERDACK SIGNL4 and activates an alerting sequence by phone call, SMS, and SIGNL4 APP on mobile phones (see Fig. 3) according to a predefined duty scheduling for the on-call service. The system is used to organize the automatic alerting during autonomous VLBI observations at Wettzell observatory.

4 Ongoing work for automated session reports

```
Quality report:
===============
Session: i23158
Antenna: wz
Scheduled sources:      32
Operated sources:       32
Failed sources:          0
Successful sources:     32
   - normal quality:    19
   - reduced quality:   13 (ONSOURCE, TSYS, METEO)
===============
List of scans and sources which might have reduced quality:
     |---> i23158_wz_158-1835(1039+811), i23158_wz_158-1837(0552+398), i23158_wz_158-1839(1846+322),
           i23158_wz_158-1841(0016+731), i23158_wz_158-1843(0602+673), i23158_wz_158-1851(0613+570),
           i23158_wz_158-1853(2229+695), i23158_wz_158-1855(1803+784), i23158_wz_158-1903(0613+570),
           i23158_wz_158-1904(0552+398), i23158_wz_158-1907(2000+472), i23158_wz_158-1909(2309+454),
           i23158_wz_158-1929(0613+570)
===============
```

Fig. 4 Sample quality report.

Currently the work is ongoing on the basis of the new features. A new Python script is under development which creates session reports directly after the session containing

- a quality report which is generated from session log files using specific regular expressions and error messages (see Fig. 4),
- plots for temperature, humidity, pressure, cable, and clock offset taken from ZABBIX via "ZabbixAPI.py" as described,
- and a list of the error messages taken from the log file.

The script is no yet completed, but quality reports are generate regularly for all Wettzell antennas, so that even quality numbers can be derived for the different months of a year and a whole year used as quality metrics for the quality process at Wettzell (see Schüler (2019). Additionally, all related files (SNP, PRC, sum-

mary files, etc.) are stored in a session archive for all Wettzell antennas, so that they can be evaluated later in case of issues found later in the processing of the sessions.

5 Conclusion

Even if currently not too many stations participate, Wettzell benefits from such an archive for it's own antennas. The system offers a live health status, so that on-call staff can interact just in time. Sytsem changes can be detected due to long time series. Trends can be found and algorithms can be evaluated against.

This would also be beneficial for the whole IVS network. In combination with other performance metrics taken from correlation and analysis reports, it would help to improve the whole network using a fast feedback loop. Some of the parameters are already prepared, e.g. for the AuScope telescopes. Therefore, an idea to combine these programs came up during the EVGA workshop. It might lead to a new working groupd for IVS Success Analyis and Station Feedback, which uses automated feedback structures. People at AuScope and at the TUM already started to generalize their codes. The TUM even funded a student job to implement the extraction of some details from log files and so on. First team meetings are already held. Further on, a combination with ideas of dynamic scheduling or VLBI Communications Center (VCC) might also lead to faster turnarounds.

Acknowledgment: This project has received funding from the European Union's Horizon 2020 research and innovation programme under grant agreement No 730884 - JUMPING JIVE.

References

Keimpema Aard: EVN Monitor. https://deki.mpifr-bonn.mpg.de/ Working_Groups/EVN_TOG/EVN_Monitor, Download 2023-10-31.

Derdack: DERDACK SIGNL4. Mobile Alerting and Anywhere Incident Management. https://www.signl4.com/?noredirect=en_US, Download 2023-10-31.

Neidhardt A., Plöotz Ch., Verkouter M., Keimpema A., Weston S.: IVS Seamless Auxiliary Data Archive (SADA) and EVN Monitor. https://ivscc.gsfc.nasa.gov/publications/gm2022/12_neidhardt_etal.pdf, Download 2023-10-31.

JIVE: JUMPING JIVE https://jive.eu/jumping-jive, Download 2021-06-29.

Schüler T., Probst W., Plötz Ch., Neidhardt A., Seidl S.: First Experiences with the VLBI Quality Control System at Wettzell Proceedings of the 26th EVGA Working Meeting, 2023

Improved modelling for future VLBI contributions to ITRF

T. Nilsson, K. Le Bail, R. Haas

Abstract In the latest realization of the International Terrestrial Reference System, ITRF2020, the VLBI scale seems to have a drift after 2013.75. The reason for this is not yet understood. In this work we investigate if it could be caused by one of the models used in the VLBI data analysis. To begin with, we show that the drift is reduced by 40 % if two additional breaks are added to the Ny-Ålesund station. Furthermore, we investigate the impact of the models for gravitational deformation, thermal deformation, pole tide, geophysical loading, celestial reference frame, and post seismic deformations. Our results show that none of the models could explain of the scale drift completely, although by changing models for geophysical loading and post seismic displacement, the drift could be reduced by 20 %. The results also show that some models – like those for thermal deformation, pole tide, and geophysical loading – could introduce seasonal signals in the estimated scale if not applied in the VLBI analysis.

Keywords VLBI, ITRF, Scale

1 Introduction

Very Long Baseline Interferometry (VLBI) is used, together with Satellite Laser (SLR), to realize the scale of the International Terrestrial Reference Frame (ITRF). Hence, it is important that the scale provided by VLBI has a high quality. However, for the latest ITRF solution, ITRF2020 (Altamimi et al., 2023), it was noted that the VLBI scale had a drift after 2013.75. For this reason, VLBI sessions observed after 2013.75 do not contribute to the ITRF2020 scale. The reason for this apparent VLBI scale drift is so-far not known.

Several suggestions on what could be causing the VLBI scale drift have been made. One possibility is problems at one or more stations. This could be either technical problems with the antenna or receiver, or non-linear station motions not taken properly into account in the ITRF combination. For example, it has been suggested that one explanation could be that the VLBI station at Ny-Ålesund, Spitsbergen, Norway, experiences a non-linear land uplift due to present-day ice-melting (Kierulf et al., 2022). Since this was not taken into account in the ITRF2020 combination, it could have affected the ITRF2020 scale.

Another possibility could be problems in one (or more) of the models used in the VLBI data analysis. For example, for ITRF2020 gravitational deformation models were applied for six stations, for the first time in an ITRF solution. It is known that correcting for the gravitational deformation affects the estimated station coordinates, especially the height, thus this might also affect the ITRF scale and possibly its drift. Other possibilities include thermal deformation and loading models used in the data analysis.

In this work we investigate the impact of a number of different models on the VLBI scale.

Tobias Nilsson[1,2] · Karine Le Bail[2] · Rüdiger Haas[2]
(1) Lantmäteriet – The Swedish mapping, cadastral and land registration authority, Lantmäterigatan 2C, SE-801 82 Gävle, Sweden
(2) Chalmers University of Technology, Department of Space, Earth and Environment, Onsala Space Observatory, SE–439 92 Onsala, Sweden

2 Data analysis

2.1 VLBI analysis

We analysed all high quality 24-h geodetic VLBI sessions with four or more stations from the period 1990-2022, in total 5351 sessions (only legacy S/X sessions were used). The analysis was done with the ASCOT software (Artz et al., 2016), using the settings and models recommended for ITRF2020. We applied gravitational deformation models for ten telescopes, using the models provided by the IVS Analysis Coordinator in January 2023 (containing models for four additional telescopes, compared to what was used in ITRF2020). The coordinates of the ICRF3 (International Celestial Reference Frame 3, Charlot et al., 2020) defining sources were fixed to their ICRF3 values, while the other radio source coordinates were estimated for each session. Non-tidal atmospheric loading were corrected, using the atmospheric loading product provided by the Vienna University of Technology (Wijaya et al., 2013).

We also calculated a number of alternative solutions to the standard solution described in the previous paragraph. In each one of these, one model was changed in the VLBI data analysis compared to the standard solution. The models we varied were: gravitational deformation models (applying it for ten, six, or no telescopes), thermal deformation (applying/not applying), using the temperature from observations from the empirical GPT2 (Lagler et al., 2013) model), pole tide (models from different IERS Conventions, or not applying), geophysical loading (applying different models, or not at all), Celestial reference frame (ICRF3 or ICRF2), and post-seismic deformation models (PSD, models from ITRF2020, ITRF2014 and DTRF2020).

2.2 CATREF analysis

After calculating the VLBI solutions, the resulting SINEX files of all sessions were combined with the CATREF software (the software used for creating ITRF2020) to create a Terrestrial Reference Frame (TRF). Here we used the same list of discontinuities as used in generating ITRF2020, except that two extra discontinuities were introduced at Ny-Ålesund (see Sec. 3.1). The origin and orientation of the TRF were realized by applying No-Net-Translation and No-Net-Rotation constraints relative to ITRF2020 for a number of stable stations with long observation history. The scale was realized through so-called internal constraints (Altamimi et al., 2023):

$$\left(A^T A\right)^{-1} A^T S = 0 \quad , \tag{1}$$

where

$$A = \begin{bmatrix} 1 & t_1 - t_0 \\ \vdots & \vdots \\ 1 & t_N - t_0 \end{bmatrix} \quad , \tag{2}$$

and $S = [s_1 \dots s_N]^T$. Here s_i denotes the scale of the i:th session, observed at epoch t_i, and t_0 is the reference epoch of the TRF. Just as in ITRF2020, we only used sessions observed before 2013.75 and having a network volume of more than 10^{19} m^3 for the scale realization.

The output of the CATREF analysis includes, among other parameters, the scale of each individual VLBI session relative to the scale of the combined TRF. By investigating these scale time series, we can study how the different models we varied in the VLBI data analysis affect the scale.

3 Results

3.1 The Ny-Ålesund station

Figure 1 shows the time series of the scale from the standard solution. As seen in the upper plot, there is a positive drift in the last couple of years (the mean drift after 2013.75 is 0.182 ppb/year, compared to 0.004 ppb/year before 2013.75). This is consistent with what was found for the ITRF2020 (Altamimi et al., 2023), showing that the scale drift seen in ITRF2020 is also present in our TRF solution.

As discussed in Section 1, one reason for the scale drift could be non-linear land uplift at Ny-Ålesund. To test the impact of this we introduced two additional velocity discontinuities at this station: one at 2015.3 and one at 2020.0. The scale time series from this 2nd solution is shown in the lower plot of Fig. 1. We can see that this approach reduces the scale drift significantly (mean drift after 2013.75 reduced to 0.111 ppb/year),

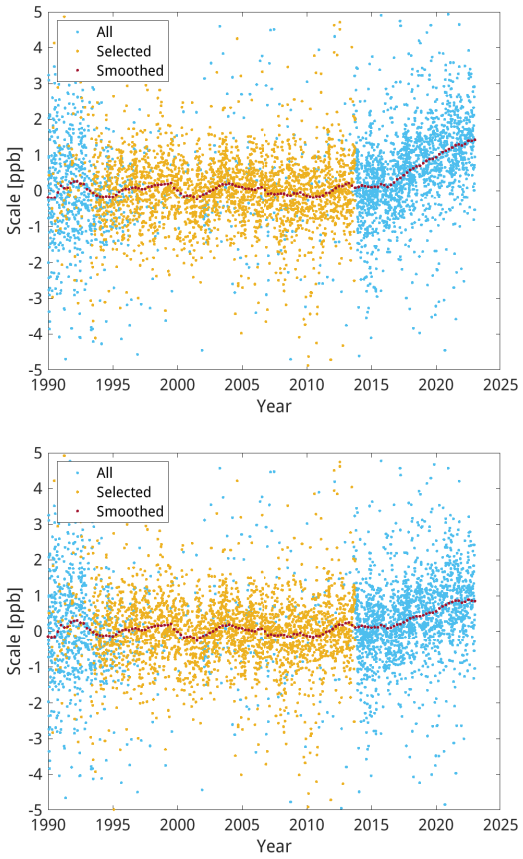

Fig. 1 Time series of the scale of the TRF derived from the standard solution. The yellow dots denote sessions included in the scale determination of the TRF, the other sessions are shown in blue. The smoothed time series (weighted average over ±1 year) is shown in red. The upper plot depicts the solution when using the same station discontinuities as used in the generation of ITRF2020 (Altamimi et al., 2023). The resulting average scale drift after 2013.75 is 0.182 ppb/year. The lower plot depicts the solution when adding two additional discontinuities for Ny-Ålesund (see text), and gives a resulting average scale drift after 2013.75 of 0.111 ppb/year.

although it did not disappear completely. We also calculated a variety of further solutions, e.g. placing the velocity discontinuities at different epochs or even removing the Ny-Ålesund station completely from the analysis. However, these attempts did not result in any significantly lower scale drift then what is seen in the lower plot of Fig. 1. Hence, non-linear motion of Ny-Ålesund seems to partly explain the scale drift, but not completely. In the following investigations, we included the two extra breaks at Ny-Ålesund at epochs 2015.3 and 2020.0 and used it as our standard solution.

3.2 Impact of different models

For each alternative solution, we compared the scale time series to that of the standard solution. We looked at possible differences in the long-term drift, especially after 2013.75, as well as other interesting differences, such as annual variations. The scale differences between three alternative solutions and the standard solution is shown in Fig. 2.

The top plot of Fig. 2 shows the difference between the solution without and gravitational deformation models and the standard solution. As can be seen, the scale differences are very small. We also calculated a solution where we used the same gravitational deformation as in ITRF2020 (which contained models for six antennas). Also for these solutions the scale did not differ significantly from that of the standard solution. Hence, our results show that the application of graviational deformation modeles do no cause any drift in the scale.

The middle plot of Fig.2 shows difference between the solution where no thermal deformation corrections were applied and the standard solution. As seen, the scale drift is not affected significantly. However, we can see that the difference in scale relative to the standard solution has a annual variation, with an amplitude of a few tenths of ppb. This could be expected. In summer, when the temperature is high, the thermal deformation will cause the telescopes to expand. If not corrected, this will cause an increase in the scale. Since most VLBI telescopes are located on the northern hemisphere, not correcting for thermal deformation will thus cause the scale to be larger in the northern hemisphere summer. We can note that the amplitude of the annual variations seems to decrease after about 2012. This is likely due to that more southern hemisphere stations have joined the VLBI network in recent years.

In the bottom plot of Fig. 2 the effect of using geophysical loading models (atmosphere, non-tidal ocean, and hydrology) from the International Mass Loading Service (IMLS, Petrov, 2015) is shown (the standard solution only used corrections for atmospheric loading). We can not see that this solution has a lower scale

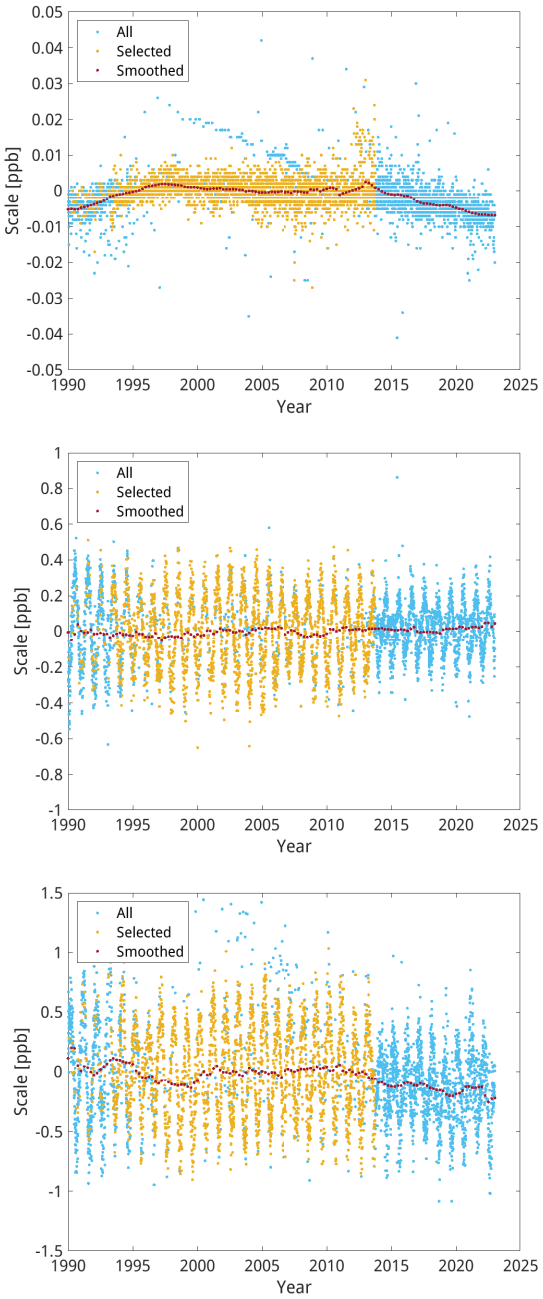

Fig. 2 Time series of the differences in scale between three alternative solutions and the standard solution (see Fig. 1). The upper plot shows the solution when no applying gravitational deformation models, the middle plot shows the solution not using thermal deformation, and the lower plot shows the solution using geophysical loading from IMLS. The yellow dots denote sessions included in the scale determination of the TRF, the other sessions are in blue, and red dots show the smoothed time series.

Table 1 The scale drift after 2013.75 from the different solutions calculated in this work.

Solution	Drift [ppb/year]	Uncertainty [ppb/year]
Standard	0.111	0.009
No Gravitational deformation	0.110	0.009
Gravitational def. for six stations	0.110	0.009
No Thermal def.	0.114	0.009
Temperature from GPT2	0.115	0.009
IERS 2010 mean pole model	0.105	0.009
No pole tide correction	0.104	0.009
Loading from IMLS	0.098	0.009
Source coordinates from ICRF2	0.132	0.009
ITR2014 PSD models	0.103	0.009
DTRF2020 PSD models	0.097	0.009

drift after 2013.75 (to 0.098 ppb/year) compared to the standard solution (0.111 ppb/year). The scale differences also show annual variations. This is probably due to annual variations in the non-tidal ocean and the hydrological loadings, together with the fact that most stations are on the northern hemisphere. Also in this case the amplitude of the annual variations decrease in recent years, likely due to the increased number of stations in the southern hemisphere.

In Table 1 the scale drift after 2013.75 is shown for the standard solution as well as for all the alternative solutions we calculated. The scale drift is not affected dramatically by any of the models, although some smaller impacts can be noted. The biggest reduction in the scale drift (about 0.01 ppb/year) we get when using loading from IMLS (as discussed above) as well as when using the Post-Seismic Deformation (PSD) models from DTRF2020 (Seitz et al., 2023) instead of those from ITRF2020. We also calculated a solution using both loading from IMLS and PSD from DRTF2020, which resulted in a scale drift of 0.085 ppb/year. Furthermore, an increase of the drift of about 0.02 ppb/year can be noted when using the radio soucre coordinates from ICRF2 instead of from ICRF3.

We have also seen that some models affect the seasonal variations of the scale. Apart from the thermal deformation and the loading models (as noted above), not applying for pole tide loading also results in an annual variation in the scale. The other investigated models do not significantly affect the seasonal scale variations.

4 Conclusions

The biggest impact on the scale drift seen in this work is when adding additional breaks to the Ny-Ålesund station. This shows that it is important to have good modelling of possible non-linear station motions when estimating a global TRF, such as the ITRF.

The results of this investigation also show that the investigated models do not affect the long-term drift of the estimated scale significantly. The reason is probably because the modelled effects do not have any significant long-term trends, hence they cannot cause any scale drift. For example, it is well-known that applying gravitational deformation in VLBI analysis affects the estimated vertical coordinates, hence an effect on the scale could be expected. However, the effect is constant in time, hence the application of such models do not affect the long-term drift of the scale. Nevertheless, it is important to use as good models as possible in the VLBI analysis to estimate a reliable scale, especially to avoid seasonal variations in the scale.

Acknowledgments

We are grateful to Zuheir Altamimi for giving us access to the CATREF software, and to the International VLBI Service for Geodesy and Astrometry (IVS) for providing the VLBI data used in this work.

References

Altamimi Z, Rebischung P, Collilieux X, Métivier L, Chanard K (2023). ITRF2020: an augmented reference frame refining the modeling of nonlinear station motions. 97(47), doi: 10.1007/s00190-023-01738-w.

Artz A, Halsig S, Iddink A, Nothnagel A (2016) ivg::ASCOT: Development of a new VLBI software package. In D. Behrend, K. D. Baver, and K. Armstrong (eds.): *International VLBI Service for Geodesy and Astrometry 2016 General Meeting Proceedings: New Horizons with VGOS*, 217–221, Johannesburg, South Africa, ivscc.gsfc.nasa.gov/publications/gm2016/045_artz_etal.pdf.

Charlot P, Jacobs C S, Gordon D, Lambert S, de Witt A, Böhm J, Fey A L, Heinkelmann R, Skurikhina E, Titov O, Arias E F, Bolotin S, Bourda G, Ma C, Malkin Z, Nothnagel A, Mayer D, MacMillan D S , Nilsson T, Gaume R (2020) The third realization of the international celestial reference frame by very long baseline interferometry. *A&A*, 644:A159, doi: 10.1051/0004-6361/202038368.

Kierulf H P, Kohler J, Boy J P, Geyman E C, Mémin A, Omang O C D, Steffen H, Steffen R (2022) Time-varying uplift in Svalbard—an effect of glacial changes. *Geophysical Journal International*, 231(3):1518–1534, doi: 10.1093/gji/ggac264.

Lagler K, Schindelegger M, Böhm J, Krásná H, Nilsson T (2013) GPT2: Empirical slant delay model for radio space geodetic techniques. *Geophys. Res. Lett.*, 40(6):1069–1073, doi: 10.1002/grl.50288.

Petrov L (2015) The international mass loading service. In: *REFAG 2014*, volume 146 of *IAG Symposia*, 79–83. Springer. doi: 10.1007/1345_2015_218.

Seitz M, Bloßfeld M, Angermann D, Glomsda M, Rudenko S, Zeitlhöfler J, Seitz F (2023) DTRF2020: Itrs 2020 realization of DGFI-TUM. Datset, 2023. zenodo.org/records/8220524.

Wijaya D D, Böhm J, Karbon M, Kràsnà H, Schuh H (2013) Atmospheric pressure loading. In: J. Böhm and H. Schuh, editors, *Atmospheric Effects in Space Geodesy*, 137–157. Springer, Heidelberg, doi: 10.1007/978-3-642-36932-2_4.

VLBI correlator Wettzell - One year of experience as IVS correlator

C. Plötz, W. Probst, R. Wildenauer, B. Fischaleck, A. Neidhardt, M. Seegerer, T. Schüler

Abstract The Geodetic Observatory Wettzell (GOW) in Germany was enhanced with a VLBI correlation facility. A high performance cluster (HPC) based DiFX VLBI correlator replaced obsolete hardware in December 2020, thus providing the performance to properly handle VGOS observations. The VLBI correlator at Wettzell is acknowledged as an official IVS correlation component, contributing to the IVS correlation resources since late 2021. A special focus was laid on serving a timely deltaUT1 estimation with a dedicated IVS VGOS Intensive observation program between McDonald Observatory (MGO) and Wettzell. Additionally, since December 2022, regular IVS VGOS 24h sessions are assigned to the Wettzell correlator. An upgrade of the storage capacity and the internet data rate to 10 Gbps was done to manage the increased amount of data of these 24h VGOS sessions. Experiences while establishing the correlation facility will be given.

Keywords VLBI correlator, DiFX, Wettzell

Christian Plötz · Willi Probst · Robert Wildenauer · Ben Fischaleck · Michael Seegerer · Torben Schüler
Bundesamt für Kartographie und Geodäsie (BKG), Geodätisches Observatorium Wettzell, Sackenrieder Str. 25, D-93444 Bad Kötzting, Germany

Alexander Neidhardt
Technische Universität München (TUM), Geodätisches Observatorium Wettzell, Sackenrieder Str. 25, D-93444 Bad Kötzting, Germany

1 Introduction

The Geodetic Observatory Wettzell contributes since 1983 with the 20 m radio telescope as a network station to the international VLBI community. During the years, several other components were added. The German Antarctic Receiving Station (GARS) O'Higgins in Antarctica was established in 1991.

Since 2002, the 6 m radio telescope TIGO (Transportable Integrated Geodetic Observatory) in Chile was operated and then moved then to Argentina in 2016. Since then, it is named Argentinian German Geodetic Observatory (AGGO). In 2013, the VGOS twin radio telescopes Wettzell-South and Wettzell-North extended the geodetic infrastructure at the GOW. All of these network stations take part in a broad range of VLBI observation programs (e.g., R1, R4, T2, VGOS, various Intensive programs). The IVS VLBI operation center DACH (Deutschland: BKG, Austria: TU Wien, Confoederatio Helvetica: ETH Zürich) started operations in November 2019. In September 2020, the IVS Seamless Auxiliary Data Archive (SADA) was initiated at Wettzell. The latest addition is the establishment of the IVS VLBI correlator Wettzell (WETZ) in September 2021. Since then, the activities were continuously enhanced and in particular within the last year, the correlation program was extended with 24h VGOS network correlations.

2 VLBI correlator Wettzell - hardware and software overview

The hardware topology was specified as a High-Performance-Cluster (HPC) configuration. Three head

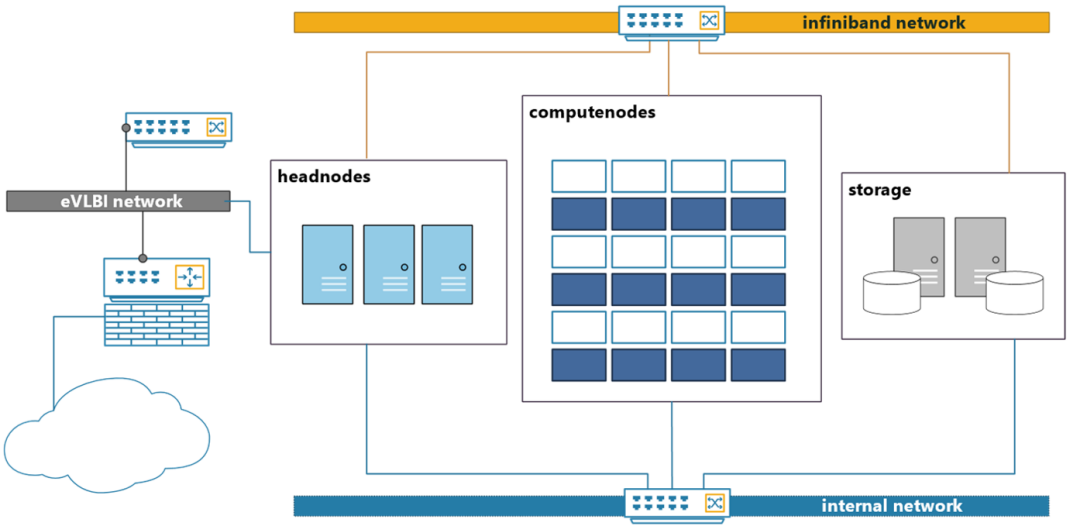

Fig. 1 Wettzell VLBI correlator: Hardware block diagram.

nodes (one of them is used for data transfers) and 24 compute nodes are available. The data is transported over an Infiniband bus system, which interconnects all related hardware units. The HPC-storage capacity with an amount of 834 Terabyte (TB) was upgraded at the beginning of 2023 with a new storage server unit. This extended the total available correlator capacity to a level of 3.1 Petabyte. A dual-UPS protects against power failures and more frequent power line transients.

Ansible is the software tool used for provisioning, configuration management and application deployment of the HPC. As software correlator application, DiFX is used (Deller et al., (2011)) and for the subsequent fringe-fitting process the Haystack Observatory Post-processing System (HOPS) is installed. To manage different users and configurations for all correlation duties, the SLURM (Simple Linux Utility for Resource Management) workload manager was introduced. Currently, two basic configuration sets are in use. One for VGOS (DiFX version 2.5.4, hops 3.24) and another one for *legacy S/X* correlation (DiFX 2.6.3, hops 3.24).

3 Current IVS correlation program

The milestones towards an official IVS VLBI correlator component were the start of VLBI short baseline observations at the GOW since 2016 (Phogat et al. (2018)). Since 2018, a domestic Intensive VLBI session program with AGGO and Wettzell was established (Plötz et al. (2019)). Furthermore, in this context, a few dedicated VLBI sessions between Wettzell, AGGO and O'Higgins were conducted. In 2019, the initial, low-throughput initial correlator hardware needed to be replaced. Therefore, the specification of a new correlation hardware was defined and after completing the acquisition process, the system was installed at the end of December 2020. This enabled the processing of much more demanding VLBI sessions in terms of computing performance.

Currently, several session types from the International VLBI Service (IVS) are assigned to the Wettzell correlator. The one hour IVS VGOS Intensive-series S23 between McDonald (Mg), located in Texas/US and Wettzell (Ws) in Wettzell/Germany is normally observed on Tuesdays at 19:45 UT. After the S23 session has finished, a short calibration session (S3A), which takes 10 minutes, is appended, with the aim to get further details about correlation, source characterization, and slewing characterization of the radio telescopes involved.

The latest addition to the Wettzell correlator is the VO session type, which takes 24 hours of observation time in the VGOS network and initiated with the first VO session in December 2022. So far, three sessions

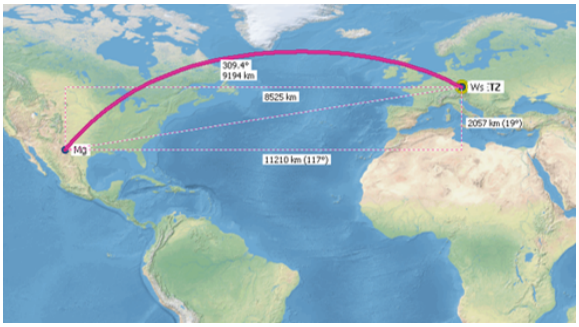

Fig. 2 VGOS Intensive baseline: McDonald (Mg) to Wettzell (Ws).

were processed, with a VGOS network size of 7 to 8 stations each and about 300 Terabyte of data were transferred to the Wettzell correlator per session. The computing time was approximately 14 hours per session.

4 Correlator experiences

The initial HPC-storage size was 834 Terabyte and without an upgrade to 3.1 Petabyte, a regular operation of VGOS 24h sessions would not be possible. The implication is that also the VGOS baseband data from the Wettzell VGOS network station (Ws) need to be stored on the HPC-storage as shared resource. Another issue was the data rate limit to 5 Gbps for up- and download of VLBI raw data, which was enhanced to 10 Gbps in May 2023. This was a necessary enhancement for being prepared to handle different and challenging VLBI raw data flow scenarios in the future. Particularly, the high-volume incoming data streams of all included 24h VGOS network stations must not disrupt the data transfers of the high priority VGOS and *legacy S/X* data transfers from and to Wettzell.

Due to a maintenance period of the VGOS network station Wettzell-South (Ws), there were no VGOS Intensive sessions (S-series) to correlate between November 2022 and March 2023. Significant improvements on the VLBI correlator software part were done with the SLURM workload manager. Furthermore, an essential step was the installation of the automatic report generation script from USNO and the current fourfit update to HOPS version 3.24 with applying a priori ionospheric delay windows within HOPS fourfit application. As part of the experience collected within the last year of correlator operations, various problems could be identified and solved. Samples are: Polarization swap, problems with low noise amplifiers (LNA) leading to lower sensitivity as well as dealing with corrupted baseband data.

5 Conclusions and outlook

The VLBI correlator Wettzell started in December 2021 its regular operations as an official IVS component. Currently, the IVS sessions S23 and S3a, dedicated 24h VGOS Intensives, as well as complete 24h VGOS sessions are assigned to the Wettzell VLBI correlator. The next step is to develop an automated VGOS Intensive correlation workflow. The configuration and setup management of the HPC-based VLBI correlator is based on the well-established software tool-chains of Ansible and SLURM. An advantage of the close integration into the infrastructure of the Geodetic Observatory Wettzell is that the recorded raw VLBI data of the Wettzell network stations are instantaneously available. This gives an advantage towards a faster processing workflow. The VLBI correlation resources at Wettzell are capable of yielding for more sessions to correlate. The prerequisite upgrades concerning the internet bandwidth with a rate of 10 Gbps and the correlator storage capacity enhancements to 3.1 Petabyte were successfully implemented. This sets the VLBI correlator at Wettzell to a the full extent usable VLBI correlation facility.

References

Deller A, Brisken W, Phillips C, Morgan J, Alef W, Cappallo R, Middelberg E, Romney J, Rottmann H, Tingay S & Wayth. R (2011) DiFX-2: A More Flexible, Efficient, Robust, and Powerful Software Correlator. *Publications of the Astronomical Society of the Pacific*, 123, 275–287.

Plötz et al. (2019) INT9 - DeltaUT1 Determination Between the Geodetic Observatories AGGO and Wettzell. In: R. Haas, S. García-Espada, and J. A. López Fernández (eds.), *EVGA 2019 Meeting Proceedings*, 124–128, doi: 10.7419/162.08.2019.

Phogat et al. (2018) Implementation and First Results of the Local Wettzell VLBI Correlator GOWL. In: D. Behrend, K. D. Baver, and K. L. Armstrong (eds.), *IVS 2018 General Meeting Proceedings*, 102–106, NASA/CP–2019-219039.

Intercontinental optical clock comparison using the geodetic VLBI technique in K-band

R. Ricci, M. Negusini, F. Perini, C. Bortolotti, M. Roma, G. Maccaferri, M. Stagni, C. Clivati, D. Calonico, M. Pizzocaro, S .Condio, I. Goti, S. Donadello, M. Risaro, M.-S. Heo, W.-K. Lee, C.Y. Park, D.-H. Yu, H. Kim, S.O. Yi, B. Cho, T. Jung, D.-Y. Byun, D.-H. Je, S. Xu, H. Yoon

Abstract Comparing distant atomic clocks is very important for international timekeeping, global positioning and tests of fundamental physics. Optical clocks are the most technologically advanced devices for frequency generation with a stability of 10^{-18}. In the near future they could be used in the redefinition of the SI second replacing the current one defined using the microwave transition of a Cs atom. Optical fiber link networks allow the most performing optical clocks to be compared on distances up to two thousand kilometers, but for longer distances clock comparisons are limited by the performances of satellite frequency transfer techniques. In this presentation we show the use of high-frequency geodetic VLBI as an alternative technique for long distance frequency transfer. A K-band 24-hour experiment involving six antennas between Europe and Korea was carried out in order to estimate the clock rate between the H-masers of Medicina and KRISS sites. These masers were connected and calibrated against two Ytterbium lattice optical clocks in INRiM (Italy) and KRISS (Korea). The fractional frequency difference between the optical clocks was thus evaluated.

Keywords Optical clocks, VLBI technique, optical fiber links

Roberto Ricci · Monia Negusini · Federico Perini · Claudio Bortolotti · Mauro Roma · Giuseppe Maccaferri · Matteo Stagni
INAF-Istituto di Radioastronomia, via Gobetti 101, Bologna, I-40129, Italy

Cecilia Clivati · Davide Calonico · Marco Pizzocaro · Stefano Condio · Irene Gatti · Simone Donadello · Matias Risaro
Istituto Nazionale di Ricerca Metrologica, Strada delle cacce 91, Torino, I-10135, Italy

Myoung-Sun Heo · W.-K. Lee · C.Y. Park · D.-H. Yu · H. Kim
Korea Research Institute of Standards and Science, 267 Gajeong-ro, Yuseong-gu, Daejeon, Republic of Korea

S.O. Yi · H. Yoon
National Geographic Information Istitute, 92 Worldcup-ro, Yeongtong-gu, Suwon-si, Gyeonggi-do, Republic of Korea

Busan Cho
Korea Istitute of Science and Technology Information, 245 Daehak-ro, Yuseong-gu, Daejeon, Republic of Korea

Taehyun Jung · D.-Y. Byun · D.-H. Je · Shuangjing Xu
Korea Astronomy and Space Science Institute, Daedeokdae-ro 776, Yuseong-gu, Daejeon, Republic of Korea

1 Introduction

Atomic clocks based on optical transitions can reach fractional frequency uncertainties at the 10^{-18} level (McGrew et al. (2018),Ushijima et al. (2015), Brewer et al. (2019)) already improving by two order of magnitude the performance of microwave clocks such as Cesium fountains (Wynards & Weyers (2005)) that are used to define the International System of Units (SI) second and are the standard in international timekeeping (Panfilo & Arias (2019)). Based on the fast improvement in optical clock technology it is foreseen that optical clocks will replace the Cs fountains in the definition of the SI second (Riehle et al. (2018)). The remote comparison of such clocks on intercontinental distances is fundamental to check their consistency in view of such a redefinition. Optical clocks are also already used in tests of special and general relativity (Sanner et al. (2019)), laboratory searches of the variation of fundamental constants (Godun et al. (2014)) and chronometric levelling (i.e. the usage of gravitational redshift to determine

absolute height differences, (Grotti et al. (2018), Mehlstäubler et al. (2018)). Future applications of clock comparisons also involve the establishment of quantum networks for secure communications and timing (Komar et al. (2014)) and gravitational wave detection (Kolkovitz et al. (2016)). Coherent optical fibre links can disseminate frequency references via optical frequency combs up to about two thousand kilometres with frequency instabilities of the order of 10^{-19} (Calonico et al. (2014), Clivati et al. (2015), Clivati et al. (2020)) but they cannot be used on intercontinental distances. On such large distances optical clock comparisons rely upon GNSS frequency transfer (via the Integer Precise Point Positioning technique, (Petit et al. (2015)) and Two-Way Satellite Time and Frequency Transfer (TWSTFT, Fujieda et al. (2014)). A recent addition to this suite of frequency trasfer techniques is space geodesy: the Very Long Baseline Interferometry (VLBI) observations of distant quasars to study Earth crustal motions and orientation parameters (Pole wobbling and Length of Day). Clock model parameters in network antennas are also adjusted in the Normal Equation minimization and are then used to compare the behaviour (in particular the clock drift) of H-maser station clocks and thus optical clocks in a metrological chain.

A successful VLBI campaign to compare optical lattice clocks between National Institute for Communication Technology (NICT, Japan) and Istituto Nazionale di Ricerca Metrologica (INRiM, Italy) has been carried out in 2018-2019 (Pizzocaro et al. (2021), Sekido et al. (2021)), in which two small (2.4-meter diameter) transportable antennas (nodes), one located in Koganei (Japan) and the other at the radio station of Medicina have observed a list of bright quasars together with a large (34-meter) antenna (the hub) in Kashima (Japan), all three antennas being equipped with broadband (2-14 GHz) NINJA feeds. The node-hub configuration was chosen because the small antenna pair do not reach enough signal-to-noise ratio in geodetic observations on enough bright targets. The baseline between the small antennas is computed as a closure delay relation starting from their baselines with the hub antenna. The relative fractional frequency difference between the H-masers commanding the Koganei and Medicina small antennas was thus computed. This was a link in the metrological chain connecting the INRiM Yb optical clock to the NICT Sr optical clock via a leg of the Italian Quantum Backbone (IQB) for optical fiber frequency reference dissemination (the Torino-Medicina 550 km link, Clivati et al. (2020)) and optical fiber link in Koganei. The resulting frequency deviation between Ytterbium and Strontium clocks measured via the VLBI link was $y(Yb/Sr) = 2.5(2.8) \times 10^{-16}$ in agreement with previous measurements and an improvement in term of uncertainty with respect to the frequency deviation obtained via GPS-IPPP ($y(Yb/Sr) = -3.2(4.0) \times 10^{-16}$).

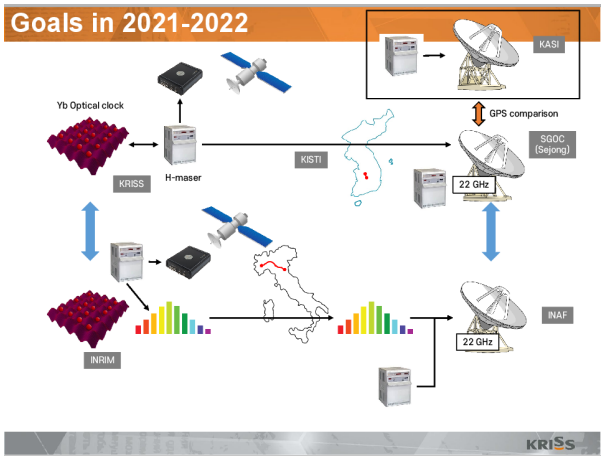

Fig. 1 Schematic view of the full experiment set-up in the 2021 Dec observations.

2 Method

We used the geodetic VLBI technique in a network of antennas between Italy (32-m antenna in Medicina), Spain (40-m Yebes antenna) and Korea (one 22-m National Geographic Information Institute Sejong VLBI antenna and three 21-m Korean VLBI Network antennas, KVN) to determine the fractional frequency difference between H-maser clocks in Korea and Medicina and thus indirectly compare the Yb optical lattice clocks in the national metrological institutes INRiM (Torino, Italy) and Korean Research Institute for Standards and Science (KRISS, Korea) by estimating their relative frequency deviation. The KRISS H-maser clock signal was transferred to Sejong station via an optical fiber link provided by the Korean Institute of Science & Technology Information (KISTI), while the IQB optical fiber link connects the optical clock

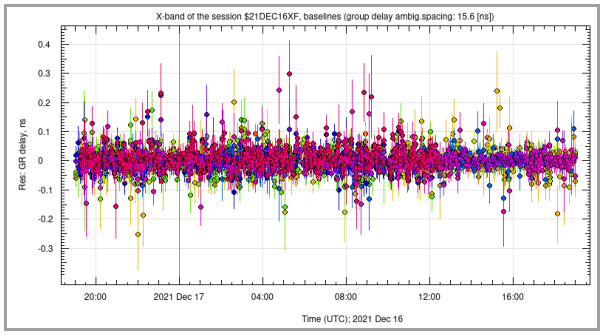

Fig. 2 Residuals of the Group Delays in the 2021 Dec experiment analysed using nuSolve. No ionospheric correction was applied at this stage.

disciplined H-maser clock in Torino with the Medicina station H-maser clock. The VLBI sessions are matched by a GPS-IPPP measurement campaign for the comparison between the two techniques (see Fig. 1 for a scheme of the full experimental set-up).

3 Results

The first observing session in the Optical Clock Comparison VLBI campaign was performed on Dec 16th-17th, 2021 in a 24-hour experiment in K-band at the frequency range 21-21.4 GHz. Six antennas were involved: Medicina, Yebes, Sejong (already part of the IVS network) plus the three antennas of the Korean VLBI Network (Tanma, Yonsei and Ulsan). Sur_sked was used to schedule the run made of 450 scans with targets chosen from a list of tens of sources in a typical geodetic scheme: short scans (2-3min) were performed spanning all azimiths and elevations available at the observing stations in order to better characterise the tropospheric parameters. The LEVEL0 raw data from the six antennas were transfered to the Bologna and KASI data centres for correlation. Fringe fitting was performed in HOPS *fourfit*. A VGOSdb database was created and read into nuSolve (Bolotin et al. (2014)) and VieVS v3.2 (Boehm et al. (2018)) for analysis. As the data are single-band in order to correct for ionospheric effects on antenna delays an External Ionospheric File matching the observing scan sequence was created in VieVS taking the vertical Total Electron Content values from the International GNSS Service Global Ionospheric maps. Standard a-priori model set-ups were used in the data modelling including Vienna Mapping Functions v3 (VMF3, Landskron & Boehm (2018)) for the treatment of tropospheric delay. The group delay residuals vs observing time are shown in Fig. 2. The relevant clock parameters (clock rate and its uncertainty) on the baseline between Medicina and Sejong were extracted from the VieVS LEVEL3 parameter output structure. The comparison between the quantitative results obtained by the Bologna and KASI datasets is still ongoing and final geodetic and metrological results will be published in a forthcoming paper.

4 Conclusions and outlook

Here we described why it is important to compare distant optical clocks for the redefinition of the SI second by 2030 using an optical frequency transition as the standard and how this purpose will be achieved: on the longest distances, where optical fiber links become unavailable, using the GNSS, TWSTF transfer and VLBI techniques. We then moved to describe the Italian-Japanese optical clock comparison via the VLBI technique achieved through the use of customed built small-dish transportable antennas which improved on the performance of the GNSS frequency transfer measurement campaign carried out simultaneously by almost a factor of 2. Finally we reported on the start of an observing and measuring campaign aimed at comparing optical clock frequency differences on intercontinental distances between Italy and Korea using the geodetic VLBI technique in K-band.

The Italian-Korean collaboration involving metrological and radio astronomical institutes will make use of the Korean-designed Compact Tri-band Receivers (CTR) operating simultanously at K-, Q- and W-band (Han et al. (2017)) and of space geodesy techniques. The CTR will also be installed on Italian radio antennas in 2024 and in Korea on the KVN Yonsei antenna and on the new Pyeonchang antenna. KISTI, KRISS and Korea Astronomy and Space Science Institute (KASI) are also working on implementing coherent wave optical fiber frequency link between KRISS and the Korean antennas. This time gap will allow our collaboration to test the general infrastructure and observing techniques. An optimal frequency set-up in the range 18-116 GHz

on the CTRs will be selected. Target sources in common view between Italy and Korea and based on antenna sensitivity and absence of source structure will be chosen from the International Celestial Reference Frame (Charlot et al. (2020)). VieSched++ (Schartner & Boehm (2019)) will be used to simulate the best scheduling strategy. High-speed dedicated link for data transfer will be implemented by GARR (Italy) and KISTI (Korea). The large volume of LEVELO data will be correlated by the DiFX (Deller et al. (2007)) correlator both in Italy and Korea. This will be performed by an upgraded Bologna computing cluster and Korea national supercomputer. Data analysis of the correlated fringe fitted datasets will be performed on VieVS or nuSolve. The Source Frequency Phase Referencing technique (Rioja & Dodson (2020)) will also be explored together with injected phase cal signal for improving phase stability and thus the uncertainty on the clock rate. A GPS-IPPP measurement campaign will be also carried out commensally to the VLBI sessions in order to compare the two techniques. The final goal of the project by the year 2026 is to to measure clock frequency differences with a relative uncertainty level of 10^{-17}.

References

McGrew, W.F. *et al* 2018. Atomic clock performance enabling geodesy below the centimeter level *Nature*, **564**, 87-90, doi: 10.1038/s41586-018-0738-2

Ushijima, I., Takamoto, M. Das, M. Ohkubo, T., & Katori, H. *et al*. 2015, Cryogenic optical lattice clocks *Nature Photonics*, **9**, 185-189, doi: 10.1038/nphoton.2015.5

Brewer, S.M., *et al*. 2019 $Al^{+} - 27$ quantum logic clock with a systematic uncertainty below 10^{-18} *Physical Review Letters*, **123**, 033201, doi: 10.1103/PhysRevLett.123.033201

Wynards, R. & Weyers, S., 2005 Atomic fountain clocks *Metrologia*, **42**, S64, 2005

Panfilo, G. & Arias, F. 2019, Coordinated Universal Time (UTC) *Metrologia*, **56**, 042001

Riehle, F., Gill, P., Arias, F. & Robertsson, L., 2018 The CIPM list of recommended frequency standard values: guidelines and procedures *Metrologia*, **55**, 188, 2018

Sanner, C. *et al.*, 2019 Optical clock comparison for Lorentz symmetry testing, *Nature*, **567**, 204–208, 2019

Godun, R.M. *et al.*, 2014 Frequency ratio of two optical clock transitions in $Yb^{+} - 171$ and constraints on time variations of fundamental constants, *Physical Review Letters*, **113**, 210801

J. Grotti, S. Koller, S. Vogt, S. Haefner, U. Sterr, *et al*. 2018 Geodesy and metrology with a transportable optical clock *Nature Physics*, 14, 437-441, doi: 10.1038/s41567-017-0042-3

T.E. Mehlstäubler, G. Grosche, C. Lisdat, P.O. Schmidt *et al*. 2018 Atomic clocks for geodesy *Reports on Progress in Physics*, 81, 064401 doi: 10.1088/1361-6633/aab409

Komar, P. *et al.*, 2014 A quantum network of clocks, *Nature Physics*, **10**, 933

Kolkovitz, S. *et al.*, 2016 Gravitational wave detection with optical lattice atomic clocks, *Phys Rev D*, **94**, 124042 doi: 10.1103/PhysRevD.94.124042

Calonico, D. *et al* 2014 High-accuracy coherent optical frequency transfer over a doubled 642-km fibre link, *Appl. Phys. B*, **117**, 979-986

Clivati, C., *et al.* 2015 A coherent fibre-optic link for Very Long Baseline Interferometry, *IEEE Trans on Ultrason. Ferroel. Freq. Contr.*, **62**, 1907-1912

Clivati, C. *et al.* 2020 Common-clock very long baseline interferometry using a coherent optical fiber link, *Optica*, Vol. 7, Issue 8, pp. 1031–1037

Petit, G. *et al.*, 2015 1×10^{-16} frequency transfer by GPS PPP with integer ambiguity resolution, *Metrologia*, **52**, 301–309

Fujieda, M. *et al.*, 2014 Carrier-phase two-way satellite frequency transfer over a very long baseline, *Metrologia*, **51**, 253–262

Pizzocaro, M. *et al.*, 2021 Intercontinental comparison of optical atomic clocks via very long baseline interferometry, *Nature Physics*, **52**, 301–309

Sekido, M., Takefuji, K., Ujihara, H. *et al.*, A broadband VLBI system using transportable stations for geodesy and metrology: an alternative approach to the VGOS concept. *Journal of Geodesy*, **95**, article 41

Charlot, P., *et al.*, 2020 The third realization of the International Celestial Reference Frame by very long baseline interferometry *Astronomy & Astrophysics*, **644**: 159 doi: 10.1051/0004-6361/202038368

A.T. Deller, S.J. Tingay, M. Bailes, C. West, 2007 DiFX: A Software Correlator for VLBI Using Multiprocessor Computing Environments, *Publications of the Astronomical Society of the Pacific*, **119**, 318-336, doi: 10.1086/513572

S. Bolotin, K. Baver, J. Gipson, D. Gordon, D. MacMillan, 2014 The VLBI Data Analysis Software *v*Solve: Development Progress and Plans for the Future, In D. Behrend, K. D. Baver and K.L. Armstrong editors, International VLBI Service for Geodesy and Astrometry 2014 General Meeting Proceedings, Science Press (Beijing), pages 253-257, ISBN 978-7-03-042974-2

Boehm, J. *et al.*, 2018 Vienna VLBI and Satellite Software(VieVS)for Geodesy and Astrometry, *Publications of the Astronomical Society of the Pacific*, **130**, 044503, doi: 10.1088/1538-3873/aaa22b

Landskron, D. & Boehm, J., 2018 VMF3/GPT3: refined discrete and empirical troposphere mapping functions, *Journal of Geodesy*, **92**: 349 doi: 10.1007/s00190-017-1066-2

Schartner, M. & Boehm, J., 2019 VieSched++: a new VLBI scheduling softwarefor geodesy and astrometry *PASP*, **131**: 084501 doi: 10.1088/1538-3873/ab1820

Rioja, M. & Dodson, R., 2020 Precise radio astrometry and new developments for the next generation of instruments *As-*

tron. Astrophys. Rev., **28**: 6 doi: 10.1007/s00159-020-00126-z

Han S.T., Lee J.W., Lee B., Chung M.H., Lee M.S., Je D.H. *et al.*, 2017 A millimter-wave quasi-optical circuit for for compact triple-band receiving system *J. of Infrared, Millimeter and Terahertz waves*, **38**: 1487–1501

First Experiences with the VLBI Quality Control System at Wettzell

T. Schüler, W. Probst, C. Plötz, A. Neidhardt, S. Seidl

Abstract The Federal Agency for Cartography and Geodesy (BKG) introduced a Quality Management System in 2022. A certification process according to the most recent international standard ISO 9001:2015 followed the same year. This was a motivation to extend the existing quality control system for the VLBI radio telescopes at the Observatory. Realtime system monitoring mechanisms already do exist since a longer period of time. In-situ auto-correlation of selected scans is possible right after recording to tackle back selected problems. In addition, the systematic analysisof output files from correlation as well as geodetic analysiswas introduced in 2022. The statistical analyses are carried out automatically. Moreover, a weekly quality review is conducted, following the established guidelines for information and feedback. In this contribution, we will briefly review the quality control system and provide a connection to the Continuous Improvement Process (CIP). The CIP is a core aspect of a well-working quality management system. Finally, we highlight the experiences gained so far regarding its effectiveness.

Torben Schüler
Geodetic Observatory Wettzell, Federal Agency for Cartography and Geodesy (BKG), Sackenrieder Str. 25, D-93444 Bad Kötzting, torben.schueler@bkg.bund.de

Torben Schüler
Universität der Bundeswehr München, University of the Federal Armed Forces Munich, Faculty of Aerospace Engineering, D-85577 Neubiberg

Christian Plötz · Willi Probst
Geodetic Observatory Wettzell, Federal Agency for Cartography and Geodesy, Sackenrieder Str. 25, D-93444 Bad Kötzting

Alexander Neidhardt · Simon Seidl
Geodetic Observatory Wettzell, Technical University Munich, Sackenrieder Str. 25, D-93444 Bad Kötzting

Keywords QMS (Quality Management System), ISO 9001, SPC (Statistical Process Control), CIP / KVP (Continuous Improvement Process)

1 Introduction

A Quality Management System (QMS) was formally introduced and externally certified according to the ISO 9001:2015 standard in 2022. The VLBI measurements as well as VLBI raw data correlation are incorporated in a so-called *core process*. One key aspect in such a management system is the effective implementation of mechanisms that warrant a continuous improvement of quality. No doubt, quality aspects are part of our everyday work at the Observatory. Our main question is: *Are our telescopes delivering the data at a quality level expected for the particular purpose?* A question that is, however, not always easy to answer right at the very moment at that very site. Mechanisms implemented earlier comprise:

Realtime system monitoring: Various telescope parameters as well as environmental conditions are constantly monitored, and error states or warnings are issued to our on-call service in case thresholds are exceeded or suspicious patterns in the data are detected. This system is of major importance, but with a focus on machine safety and technical functionality. Therefore, we cannot always nor fully answer whether the group delay arriving on the virtual desk of an analyst is sufficiently precise or not.

In-situ correlation: Wettzell features a local correlation facility for mission-critical sessions. Before any kind of cross-correlation is starting, the data from our telescopes can be auto-correlated locally. This enables

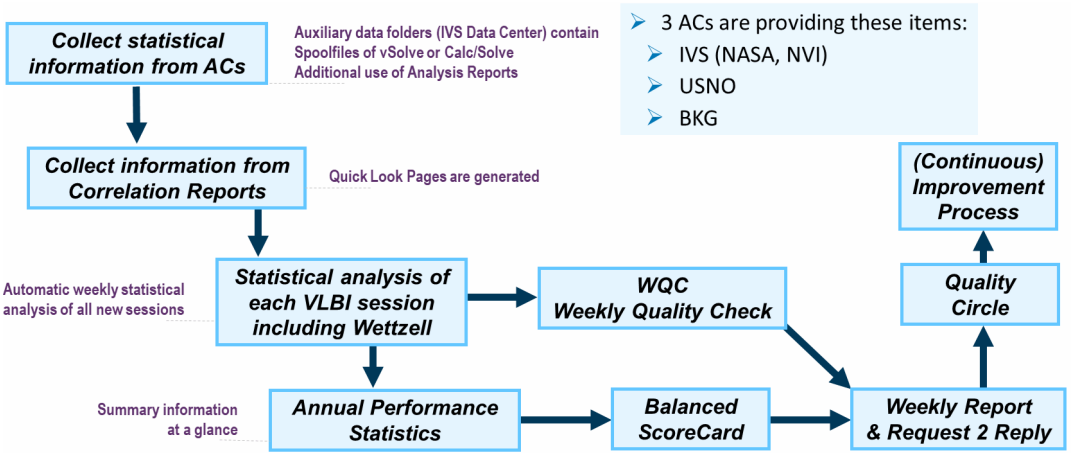

Fig. 1 Processing and decision chain illustrating the steps from data collection for statistical process control, its analysisand the organization of weekly and annual quality control reviews as well as the formation of quality circles and the initiation of a (continuous) improvement process to implement changes leading to improved quality.

us to tackle back problems such as an instable local oscillator, for instance. Clearly, though a useful tool, this method only covers selected aspects. It is one facet in the quality assurance chain.

2 SPC - Statistical Process Control

Many ways exist regarding how to deal with quality improvement. ISO 9001:2015 does not demand to employ any dedicated method. This is free to the particular organization to decide. Our approach is a combination of classical elements of CIP[1], we make use of regular Quality Circles, and we try to base our decision on statistical analyses. Note that this contribution does not cover the whole picture of an SPC in a way this term is usually understood in industry. Instead, this first paper is devoted to an initial overview about the basic functionality of the statistical analysissystem and its organization at the Geodetic Observatory Wettzell (GOW). Fig. 1 illustrates our approach:

1. *Collect statistical information from ACs*: Our data source for statistical analysisare the spool files and analysisreports output by the *CALC/SOLVE* and *vSolve* adjustment packages as provided by the following primary AnalysisCenters (ACs) of the IVS: NASA/NVI Inc., USNO (US Naval Observatory) and the analysisgroup at BKG. We also make use of the correlation reports provided by the correlators. The spool files contain a wealth of information suitable for our purpose such as the group delay RMS for each baseline, we can derive the analysisloss[2] as well as the measurement and correlation loss[3].
2. *Collect information from Correlation Reports*: The correlation reports are a valuable source, too. Its analysisallows for a deeper look into possible problems due to interference, for instance. We can possibly distinguish between missing data from the telescopes and poor quality of the scans yielding misdetections in the worst case.
3. *Statistical analysisof each VLBI session*: All sessions with data of at least one of the Wettzell telescopes as well as AGGO[4] and O'Higgins[5] are analyzed. This weekly analysisis fully automatic. Quick-look pages are generated giving a session overview (see Fig. 3), portraying the baseline performance (see Fig. 4) and various other pieces of information.

[1] The Continuous Improvement Process is related to the original Japanese version called *Kaizen*. The German abbreviation is KVP for *Kontinuierlicher Verbesserungsprozess*.

[2] The percentage of group delays deleted by the analyst.

[3] The percentage of data that did either not arrive at the correlation facility, or was taken out of the process upon correlation.

[4] Argentinean-German Geodetic Observatory; AGGO has a transportable 6 m VLBI antenna for legacy measurements.

[5] The German Antarctic Receiving Station GARS O'Higgins features a 9 m antenna capable for use in geodetic VLBI.

Station Statistics by Long and Short Sessions:

First Session:	Last Session:	Total Number of Sessions:	Qualifying Sessions:	Issue:	Originator (DCO):
07.01.2021 18:00	**29.12.2021 18:30**	**648**	**157** (Duration > **5 h**)	**12.12.2022 17:02:14**	**Schüler, Torben**

Name of Telescope	Applicable Sessions	Std.Dev. UT1-TAI			Observations in Total	Group Delay RMS			Scheduled Observations	Quality Codes 5-9			Meas. & Corr. Loss			Observations Used in Analysis	Analysis Loss		
		Min	Median	Max		Min	Median	Max		Min	Median	Max	Min	Median	Max		Min	Median	Max
WETTZELL	107	1.5 µs	**3.2** µs	5.9 µs	159000	5.5 mm	**8.6** mm	21 mm	1965	0.0%	**91%**	99%	4.0%	22%	82%	1393	0.6%	2.7%	21%
WETTZ13S	26				84654	2.6 mm	**5.0** mm	9.5 mm	4399	69%	**90%**	99%	0.1%	17%	49%	3050	2.2%	6.4%	13%
WETTZ13N	40	1.5 µs	**5.9** µs	11 µs	48985	6.4 mm	**8.7** mm	24 mm	1586	0.0%	**89%**	97%	6.4%	21%	78%	1091	1.0%	3.5%	21%
AGGO	34	1.5 µs	**7.2** µs	7.9 µs	12308	9.3 mm	**13.7** mm	23 mm	652	0.0%	**72%**	91%	15%	41%	88%	352	0.0%	1.8%	11%
OHIGGINS	14	1.5 µs	**6.7** µs	11 µs	2635	8.5 mm	**18.8** mm	27 mm	370	0.0%	**62%**	88%	7.4%	59%	79%	193	0.7%	4.3%	59%

First Session:	Last Session:	Total Number of Sessions:	Qualifying Sessions:	Issue:	Originator (DCO):
03.01.2021 07:30	**31.12.2021 18:30**	**648**	**490** (Duration < **5 h**)	**12.12.2022 17:02:14**	**Schüler, Torben**

Name of Telescope	Applicable Sessions	Std.Dev. UT1-TAI			Observations in Total	Group Delay RMS			Observations Used in Analysis	Quality Codes 5-9			Analysis Loss		
		Min	Median	Max		Min	Median	Max		Min	Median	Max	Min	Median	Max
WETTZELL	371	2.8 µs	**11** µs	79 µs	16204	0.9 mm	**12.7** mm	67 mm	20	38%	**92%**	100%	0.0%	0.0%	43%
WETTZ13S	119	2.9 µs	**7.7** µs	33 µs	4774	5.6 mm	**14.0** mm	32 mm	40	76%	**98%**	100%	0.0%	2.3%	17%
WETTZ13N	21	3.8 µs	**5.1** µs	30 µs	1563	5.6 mm	**8.4** mm	39 mm	67	0.0%	**95%**	100%	2.8%	15.9%	33%

Fig. 2 Annual performance statistics for 2021. The first block contains results for long sessions (usually one day) such as Rapids. The second block is devoted to short duration sessions, i.e. the Intensive sessions.

4. *Annual Performance Statistics*: An annual summary is provided (see Fig. 3) from all these analyses.
5. *Balanced Score Card*: This score card contains performance indicators from various ”perspectives”. The process-internal perspective is populated with help of the performance indicators derived from the before-mentioned annual statistics. The score card serves as an overall orientation in terms of all aspects related to quality.
6. *WQC - Weekly Quality Check*: All session results of the past 7 days are automatically evaluated and are personally reviewed afterwards, usually each Tuesday. This process is organized in detail and carried out within the responsibility of the *Domestic Coordination Office (DCO)* at the Observatory. The DCO members dedicated to the WQC comprise a certified Quality Assistant, an Analyst and a Technician. Whilst the standard procedures are carried out by the Quality Assistant, detected problems may be further inspected by the Analyst who delves deeper into the details.
7. *Weekly Quality Check & Request 2 Reply*: The DCO prepares a Weekly Quality Report distributed to all members of the VLBI group. Rules exist to communicate possible or clearly severe problems to the responsible group leaders for telescope operations or the correlation facility, including a mechanism to verify that the problems are actually addressed (as indicated by ”request 2 reply”).
8. *Quality Circle*: A Quality Circle is not necessary for smaller ”ordinary” issues that can be fixed quickly (either by individuals or a small team). This Quality Circle team is formed to address larger improvement processes or projects. The topics are collected and put into order according to a priority assessment.
9. *(Continuous) Improvement Process*: Each item handled within a Quality Circle is a kind of project aiming at improving the system and data quality. CIP employs mechanisms of project management, moderation of workshops and success indicators following the PDCA cycle (Plan - Do - Check - Act).

The annual summary for the entire year 2021 is shown in Fig. 2. The formal error of UT1-TAI (standard deviation) is printed for information purposes. UT1 precision is a function of baseline length and proper baseline orientation. So it cannot be easily interpreted in terms of data quality of a single telescope. However, UT1-TAI is a very important parameter obtained from the Wettzell VLBI sessions, hence it is included here as a kind of final result of our work. In contrast, the group delay RMS is certainly related to data quality. Nevertheless, have in mind that this quantity can be influenced by analysisartifacts that have nothing to do with the data themselves, but are subject to mismodelling. One example are remaining tropospheric delay errors which may grow with increasing baseline length,

Session:	Database:	AC:	Start of Session:	Duration:	Frequency:
R11103	**r11103**	**NASA (IVS)**	**15.05.2023 @ 17:00:10**	**24.0 h**	**8.2 GHz**

Station Statistics:

Telescope	# Obs	M&C Loss	Ana Loss	StdDev [mm]	Obs Weight
BADARY	1503	7.8%	2.8%	9	15.5%
HART15M	675	33.2%	4.3%	13	5.4%
HOBART12	122	79.7%	3.2%	16	2.5%
KATH12M	230	63.9%	3.0%	12	4.3%
KOKEE	946	13.0%	2.4%	12	7.7%
NYALE13S	1277	5.9%	2.8%	9	13.6%
NYALES20	1677	9.1%	1.4%	9	17.6%
SVETLOE	881	9.1%	1.7%	23	4.0%
WETTZELL	**1454**	**10.6%**	**3.1%**	**8**	**16.4%**
ZELENCHK	1477	11.7%	3.1%	11	12.9%
TOTAL:					**16.4%**

Fig. 3 Rapid session R1 1103 (May 2023). The first part of the session performance overview for a typical IVS network session (Rapid R1 series). The second part - not shown here - comprises the product delivery latency information as well as a collection of problem statements from both the correlation staff as well as the geodetic data analyst. Underlined telescope names indicate that cable delay calibration data were used (# Obs = Number of group delays; M&C Loss = Measurement & Correlation Loss; Ana Loss = AnalysisLoss; StdDev = Standard deviation (aka RMS); Obs Weight = Observation weight).

maybe larger during hot summer and smaller in winter. The statistics for quality codes 5-9 are obtained from the correlation reports. We usually consider scans with these quality numbers as usable to good. The measurement and correlation loss is explained earlier in this paper as well as the analysisloss. We intentionally separate short duration sessions (i.e. Intensives) from long duration sessions (session usually covering 24 h such as Rapid network sessions).

You can clearly see an improved group delay precision of VGOS telescope WETTZ13S (Wettzell South) over the WETTZELL legacy telescope (Wz, 20 m). WETTZ13N (Wettzell North) was equipped with a tri-band feed in 2021 sensing classical S- and X-band data, it was not part of the VGOS network at that time.

3 Session Results

The session performance results shown in Fig. 3 are extracted from the corresponding spool file issued by the respective analysiscenter, NASA/NVI in this case. Note that the VLBI observable is a difference quantity, i.e. the group delay observed between two telescopes over a baseline. Consequently, it is theoretically not possible to yield an individual station RMS from these data. This is subject to assumptions. One important point here is a fitting stochastic model. The measurement & correlation loss is moderate for WETTZELL, the analysisloss within reasonable limits, and the group delay standard deviation (RMS) slightly above the median (compared to Fig. 2, though for a different year). The observation weight is computed from both the number of group delays that entered into the geodetic analysis(50% ”quantity”) as well as the group delay RMS (50% ”quality”). Weights are computed from a combination of both types of information (the squared values are used). We can then deduce what we call the ”weight of the telescope” within the network adjustment, i.e. about 16% for WETTZELL in this case.

4 Baseline Results

Since assumptions are made with respect to the data contained in Fig. 3, we should not forget to

Session:	Database:	AC:	Start of Session:	Duration:	Frequency:
R11098	**r11098**	**BKG**	**11.04.2023 @ 17:00:10**	**24.0 h**	**8.2 GHz**

Baseline Statistics:

Baseline		# Obs	M&C Loss	Ana Loss	StdDev [mm]
AGGO	HART15M	25	90.1%	7.4%	19
AGGO	MATERA	10	88.3%	9.1%	17
AGGO	**WETTZELL**	10	89.7%	0.0%	14
WETTZELL	HART15M	98	3.5%	28.5%	16
WETTZELL	MATERA	309	5.3%	3.7%	10
WETTZELL	NYALE13S	218	2.1%	5.6%	12
WETTZELL	ONSALA60	101	0.9%	5.6%	8
WETTZELL	SEJONG	123	3.8%	3.1%	21
WETTZELL	YARRA12M	24	57.4%	7.7%	20

Fig. 4 Baseline performance numbers for Rapid session R1 1098 (April 2023) showing the baselines containing telescopes AGGO (Argentina, Ag) and WETTZELL (GOW, Wz) with major data losses at AGGO.

have a look at the baseline results as depicted in Fig. 4. These are somehow the ”original results”. Baseline results have to be assessed for all network sessions during the WQC (Weekly Quality Check) by the reviewer. A quality report cannot be issued without having accomplished this review. In this case, the baseline AGGO to WETTZELL suffers from a large M&C Loss. So, is AGGO responsible for this poor performance or WETTZELL? As a matter of fact, all AGGO-related baselines exhibit a considerable M&C Loss, whereas only WETTZELL-AGGO as well as WETTZELL-YARRA12M show a problematic behavior, the other 5 baselines containing WETTZELL as a telescope are more or less okay (the AnalysisLoss over WETTZELL-HART15M is quite large, though). Consequently, we conclude that a quality problem cannot be attributed to WETTZELL. The high M&C Loss over baseline WETTZELL-YARRA12M is possibly caused by interference problems at YARRA12M. A look at the correlation report (not shown here) reveals a percentage of misdetections as high as 46% over that very baseline that is not present in other baseline data.

5 Conclusions

This first paper on the quality control system at the Geodetic Observatory Wettzell provides a brief overview about the system and the organization of quality assurance within the corresponding core process. The benefits, but also the limitations are outlined. One limitation is that this statistical information cannot always easily (i.e. directly) be traced back to the data quality obtained at Wettzell, because overlying effects such as data modeling errors can leave artifacts in those numbers. However, the advantage of this system is that a good orientation regarding quality matters is possible, and the performance of the Wettzell telescopes relative to the other participating stations in a dedicated session can be well-assessed.

References

DIN-Taschenbuch 223. Qualitätsmanagement und Statistik. Begriffe. Normen. Beuth-Verlag, 1997, ISBN 3-410-13763-4

DIN-Taschenbuch 224. Statistik. Auswertungen und Genauigkeitsanalysen. Beuth-Verlag, 1998, ISBN 3-410-14229-0

Edgar Dietrich, Stephan Conrad. Anwendung statistischer Qualitätsmethoden. 3rd edition. Hanser-Verlag, 2009, ISBN 3-446-41866-0

Claudia Kostka. Der Kontinuierliche Verbesserungsprozess. 7th edition. Hanser, 2017, ISBN 3-446-44659-5

Alexander Neidhardt. Applied Computer Science for GGOS Observatories. Springer Int., 2017.

Analysis of Non-Tidal Loading Deformation at VLBI Sites

S. Singh, J. Böhm, H. Krásná, N. Balasubramanian, O. Dikshit

Abstract Very Long Baseline Interferometry (VLBI) is one of the geodetic techniques used to establish the International Terrestrial Reference Frame (ITRF). It relies on data collected from multiple antennas situated at various locations across the Earth's surface. However, the accuracy of VLBI measurements can be compromised by Earth's crust deformation caused by a range of geophysical factors, including plate tectonics, solid Earth tide-induced loading, atmospheric pressure variations, and redistribution of water masses, both over land and in the oceans. Among these factors, non-tidal loading (NTL) deformations can also lead to positional shifts in VLBI sites, thus affecting measurement accuracy. To address these NTL effects in VLBI analysis, geophysical models are employed to correct the displacement of VLBI stations. The objective of this study is to compare the NTL products obtained from different loading services, such as the VieAPL, ESMGFZ, IMLS, and EOST. The evaluation of how these NTL products impact VLBI analysis is carried out using the VieVS software. This assessment entails the computation of baseline length repeatability and station height standard deviation, both before and after applying the loading corrections.

Keywords Non-tidal loading, VLBI, VieVS

Shivangi Singh · Nagarajan Balasubramanian · Onkar Dikshit
Geoinformatics, Department of Civil Engineering, IIT Kanpur, Kanpur, Uttar Pradesh 208016, India

Johannes Böhm · Hana Krásná
Department of Geodesy and Geoinformation, TU Wien, Wiedner Hauptstraße 8-10, 1040 Vienna, Austria

1 Introduction

The establishment and maintenance of the ITRF and International Terrestrial Reference System (ITRS) represent essential endeavours in modern geodesy. These efforts are pivotal because they provide the foundation for measuring and interpreting geophysical phenomena and their impact on Earth's shape and orientation. Geophysical factors, such as post-glacial rebound, seismic events, and variations in Earth's rotation, induce deformations in the Earth's surface. Consequently, accurate correction models are required to maintain the stability and accuracy of the reference frame, as they can introduce significant discrepancies in geodetic measurements (Altamimi et al., 2016). Calculating the displacements due to various geophysical effects allows us to reduce them from the station coordinates, obtaining the long-term linear station motion. Unlike other geophysical models, NTL models are not accurate enough. Therefore, it is advised not to adjust station positions for these effects, as per the International Earth Rotation and Reference Systems Service (IERS) Convention 2010. In recent years, numerous studies have been conducted on specific space geodetic techniques aimed at reducing non-tidal loading effects (Schuh et al., 2004; Petrov and Boy , 2004; Eriksson and MacMillan , 2014; Roggenbuck et al., 2015; Glomsda et al., 2020).
Non-tidal loading effects displace geodetic stations by a few centimetres on an annual to sub-daily basis (Wijaya et al., 2013). Also, the Global Geodetic Observing System (GGOS) was established with the ambitious objective of achieving 1mm accuracy in determining Earth's geometric parameters, as outlined in its strategic plan. Pursuing such unprecedented accuracy has revitalized the focus on correcting NTL effects, given

their substantial impact on geodetic measurements and the realization of GGOS's objectives.

2 NTL components and loading services

In this section, we will elucidate the NTL components employed in our investigation, the sources from which this data is extracted and the process of standardizing data from various services to ensure uniform formatting for comparison. In geodesy, NTL data refers to the utilization of diverse geophysical models aimed at correcting the theoretical signal delay encountered during VLBI observations. These models encompass non-tidal atmospheric loading (NTAL), non-tidal oceanic loading (NTOL), and hydrological loading (HYDL), which can be employed either independently or in combination to address the cumulative loading effects. NTAL is specifically designed to consider the impact of atmospheric pressure fluctuations on the Earth's surface, arising from dynamic changes in atmospheric pressure driven by meteorological events and factors unrelated to tidal forces. HYDL, on the other hand, addresses the deformation of the Earth's crust resulting from shifts in continental water storage. Lastly, NTOL is concerned with the deformation of the Earth's crust caused by the redistribution of mass within the oceans.

The displacement data resulting from these three loading factors is obtained from four distinct sources, which are as follows:
1. VieAPL (Vienna Atmospheric Pressure Loading) (https://vmf.geo.tuwien.ac.at/products.html)
2. ESMGFZ (Earth-System-Modelling group at GFZ)(http://rz-vm115.gfz-potsdam.de:8080/repository)
3. IMLS (International Mass Loading Service)(http://massloading.net/)
4. EOST (École & observatoire des sciences de la Terre)(http://loading.u-strasbg.fr/index.php)

VieAPL, IMLS, and EOST provide users with both pre-calculated global Grid-based mass loading time series and pre-calculated time series customized for particular space geodesy stations. Furthermore, IMLS enhances its offerings by delivering an on-demand Internet service, granting users the capability to request data for specific stations and specify their desired time intervals. In parallel, ESMGFZ delivers pre-computed global Grid-based mass loading time series and also allows users the option to retrieve data for particular stations while tailoring the time ranges according to their requirements. Within each loading category, numerous models are available for generating the associated loading products. In our study, the choice of models for different loading categories and services depends on factors such as data availability, time steps, update frequency, and spatial resolution level. Table 1 presents the characteristics of the chosen models. VieAPL and ESMGFZ data is updated daily, while IMLS data is updated monthly. EOST data undergoes updates every few months.

After selecting models for each loading category and service, we acquired center-of-mass frame NTL data for the year 2020 for this study. We identified a total of 163 VLBI stations, which remained consistent across all services and were categorized as ITRF sites. Following the data extraction process, the next pivotal step involves data formatting. It's important to note that data obtained from different services come in various formats. To facilitate meaningful comparisons within VieVS, we formatted the data obtained from the models selected from EOST, IMLS, and ESMGFZ into the VieAPL format of the loading corrections.

3 Data comparison

To compare the NTL products from four different services, we initiate the process by generating a time series graph illustrating NTAL displacement. This initial step is crucial because VieAPL exclusively offers NTAL data. It's worth highlighting that the NTAL products derived from all four services display a substantial level of concurrence among them (see Figure 1). This alignment can be ascribed to the fact that all services utilize the ECMWF model for extracting loading data.

In addition to the NTAL displacement graph, we generate another time series graph to evaluate the cumulative sum of all NTL components. It is evident that most services demonstrate a high degree of agreement among themselves in the cumulative NTL trend (see Figure 2). However, it's worth highlighting that there is a significant deviation observed, particu-

Table 1 Attributes of the selected non-tidal loading models corresponding to different loading components of various services.

Service	Loading	Model	Spatial Resolution	Time-steps	Data Availability
VieAPL	NTAL	ECMWF	1° × 1°	6h	1994-present
IMLS	NTAL	MERRA2	2' × 2'	6h	1980-present
IMLS	NTOL	MPIOM06	2' × 2'	3h	1980-present
IMLS	HYDL	MERRA2	2' × 2'	3h	1980-present
EOST	NTAL	ECMWF	0.5° × 0.5°	3h	2000-present
EOST	NTOL	ECCO1	1° × 1°	12h	1993-2021
EOST	HYDL	GLDAS2	0.25° × 0.25°	3h	2000-2022
ESMGFZ	NTAL	ECMWF	0.5° × 0.5°	3h	1976-present
ESMGFZ	NTOL	MPIOM	1° × 1°	3h	1976-present
ESMGFZ	HYDL	LSDM	0.5° × 0.5°	24h	1976-present

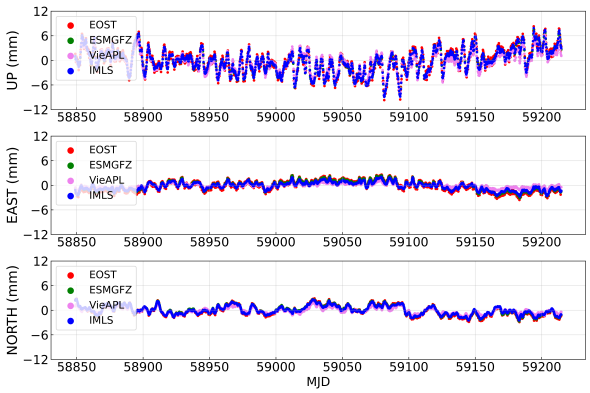

Fig. 1 Site displacement time series due to NTAL in CM-frame at AGGO station.

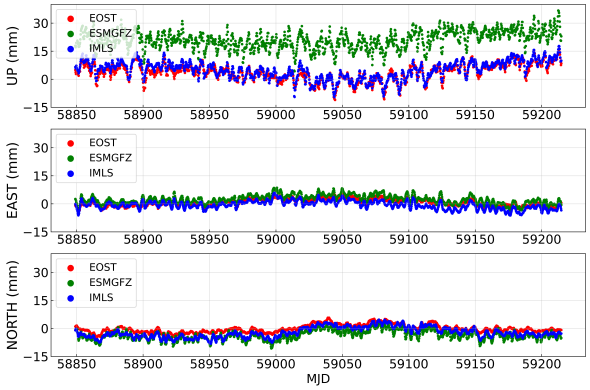

Fig. 2 Site displacement time series due to all NTL components in CM-frame at AGGO station.

larly in the up component of ESMGFZ.

To gain insight into the variations in data related to each NTL component of different services, we've plotted Root Mean Square (RMS) values of the difference in site displacement due to NTL between two services in the CM-frame and for 163 VLBI stations (refer to Figures 3,4,5). The RMS values are organized based on the latitude of each respective VLBI station. Notably, we observe significant RMS values of more than 8 mm, mainly occurring within the latitude range of 30°N to 65°N, particularly in the Up direction. Among the different loading components, the NTAL component shows the least variation between the two services, while the HYDL component exhibits the most substantial differences. This discrepancy is especially pronounced in the case of HYDL component of ESMGFZ vs. EOST, with an average RMS value of 6.7 mm and a maximum RMS value of 18.5 mm for the up direction. These disparities can be attributed to the use of distinct models with varying resolutions by different services. Additionally, the separate treatment of Sea Level Loading (SLEL) in order to achieve global mass conservation, as undertaken by ESMGFZ, may contribute to this observed variation. In contrast, other services incorporate partial mass conservation in both NTOL and HYDL, which could influence the level of agreement in these components.

4 Data processing in VieVS

We investigated the influence of non-tidal loading displacement models within VLBI analysis. These displacements resulting from non-tidal loading were incorporated as adjustments to the station coordinates at the observation level. The entire processing was conducted using VieVS, utilizing a one-year process list of R1/R4 sessions and OPT files for the year 2020. Notably, the VieVS graphical user interface (GUI) initially featured the option for loading displacement due to NTAL data, and subsequently, options for NTOL

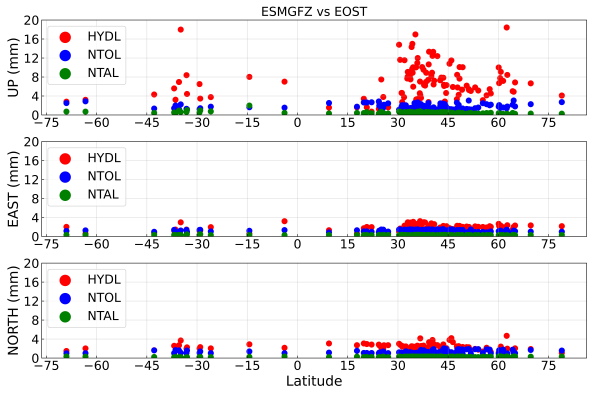

Fig. 3 RMS values of difference of site displacement due to different NTL components between ESMGFZ and EOST in CM-frame. The RMS values of stations are organized latitude-wise.

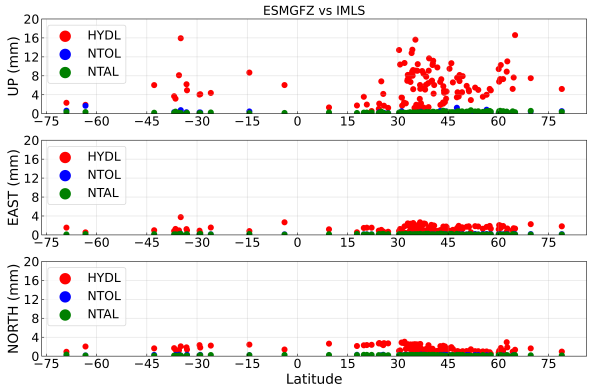

Fig. 4 RMS values of difference of site displacement due to different NTL components between ESMGFZ and IMLS in CM-frame. The RMS values of stations are organized latitude-wise.

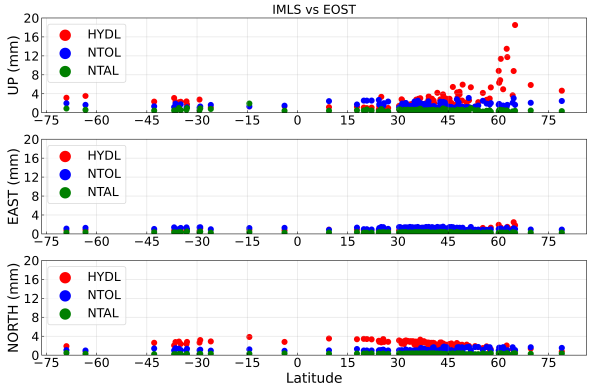

Fig. 5 RMS values of difference of site displacement due to different NTL components between IMLS and EOST in CM-frame. The RMS values of stations are organized latitude-wise.

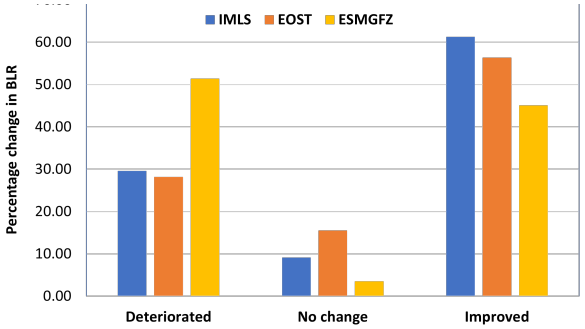

Fig. 6 Percentage change in BLR before and after applying all NTL models in CM-frame for 142 baseline.

and HYDL were introduced later in the process.

In VLBI analysis, the term ”baseline length repeatability” (BLR) denotes the degree of precision in measuring the length of a baseline connecting two VLBI stations over a period of time. BLR holds significant importance in VLBI because it directly influences the accuracy of both geodetic and astrometric measurements. By assessing BLR before and after applying NTL displacement products, we can determine whether there is an improvement in BLR as a result of using NTL models. In Figure 6, we present the percentage change in BLR before and after incorporating all NTL data, focusing on a total of 29 stations. The results reveal that 71.83% of baselines demonstrate improvement or remain unchanged when using EOST data, while 70.4% of baselines show improvement or stability with IMLS data. In contrast, only 48.59% of baselines exhibit improvement or stability when utilizing ESMGFZ data. Likewise, we've computed the standard deviation of station heights both before and after the application of NTL models for a total of 142 baselines (see Figure 7). The result revealed that a total of 67% of station height standard deviation improves after the application of NTL in the case of EOST and IMLS. However, in the case of ESMGFZ, the improvement is only 52.38%.

5 Conclusions and outlook

The application of NTL displacement corrections to VLBI station coordinates is essential for achieving high-precision BLR. It helps reduce systematic errors,

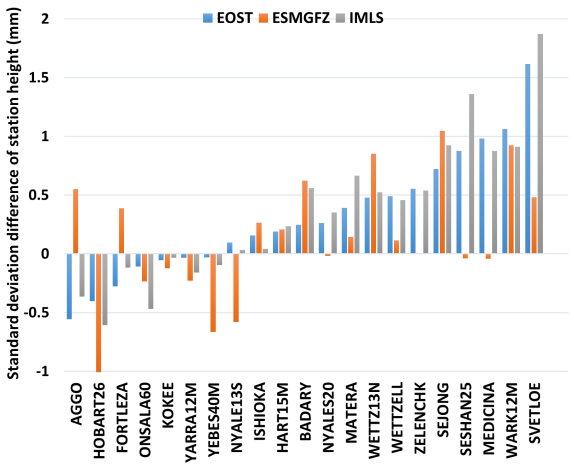

Fig. 7 Difference in the standard deviation of station heights both before and after the application of NTL models in CM-frame for 21 stations.

improve station coordinate accuracy, and enhance the long-term stability of VLBI measurements. Variation in the improvement of BLR among services (see Figure 6) is primarily due to HYDL and NTOL. The standard deviation difference of the time series of station height with and without NTL shows that the estimation of station coordinates improves upon the application of NTL models (see Figure 7). Also, results from different services are consistent with each other except in the case of ESMGFZ. The distinct approach taken by ESMGFZ in addressing Sea Level Loading (SLEL) with a focus on global mass conservation might be a contributing factor to the observed variation. In order to enhance our understanding, we will incorporate a broader range of data spanning approximately 20 years. We expect that this extended timeframe will provide valuable insights and contribute to a more comprehensive analysis.

Acknowledgement

This research has received joint support from the Austrian Agency for International Cooperation in Education and Research (OeAD-GmbH) and the National Centre for Geodesy (NCG), India.

References

Altamimi Z, Rebischung P, Métivier L, & Collilieux X (2016) ITRF2014: A new release of the International Terrestrial Reference Frame modeling nonlinear station motions. *Journal of Geophysical Research: Solid Earth*, 121(8), 6109-6131, doi: 10.1002/2016JB013098.

Böhm J, Böhm S, Boisits J, Girdiuk A, Gruber J, Hellerschmied A, Krásná H, Landskron D, Madzak M, Mayer D, McCallum J, McCallum L, Schartner M, Teke K (2018) Vienna VLBI and Satellite Software (VieVS) for Geodesy and Astrometry. *Publications of the Astronomical Society of the Pacific*, doi: 10.1088/1538-3873/AAA22B.

Dill, R., & Dobslaw, H. (2013) Numerical simulations of global-scale high-resolution hydrological crustal deformations. *Journal of Geophysical Research: Solid Earth*, 118, doi: 10.1002/jgrb.50353.

Eriksson D, MacMillan DS (2014) Continental hydrology loading observed by VLBI measurements. *Journal of Geodesy*, 88:675–690, doi: 10.1007/s00190-014-0713-0.

Glomsda M, Bloßfeld M, Seitz M, Seitz F (2020) Benefits of non-tidal loading applied at distinct levels in VLBI analysis. *Journal of Geodesy*, doi: 10.1007/s00190-020-01418-z.

Petrov L, Boy J P (2004) Study of the atmospheric pressure loading signal in very long baseline interferometry observations. *Journal of Geophysical Research*, 109(B3):B03405, doi: 10.1029/2003JB002500.

Roggenbuck O, Thaller D, Engelhardt G, Franke S, Dach R, Steigenberger P (2015) Loading-induced deformation due to atmosphere, ocean and hydrology: model comparisons and the impact on global SLR, VLBI and GNSS Solutions. *T. van Dam (eds), REFAG 2014, International Association of Geodesy Symposia, Vol. 146, Springer International Publishing Switzerland*, pp. 71-77, doi: ISBN:978-3-319-45628-7.

Schuh H, Estermann G, Crétaux J F, Bergé-Nguyen M, & van Dam T (2004) Investigation of hydrological and atmospheric loading by space geodetic techniques. *In Satellite Altimetry for Geodesy, Geophysics and Oceanography: Proceedings of the International Workshop on Satellite Altimetry, a joint workshop of IAG Section III Special Study Group SSG3. 186 and IAG Section II, September 8–13, 2002, Wuhan, China. Springer Berlin Heidelberg*, pp. 123-132, doi: 10.1007/978-3-642-18861-9_15.

Wijaya DD, Böhm J, Karbon M, Krásná H, & Schuh H (2013) Atmospheric pressure loading. *In: Böhm J, Schuh H (eds) Atmospheric effects in space geodesy. Springer, Berlin, Heidelberg*, pp 137–157, doi: 10.1007/978-3-642-36932-2_4.

Status of Ishioka Geodetic Observing Station

Y. Takagi, M. Ishigaki, T. Nakakuki, H. Yoshifuji, M. Honda, K. Mori, Y. Sato

Abstract We report the current status of the Ishioka Geodetic Observing Station. In order to improve the availability of the Ishioka station, we conducted experiments to investigate how to participate in both S/X and VGOS sessions without changing receivers. We are also testing new recording systems: DBBC3 and Flexbuffs. Local-tie surveys are regularly conducted in the Ishioka station. The position and velocity of Ishioka station were given in ITRF2020, which is the first time for the station since its operation has started. The results of the local-tie surveys for 2021 and 2022 show relatively larger difference from the value calculated from ITRF2020 than those for 2018-2020.

Keywords Polarizatoion, DBBC3, Flexbuff, Local-tie survey

1 Introduction

The Ishioka 13-m telescope at the Ishioka Geodetic Observing Station (hereafter Ishioka station), operated by the Geospatial Information Authority of Japan, has participated in the IVS sessions since 2015. One of the goals of Ishioka station is to participate in international observations to contribute to the development and maintenance of the ITRF and ICRF as well as the Japanese national geodetic datum. To achieve these goals, we have been involved in the following topics recently:

Yu Takagi · Masafumi Ishigaki · Tomokazu Nakakuki · Hiroyuki Yoshifuji · Masaki Honda · Katsuhiro Mori · Yudai Sato
Geospatial Information Authority of Japan, 1 Kitasato, Tsukuba city, Ibaraki Prefecture, 305-0811 Japan

- polarization conversion
- installation of new recording systems
- local-tie surveys

In this proceeding, we report these topics.

2 Management of polarization

Currently, the Ishioka station is involved in VGOS observations for several months a year and in legacy S/X observations for the rest of the year by switching their respective receivers (Fig. 1). This causes two problems; observations must be interrupted while switching the receivers, and the receiver change requires a lot of manpower. To solve these issues, we are exploring the way in which we use the broad-band receiver for both VGOS and S/X observations. One of the major problems was the RFI below 3 GHz. It was fixed by installing the superconducting filters in the receiver (Takagi et al., 2021), which mitigates the RFI when observing S-band frequency with the broad-band receiver. The remaining challenge is how to handle the polarization. Circular polarization is used in S/X sessions, whereas linear polarization is used in VGOS sessions. The broad-band receiver can only detect linear polarization. For this reason, it is not directly applicable to S/X observations. There are two methods which could resolve this problem as explained in the following subsections.

2.1 Conversion at the station

We conducted an experiment in corporation with the Mizusawa station (NAOJ) to investigate the possibility

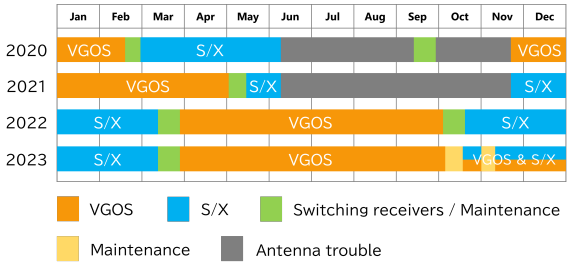

Fig. 1 Recent status of the Ishioka station. The status after October 2023 shows the planned schedule as of September 2023.

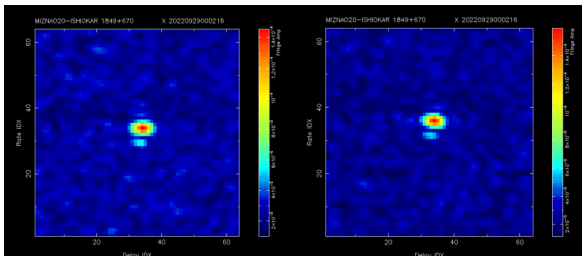

Fig. 2 Fringes detected in AOV075 (left) and the additional experiment (right), respectively. .

of converting linear polarization to circular one. In this experiment, AOV075 and additional experimental data of the Ishioka station were converted from linear to circular polarization by shifting the phase of horizontal component by 90 degrees and combining it with the vertical component, then they were correlated with the circular polarization data of the Mizusawa station. Fig. 2 shows the result of fringe fittings. We successfully obtained fringes; however, the SNRs were smaller than the expected values, which should have been 1.41 times larger than those without conversion. We need further investigation in order to improve this method.

2.2 Mixed-mode correlation by IVS correlators

The Ishioka station participated in S/X sessions, R11098 and R41098, with the VGOS receiver in April 2023. IVS correlators tested mixed-mode correlation which enable for both S/X and VGOS stations to join the same session. In both test sessions, fringes were successfully detected (Fig. 3). We plan to have another test session before participating in mixed-mode sessions regularly.

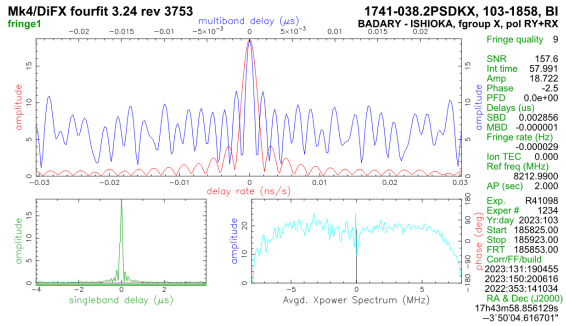

Fig. 3 Fringe detected in R41098 (provided by Sara Hardin (WASH)).

Fig. 4 (Left) Front view of the DBBC3 newly installed at the Ishioka station. (Right) Top-down view.

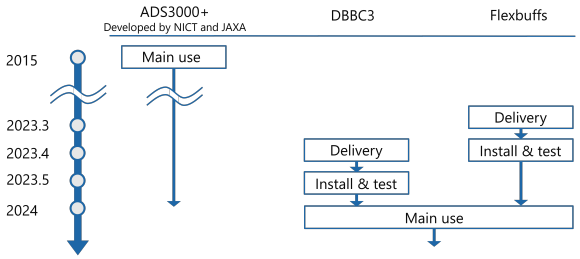

Fig. 5 Upcoming schedule of installation & test of new instruments in the Ishioka station.

3 New recording system

At the Ishioka station, ADS3000+ developed by NICT and JAXA is currently used for the recording system. The issue is that new servers connectable to it are no longer available. Thus, we decided to install a DBBC3 and Flexbuffs (Fig. 4). New Flexbuffs and a DBBC3 were delivered in March and April, 2023, respectively. Now, they are being installed and tested (Fig. 5).

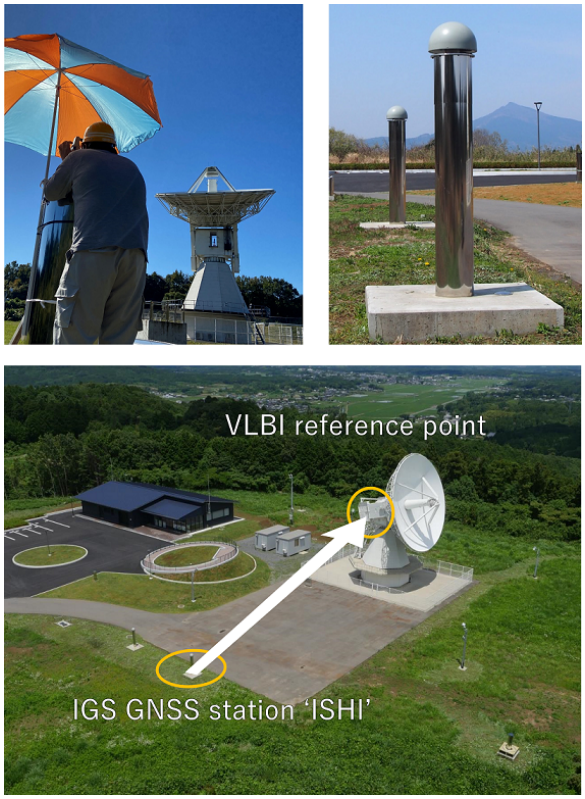

Fig. 6 (Upper left) Measuring the positions of the mirror installed in the AZ cabin from the pillar using the TS. (Upper right) GNSS station called ISHI, which is registered as an IGS station. (Bottom) VLBI-GNSS local-tie vector.

4 VLBI-GNSS Local-tie survey

We carry out local-tie surveys regularly to estimate the local-tie vector between the reference points of the telescopes and the IGS GNSS station operated at the Ishioka station (Fig 6). We have adopted 'inside method' (Matsumoto et al., 2022) to conduct the surveys efficiently. The results of the 2018 and 2020 surveys were submitted to the IERS to contribute to the construction of ITRF2020. The surveys were also conducted in 2021 and 2022.

The results for local surveys were compared with the calculated value based on ITRF2020 (Fig. 7). The value obtained by the surveys are consistent with the calculated value from 2018 to 2022. On the other hand, the deviation becomes larger in 2021 and 2022. It is possibly because the ITRF2020 does not reproduce the velocity of the Ishioka station after 2021. The ITRF2020 uses only a linear function to represent the position of

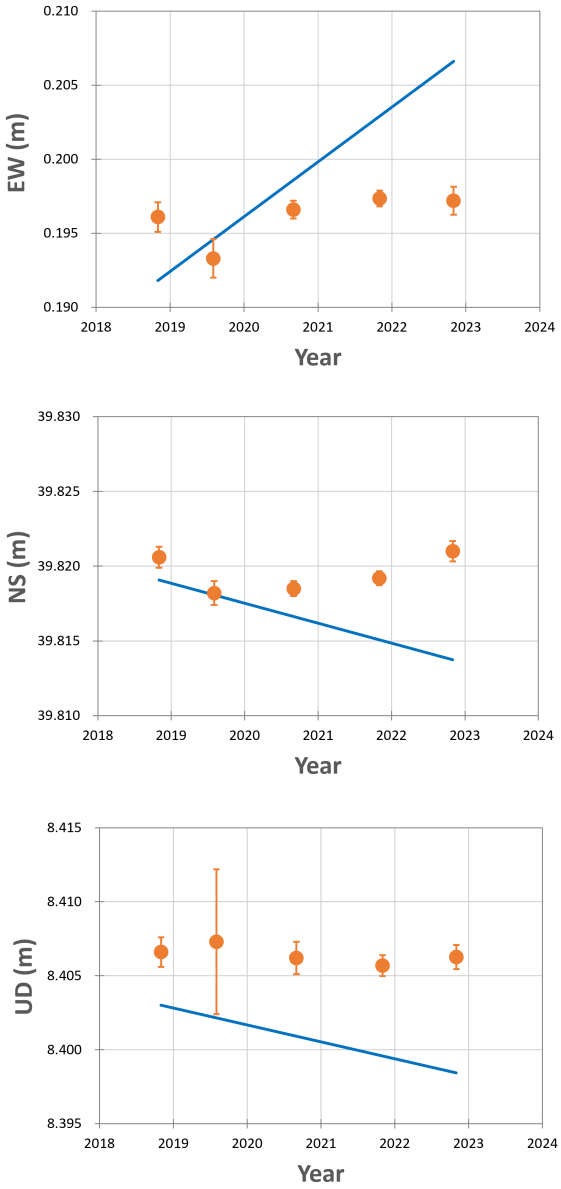

Fig. 7 Results for local-tie surveys (orange circles with error bars) are compared to the calculated values based on ITRF2020 (blue line). Top, middle, and bottom panels represent the east-west, north-south and up-down components, respectively.

the Ishioka station although it has experienced large post-seismic deformation caused by the 2011 off the Pacific coast of Tohoku Earthquake. Further monitoring of the velocity is necessary by regular local-tie survey for revealing what causes this deviation.

5 Summary

The current status discussed in this report is summarized as follows:

- The position and velocity of Ishioka station were given in ITRF2020.
- Experiments were conducted to investigate how to participate in both S/X and VGOS sessions without changing receivers.
- DBBC3 and Flexbuffs are installed and being set up.
- Local-tie surveys are regularly conducted. The results for 2021 and 2022 show relatively larger difference from the value calculated from ITRF2020 than those for 2018-2020. The local-tie continues to be monitored.

Acknowledgement

We are grateful to Dr. Oyama and Dr. Jike in NAOJ for their extensive contribution to the polarization conversion experiment.

References

Takagi Y, Ueshiba H, Nakakuki T, Matsumoto S, Hayashi K, Yutsudo T, Mori K, Kobayashi T, Sekido M, McCallum J, Shu F (2021) A superconductor filter installed in the broadband feed of Ishioka VLBI. *EVGA2021 proceedings*.

Matsumoto S, Ueshiba H, Nakakuki T, Takagi Y, Hayashi K, Yutsudo T, Mori K, Sato Y, Kobayashi T (2022) An effective approach for accurate estimation of VLBI–GNSS local-tie vectors. *Earth, Planets and Space*, 74, 147, doi: https://doi.org/10.1186/s40623-022-01703-5.

How to deal with expanding spectrum of telecommunication networks threatening VLBI?

V. Tornatore, M. Bautista-Duran, J.S. Ferreira, S. García, H. Hase, J. Kallunki, M. Lindqvist, J.A. López-Pérez, W. Madkour, D. McKay, W. Probst, L.M. Tangen, B. Winkel

Vincenza Tornatore
Politecnico Milano, Piazza Leonardo da Vinci 32, I-20133 Milano, Italy

Marta Bautista-Duran
Instituto Geográfico Nacional, Observatorio Yebes, Cerro de la Palera sn, E-19141 Yebes, Guadalajara, Spain

Joao Salmin Ferreira
Associaçao RAEGE Açores, Estação RAEGE de Santa María, Estrada dos Piquinhos s/n, 9580-324 Vila do Porto, Portugal

Susana García
Kartverket, Geodetic Earth Observatory, P.O. Box 13, N-9173 Ny-Ålesund, Svalbard, Norway

Hayo Hase
Bundesamt für Kartographie und Geodäsie, BKG Wettzell-AGGO, Sackenrieder Str. 25, D-93444 Bad Kötzting, Germany

Juha Kallunki
Aalto University, Metsähovi Radio Observatory, Metsähovintie 114 , FI-02540 Kylmälä, Finland

Michael Lindqvist
Department of Space, Earth and Environment, Chalmers University of Technology, Onsala Space Observatory, S-439 92 Onsala, Sweden

José Antonio López-Pérez
Instituto Geográfico Nacional, Observatorio Yebes, Cerro de la Palera sn, E-19141 Yebes, Guadalajara, Spain

Waleed Madkour
Joint Institute for VLBI ERIC, Oude Hoogeveensedijk 4, NL-7991 PD Dwingeloo, The Netherlands

Derek McKay
Aalto University, Metsähovi Radio Observatory, Metsähovintie 114 , FI-02540 Kylmälä, Finland

Willi Probst
Bundesamt für Kartographie und Geodäsie, BKG Wettzell, Sackenrieder Str. 25, D-93444 Bad Kötzting, Germany

Leif Morten Tangen
Kartverket, Kartverksveien 21, 3511 Hønefoss, Norway

Abstract New plans from telecommunication enterprises foresee the demand of wide sub-band allocations in the range of 1-100 GHz during the upcoming World Radio Conferences (WRC23, WRC27, ...), which go beyond the known expansion of spectrum use by 5G and large satellite constellations. New disturbing signals have been detected and some of them also monitored at VLBI stations. The radio-quiet sky is at risk and so it is VLBI. How can this situation be addressed in the most effective way? The current strategy is presented here to motivate activities in the different areas of spectrum administration, technical development and a standardization of the IVS service work.

Keywords VGOS, telecommunication, satellite constellation, base station, interference, protection

1 Introduction

VLBI stations are increasingly exposed to undesired signals from artificial transmitters, both in space and from the ground.

In space, large non-geostationary orbit (non-GSO) constellations aim at providing global internet telecommunication coverage, with a very low latency. The consequence is thus a very large number of satellites in orbit. This number is increasing on a weekly basis. For example, the Starlink constellation works with downlink signals in the range of 10.7-12.7 GHz and uplink signals in the range of 14.0-14.5 GHz

Benjamin Winkel
Max-Planck-Institut für Radioastronomie, Auf dem Hügel 69, D-53121 Bonn, Germany

that have power levels higher than 40 dBm with respect to -110 dBm of cosmic signals observed with VLBI. The downlink signals may saturate the low noise amplifiers (LNA) of the VGOS broadband receivers or even destroy them when the satellite antenna main beam points into the main beam of the radio telescope (see also (ECC-Report 271 , 2018, 2021)).

Development of cell-phone base stations on communication satellites to reach remote areas is currently under discussion. The typical power levels of terrestrial cell-phone base stations are already an interference problem to radio astronomy. This becomes a more serious issue for space-based stations, as a result of the stronger signals involved and the potential for main-beam to main-beam coupling.

On the ground, International Mobile Telecommunication (IMT) is requesting for more additional bandwidth (e.g. for 5G, 6G and UWB radars) between ∼2 and 12 GHz. The spectrum of 6.425-7.125 GHz is targeted for the use by 5G and RLAN (WiFi). Both will overlap and disturb unprotected channels of the actual VGOS B- and C-band. If these new allocations for IMT become effective, they would degrade sensitivity and accuracy of VGOS measurements in these bands. The radio astronomy community is concerned about losing the important spectral line of methanol at 6.650-6.6752 GHz (Fig. 4), even though it has a protection by footnote 5.149 in the Radio Regulation.

Important achievements in increasing the awareness of scientific communities on the importance of geodetic VLBI and VGOS activities have been accomplished. Nevertheless, further efforts are required in order to gain proper protection of the geodetic VLBI observations in general and, in particular, protection of the VGOS bands before they will be overwhelmed by signals of active radio services.

This article presents two monitoring examples of undesired signals observed at VLBI stations and summarizes the efforts which could be undertaken in order to secure the provision of geodetic VLBI data in the future.

2 Spectrum Monitoring at Santa Maria VGOS station

Spectrum monitoring studies were conducted at the Portuguese VGOS station at Santa Maria Island (Fig. 1). The very strong interference signals at 2.942 and 2.958 GHz caused saturation and inter-modulation in the VGOS receiver. Out-of-band emissions and their associated harmonic emissions are also present up to the 4th order. As a consequence, an attempt at mitigation was made using high pass filters. These filters had to be installed to reject the powerful unwanted signals and enable VGOS observations again. Despite of the strong attenuation by 50 dB (a factor of 100 000 in power!) of the unwanted signals, the remaining power of -37 dBm in Fig. 1 is still considerable and it did not prevent the VGOS observation from losing the VGOS Band A (3.0-3.48 GHz). The data loss caused is 25% and the sensitivity loss reaches 17%. The receiver could only be used where the signal path was not saturated in the range of 4-14 GHz.

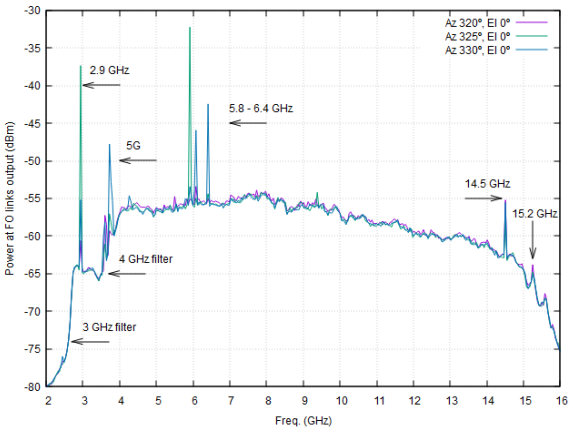

Fig. 1 Radio spectrum measured in the frequency range of 2-16 GHz at azimuth angles 320°, 325°, 330° and 0° elevation pointing into the direction of the ESA teleport as transmitter. The broadcast signal of 2.9 GHz and its unfiltered 2nd harmonic at 5.8 GHz are clearly identified as strong signals.

A second example is given in Fig. 2. When the radio telescope points to zenith direction it catches all kinds of signals through the main lobe and the associated side lobes which are pointing to different directions. This makes it difficult to identify a specific transmitter. However, the signals present in Fig. 2 fall in the satellite downlink range of 10.7-12.7 GHz and the first assumption is, that this snapshot shows a satellite downlink. The measured power levels are not far from the maximum input power level for linear operation of the low noise amplifiers (-40 dBm). If such a downlink signal is caught during a VLBI observation by a VGOS broad-

band receiver, it increases the noise in the receiver. This may result in the loss of the effected observation scan during the correlation process, when the expected (cosmic) signal-to-noise ratio could not be attained within the scheduled observation time, resp. integration time.

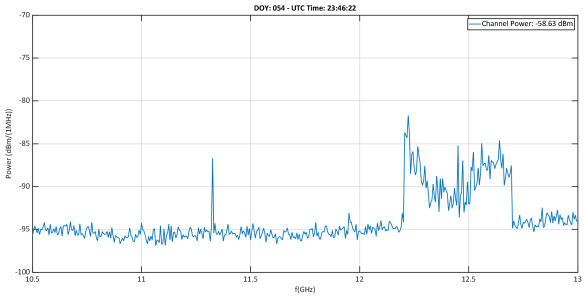

Fig. 2 Radio spectrum measured in the frequency range of 10.5-13.0 GHz for satellite downlink monitoring in the zenith direction. The deviations from the ground noise level should be caused by satellite downlink beacons.

The problem of satellite downlinks will increase with time, as more satellites are installed. As of May 25th, 2023, we already encounter many satellites of the mega constellations from Starlink and OneWeb. This is shown for the location Wettzell in Fig. 3. In this snapshot, already 3 out of approximately 250 visible satellites are higher than 60° elevation and are potential interferers. Projected future numbers range from 50 000 satellites in orbit by the end of this decade to more than 500 000 beyond 2030 and scale the potential for interferers over all stations accordingly. Table 1 lists the known constellation projects with the anticipated number of transmitting and receiving satellites.

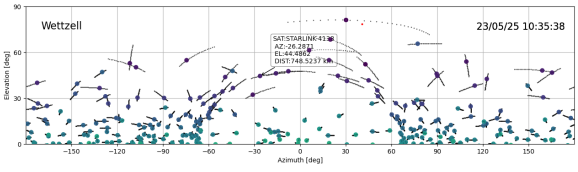

Fig. 3 Mega satellite constellations (Starlink, OneWeb) above Wettzell as of May 25, 2023, 10:35. The commercialization of space contributes to the loss of a radio-quiet sky.

Constellation	No. of sat.	Downlink bands	Altitude [km]
Starlink Phase 1	4,400	Ku, Ka	550
OneWeb Phase 1	648	Ku, Ka	1,200
Amazon Phase 1	3,200	Ka	600
Guo Wang (GW)	13,000	Ku, Ka	590-1,145
Starlink VLEO	7,600	V	340
Telesat	1,700	Ka	
Starlink Phase 2	30,000	Ku, Ka, E	328-614
OneWeb Phase 2	6,372	Ku, Ka, V	1,200
Boeing	5,789		
Astra	13,620		
Amazon Phase 2	7,774		
Cinnamon-937	300,000		

Table 1 Large Low Earth Orbiting (LEO) satellite constellation features. With 64,800 satellites in orbit, there will be statistically one transmitter in each square degree of the sky. The impact on the provision of geodetic products by VLBI are unknown and that is of grave concern.

3 IMT: Present and planned frequency allocations

The expansion of mobile communication networks requests more and more bandwidth. The IMT industry is supported by policy makers in many countries, who associate economic growth with the expansion of mobile telecommunications. Over the last decade, a huge amount of spectrum had been allocated to IMT. The introduction of new technical devices will require even more bandwidth. As the spectrum is a limited resource, from year to year it will be harder to find unused bands for geodetic VLBI observations. Fig. 4 illustrates that IMT is even requesting protected bands for radio astronomy such as the methanol line at 6.650 GHz.

Cell-phone base stations are usually so powerful, that radio astronomy or VLBI is not possible within up to 100 km if operating in the same frequency bands. And even in adjacent bands large protection distances are required. In other words, spectrum assigned to IMT is usually lost completely for VLBI observations.

4 What can be done to ensure the conditions for VLBI observations?

The International VLBI Service for Geodesy and Astrometry (IVS) is charged to provide geodetic products.

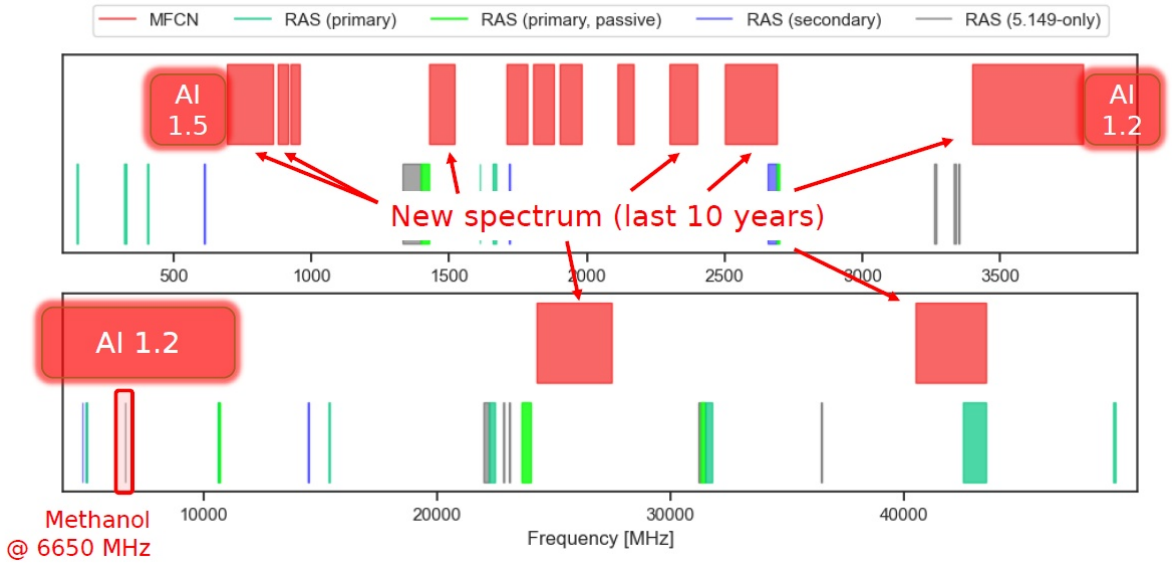

Fig. 4 Present and planned frequency allocations for the International Mobile Telecommunications (IMT) service. The upper part shows the spectrum from 0 to 4.0 GHz, the lower from 4.0 to 50.0 GHz. The VGOS spectrum 2-14 GHz is widely covered by red boxes. The red boxes mark parts of the spectrum which had been allocated to IMT during the World Radio Conference (WRC) 2019 and had been prepared over the past 10 years. The boxes marked with "AI 1.2" and "AI 1.5" (AI = agenda item) indicate new spectrum which will probably be allocated during the WRC 2023 to IMT and afterwards used for active services. The tiny blue and green lines are mostly spectral lines allocated to radio astronomy. Up to now allocations to RAS for the needs of VGOS do not exist.

Therefore, it is the task of the IVS member institutions and associates to develop a strategy against the deteriorating predicament of VLBI. The conservation of the conditions for needed VLBI observations requires activities in

- spectrum management and administration,
- new technical developments to mitigate inference to VLBI receivers,
- update of the technical specifications for VGOS.

4.1 Spectrum management and administration

According to the Radio Regulations, geodetic VLBI is categorized to the Radio Astronomy Service (RAS) because it is observing cosmic radiation. But, geodetic VLBI does not make use of the already allocated bands to RAS, because it observes a wider channel width (32 MHz) than most of the allocated spectral lines. However, from the point of view of spectrum management it would be a small advantage to cover some of the RAS bands with VGOS-channels, if possible.

Geodetic VLBI network stations require globally-simultaneous access to the same cosmic radio source. The global infrastructure needs protection, but only national administrations can provide this protection. The global affairs are regulated by the International Telecommuncation Union (ITU), whose member countries (represented by national administrations) must understand, and agree on, the needs of global geodetic VLBI networks.

The authors have already initiated three successful initiatives in support of geodetic VLBI and VGOS by increasing the awareness of the geodetic VLBI needs:

- IAU Resolution B1 (2021) in support of geodetic radio astronomy against radio frequency interference (IAU Resolution B1 , 2021);
- ITU-R Report RA.2507 Technical and operational characteristics of the existing and planned Geodetic Very Long Baseline Interferometry (ITU-R Report RA.2507 , 2022);
- IUGG Resolution 1 (2023) Improving Protection of Geodetic Observatories from Active Radio Services (IUGG Resolution 1 , 2023).

A fourth document, an ITU-R Recommendation on "guidance to administrations regarding geodetic very long baseline interferometry networks" is under discussion at ITU-R Working Party 7D. The idea of setting up radio quiet zones (or coordination zones) around all geodetic VLBI stations in order to protect the global infrastructure of geodetic VLBI networks is one plausible request. Radio quiet zones were invented to enable RAS observations of non-allocated frequency bands.

Besides the protection of the network by radio quiet zones (which is a longer procedure), the IVS has the task to define a final VGOS frequency configuration which addresses the needs of the Global Geodetic Observing System (GGOS) in an effective and productive manner (GGOS , 2009). This process of evaluating different configurations is on-going, and is managed by an IVS working group. It shall report by the end of 2024. Once the "fixed" frequency bands have been established, the next step is the request for protection of these particular channels by footnotes in the Radio Regulations, e.g. protection by footnote 5.149 which "urges administrations to take all practicable steps to protect the radio astronomy service from harmful interference". The footnote request seems to be more realistic for acceptance than a request for allocations (although this is still an option).

A strong argument for a national administration to provide protection, is the classification of the geodetic VLBI station as "critical infrastructure". This could imply that the unhindered access to a radio-quiet sky must be provided each day and night (24/7). Consequently, spectrum administrations must regulate the environment of a geodetic VLBI station in such a way, that no interference disturbs VGOS observations.

Another strong argument is to obtain a legal basis for the execution of geodetic VLBI observations. Then the operation becomes a "sovereign task" and national spectrum administrations have to provide assistance, that this task can be executed. The "sovereign task" can be derived from the UN-GA Resolution 69/266 on the "Global Geodetic Reference Frame for a sustainable development" (UN GA Resolution 69/266 , 2015). The global geodetic reference frame needs VLBI observations and UN member states are called to contribute to it.

"Critical infrastructure", in conjunction with the "sovereign task" of Earth orientation monitoring as a fundamental service for any kind of space control and navigation, reflects the importance of geodetic VLBI for the standard of today's quality of life.

4.2 Technical developments

The mitigation of unwanted interference requires the use of filters, which ideally are located in front of the first amplifier. Several VLBI stations are already implementing filters due to the worsening situation. Mitigation is always a second choice, when the interference is already present. It may cure the symptom not the cause. However, the degradation of system performance by the introduction of filters should be always less than the performance with the interference signal untreated.

The same is valid for interference reduction by digital bit-clipping. Information of cosmic noise will be lost, which otherwise would be hidden under the interference noise. This approach may improve the performance under the given circumstances.

If the IVS fixes the observation frequencies, new receivers could be developed. The filter characteristics of the feed could be used to tailor a receiver to the observation frequency bands and replace the current broadband VGOS receiver.

4.3 Update of technical specifications for VGOS

20 years after the initiative of developing the VGOS concept, it is challenged now by the changed electromagnetic environment at VLBI sites and in space. The VGOS specifications should be reviewed to reach a sustainable operation in this changing environment. The frequency range 2-14 GHz seems to be obsolete as the man-made signals in the range of 2-3 GHz make VLBI almost impossible at many sites and other targeted bands seem to become unusable as well. New radio telescope projects need to know which are the future observation modes and conditions to become compatible with the VGOS network, but being better prepared and less affected by interference.

5 Conclusion

Until the end of this decade (2030) the electromagnetic environment will change dramatically for geodetic VLBI stations. It is difficult to predict in detail, to which degree VLBI stations will be affected by the present and upcoming new active radio services. National spectrum administrations have the key role of providing local radio quiet zones or coordination zones and of providing support for geodetic VLBI at the global level at the ITU-R conferences. The global geodetic VLBI networks as global infrastructure cannot be protected by one national administration alone; it requires a common understanding among nations, that geodetic VLBI is important for humanity.

The IVS should prepare itself on how it can provide its service in the most productive and sustainable manner to meet the objectives of GGOS, while simultaneously facing the problems caused by less and less available spectrum for passive users. A "fixed frequency bands" configuration allows spectrum management activities to search for protection of these bands at the level of ITU-R.

The IVS should also pro-actively encourage development projects for a sustainable VLBI operation in the future with new concepts for new receivers and mitigation of interference.

Acknowledgement

V. Tornatore thanks for the support of her participation at the EVGA2023 meeting by IRA-INAF.

References

ECC Report 271: Compatibility and sharing studies related to NGSO satellite systems operating in the FSS bands 10.7-12.75 GHz (space-to-Earth) and 14-14.5 GHz (Earth-to-space) (2018, 2021)
https://docdb.cept.org/download/3422

IAU Resolution B1 (2021) in support of geodetic radio astronomy against radio frequency interference
https://www.iau.org/static/archives/announcements/pdf/ann21040a.pdf

ITU-R Report RA.2507: Technical and operational characteristics of the existing and planned Geodetic Very Long Baseline Interferometry, 10/2022
https://www.itu.int/dms_pub/itu-r/opb/rep/R-REP-RA.2507-2022-PDF-E.pdf

IUGG Resolution 1 (2023) Improving Protection of Geodetic Observatories from Active Radio Services.
https://iugg.org/wp-content/uploads/2023/09/2023_IUGG-GA-Resolutions.pdf

H. P. Plag, M. Pearlman (eds.): Global Geodetic Observing System - Meeting the Requirements of a Global Society on a Changing Planet in 2020, Springer Berlin, Heidelberg, 2009
https://doi.org/10.1007/978-3-642-02687-4

United Nations General Assembly Resolution 69/266: A global geodetic reference frame for sustainable development, 2015
https://digitallibrary.un.org/record/790376

DBBC4 - A Next Generation VLBI Backend

G. Tuccari[1,2], H. Rottmann[2], W. Alef[2], S. Buttaccio[1], S. Dornbusch[2], A. Felke[2], A. Roy[2], M. Wunderlich[2]

Abstract The development of the DBBC4, the latest version of the DBBC family of digital front- and backends for VLBI is ongoing. The DBBC4 makes use of the latest high-speed digital devices to expand the sampled bandwidth by a factor 8 over the DBBC3 (up to 274.4 GHz), introduces a distributed architecture with the sampler located optionally at the receiver, offers burst-mode recording with 56 Gbps/disk, and provides near-real-time RFI mitigation using AI. We describe the general system architecture and the current development status. A particular focus is given to elements of relevance for the VGOS network.

Keywords VLBI, Backend, DBBC, Artificial Intelligence

1 Introduction

The DBBC4 will be a key technical component in enabling new scientific applications in the rapidly evolving field of wide-band, multi-frequency astronomical and geodetic VLBI and will set a new standard in the area of VLBI backends. Technically the DBBC4 will incorporate the latest state-of-the-art sampling technology enabling an increase of the processed bandwidth by a factor of eight compared to the DBBC3, the predecessor system and current de-facto standard for astronomical and geodetic VLBI. The use of artificial intelligence algorithms will allow mitigation of radio frequency interference (RFI) in near real-time; one of the most severe issues to be addressed when increasing the observing bandwidth. The DBBC4 is the latest in the successful family of DBBC backends (DBBC, DBBC2, DBBC3) developed in a long-lasting collaboration between the MPIfR and INAF (Istituto Nazionale di Astrofisica, Italy). The DBBC4 key technologies are based on and extend the developments of the BRAND (BRoad-bAND) digital receiver project covering the 1.5 - 15.5 GHz band, including the IVS VGOS bands. Fig. 1 shows in logarithmic scale the evolution path of the performance of the various backend systems.

The DBBC4 backend is intended to offer the following capabilities and features:

- **Input bandwidth:** 274.4 GHz maximum full aggregate bandwidth realized by 8 x 28.8 GHz in digital front- or backend plus 8 x 5.5 GHz in ancillary digital front-end.
- **Output data rate:** up to: 1 Tbps @ 2-bit, 2 Tbps @4-bit, 4 Tbps @ 8-bit
- **Processing modes:** DSC (full band for data transfer), OCT (wide bands defined in the input band), DDC (narrow band tunable down-conversion)
- **New functionalities:** Burst-mode, AI-mode for RFI-mitigation and transient detection, net-to-memory/disk capability

2 General Architecture

The new system provides vastly greater bandwidth and agile signal processing capabilities, while simultaneously offering a feature-compatible upgrade path

(1) INAF-Istituto di Radioastronomia, via Gobetti 101, 40129, Bologna, Italy
(2) Max Planck Institut fuer Radioastronomie, Auf dem Huegel 69, 53121, Bonn, Germany

DBBC Family Evolution (Table)

	DBBC1 (2004)	DBBC2 (2009)	DBBC2010 (2010)	DBBC3 (2014)	BRAND (2020)	DBBC4 *(2024)*
Max Input Bandwidth (MHz)	512	4096	8192	32768	57600	256000
Max Output Data rate (Mbps)	1024	8192	16384	131072	460800	4000000

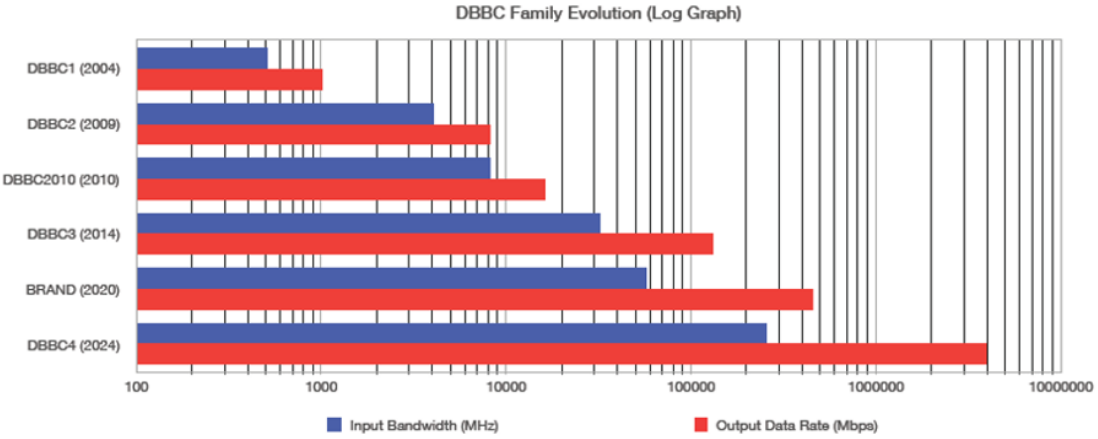

Fig. 1 Development of the max. input bandwidth and output data rates provided by the various models of the DBBC family of backends. The DBBC4 will increase the IF-bandwidth that can be processed by a factor of 8 in comparison with the current DBBC3 model.

from earlier DBBC installations. The main architectural difference in the DBBC4 is that it is a distributed system. Traditionally in radio-astronomical data acquisition systems, the digital back-end is well separated from the analogue part of the receiver, they being in widely-different physical locations. Typically the interface between analogue and digital domains, the sampler, is located with the digital system since these systems must run synchronously. This architectural choice was revisited n the BRAND-EVN project, where we split the traditional monolithic back-end into a network-attached ultra wideband digitizer front-end (called 'DI-FR-END') and a remote digital back-end; the front-end carries out simple digitization right at the receiver, while the bulk of signal processing is done by the digital backed at a different location where, e.g. cooling and RFI suppression is easier.

The choice to locate the sampler with the receiver offers us superior performance in terms of bandwidth, phase stability, higher dynamic range, and offers the greater ease of transporting digital rather than analogue signals to the backend area. Such digital data transport is robust and simple and can carry pure sampled or digital preprocessed data. This architecture comes with its challenges though, in terms of RFI shielding between the digital sampler and the nearby and very sensitive front end.

Although we envisage that most DBBC4 installations would use the distributed configuration between digital front- and back-ends, we have designed in the possibility to perform the entire functionality in a single unit in the back-end area. This can be useful in particular when existing receivers are already routed to this area, or when very high frequency (sub-millimeter) receivers are used, and they include frequency conversions in the antenna focal area. To accommodate such solutions, dedicated analogue conditioning and sampler modules are provided.

The distributed system is considered not only for the digital front-end, but includes other possible 'dislocated' elements in support of the more advanced functionalities offered by the DBBC4. These elements are sensors which collaborate with the DBBC4 main unit to provide information in support of new functionalities. Some of those will be described later in this document, while still a larger number will be defined during the period of development and even at a later stage when the DBBC4 is operational in the field.

The DBBC4 contains several functional entities already present in previous backend models, but introduces a number of new elements:

- 100GCoMo Module, analogue conditioning
- ADCore4 Module, A/D converter and digital processor
- FILA100G, data storage and network interface
- A-EYE, AI deep neural network controller
- DiFrEnd28, digital 28 GHz front-end,
- DiFrEndVGOS, implementation of the DiFrEnd28 dedicated to the VGOS observations to be used even in conjunction with a DBBC3
- DiFrEnd4T, digital 40 GHz front-end
- CONE, a number of different elements with dedicated functionalities to operate with the A-EYE Controller
- ROD, a number of different elements with dedicated functionalities to operate with the A-EYE Controller

The signal coming from the analogue front-end requires conditioning to be applied before being converted to digital format. For this purpose, the 100GCoMo module performs the functions of optimizing the amplitude, measuring the total power in pre-determined frequency ranges inside the input band, and applying ad-hoc filters. The output signal from the 100GCoMo is connected to the analogue input of the ADCore4.

Alternatively to the analogue input at the DBBC4, the analogue signal at the receiver can be digitized by the digital front-end with 28 GHz bandwidth DiFrEnd28 and be transported and inserted into the system through the digital input. Similarly a 5.5 GHz bandwidth in the range up to 40 GHz input can feed the DiFrEnd4T part.

The ADCore4 is the central element of the 'control room' system and is able to perform the double functionality of analogue to digital conversion and digital data processor. After conversion, the functionality as required by the particular observation is applied. The modes available are DSC, OCT, and DDC, as already well established in the previous versions of DBBC. Improvements to these modes are being applied, but still maintaining compatibility with the existing modes. More details are provided in section 4.

The data with the final bandwidth and data rate, ready to be transferred to the correlator or to be recorded, are sent via the FILA100G to prepare the final aggregate format in single- or multi-stream, depending on the output data rate. Before the composition of the final format it is possible to store an amount of data useful for the burst mode functionality. An additional possibility is offered by performing the data storage on external NVMe SSD units. Here, the direct connection net to PCI-e offers the possibility to skip any intermediate data transfer with great advantage to the writing data rate.

Notice particularly the newest addition in the DBBC family offered by the DBBC4, namely the Artificial Intelligence controller, called A-Eye. This has great potential in a number of functions it provides for both single-dish and VLBI observations, for example in RFI mitigation. To operate in real time, the controller can make use of a number of additional elements, named CONE and ROD. The first type supports the more complex functionalities to preprocess the signal than does the second, which simply forwards the required information to the mixed hardware-software deep neural network that performs the planned functionality. The A-Eye controller can then interact in both directions with the elements mentioned above to perform the required functionality. More details are described in the dedicated section of this document.

3 100GCoMo

The 100GCoMo is the analogue conditioning module responsible for coupling the analogue input signal (0-40 GHz) to the digital conversion step. A DBBC4 system can contain up to 4x 100GCoMo modules (each processing two analog input signals). The core functionalities of 100GCoMo are automatic gain control (AGC) or manual power level control for optimal conversion of the signal with the 8-bit converter, and total power measurement in defined frequency ranges. Optionally, the component can contain a section for the ad-hoc band definition used by the DiFrEnd4T sampling unit (see Sec. 8).

The communication with the general DBBC4 controller is realized through the traditional PCI method already adopted in previous DBBC systems.

A 100GCoMo prototype unit covering the frequency range up to 33 GHz has been built and is currently undergoing testing.

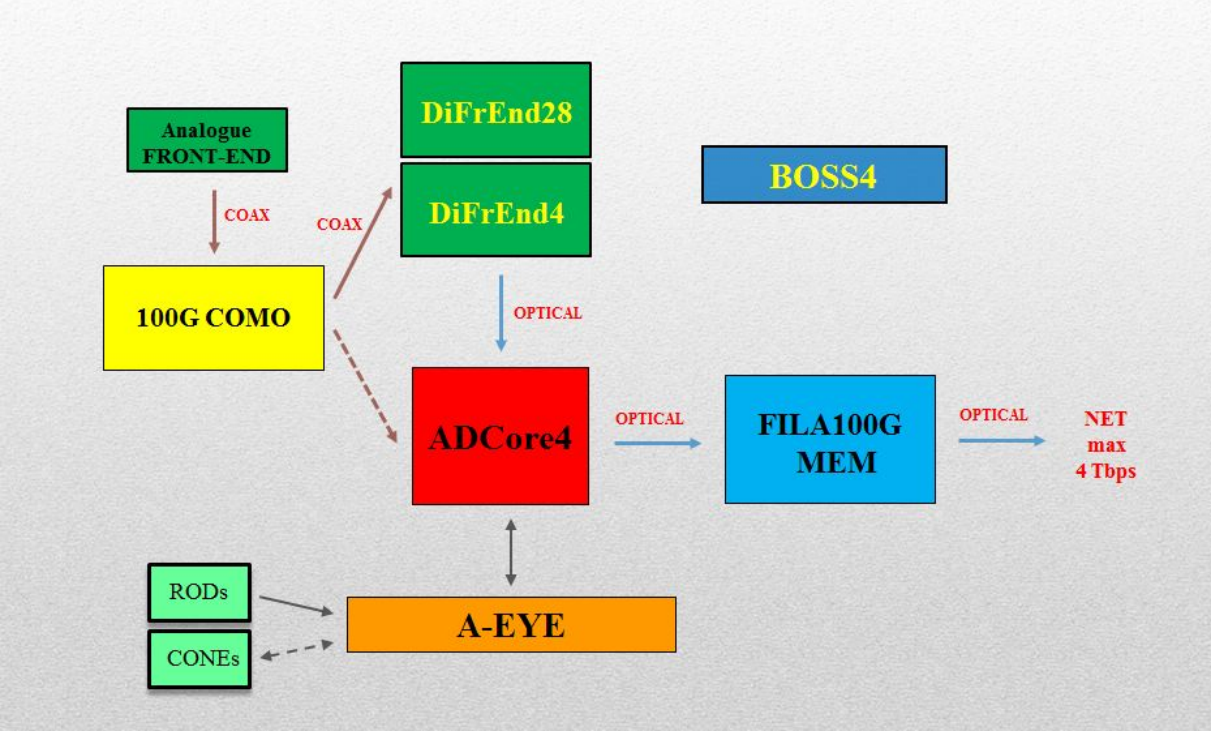

Fig. 2 Schematics of the DBBC4 VLBI System. The architecture is modular and can be adapted to the requirements of the individual telescope. The DBBC4 will allow one to process analogue IF signals as well as digital inputs. A novel AI controller can identify and mitigate RFI signals and can mark non-statistical noise signals for offline transient searches.

4 ADCore4

The ADCore4 is the central component of the DBBC4 and performs the analogue to digital conversion and further digital data processing. Like the previous models of the DBBC family, a DBBC4 can contain a variable number of up to 4x ADCore4 boards depending on the number of IFs to be processed.

The ADCore4 component can be operated in two modes: it can either accept 2x 28.8 GHz of *digitized* input bandwidth, or alternatively the ADCore4 can be equipped with an ADC stage (ADB4) performing direct sampling of two 0-28.8 GHz *analogue* input signals. The optional sampler component will make use of a high-end specialized ASIC device capable of sampling at 2x 57.6 Gsps. In both scenarios the data will be passed to the CORE4 FPGA element for the digital processing in the desired mode (DSC, OCT, DDC). The processed data will be sent out to the data recorders and/or the FILA10GMem component (see Sec. 5).

The ADCore4 PCB design has been finalized and production of a prototype is in realization.

5 FILA10GMEM

The FILA10G is an optional component that provides fast buffered memory for bust-mode operations and direct writing of the received packets on SSD NVMe (PCIe mode) disk modules. Additionally the component will support functionalities present in previous versions of the DBBC systems (FILA10G) like channel reordering as well as channel extraction allowing e.g. streaming of sub-bands to correlator for real-time fringe verification.

Because packets will be recorded on-the-fly onto the fast NVMe disks without any CPU data handling, we expect to achieve burst speeds of 56 Gbps/disk over 80 s and sustained output data rates of 13 Gbps/disk. The module can allocate a variable number of SSD NVMe units as required by the burst mode duty cycle/number of channels/data rate.

6 A-EYE Controller

Artificial Intelligence functionality meets VLBI technology. The A-EYE controller is an advanced component that implements artificial intelligence methodology to perform a number of critical operations for wide-band VLBI and single-dish operations in near-real-time, e.g. RFI recognition and mitigation, extraction of non-statistical-noise signals, recognition of human-like extraterrestrial emissions, and other similar applications.

The controller is a multi-CPU FPGA device optimized for these applications and will make use of pre-trained neural networks. The general development workflow consists of a session dedicated to selecting and training a suitable DNN (deep neural network) configuration. The configuration is then synthesized in a hardware DNN. The entire synthesized solution is run on the internal FPGA device. The A-EYE controller provides interfaces to interact with and drive special functionality in the other DBBC4 components. When a larger network is required, a direct link to a neural network operating e.g. in the cloud is possible.

To perform the AI operations, the A-EYE controller can interact with two types of supporter satellite elements: ROD and CONE. The ROD element is able to provide information, like temperature, total power, or other physical parameters. The CONE element acts like an edge processor to provide more elaborated information, like FFT-ready data, visual decoded data, sequence recognition, and similar preprocessed elements. A dedicated CONE functionality is operating on the ADCore4 board. In addition, training the DNN in piggy-back mode during ordinary system operation will be implemented to permit ad-hoc network generalization. A dedicated board was defined for this functionality.

7 DiFrEnd28 and DiFrEndVGOS

The DiFrEnd28 is a digital frontend component responsible for direct digitization and formatting of the analogue IFs. This device is optional and is necessary in situations where analogue transport of the broadband IF signals to the backend location over larger distances is not possible/desirable. This unit can be connected to the ADCore4 or can be fully independent. Indeed, the possibility to implement OCT and DDC filters on the internal FPGA would permit to directly connect to a VLBI recorded or to stream data to a correlator through a number of digital fibres.

For VGOS observations, a dedicated unit has been developed making use of the same hardware, but running a specialised firmware version. The so-called DiFrEndVGOS component can be connected to a DBBC3 backend in order to perform the full VGOS sampling in dual-polarization, close to the receiver thus greatly reducing the required analogue connections to the sampling point. The unit can also act as a standalone front- and back-end offering the possibility to provide a large number of tunable DDC channels.

The hardware design has been finalised and a prototype unit is in realization.

8 DiFrEnd4T

Complementary to the DiFrEnd28, the DiFrEnd4T is a standalone sampling unit which provides 5.5 GHz of sampled bandwidth in a range of 0-33 GHz. The desired portion of the band can be selected by an appropriate filter. In the case of the DBBC4 the DiFrEnd4T is planned to cover the frequency range 27.5-33.0 GHz. Similar to the DiFrEnd28, the internal FPGAs can produce filtered output streams that can be directly recorded or processed by a correlator.

9 Summary

The DBBC4 will provide a VLBI front/backend system that is offering solutions for the technical challenges in the era of multi-frequency, large-bandwidth VLBI observations. The development of the DBBC4 VLBI backend is progressing as planned, with the first prototype system components already available and undergoing testing. Additional units are either under construction or in the design stage. Integration of the various components into a first prototype system to be used for end-to-end testing is estimated to be realized by 2025.

The Level 1 Data: Availability and Benefits

A. Walenta, M. Goltz, D. Thaller, G. Engelhardt, D. Ullrich

Abstract Since 2022 the Level 1 Data, also referred to as SWIN files (as short for Swinburne) are available for the most recently observed sessions. The SWIN data is produced by the DiFX correlator, where the main set of data, i.e., called "visibility data", is provided along with various meta data. The source structure can be derived from the visibility data, which application was pointed out already to enhance the geodetic analysis. As we speak about a substantial amount of data, any exhaustive studies in geodetic analysis were limited until now due to the absence of the SWIN data. This contribution is intended to encourage the use of these data and corresponding meta data in the geodetic analysis. The availability of the SWIN files is provided by the IVS Data Centers at BKG and CDDIS as their best effort due to the high disk space demand. In addition to the currently observed sessions, the data transfer of the historical data stored at the Haystack correlator has been initiated from the "cold data storage" to CDDIS. The total amount of these data reaches up to 60TB, where about half of the data are available at the correlator in Bonn. Because of the technical requirements, we are interested in the discernible use of these data. The SWIN files provide the potential to be exploited far beyond the geodetic IVS community, and the geodetic analysis is expected to benefit vise versa. Driving by these reasons we are aiming to reach out to all relevant communities and to announce and advertise the availability of this new data set. The first activity in this direction was the meeting in Bologna 2023, where a broad variety of astrophysical researchers were present. The BKG Data Center team is eager to improve the services related to the SWIN data. Following our goals, we work on the support and facilitation of the barrier free data access as an essence of the SWIN data content understanding.

Keywords IVS, VLBI, datacenter, SWIN data, visibility

Federal Agency for Cartography and Geodesy, Division G1 - General Issues, Combination of Space Techniques, Richard-Strauss-Allee 11, 60598 Frankfurt a.M, Germany

1 General Information

SWIN files (as short for Swinburne) are the output of the DiFX (Distributed FX) correlator and contain the fringe visibility data, which IVS is referring to as the so-called "Level 1 Data".

The data set of SWIN files amounts to about 1000 sessions at the moment. Most of the sessions are correlated by the correlators at WASH, BONN and HAYS as it is shown in Figure 1. The majority of the sessions with SWIN data available corresponds to R1 (WASH), R4 (BONN), VGOS sessions and intensive sessions. More data from the earlier years are expected to be provided from the "cold" storage at HAYS and BONN correlators during next years on their earliest convenience as a session at a time. The VGOS sessions are shared in the recent years among six correlators including WASH, BONN, VIEM, SHAO and WETZ in addition to HAYS initially. The local sessions at Onsala are correlated at correlator OSO providing outstanding contribution to ITRF2020. The GSI center is responsible for the INT2 session correlation and analysis as well as VGOS-INT-B in 2022 between Onsala and Ishioka. As it can be seen, GSI and SHAO share the processing of the Australian observing program as well as the other special types of S/X sessions. New correlators have recently been

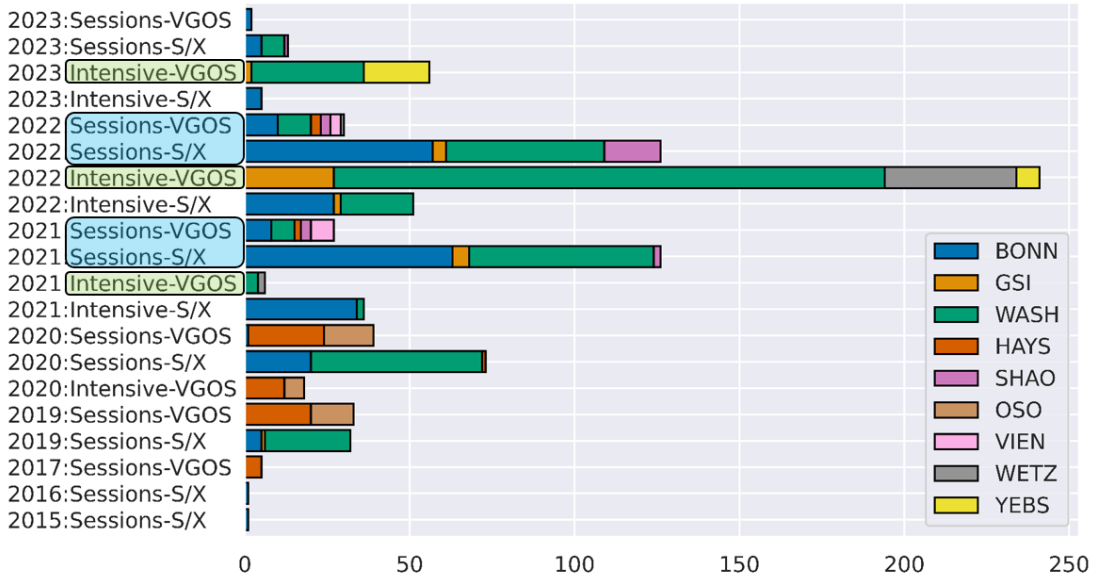

Fig. 1 Availability of Level 1 Data depending on the session type, year and correlator. The figure shoes the status as of June 2023.

established at YEBS and WETZ, and they produce the Level 1 Data for the intensives 'Y' and 'S2', respectively.

2 Use of Meta Data of Level 1 Data

The most important content of the Level 1 Data set is the visibility data. The visibility data set is supplied with very valuable meta data. These meta data is essential if one wants to make use of the visibility data in the geodetic analysis.

In this paper we attempt to make use of the meta data provided along with the Level 1 Data by considering the single scan characteristics. A single scan can be described, for instance, by the scan length and reference epoch. Both informations are contained in the meta data of the Level 1 Data. These two parameters are chosen in order to have common characteristics among the VLBI observation processing chain, i.e., starting with the scheduling and covering all steps up to the geodetic data analysis. As shown in Fig. 2, scan-wise scheduling, observation and correlation are subsequent parts within the VLBI scan processing chain. Subsequently, the group delay analysis follows as the very last step. During this step, epoch-wise group delay residuals are processed, but

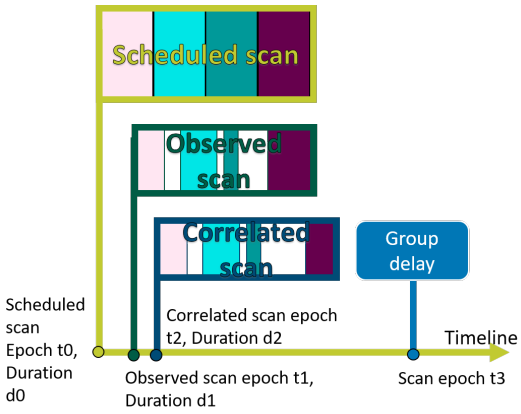

Fig. 2 The single VLBI scan processing chain.

this final step of the VLBI analysis for generating the desired geodetic VLBI-based products for external use is carried out without making use of the meta data like scan length.

The first steps of this chain, however, are opposed to this practice quite substantially. The scan epoch and duration are defined thoughtfully during scheduling. The field system controls the antennas to follow this scheduling sharply. Next, the correlation process aims to generate the best-possible results out of the observational effort. Consequently, the theoretical scan

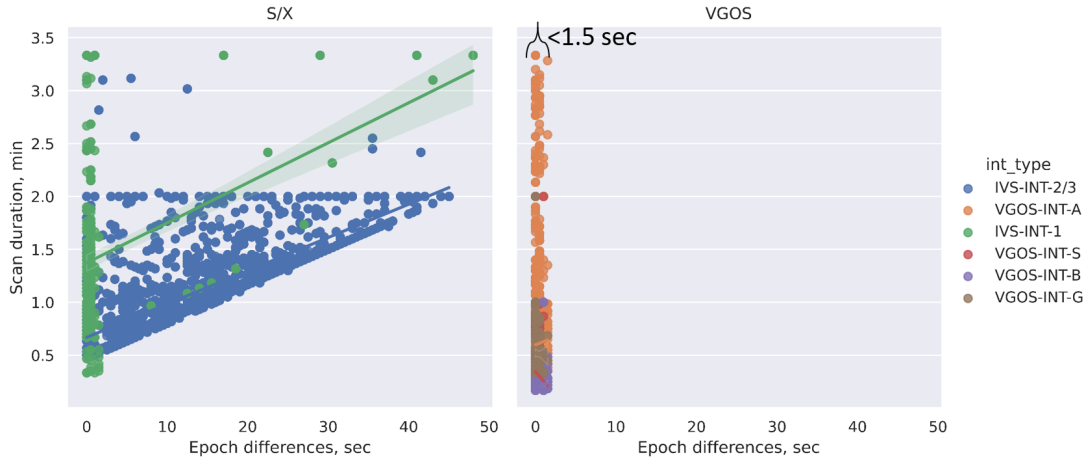

Fig. 3 Epoch differences are represented in seconds between correlated epoch t2 and group delay (analysis) epoch t3 taking after accounting for ½ scan duration. Different session types are highlighted accordingly to the figure legend.

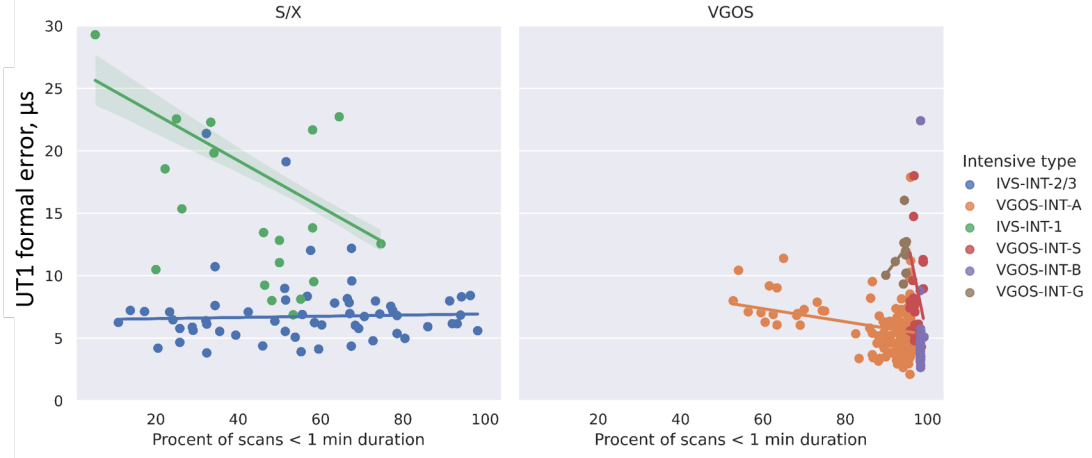

Fig. 4 Percent of scans in one session, which duration is under 1 minute, is shown in dependence of the obtained dUT1 formal errors.

duration and epoch may vary from the characteristics given in the scheduling file, observations and meta data of the Level 1 Data as the output of the correlation processing.

In this paper, we compare the scan duration and epoch provided by the scheduling file, the meta data of the Level 1 Data and the vgosdb. In the available data set of Level 1 Data, the SWIN files of shorter intensives are considered only for illustration purposes.

The correlated scan duration d2 is identical to the scheduled scan duration d0 among all intensive types. The only exceptions are the IVS-INT-2/3 sessions, where the differences reach up to 80 seconds for the scans of 30 and 120 second duration. The epochs of the considered scans t2-t0 show differences below the level of 4 milliseconds. The analyzed group delay inherit the scan duration of the correlated scan by definition. However, the epochs of the group delay t3 are different from epoch of the correlated scan t2 by half of the scan duration (Figure 3). In case of VGOS sessions the differences t3-t2 stay below the level of 1.5 seconds. Most of these differences are reduced for the IVS-INT-1 sessions as shown on the left of Figure 3, while the IVS-INT-2/3 sessions show a more complicated dependency.

Finally, the formal errors of the main estimated parameter from the intensive sessions, i.e. dUT1, is considered (Figure 4) as a function of the percent of observations for those scans with a duration below 1 minute.

A decrease of the dUT1 formal errors may be seen for some session types, i.e. INT1.

3 Summary and Outlook

This paper is intended to draw attention of the IVS community to the new data type provided by the IVS Data Centers at BKG and CDDIS, i.e., the so-called Level 1 Data. Since 2022, the IVS Data Centers provide SWIN files at their best effort as this data set has very high demands related to disk space. The Level 1 Data is available for the most recently observed intensives and 24-hour sessions. The data of the earlier years are to be provided in future by the responsible correlators at their earliest convenience.

The IVS community realises the outstanding effort in observing operationally on a global network, so that the availability of the Level 1 Data facilitates its dissemination. In its own turn, the appropriate extension of the IVS Data Centers needs to be supported by the users to demonstrate the necessity of storing these huge data sets. While the dissemination characteristics are not defined yet, all possible references of the data sources are encouraged.

The most important advantage when providing the Level 1 Data is that the visibility data is included, which the basis for studying the variable source structure. The impact of the source structure on the geodetic VLBI observation and the geodetic products derived thereof is demonstrated by Anderson and Xu (2018). The IVS community is encouraged to make further use of the Level 1 Data in order to pinpoint the impact on the geodetic products.

In this paper the meta data of the Level 1 Data is considered as the essential basis for understanding the content of Level 1 Data. The chosen characteristics of the scan, i.e., scan epoch and duration, have allowed us to understand better how the data are treated throughout the entire VLBI processing chain starting with the observations and finishing with the analysis.

References

M. Goltz, A. Girdiuk, D. Thaller (2022), Current Status at BKG IVS Data Center, 2023, EVGA Proceedings.

Anderson, J. M., & Xu, M. H. (2018). Source structure and measurement noise are as important as all other residual sources in geodetic VLBI combined, Journal of Geophysical Research: Solid Earth, 123, 10,162–10,190. https://doi.org/10.1029/2018JB015550

Absolute orientation of Galileo orbits from simulated VLBI and GNSS observations

H. Wolf, J. Böhm, U. Hugentobler

Abstract The possibility of observing Galileo satellites with Very Long Baseline Interferometry (VLBI) telescopes may become possible in future as there are plans to put VLBI transmitters on these satellites. This would not only bring improvements for products, such as the International Terrestrial Reference Frame (ITRF), but would also allow to determine the absolute orientation of the satellite orbit with respect to the celestial frame. In this study, we investigate the determination of the right ascension of the ascending node Ω of a Galileo satellite orbit using simulated VLBI observations to quasars and a Galileo satellite. Therefore, a schedule including VLBI observations to a satellite covering an ultra short orbit arc of 40 minutes of the satellite surrounded by quasar observations is created, simulated and analysed. There are two different analysis options examined, first estimating Ω in a shorter interval of ten minutes and secondly estimating only one value for the whole 40 minute satellite period. The repeatability of Ω by estimating it in a ten minute interval is between 0.3 and 0.5 mas which corresponds to 4.5 cm and 7.5 cm at the altitude of the orbit. If there is only one value estimated the repeatability is below 0.2 mas which corresponds to approximately 3 cm at the altitude of the orbit.

Keywords Galileo, satellite orbits, VieVS, absolute orientationlo

Helene Wolf · Johannes Böhm
TU Wien, Department for Geodesy and Geoinformation, Wiedner Hauptstraße 8-10, 1040 Wien, Austria

Urs Hugentobler
TU München, Institute for Astronomical and Physical Geodesy, Arcisstr. 21(0506)/III, 80333 München, Germany

1 Introduction

The mounting of a Very Long Baseline Interferometry (VLBI) transmitter (VT) on one or more Galileo satellites enables to observe both, satellites and quasars, with VLBI antennas. Observing a satellite with more than one space geodetic technique permits to determine and use so called space ties. This allows high precision tying of the space geodetic techniques if the tie vectors on the satellite are known with high accuracy. Wolf and Böhm (2023) showed that having VT on Galileo satellites will contribute to an improvement of the International Terrestrial Reference Frame (ITRF) (Altamimi et al., 2023), which is a product of combining all four space geodetic techniques, namely VLBI, Satellite Laser Ranging (SLR), Global Navigation Satellite Systems (GNSS) and Doppler Orbitography by Radiopositioning Integrated on Satellite (DORIS). Currently, the ITRF's accuracy is still limited due to errors in local ties on ground (Altamimi et al., 2016).

Further, VLBI observations to satellites and quasars allow Precise Orbit Determination (POD) of the satellites (Klopotek et al., 2020). This can be realized by estimating the position of the satellite in the orbit fixed satellite system (NTW-frame). For that, three so-called Dilution of Precision (DOP) factors representing the sensitivity of a VLBI observation towards the individual components of the satellite position are introduced (Wolf et al., 2022).

However, as VLBI is observing distant celestial objects and therefore realizing the celestial reference system, VLBI observations to satellites permit connecting the satellite orbit with this frame. This allows the determination of the absolute orientation of the satellite constellation with respect to the International Celestial Reference Frame (ICRF) (Charlot et al., 2020).

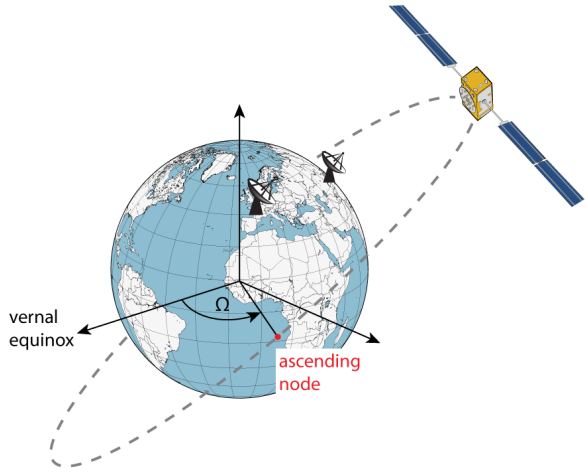

Fig. 1 Illustration of VLBI radio telescopes observing a satellite in its orbit.

Currently, satellites are routinely observed with GNSS, SLR and DORIS but VLBI observations are still missing in satellite geodesy. Anyway, there are plans to mount a VLBI transmitter on board of Galileo satellites which would enable to carry out VLBI observations to these satellites. Moreover, the European Space Agency (ESA) plans the launch of a co-location satellite called Genesis for 2027/2028. This satellite will combine all four space geodetic techniques orbiting the Earth in a polar orbit with 6000 km altitude (Delva et al., 2023).

This study investigates the estimation of the orbital parameter right ascension of ascending node Ω which is related with the absolute orientation of the satellite around the polar axis. This is done using simulated VLBI observations and partial derivatives of the state vector with respect to Ω obtained from the Bernese GNSS Software (Dach et al., 2015). These partial derivatives are introduced in the VLBI analysis and used for estimating the right ascension of the ascending node in the least squares adjustment. In section 2 we describe the network and settings of the scheduling, simulation and analysis of the VLBI observations and the determination of the partial derivatives. Section 3 shows the results and section 4 provides the summary, discussion and outlook.

2 Method

The study is based on a network of nine VLBI Global Observing System (VGOS) (Petrachenko et al., 2012) type stations (Fig. 2) and considers one satellite of the European Global Navigation Satellite System Galileo GSAT0101 (E11). The session starts on January 1, 2021 00:00:00 UTC with a 24 hour duration. We investigate the scenario of covering an ultra short orbit arc with VLBI observations by applying two different analysis options.

2.1 Scheduling

The creation of the schedules is done using the software VieSched++ (Schartner and Böhm, 2019). This software has been equipped with a satellite scheduling module which allows to schedule quasar observations together with satellite observations in an either manual or automatic fashion (Wolf, 2021). In this study the generation of the schedule including satellite observations covering the ultra short orbit arc is done manually. Therefore, during a 40 minute period, from 10:20 UTC to 11:00 UTC, for all five stations for which the satellite is visible satellite scans are scheduled every 90 seconds. For all the stations for which the satellite is not visible during that time quasar scans are scheduled and also the remaining part of the schedule is filled with quasar scans. As the network consists only of VGOS type stations the scan length of satellite and quasar scans is set to 10 seconds in order to meet the VGOS approach of a large number of short scans well distributed over the sky at the individual stations.

2.2 Simulation

The schedules are simulated 1000 times using the Vienna VLBI and Satellite Software (VieVS) (Böhm et al., 2018). These simulations are carried out by using three main error sources, which are tropospheric turbulence, clock errors, and the thermal noise (Pany et al., 2011). The tropospheric refractive index structure constant C_n of all stations is set to 1.8×10^{-7} m $^{-1/3}$ with a scale height of 2000 m (Nilsson et

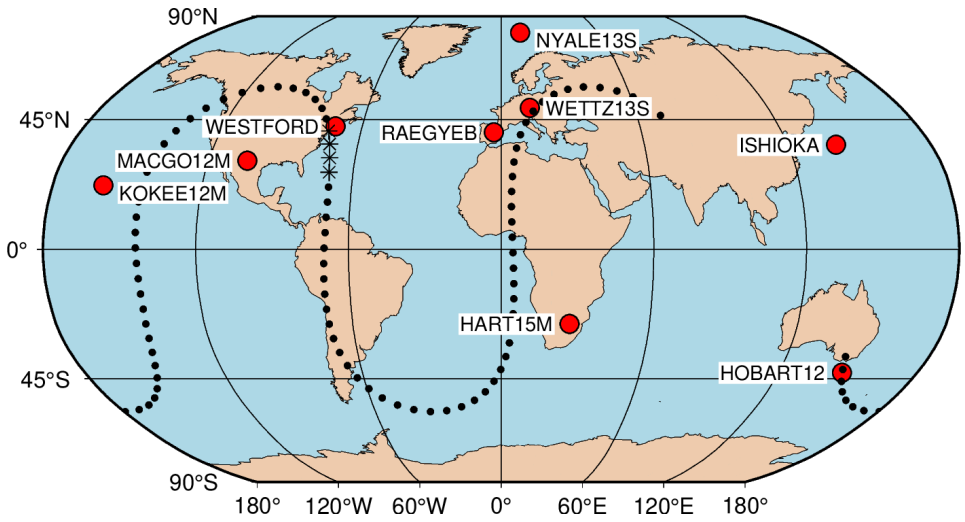

Fig. 2 VGOS station network considered in this study and ground track of the satellite GSAT0101 (E11) during 24 hours starting on January 1, 2021 at 0 UT. The dots represent the ground track of the satellite at a fifteen-minute interval. The asterisks represent the position of the satellite during the observation period.

Fig. 3 Illustration of the scheduling approach. The schedule consists of a 40 minute period of satellite scans surrounded by quasar scans.

al., 2007). The stochastic error of the station clock is simulated as the sum of a random walk and an integrated random walk assuming an Allan Standard Deviation of 1×10^{-14} after 50 minutes (Herring et al., 1990). Additionally, white noise of 10 ps for quasar and satellite observations is added.

2.3 Partial Derivatives

The determination of the partial derivatives of the observable τ with respect to Ω is shown in Figure 4. Therefore, files obtained from the Bernese GNSS Software (FSO and FRP files) are loaded in VieVS. These files include the orbits of the satellites as state vectors and the derivatives of the state vectors with respect to the orbital parameters among other parameters. Within VieVS the partial derivative of the observable τ with respect to the position vector of the satellite is determined. Further, it is used to form the dot product with the partial derivative of the position vector with respect to Ω in order to retrieve the partial derivative of the observable τ with respect to Ω, see Eq. 1.

$$\frac{\partial \tau}{\partial r(t)} \cdot \frac{\partial r(t)}{\partial \Omega} = \frac{\partial \tau}{\partial \Omega} \tag{1}$$

This parameter is introduced in the least squares adjustment and used to estimate piecewise linear offsets (PWLOs) of the Right Ascension of Ascending Node from the a-priori orbit.

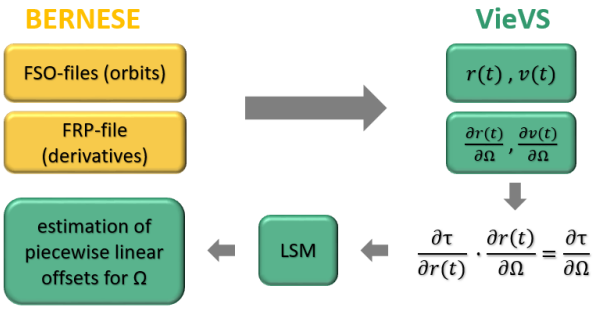

Fig. 4 Flowchart of the concept determining the partial derivatives of the observable τ with respect to Ω in VieVS using data from Bernese and estimating piecewise linear offsets from the a-priori orbit.

2.4 Analysis

The simulated observations are analysed using VieVS by estimating Ω as PWLOs from the a-priori orbit. The a-priori orbit is introduced by using SP3 files. During the analysis the station and source coordinates are fixed to their a priori values and all five Earth orientation parameters are estimated as constant parameters per session. The precision of the estimated right ascension of ascending node of the orbit arc is assessed and evaluated in terms of the repeatability and the mean formal error. Ω is estimated either in shorter, e.g. ten minute intervals, or one value for the whole satellite observation period which has a duration of 40 minutes.

3 Results

Figure 5 shows the repeatability and the mean formal error of the estimated piecewise linear offsets for Ω from the a-priori orbit. If it is estimated within a ten minute interval the repeatability and the mean formal error are higher than if there is only one value estimated for the whole 40 minute period.

This is due to the smaller amount of observations used for the estimation applying a shorter estimation interval rather than using all observations as it is done if only one offset is estimated.

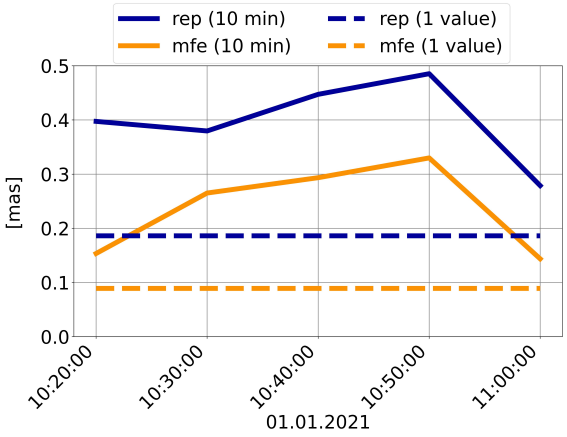

Fig. 5 Repeatabilities (blue) and mean formal errors (yellow) of the estimated PWLO of Ω by either estimating it in a ten minute interval (solid lines) or only one value for the whole observation period (dashed lines).

For the shorter estimation interval both, repeatability and mean formal error, have a peak in the middle of the interval. This is related to the worse estimation of the troposphere parameters (zenith delays and gradients) coming from the worse sky coverage at the individual stations as these only observe the satellite during that time period.

However, when estimating Ω in a ten minute interval the repeatability is below 0.5 mas which corresponds to approximately 7.5 cm at the altitude of the orbit. The repeatability for estimating one value for the whole period is below 0.2 mas which corresponds to approximately 3 cm at the altitude of the orbit.

4 Summary and Discussion

In this study, the absolute orientation of a Galileo satellite orbit is estimated using simulated VLBI observations to one satellite and quasars. This is possible as VLBI enables the connection between the satellite orbit and the celestial frame. Therefore, a schedule including VLBI observations to the Galileo satellite GSAT0101 (E11) covering an ultra short orbit arc using a nine station VGOS network is created and simulated. Further, in the analysis partial derivatives of the observable τ with respect to Ω are retrieved using data obtained from the Bernese GNSS Software. These parameters are introduced in the least squares adjustment for estimating piecewise linear offsets from the a-priori orbit for Ω. The analysis is done by using two different estimation intervals, on the one hand a shorter interval with ten minutes and on the other hand estimating only one value for the whole 40 minute satellite observation period.

The estimates are assessed based on the repeatability and the mean formal error. The results clearly indicate that the repeatability is higher, between 0.3 and 0.5 mas, if the parameter is estimated in a shorter interval than only once for the whole time period, when it is between 0.15 and 0.35 mas. This is linked with the amount of observations used for the estimation as there is only a part of the observations used for the individual estimates if the interval is shorter and all observations are used in case only one value is estimated for the overall time period.

This study also indicates that quasar scans are important for the determination of the troposphere as the repeatability and the mean formal error become higher in the middle of the interval. This is related to the missing quasar scans as the stations only observe one satellite and the therefore worse sky coverage during that time.

In future, the results from VieVS and Bernese could be combined based on the normal equation level by using the ADDNEQ2 module from Bernese. This would allow to retrieve fully consistent results based on VLBI and GNSS observations.

Acknowledgements

The authors thank the Austrian Science Fund (FWF) for supporting this work within project VLBI2Galileo (P 33925N).

References

Altamimi Z, Rebischung P, Collilieux X et al. (2023) ITRF2020: an augmented reference frame refining the modeling of nonlinear station motions. Journal of Geodesy 97, 47 (2023). https://doi.org/10.1007/s00190-023-01738-w

Altamimi Z, Rebischung P, Métivier L, and Collilieux X (2016), ITRF2014: A new release of the International Terrestrial Reference Frame modeling nonlinear station motions, J. Geophys. Res. Solid Earth, 121, 6109– 6131, doi:10.1002/2016JB013098.

Böhm J, Böhm S, Boisits J, Girdiuk A, Gruber J, Hellerschmied A, Krásná H, Landskron D, Madzak M, Mayer D, McCallum J, McCallum L, Schartner M, Teke K (2018), Vienna VLBI and Satellite Software (VieVS) for Geodesy and Astrometry, Publications of the Astronomical Society of the Pacific, 130, 044503, doi:10.1088/1538-3873/aaa22b.

Charlot P, Jacobs C S, Gordon D, Lambert S, de Witt A, Böhm J, Fey A L, Heinkelmann R, Skurikhina E, Titov O, Arias E F, Bolotin S, Bourda G, Ma C, Malkin Z, Nothnagel A, Mayer D, MacMillan D S, Nilsson T, Gaume R (2020), The third realization of the International Celestial Reference Frame by very long baseline interferometry, A&A 644:A159, doi:10.1051/0004-6361/202038368.

Dach R, Lutz S, Walser P, Fridez P (Eds); 2015: Bernese GNSS Software Version 5.2. User manual, Astronomical Institute, University of Bern, Bern Open Publishing. DOI: 10.7892/boris.72297; ISBN: 978-3-906813-05-9.

Delva P, Altamimi Z, Blazquez A et al. GENESIS: co-location of geodetic techniques in space. Earth Planets Space 75, 5 (2023). https://doi.org/10.1186/s40623-022-01752-w

Herring T, Davis J, Shapiro I (1990) Geodesy by radio interferometry: The application of Kalman Filtering to the analysis of very long baseline interferometry data, Journal of Geophysical Research, 95, 12561-12581, doi:0.1029/JB095iB08p12561.

Klopotek G, Hobiger T, Haas R (2020), Geodetic VLBI for precise orbit determination of Earth satellites: a simulation study, Journal of Geodesy 94:56, doi:10.1007/s00190-020-01381-9

Nilsson T, Haas R, Elgered G (2007), Simulations of atmospheric path delays using turbulence models (2007), Simulations of atmospheric path delays using turbulence models, Proceedings of the 18th European VLBI for Geodesy and Astrometry Working Meeting, 175–180.

Pany A, Böhm J, MacMillan D, Schuh H, Nilsson T, Wresnik J (2011) Monte Carlo simulations of the impact of troposphere, clock and measurement errors on the repeatability of VLBI positions, Journal of Geodesy, 85, 39–50, doi:10.1007/s00190-010-0415-1.

Petrachenko W, Schuh H, Niell A, Behrend D, Corey B, (2010), VLBI2010: Next generation VLBI system for geodesy and astrometry, In: Kenyon, S., Pacino, M., Marti, U. (eds) Geodesy for Planet Earth, International Association of Geodesy Symposia, vol 136, Springer, Berlin, Heidelberg, doi:10.1007/978-3-642-20338-1_125.

Schartner M and Böhm J (2019), VieSched++: A New VLBI Scheduling Software for Geodesy and Astrometry, Publications of the Astronomical Society of the Pacific, vol. 131, no. 1002. IOP Publishing, p. 084501, Jun. 18, doi: 10.1088/1538-3873/ab1820.

Wolf H, Böhm J, Schartner M, Hugentobler U, Soja B, Nothnagel A (2022), Dilution of Precision (DOP) factors for evaluating observations to Galileo satellites with VLBI, Proceedings of IAG Scientific Assembly 2021, International Association of Geodesy Symposia, Springer, in press.

Wolf H (2021), Satellite Scheduling with VieSched++, Department für Geodäsie und Geoinformation / Höhere Geodäsie.

Wolf H, Böhm J (2023), Optimal distribution of VLBI transmitters in the Galileo space segment for frame ties, submitted to Earth, Planets and Space

Recent developments at Metsähovi Geodetic Research Station

N. Zubko, J. Eskelinen, J. Näränen, N. Kareinen, U. Kallio, H. Koivula, M. Poutanen, J. Peltoniemi

Abstract The Metsähovi Geodetic Research Station, a Global Geodetic Observing System core station, has undergone a major renovation and upgrade of the geodetic measurement instrumentation and general station infrastructure in recent years. We report here the current status of the Metsähovi VGOS telescope system and the related activities.

Keywords VGOS, radio telescope

1 Introduction

The Metsähovi Geodetic Research Station (MGRS) is located in Southern Finland, near the capital area. It is one of the northernmost geodetic core stations in the station network of the International Geodetic Association's (IAG) Global Geodetic Observing System (GGOS). During the last decade, MGRS has modernized the Global Navigation Satellite System (GNSS) measurement systems and obtained a modern Satellite Laser Ranging (SLR) system and a dedicated geodetic Very Long Baseline Interferometry (VLBI) system (Fig. 1). The SLR and VLBI systems are currently under commissioning. Major infrastructure renovation has also been carried out at the station to meet the requirements of the new instrument systems. Most recent upgrades and activities at the MGRS are described in detail in Poutanen et al. (2023). In this report, the current status of the MGRS VLBI Global Observing System (VGOS) telescope and its related activities are presented.

Department of Geodesy and Geodynamics, Finnish Geospatial Research Institute (FGI), National Land Survey of Finland, Vuorimiehentie 5, Espoo, 02150, Finland

2 VGOS telescope status

The MGRS VGOS telescope was constructed during 2018-2020. A broadband receiver with a quad-ridge feed (QRFH) was installed in 2019. The receiver, as well as the phase and the cable calibration systems were manufactured by IGN-Yebes (Spain) technology development centre. The initial tests and calibration of the antenna and the receiver were conducted during 2020-2022.

The RFI circumstances at Metsähovi are similar to the RFI conditions at other VGOS stations. An RFI investigation on the site revealed numerous interference sources disturbing especially in the 2-3 GHz frequency band. High-pass filters with 3 GHz cut-off are needed to avoid the saturation of the fiber link. However, further measures are required to reduce RFI influence in the wider VGOS band. RFI mitigation work is ongoing.

The VGOS signal chain includes DBBC3-backend and a Flexbuff recording system, which are currently being tested and integrated into the whole chain. The current Flexbuff capacity is 440 TB and it uses *jive5ab* software. The station's internet connection link was upgraded to 100 Gb/s in 2021, making it possible to transfer bulk VGOS data with fast speed.

Special attention has been dedicated to the monitoring of the antenna reference point stability. The telescope dish in our VGOS antenna is mounted on the top of a steel pedestal. The pedestal houses a cable wrap system in the bottom and an antenna control unit on the upper level. Temperature sensors have been in-

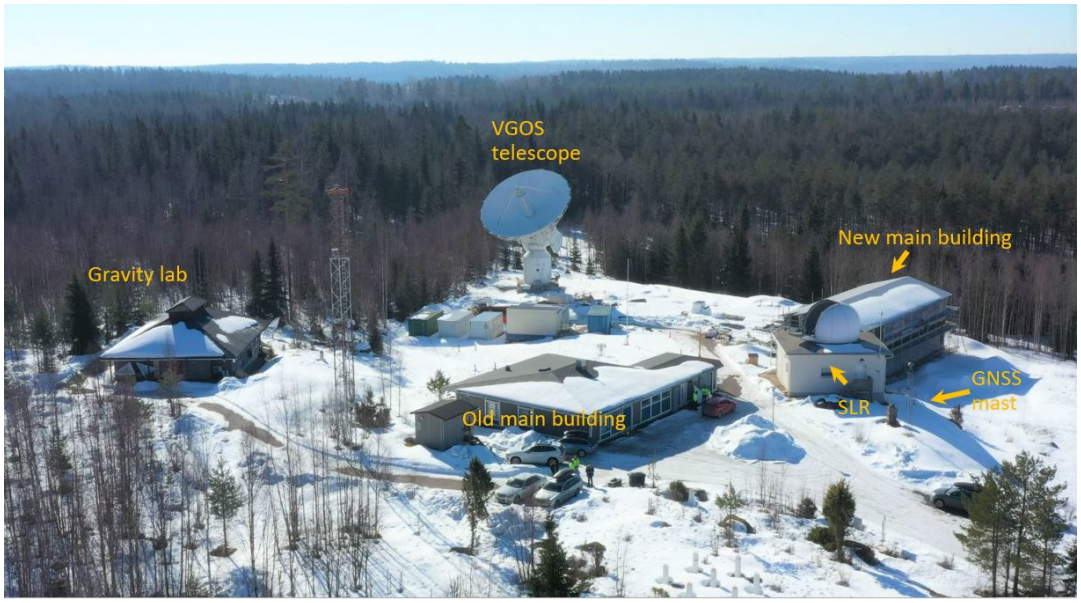

Fig. 1 Metsähovi Geodetic Research Station.

stalled inside the pedestal to monitor its temperature stability. Analysis of the thermal stability of the telescope steel pedestal revealed that additional insulation of the pedestal was required to avoid the effect of uneven temperature distribution and its rapid fluctuations, mainly, due to solar radiation. At the end of 2022 the telescope pedestal was covered with an additional insulation shell (Fig. 2). Initial analysis of the temperature sensor data shows improvement of the pedestal temperature stability, however the pedestal's heating/conditioning system requires further optimisation for efficient and automated temperature control.

Fig. 2 Work on the telescope pedestal insulation (October 2022).

3 Local tie measurements

VGOS telescope dish is equipped with two GNSS antennas, which are used for kinematic GNSS local tie measurements. Similar work was made earlier with a radio telescope owned by neighboring Aalto University Kallio et al. (2012). The MGRS VGOS telescope was also connected to the local survey network with tachymeter measurements, that refer to the terrestrial local tie measurements. The terrestrial and GPS-based monitoring local tie measurements were done during 2020-2021 and results were reported in Kallio et al. (2023a) and Kallio (2023b).

Fig. 3 New main building.

4 Other related activities

A new main building for the research station was constructed during 2021-2022 (Fig. 3). The building houses a dedicated laboratory space for the instrumentation maintenance work and a temperature-controlled server/electronics room. The new building has an RFI shield-mesh (Faraday cage) installed on all outer walls, floor, ceiling, and on some inner walls to prevent RFI towards the radio telescope and the internal electronics. Commissioning of the new building is in progress.

FGI, together with Aalto University Metsähovi Radio Observatory, have been participating in IVS geodetic VLBI observations utilizing Aalto university radio telescope (Mh) since 2004. The Aalto telescope is dedicated to astronomical observations and only a few geodetic sessions per year were performed there. Mainly *IVS-T2* and *EURO* sessions were observed in the past. Those observations were interrupted in 2022 due to an S/X receiver malfunction. It was then decided to direct all available resources towards commissioning the VGOS system, which meant discontinuing the legacy observations. Currently, the regular IVS geodetic observations are not foreseen with the legacy telescope in the future.

5 Outlook

Work on the integration of the signal chain components and the commissioning of the whole VGOS system is ongoing. The backend will be relocated from the old premises to the new main building after the instrument/server room is ready to accommodate the equipment (winter 2023/2024). The reference point stability requires further monitoring and work, including improvement of the heating and thermal stability of the whole antenna. The new tilt meters will be installed in the telescope azimuth cabin. The usability of the tilt meter data will be investigated. Work on building a proper time and frequency reference for the whole station is also ongoing.

References

Kallio U and Poutanen M (2012) Can we really promise a mm accuracy for the local ties on a Geo-VLBI Antenna. In: Geodesy for Planet Earth. Springer Science Business Media, pp 35–42. doi: https://doi.org/10.1007/978-3-642-20338-1-5.

Kallio U, Eskelinen J, Jokela J, Koivula H, Marila S, Näränen J, Poutanen M, Raja-Halli A, Rouhiainen P, Suurmäki H (2023a) Validation of GNSS-based reference point monitoring of the VGOS VLBI telescope at Metsähovi. In: 5th Joint International Symposium on Deformation Monitoring (JISDM), 20–22 June 2022, Valencia, Spain. doi: https://doi.org/10.4995/JISDM2022.2022.13691.

Kallio U (2023b) Towards daily-based local ties at Fundamental Geodetic Sites - Development of local tie processes as a part of the renovations at Metsähovi Geodetic Research Station. Doctoral thesis, Aalto University, School of Engineering. http://urn.fi/URN:ISBN:978-952-64-1403-4.

Poutanen M, Bilker-Koivula M, Eskelinen J, Kallio U,Kareinen N, Koivula H, Lahtinen S, Näränen J, Peltoniemi J, Raja-Halli A, Rouhiainen P,and Zubko N (2023) Upgrading the Metsähovi Geodetic Research Station. In: International Association of Geodesy Symposia, Springer, Berlin, Heidelberg. doi: https://doi.org/10.1007/1345-2023-203.